Why do Growing Cracks Branch? An Optical Investigation of Brittle Monolithic and Bilayer Transparencies Under Stress Wave Loading

by

Balamurugan Meenakshi Sundaram

A dissertation submitted to the Graduate Faculty of
Auburn University
in partial fulfillment of the
requirements for the Degree of
Doctor of Philosophy

Auburn, Alabama
May 6, 2017

Keywords: Transparent Polymers and Ceramics; Layered Structures; Dynamic Fracture; Crack Branching; Optical Measurements; Digital Gradient Sensing

Approved by

Hareesh V. Tippur, Chair, McWane Professor of Mechanical Engineering
Jeffrey C. Suhling, Quina Distinguished Professor of Mechanical Engineering
James S. Davidson, Gottlieb Professor of Civil Engineering
Maria L. Auad, Associate Professor of Chemical Engineering

Abstract

Understanding the fracture mechanics of materials due to stress wave (or impact) loading under combined tensile and shear (mixed-mode) conditions is important for two opposing reasons: (a) for creating impact resistant structures; e.g., aircraft canopy, (b) for inducing maximum damage with minimum effort; e.g., mining and pulverization. In transparent armor systems such as fighter aircraft canopies and automotive windshields, layering is often used to promote crack branching to create more surface area and increase energy absorption.

In this context, the first part of this research deals with mixed-mode dynamic fracture mechanics investigation of relatively brittle poly(methyl methacrylate) (PMMA) and ductile polycarbonate (PC), the two most common structural polymers used for transparent armor construction. As these fracture events last only a few hundred microseconds, quantifying the mechanical fields in real-time and over the whole field of interest is rather challenging. A full-field, non-contacting, optical measurement technique called Digital Gradient Sensing (DGS) used in conjunction with ultrahigh-speed photography (up to 1 million frames per second) has been extended in this dissertation for measuring the mixed-mode fracture parameters for PMMA and PC.

Next, the dynamic interactions of fast fracture fronts with weak interfaces oriented normally to incoming cracks in nominally homogeneous PMMA bilayers with discrete planes of weakness are studied. The interfaces drastically perturb crack growth behavior

resulting in higher absorption of energy by exciting mixed-mode crack growth, crack branching, and fragmentation. Using measured fracture parameter histories, the energy release rate of growing cracks have been quantified in bilayers with different degrees of interfacial weakness. The mechanics of crack penetration vs. branching at a weak interface is further investigated by focusing on the effect of interface location in PMMA bilayers and the associated crack-tip parameters on ensuing fracture behaviors for constant impact velocity. The results show that the crack path selection at the interface and the second layer are affected by the location of the interface within the bilayer. Using fracture parameter histories, reasons for direct crack penetration instead of branching are mechanistically explained and visual evidence is offered. The explanation is further validated by increasing the impact velocity to promote crack branching in configurations that produced direct penetration at a lower impact velocity.

The experimentally challenging problem of dynamic crack growth and branching in monolithic glass is explored in the next part of the dissertation. Plate glass being a stiff and extremely brittle material, deformations are highly localized to the crack-tip while crack speeds exceed 1600 m/s (or 3600 mph). A methodology to make full-field optical measurements using DGS in conjunction with ultrahigh-speed photography (> 1 million frames per second) is developed. The method has been first calibrated under both quasi-static and dynamic loading conditions for soda-lime glass. Subsequently, the crack branching problem in glass is tackled. A potential mechanism for crack branching phenomenon is proposed based on empirical evidence and elasto-dynamic fracture mechanics of brittle solids.

Lastly, the fracture behavior of transparent graft Interpenetrating Polymer Networks (graft-IPNs) as alternative lightweight armor materials is examined. The graft-

IPNs with a copolymer (CoP) made from PMMA as the stiff phase and polyurethane (PU) as the ductile phase with varying CoP:PU ratios and two molecular weights of poly(tetramethylene ether) glycol (PTMG), 650 g/mol and 1400g/mol, are synthesized and studied. Quasi-static tests provide an optimum range of CoP:PU ratio for enhanced fracture toughness (~130%) when compared to PMMA especially using the higher molecular weight PTMG. Under high strain rate loading conditions, the 80:20 composition of graft-IPNs with 650 g/mol PTMG showed crack initiation toughness improvement of approx. 190% and 38% over PMMA and PC, respectively.

Acknowledgements

I thank my research advisor, Dr. Hareesh V. Tippur, for his academic guidance, valuable suggestions and financial support without which this work would not have been possible. I consider the time I spent in the "Laboratory for failure mechanics and optical metrology" at Auburn University, USA under Dr. Tippur's supervision to be of immense value for my personal and professional advancement. I thank my committee members Dr. Jeffrey C. Suhling, Dr. James S. Davidson and Dr. Maria L. Auad for reviewing this dissertation. I would like to thank Dr. James M. Stallings for agreeing to become the external reader for my thesis. My sincere thanks to Ricardo B. Mendez and Dr. Maria L. Auad, department of polymer and fiber engineering with whom I collaborated on a project. I would like to thank Wesley Hunko and Dr. Lewis N. Payton, design and manufacturing laboratory for their assistance in machining the samples for my research. Financial support for this research from U.S. Army Research Lab through research grants W911NF-12-1-0317 & W911NF-16-1-0093 and research instrumentation grants W911NF-15-1-00295 & W911NF-15-1-00357 are gratefully acknowledged. I appreciate the companionship of my colleagues and friends for the wonderful time I spent in Auburn.

Finally, the support and encouragement from my wife Deepika Muthukumar is immeasurable and invaluable. I dedicate this work to her.

TABLE OF CONTENTS

LIST OF TABLES

LIST OF FIGURES

Chapter 1

INTRODUCTION

Optically transparent structural materials are found in numerous engineering applications, both civilian and military. They include automotive windshields and windows, aircraft canopies, helmet visors, blast resistant shields and enclosures, electronic displays, skyscraper scaffolding, etc (Fig. 1.1). In many of these applications, the materials involved are highly susceptible to stress wave loading and hence it is important that they remain transparent and perform the intended function even after they have experienced dynamic loading. In military applications, it is critical that they absorb energy of an incoming projectile as lives are often at stake. In this context, this research is predicated on a hypothesis that it should be possible to engineer monolithic or layered material architectures which are both stiff and energy absorbent without compromising valuable lightweight characteristics. The latter strategy of layering multiple materials is often used to enhance performance under stress wave dominant or impact loading conditions. Commonly used materials in such layered constructions are poly(methylmethacrylate) (PMMA), polyurethane (PU), polycarbonate (PC), poly(vinylbutyrate) (PVB) and glass [1]. While PMMA and glass are stiff and endure brittle fracture, PC is stiff yet highly ductile and undergoes substantial inelastic fracture. On the other hand, PU based materials are softer and ductile.

Figure 1.1 : Some examples of transparent constructions to withstand impact and shock loads. (Source: (a) www.motortrend.com, (b) www.blog.sfgate.com, (c) www.johnwright.smugmug.com, (d) www.big-D.com)

Layered structures used to withstand stress wave loading generally consist of three different units (see Fig. 1.2). The hard disrupting layer/s that interrupts incoming projectile by inducing fragmentation and/or erosion thereby redirecting and dispersing the kinetic energy onto a larger area [2]. This layer is made of a stiff/hard material such as a ceramic. Multiple disrupting layers are bonded together using an intermediate layer, which is often a softer material with good adhesive strength such as PU or PVB. Finally, a backing or an absorber layer is placed at the end of the layered structure to transfer the kinetic energy of

the incoming projectile into heat through inelastic deformation. PC is usually used as a backing layer in armor applications.

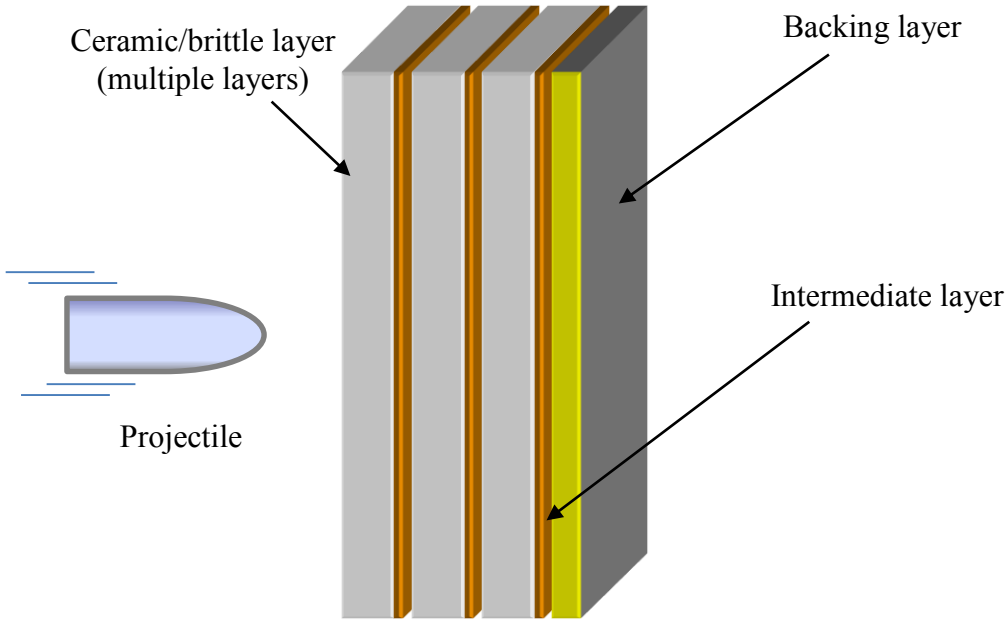

Figure 1.2: Schematic of a transparent layered structure used in an impact resistant application.

In many engineering applications, catastrophic failures occur when crack/s initiate under dynamic loading conditions. Failure of an armor due to projectile impact, cracking of an electronic display due to accidental drop, shattering of automotive windshields during accidents, breaking of aircraft canopy due to blast load or bird strike, are among such examples. Even though there have been several studies in the past, both theoretical and experimental [3] [4] [5], there still remains several aspects of fracture under transient loading conditions that needs further understanding. These include loading rate effects, interaction of reflected stress waves due to finite geometry, material response to mixed-mode crack fracture, effect of multilayer geometry, etc. Advent of ultrahigh-speed digital

cameras, have garnered significant attention of the dynamic fracture community as they could help address some of these aspects. A dynamic fracture event can be typically categorized into three modes depending on the relative motion of crack faces, namely mode-I (opening mode), mode-II (sliding mode or in-plane shear) and mode-III (tearing mode or out-of-plane shear). If a combination of any of these modes occur during fracture, it is categorized as mixed-mode fracture. In real situations, mixed-mode fractures under transient loading conditions are much more common. Figures 1.1(a), (d) represent some examples of such failures. The mechanism governing such failures are not fully understood, especially regarding crack branching. Based on the theory proposed by Erdogan and Sih in 1963 [6], under quasi-static conditions the crack initiates in the direction of maximum tensile stress (MTS) in brittle materials. That is, as it is energetically favorable for a crack to grow under mode-I conditions, it is often observed that the crack tends to grow locally under mode-I conditions even though it may have initiated under mixed-mode conditions.

1.1 Motivation and literature review

Several experimental and numerical studies have been reported on mode-I dynamic fracture of homogeneous and layered transparent materials. However, in real world, fractures often occur under mixed-mode conditions. However, there is limited research on mixed-mode fracture and much needed insight into the mechanics of crack initiation. Among the reasons for this significant gap, the challenges associated with making accurate measurement of mechanical fields and fracture parameters during dynamic mixed-mode

events are at the forefront. In the event of a mixed-mode fracture, the crack typically changes its direction continuously and needs to be accounted for during analysis apart from making measurements. Further, unlike in uniform homogeneous material configurations, mixed-mode dynamic crack propagation is much more complex when multiple layers and interfaces are involved. When a propagating crack encounters an interface, the crack may branch into multiple cracks before propagating into the next layer or may directly penetrate it without branching. These differences depend on the mechanical characteristics of the interface, velocity of the approaching crack, the material/s used in the layered structure, etc. As there are multiple factors that determine the crack growth mechanics, a detailed study of them are challenging but very important if well-designed layered structures are to find real world application. Though many studies have dealt with the visualization of crack initiation and growth along interfaces, quantitative examination of a dynamically growing crack approaching an interface oriented normally (or perpendicularly) resulting in interfacial debonding with subsequent growth along the interface, and branching into the next layer is sparse. Hence, the mechanics of a dynamically growing crack entering and exiting an interface besides growing within an interface needs further insight.

The most common material used as the disruptor in a transparent layered armor system is glass. Although it is relatively hard, it is very brittle; often it shatters even at low impact energy. As crack speeds in glass could be as high as 1800 m/s and deformations are localized to regions as small as a few microns if not submicron, glass is a challenging material to make measurements on. Interestingly, there are hardly any studies on dynamic fracture of glass where fracture parameters (stress intensity factors or fracture toughness)

are measured during crack growth. Also, it is observed that a single dynamically growing mode-I crack in monolithic glass plate often branches into multiple (usually two) cracks before each one branches again and again resulting is fragmentation. Various mechanisms regarding the underlying phenomenon have been hypothesized, but they are mainly based on post-mortem fractography and/or by studying similar materials such as brittle polymers; e.g., acrylics and polyesters. Thus, there is an acute shortage of dynamic crack branching studies in glass with an emphasis on direct measurement of fracture parameters in real-time. Furthermore, there is also a need for developing alternate transparent materials to be used as disruptor in layered architectures as glass adds significant weight to the armor system since its density (~2500 kg/m^3) is about 2.5 times that of most polymers.

In the current work, a full-field optical measurement technique based on Digital Image Correlation (DIC) called the Digital Gradient Sensing (DGS) technique is extended to study mixed-mode crack growth and dynamic failure of layered and monolithic transparent materials. The methodology is first calibrated using mixed-mode quasi-static and dynamic fracture problems in acrylics (PMMA) along with complimentary finite element simulations. The dynamic crack growth mechanics in monolithic and bi-layered PMMA system is investigated and a fracture mechanism is hypothesized. Subsequently, using this optical methodology, experimentally more challenging problem of dynamic crack growth and branching in soda-lime glass plates is investigated. Glass being a highly brittle solid, feasibility of DGS to make full-field measurement of deformations in glass is undertaken first by performing calibration experiments. It includes the classical Flamant problem and edge cracked samples under both quasi-static and dynamic loading conditions

in a soda-lime glass plate along with complimentary finite element simulations or analytical solutions. This has led to the investigation of dynamic crack branching phenomenon in soda-lime glass plates. In the end, synthesis and mechanical characteristics of transparent graft-Interpenetrating Polymer Networks (graft-IPN) are also investigated as alternative lightweight materials for the purpose of transparent armor development.

In the following, the literature review for the current research is provided in three parts. In the first part, works on dynamic crack growth including branching in monolithic brittle materials is reviewed. In the second part, the dynamic crack interactions with an interface are explored. In the third and final part, research on the synthesis and mechanical characterization of transparent graft-IPNs is examined.

1.1.1 Dynamic crack growth and branching in brittle monolithic materials

In homogenous brittle solids it has been observed that a dynamic crack usually propagates under locally mode-I conditions at sub-Rayleigh wave speeds and below the crack branching velocity [3] [7]. As Xu et al. [8] reported, even when an asymmetric far-field load is imposed, a dynamically growing crack tends to reorient itself to follow a locally mode-I path which avoids propagation in mixed-mode or pure mode-II conditions in homogeneous materials. Further, as the crack approaches a 'critical' speed, it becomes favorable for it to branch and produce multiple crack-tips although the exact mechanics for the same is not fully understood. Washabaugh and Knauss [9] reported that if formation of multiple micro-cracks ahead of the main fracture is suppressed by creating a weak path in an otherwise homogenous solid, the crack branching can be prevented. This in turn causes

the crack speed to increase to a point where could approach the Rayleigh wave speed. The main focus of their work was to investigate the discrepancy between the theoretically expected maximum crack speed and that observed experimentally in an amorphous, isotropic solid. On this topic, Rosakis et al. [10] reported that crack speeds as high as $\sqrt{2}$ times the shear wave speed in the material are possible. These are contrary to the classical dynamic fracture theory [3] which predicts the Rayleigh wave speed to be the terminal speed for propagating in-plane cracks in homogeneous, linear elastic materials subjected to far field loading. Supersonic speeds are observed only when loading is applied directly at the crack-tip. Winkler et al. [11] have observed supersonic crack speed in weak crystallographic planes of monocrystalline KCl by loading the crack-tip by an impulse using Q-switched ruby laser. Several attempts have been made to understand this brittle fracture behavior and bridge the gap between the continuum theory and empirical evidence. One such attempt has been reported by Marder and Gross [12]. They created a lattice dynamics based model for fast crack propagation by idealizing crack growth in a mass-spring lattice. They have predicted that the steady crack growth is not possible at speeds up to $0.25C_R$ above which they are linearly stable. If the speeds are sufficiently large (fast crack) then they become unstable and produce microcracking. Other attempts have been made by Abraham et al. [13] and Nakano et al. [14] to formulate a molecular dynamics based simulation of the problem. In those simulations, the limiting value of crack speed was 57% of the Rayleigh wave speed as erratic crack-tip oscillations were observed at that speed due to crack path deflection resulting in significant roughness of cracked surfaces due to coalescence of secondary cracks formed away from the primary crack. Thus, these

simulations exhibit many of the features not observed in the continuum model. Another formulation based on a micromechanical point of view that considers kinetics of microcrack nucleation, growth and coalescence [15, 16, 17] also exists.

Many of the early studies on dynamic fracture mechanics measured crack speed and related it to the "crack driving force" to hypothesize a crack growth criterion [18] [19] [20]. Ravi-Chandar and Knauss, in a series of four articles [21, 22, 23, 24] and another complementary study [25], have investigated the underlying mechanisms associated with the dynamic fracture processes and proposed that the dynamic fracture problem is related to the generation of multiple flaws ahead of a dynamically growing crack-tip. That is, the macroscopic crack creates a highly localized, intense stress and strain concentration due to which micro fracture and/or void growths occur in the material.

In the first of their reports by Ravi-Chandar and Knauss [21], the dynamic fracture mechanics of Homalite-100 has been studied. They have reported that when the rate of loading increased, the stress intensity factor required to initiate the crack increased significantly. They have seen that for a "semi-infinite crack in an infinite plate" configuration, the crack arrest occurs abruptly without any deceleration. Further, the crack arrests at a constant value of stress intensity factor, slightly lower than the critical/initiation stress intensity factor of the material. In the second article [22], they have observed that the occurrence of micro cracks ahead of the running main crack and their interactions control the overall crack growth behavior. They were able to record high-speed photomicrographs that showed the continuous development of crack branches as the crack propagated. In their third report [23], they have observed that the crack can propagate at

nearly a constant velocity even though the apparent stress intensity factor may change significantly. This terminal velocity was said to be governed by the initial stress wave loading on the crack-tip and can be changed only by the stress pulse of sufficient magnitude and lower rise time. The terminal crack velocity in Homalite-100 was recorded to be about half its Rayleigh wave speed. The microscopic fracture surface produced by a propagating crack at high speed had a multi-stage appearance classified as the "mirror", "mist" and "hackle" regions. Crack branching was shown to occur towards the end of the "hackle" region. These features were first reported by Andrews [26] as early as 1959 by examining the surface markings observed in brittle fracture study on *frozen* rubber. Several well defined types of fracture markings were observed in non-crystalline materials. First being those associated with the roughness of the fractured surface, namely the "mirror", "mist" and "hackle" regions. The "mirror" region is an extremely smooth fracture surface which essentially reflects light specularly whereas "mist" is a matte surface with a mild whitish hue and "hackle" is an extremely coarse region generally possessing directional jagged features. Second is the conical markings, - hyperbolic, elliptic or parabolic markings on the surface - which spot the intersection of fractures spreading radially. Third is the formation of Wallner lines caused by the interaction of the fracture front with stress waves emanating from the region of the fracture surface (specimen edges in the thickness direction). Finally, in the fourth one [24], the effect of stress waves interacting with a running crack-tip was studied. Compressive stress waves were made to interact with the propagating crack by either choosing a particular geometry to reflect them off the specimen boundaries or by using an alternate stress wave generator during the event. The stress waves were observed

to influence the crack speed, its direction and the branching phenomena. If the reflected waves were of compressive nature, they decelerated the crack and suppressed branching. This suppression of crack branching was concluded from a transition of the fracture surface from "mirror" to "mist" to "hackle" and back to "mist" without the occurrence of branching. Sharon and Fineberg [27] have investigated the very same problem of dynamic brittle fracture but in PMMA. The specimens were coated with a conductive layer (0.1-1 μm) and interruption of electric current as a result of fracture was used to locate the propagating crack-tip. They have also observed a steady state crack growth up to a certain critical velocity after which instabilities set in producing micro branching. This critical velocity also ushers in the onset of oscillations in velocity history. This is said to be a result of repetitive branching with a decrease in velocity at the birth of a side branch and increase in velocity when the branch dies out. As the velocity increases further, these microbranches coalesce and develop into a periodic rib-like pattern with an increased spacing of the order of 1 mm. Although the length of these microbranches vary with velocity, the mean profile of a branch has a rather well defined power-law form [28] that is independent of crack length and crack velocity. Hence the angle of the microbranches is a function of measurement scale. For a measurement scale of the order of 100-300 μm, the angle is 10˚ - 15˚ whereas for a scale of the order 5 μm the angle is ~30˚. By measuring the crack-tip energy, they observed that the fracture energy is constant and absorption of the excess energy is by the evolution of more surface area through microbranching. Thus, the crack

preferred not to accelerate beyond a certain limit, and expended the excess energy by producing new fracture surfaces.

The dynamic crack branching in brittle solids is of particular interest and yet only limited understanding exists about it. One of the earliest experimental investigations by Shand [29] dates back to 1954. The brittle fracture of glass was investigated in this study encompassing the branching phenomena. The main conclusions of that study were: (a) fracture originates at a pre-existing flaw usually on the surface, (b) crack propagation begins with a minimal stress at the crack-tip which later increases rapidly with the extension of the crack, (c) as the crack continues to propagate, a limiting velocity and critical stress are attained beyond which a transition, characterized by roughening of the fracture surface ('hackle') that absorbs the excess energy released occurs, (d) the critical stress for common commercial glass is estimated to be in the range of 17-34 GPa. Later in 1967 Bowden et al. [30] used a measurement technique based on interruption of an electrical current through the sample during crack growth to study dynamic fracture of brittle solids (specifically crack length history) such as glass, magnesium oxide, tungsten, etc. The velocity histories were evaluated during brittle fracture leading to crack branching. Subsequently, Field in 1971 [31] reported a very detailed study on brittle fracture including branching. The measurement system used was again based on interruption of electric current similar to Ref. [30]. Multiple materials including glass, magnesium oxide, lithium fluoride were studied. Crack velocity histories, fractography and potential application of crack branching were all discussed. He noted that there exists a maximum crack velocity for brittle solids and crack branching occurs under two scenarios: (a) when the crack

velocity reaches a critical value, and (b) when stress waves pass over the crack. He reported a decrease in crack velocity before crack branching accompanied by an increase in surface roughness. Cramer et al. [32] investigated crack velocities during dynamic fracture of glass and single crystal silicon to address the hypothesis on the existence of critical velocity for a dynamic fracture process and its effect on the onset of instabilities leading to branching. Velocities were measured via resistance change in a 100 nm thick conductive coating deposited on the specimen. A maximum velocity of 0.3-0.5 times the shear wave speed was observed in glass whereas in silicon it reached up to 0.75 times the shear wave speed. In 1975 Doll [33] investigated crack branching in soda-lime glass (plate glass). It was reported that crack branching depended on two conditions; the crack attaining the maximum fracture velocity in the material and the strain energy release rate exceeding a critical value. The maximum fracture velocity was observed to be ~1500 m/s and strain energy release rate at branching was ~ 135 J/m^2. It was hypothesized that crack branching occurred at strain energy release rates such that both crack branches could continue to run at approximately maximum crack velocities. That is, strain energy release rate at crack branching was twice that when crack attained its maximum velocity. Aratani et al [34] studied crack growth and subsequent branching in tempered glass using the method of caustics. A nearly 50% reduction in stress intensity factor (SIF) after crack branching was reported. Recently Murphy et al. [35] observed the dynamic crack branching in PMMA. Uniaxially loaded SEN tensile specimens were used to produce crack branching. They reported that the crack branched in specimens with extremely short cracks (0.1 mm and 0.15 mm crack length in 25 mm wide specimen) and higher thickness.

There are several finite elements [36] [37] [38] [39] [40] [41] [42] and peridynamics [43] [44] [45] based numerical studies on dynamic crack branching. The finite element methods employ cohesive zone modeling, embedded discontinuity, enhanced extended finite elements (XFEM), two-dimensional rock failure process analysis (RFPA2D), etc. Xu et al [37] used the critical velocity as the branching criteria in their work. They were able to mimic the crack path and its angle during branching. Zhang et al. [36] used maximum tangential stress as the branching criteria. The major results were: (a) micro cracks were observed during crack propagation, (b) the macroscopic branching angles became larger with increase in tensile stress, (c) the crack-tip velocity was independent of loading conditions but determined by material properties, (d) crack velocity remained nearly same at ~0.48 times shear wave speed. Paulino et al. [42] used extrinsic cohesive zone elements to model the dynamic fracture behavior of PMMA. The increase in surface roughness, length of microbranches and crack-tip velocities were seen with increase in energy input. Armero and Linder [38] used embedded discontinuities to simulate dynamic fracture. The critical crack velocity was used as the branching criteria in their study as well. The simulation was able to capture aspects of overall crack path and its velocity during branching. Ha and Bobaru [43], and Bobaru and Zhang [44] have investigated the brittle fracture and crack branching using peridynamics. They have observed that crack velocity could reach high proportion of its maximum velocity in the region of crack branching and decrease prior to branching along with roughening of the fracture surface. An increase in crack velocity was observed thereafter. They have hypothesized a mechanism for crack branching based on "stress wave pile-up." For a propagating crack initiated under mode-I

loading conditions and no interaction with reflected stress waves, mixed-mode conditions are said to be induced near the crack-tip by stress waves (generated by the fracture process) that pile-up around the crack-tip due to reflections by the material ahead of the crack-tip that moves against the direction of crack propagation. This wave pile-up leads to "migration" of damage away from the line of symmetry, indicating an enlargement of the process zone (possible roughening of the crack surface resulting in increased crack thickness). When this migration is sufficiently large, the material ahead of the crack-tip is unloaded, and damage growth no longer occurs along the original crack direction, but splits into two separate process zones which continue to propagate with a reduced thickness compared to that before the branching event. In case of a reverse impact geometry where the crack branching is the result of the waves traveling towards the propagating crack, they note that the mechanism of crack branching is due to stress wave reinforcement.

1.1.2 Dynamic crack interactions with an interface

As discussed earlier, cracks in brittle, isotropic, and homogeneous materials tend to propagate under pure mode-I conditions when they do not attain crack branching speeds. However, an interface if introduced in a homogeneous material can in principle interfere with crack propagation and alter the crack path even at speeds much lower than the one needed for branching in monolithic counterparts. Hutchinson and Suo [46] reported on mixed-mode cracks in layered materials and their tendency to propagate along the interface vs. kink out of the interface depending up on its properties, specifically its fracture toughness, relative to the parent/joined materials. Also, a crack may arrest at or get trapped

in the interface depending on the direction of its growth relative to the interface [47]. The competition between crack penetration, deflection, and branching behaviors at interfaces govern the overall fracture mechanics of brittle solids and layered structures. If the interface has a lower fracture toughness relative to the adjoining materials, the crack tends to enter the interface and propagate as a trapped mixed-mode crack. The dissimilarity in the moduli of the joined materials, far-field loading, and geometry also contribute to the mode-II component in such scenarios [47] [48] [49]. Early work by Cook and Gordon [50] has suggested the possibility of strength and toughness enhancement of layered systems by optimizing the ratio between the adhesive strength of the interface and the cohesive strength of the brittle phase. Several works reported since, most performed under quasi-static conditions [51, 52, 53, 54, 55], studied various aspects of this problem. The dynamic counterparts of these introduce a host of additional parameters such as crack velocity, inertia, stress-wave interactions, making the problem much more challenging.

From the above works it is evident that an interface could greatly affect the crack growth behavior. One of the earliest studies on dynamic interface crack growth was carried out by Tippur and Rosakis [56] using an interferometric method called CGS. They reported unusually high crack velocities as the crack propagated along an interface approaching the Rayleigh wave speed of the compliant constituent of a bi-layered dissimilar material. Subsequent investigations showed that the interfacial crack speeds could become intersonic [8] [10] [57] and supersonic [11] [58] in such bimaterials. Xu and Rosakis [59] have visualized different modes of failure in homogeneous but layered configurations subjected

to impact loading and reported various failure mechanisms comprising of *inter*-layer and *intra*-layer cracking.

Most reports that deal with dynamic interfacial crack growth along interfaces [9, 56] have brought to light several previously unknown aspects of fracture mechanics such as unusually high crack speeds and the possibility of crack propagation at intersonic speeds [60, 61, 62]. Further, to fully comprehend the dynamic fracture of layered materials, crack growth across interfaces needs to be understood as well. The existing studies on this subject generally deal with interfaces *inclined* to the crack propagation direction where deflection/penetration mechanics of a single crack-tip has been analyzed. Rosakis and his co-workers [8, 48] are among the few who have studied in detail interactions between a dynamically growing crack and an inclined interface experimentally. Xu et al. [8] have examined the effect of interface angle and its strength in a homogeneous bilayer with an inclined interface on crack penetration/deflection mechanisms. They have reported that the angle of incidence of the crack relative to the interface plays a significant role in its penetration vs. deflection mechanisms. In a study by Chalivendra and Rosakis [48], the effect of crack velocity as it approached the inclined interface was examined. They have used optical methods to visualize crack-tip fields and crack-tip location during highly transient fracture events. Overall, understanding the mechanics of a dynamically growing crack becoming an interfacial crack when it encounters an interface is addressed. They have observed significant jumps in crack velocity as well as crack deflection at an interface. Xu and Wang [63] have recently revisited those measurements and suggest that the so-called *T*-stress - the second term in the crack-tip asymptotic series for stress in the crack

growth direction - could also play a significant role in the interfacial debond initiation besides stress intensity factors. Another recent study by Park and Chen [49] has reported on crack growth visualization in glass bilayers using high-speed photography. Specifically, they have examined crack branching and arrest behaviors at an interface as a function of interface thickness and impact velocity of the projectile. An interface layer without any adhesive (unbonded) arrests the crack whereas an interface of zero thickness lets the crack to penetrate the interface as single crack. When the interface thickness was increased, the crack got trapped in the interface delaying crack from propagating into the second layer. When a single crack in the first layer entered the second, a fan of cracks originated from the narrow region of incidence. Further, increase in projectile velocity increased the number of crack branches in the first layer and hence multiple cracks arrived at the interface producing a wider fan of cracks in the second layer. Parab and Chen [64] have also investigated glass bilayers (soda-lime and borosilicate glass) and glass ceramics with an emphasis on the effect of interface thickness. Similar observations have been reported in this study as well. An additional observation that crack penetration in case of glass ceramic bilayers did not occur has been made.

A few numerical investigations using finite element analyses, either in conjunction with stiffness degradation techniques [65] or using cohesive elements [66], and peridynamic simulations [67] have also been reported on crack growth across interfaces. The stiffness degradation or element erosion techniques usually suffer from mesh refinement issues. The analysis based on cohesive elements, on the other hand, are more common; for example, in Ref. [66] the role of interface strength on crack penetration vs.

deflection at an interface situated perpendicularly to the crack growth direction using cohesive elements is examined. Higher strength of the interface is shown to promote crack penetration whereas the weaker one causes the crack to deflect at the interface. In a more recent study, Liu et al. [68] have studied strain rate effects on growth dynamics of a crack-tip lodged in the interface perpendicular to the crack. The possibilities of crack growth through the interface as well as its bifurcation along the interface before entering the next layer are examined in their work.

1.1.3 Graft- Interpenetrating Polymer Networks (graft-IPNs)

The so-called Interpenetrating Polymer Networks or IPNs were first synthesized as early as 1914 by Jonas Aylsworth and Thomas Edison by mixing phenol formaldehyde with rubber and sulfur to produce tougher phonograph records [69, 70]. It gained attention during 1960s leading to coining of the name IPN by Millar [71]. IPNs are polymeric systems comprising of two or more networks which are at least partially interlaced on a molecular scale but not chemically crosslinked and cannot be separated unless individual crosslinks are broken [72]. Following these works, a great deal of research on IPNs [70, 73, 74, 75] has been reported in the last few decades. The reason for developing IPNs has been to combine best features of two different polymers so that a new material could be engineered with desired characteristics such as stiffness, strength, optical transparency, etc. An example of an IPN is one that combines a thermoplastic with a thermoset where each phase contributes its inherent characteristics to the composite. Thermoplastics offer good ductility but have lower stiffness and glass transition temperature (Tg) while thermosets

are generally more brittle but stiffer, stronger and have higher Tg. IPNs usually present some degree of phase separation during synthesis. This has been observed in both simultaneous and sequential polymerizations employed for synthesizing IPNs [76, 77]. In the early works done by Chen et al. [78] and Fan et al. [79], vinyl ester resin (VE) was used with a polyurethane network for synthesizing simultaneous IPNs. Here the formation of crosslinks between networks was never the objective. In fact, the generation of crosslinks was avoided. Its morphology showed the presence of phase separation between networks. Recently, Bird et al. [80] synthesized IPNs based on PU and PMMA. By performing UV spectroscopy, they were able to demonstrate a fairly high degree of transparency for certain compositions with mild phase separation while certain other compositions showed significant phase separation. The effect of PU to PMMA ratio was studied and 80:20 composition showed higher elastic modulus, glass transition temperature and transparency. Subsequently, Jajam et al. [81] studied these IPNs for their mechanical characteristics using the optical method of DIC. A reduction in elastic modulus, loss of strength and increase in ductility with increase in PU fraction was reported. Under quasi-static loading conditions, the 80:15 composition showed ~60% and ~48% improvement in fracture toughness over commercial PMMA under quasi-static and dynamic loading conditions, respectively.

The challenge of phase separation in IPNs can be addressed by generating chemical crosslinks between the two networks, thus generating a class of IPNs called graft-IPNs. Hsieh et al. [82, 83] synthesized graft-IPNs based on PU and epoxy by simultaneous polymerization to study the effect of PU to epoxy ratio. The optimum composition was observed to be between 80:20 and 70:30, which is the result of intimate interpenetration

between PU and epoxy in the graft structure. Further, Hsieh et al. [84] synthesized graft-IPNs based on urethane-modified bismaleimide (UBMI) and epoxy. The optimum composition was determined to be 15% UBMI. Although improvement in mechanical characteristics was reported in all these studies, there has been limited insight into their dynamic/impact characteristics and the optical transparency is relatively low. For applications such as transparent armor materials, the characteristics of strength, stiffness, fracture toughness as well as optical transparency have to be optimized.

1.2 Objectives

The above literature review suggests that the there is a need for evaluating dynamic fracture parameters during crack propagation in monolithic and layered transparencies and under mixed-mode conditions to explain the mechanics of crack branching phenomena. Further, with regards to crack branching, most studies hypothesize plausible reasons for crack branching rather than provide empirical evidence on the underlying mechanics. Since the transparent layered systems are widely used, especially in critical applications, the fracture of transparent monolithic and layered systems are to be investigated. Hence, the following are the primary objectives of this research:

- Investigate failure behavior of transparent monoliths and layered systems under mixed-mode loading conditions.
- Develop a methodology to evaluate dynamic stress intensity factors (SIFs) for cracks propagating under mixed-mode conditions.

- Perform calibration experiments for the developed methodology and complement the results with finite element simulations.
- Investigate the interactions of dynamically propagating cracks with interfaces when they are normally oriented to the incoming crack.
- Study the effects of interface strength, interface location, and impact velocity on the crack path, crack velocity, and stress intensity factor histories of dynamically growing crack/s.
- Hypothesize a mechanism for the observed crack branching and penetration at a weak interface and etablish an experimental evidence for the same.
- Investigate the feasibility of an optical method called DGS to visualize and quantify crack-tip deformations in soda-lime glass leading to dynamic crack branching.
- Study crack branching in monolithic glass plates and suggest an experimentally rooted mechanism for branching.

A secondary objective of this research is to investigate the mechanical behavior including the dynamic fracture characteristics of novel interpenetrating polymer networks (IPN) called graft-IPN (or, graft-IPN). These molecular scale composite materials are being conceived in order to provide alternative transparent lightweight material systems or adhesive materials for high impact energy absorption required for armor applications. The following are some of the objectives related to this aspect of the current research:

- Synthesize graft-IPN molecular composites made of PMMA based CoP and PU phases.

- Perform quasi-static and dynamic material characterization studies on graft-IPNs to evaluate tensile and fracture responses of graft-IPNs.

1.3 Organization of the dissertation

This dissertation is organized into nine chapters including the current introductory one. In Chapter 2, the experimental methods for evaluating fracture parameters is explained. The concept of DIC is explained first followed by the working principle of an optical method called Digital Gradient Sensing or DGS and its governing equations. The extension of DGS to measure SIFs is explained through quasi-static and dynamic mode-I fracture problems. The data analysis using Williams' asymptotic expression and least squares analysis is also described.

In Chapter 3, dynamic mode-I and mixed-mode fractures in two popular transparent (armor) polymers, PMMA and PC, is described. The experimental setup, material geometry and methodology to obtain various mode mixities are discussed. The results include SIF histories, crack kink/deflection angle measurements, and dynamic fracture envelopes for both the materials. The dynamic fracture behaviors of PMMA and PC are also contrasted.

Fracture mechanics of elastically homogeneous, transparent PMMA bilayers containing a discrete plane of weakness are discussed in Chapter 4. The dynamics of crack interaction with an interface oriented normally to the incoming crack is described. The crack growth in two types of interfaces, 'strong' and 'weak,' are comparatively investigated by optically evaluating crack velocity and SIF histories.

The effect of interface location within the bilayer geometry of a 'weak' interface geometry is reported in Chapter 5. It includes the experimental results on crack velocity and SIF histories for four different configurations. Based on empirical evidence, a mechanism of crack branching vs. direct penetration is put forward. Equipped with this understanding, the effect of impact velocity on the fracture mechanics of bilayers is examined and reconciled with the prior conclusions.

Chapter 6 deals with an experimentally challenging problem of extending DGS for visualizing and quantifying deformations in highly brittle and stiff transparent ceramics such as soda-lime glass. It includes, experiments conducted under both quasi-static and dynamic loading conditions on monolithic soda-lime glass sheets. Problems associated with impact induced deformations, and deformations near dynamically loaded stationary and growing cracks are studied. The comparison of experimental results with those from either finite element simulations or boundary collocation are used to establish the feasibility of the optical methodology.

In Chapter 7, the crack branching observed in soda-lime glass is investigated optically using DGS. The experimental details include optical fields before and after crack branching, the associated crack-tip parameters - velocities, SIFs, followed by fractographs. A plausible mechanism for the observed crack branching is suggested.

The mechanical characterization of transparent graft interpenetrating polymer networks (graft-IPNs) synthesized using poly(methyl methacrylate) (PMMA) based copolymer as the stiff phase and polyurethane (PU) as the compliant phase are discussed in Chapter 8. The

effect of PMMA-PU compositions on tensile and fracture behaviors of graft-IPNs under both quasi-static and dynamic loading conditions is discussed.

Finally, the major conclusions of this dissertation are summarized in Chapter 9. A few potential topics for future research stemming from this dissertation are highlighted.

Chapter 2

OPTICAL MEASUREMENTS AND ANALYSIS

In this chapter, the optical method of Digital Gradient Sensing (DGS) and its extension for evaluating Stress Intensity Factors (SIFs) to characterize the dynamic fracture behavior of transparent monoliths and multilayered systems is discussed. DGS, which utilizes 2D Digital Image Correlation (DIC) method, can quantify the angular deflections of light rays in two orthogonal planes as they pass through the specimen. The measured angular deflections are proportional to the gradients of stresses in the corresponding directions. The calibration of the methodology for evaluating SIFs under mixed-mode conditions is presented. A complimentary finite element analysis is also described.

2.1 2D Digital Image Correlation (DIC)

Two dimensional DIC involves a gray scale pattern matching method wherein a point or small region of an image in the deformed state is located relative to its position in the corresponding one in the undeformed state, and the relative displacement vector and hence two orthogonal displacement components are evaluated. This method requires the specimen surface to be covered with random speckles/gray-scale pattern, typically created by spraying a mist of white and black paints if a natural random surface texture is absent. This creates a unique pattern of speckles on the object essential for performing DIC.

Ordinary white light is used to illuminate the specimen uniformly. The specimen with the speckle pattern is first photographed under no-load conditions using a digital camera and it serves as the reference image. Then, the specimen is loaded due to which speckles get distorted and displaced. This pattern is recorded by the camera as the deformed image. The two images are then segmented into an array of sub-images (or facets) containing a rectangular array (say, 25× 25) of pixels with or without any overlap (say, step size of say 5 pixels or sub-image overlap of 20 pixels) as shown in Fig. 2.1.

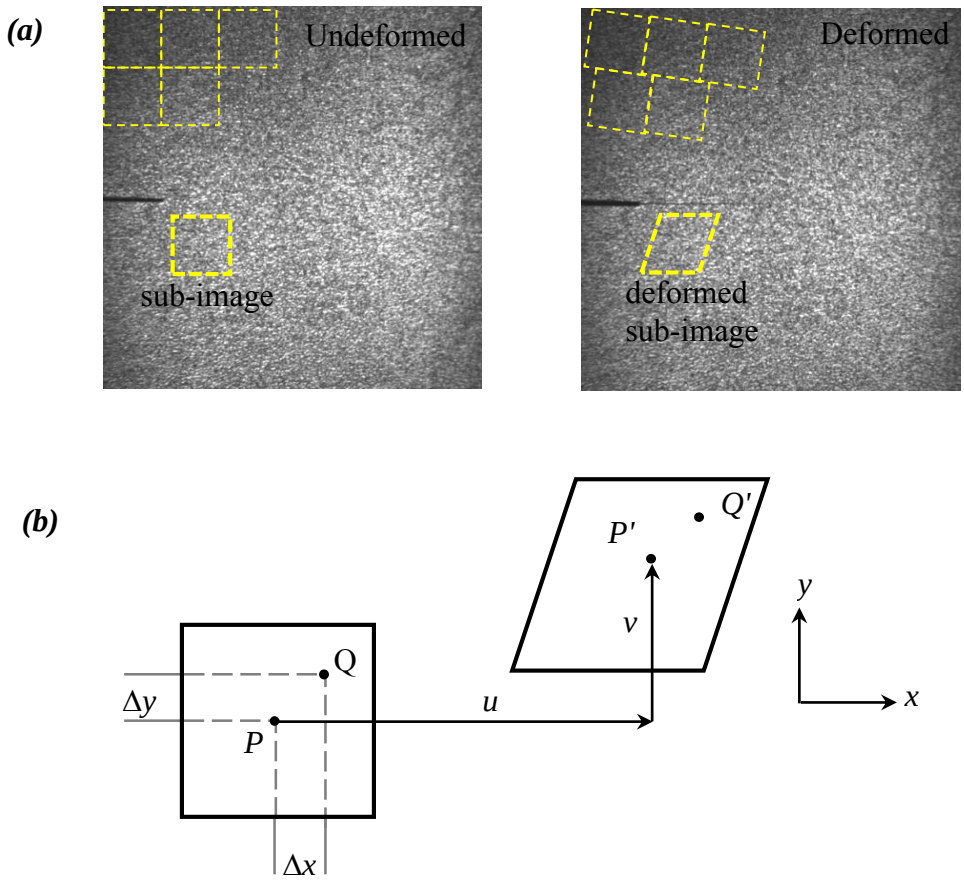

Figure 2.1: Principle of DIC. (a) A pair of undeformed and deformed speckle images recorded by the digital camera which is segmented into sub-images, (b) Displacement mapping between undeformed and deformed sub-images.

Each sub-image represents a unique distribution of intensities. For every sub-image in the reference image, the corresponding sub-image in the deformed state is searched and located. For example, if a sub-image centered at P in the undeformed image has translated such that its new center is P' in the deformed image (see Fig. 2.1), the displacement components u and v can be obtained using a correlation algorithm. In this study, a commercial image analysis software called Aramis® is used for obtaining the sub-image displacements.

2.2 Principle of Digital Gradient Sensing (DGS)

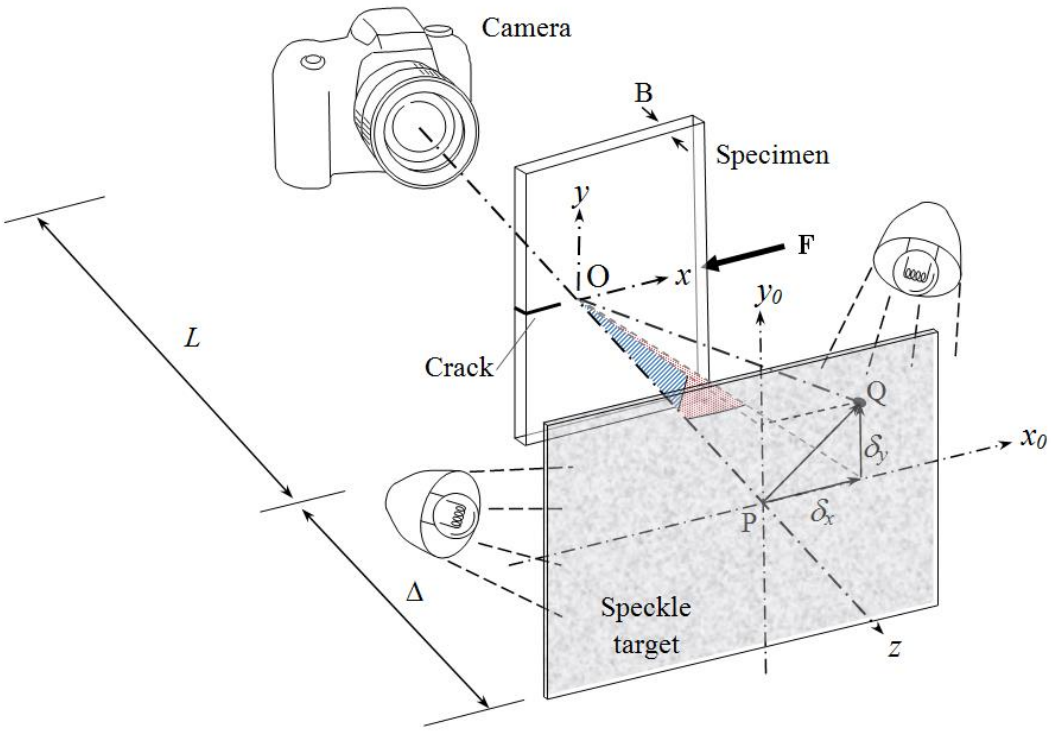

Figure 2.2: Schematic of experimental setup for Digital Gradient Sensing (DGS) method to determine the angular deflections of light rays in two in-plane orthogonal directions.

DGS is a full-field optical method based on 2D-DIC but measures angular deflections of light rays propagating through a transparent specimen [85]. These angular deflections of light rays are due to the state of stress in the specimen. The schematic of the experimental setup for DGS is shown in Fig. 2.2. It consists of a rectangular specimen of initial thickness B and an edge crack as a stress riser. A flat surface coated with random black and white speckles, called the target plate, is placed at a known distance Δ behind the transparent specimen from its mid-plane. A digital camera with a long focal length lens is placed in front of the specimen at a distance L ($>> \Delta$) such that the camera is focused on the target plate through the region of interest (ROI) on the specimen, which in this example is the vicinity of the crack-tip.

The specimen, the camera and the target plate planes are parallel to each other. Using a CFL light source, the target plate is illuminated uniformly. Sufficient care is taken to position the light source so as to obtain a near Gaussian distribution of gray scale in the image recorded by the camera. The digital camera settings and lens parameters are optimized such that the aperture is small enough for achieving a good depth of focus with the target plate is in focus while keeping the important features of the specimen plane (say, specimen edges, load point, crack-tip etc.) evident in the recorded image as well.

The speckle pattern is first photographed through the specimen in its undeformed state to obtain a reference image. That is, a point P on the target plane (x_0 - y_0 plane) is recorded by the camera through point O on the specimen plane ($x - y$ plane). Upon loading, the non-uniform stresses due to the imposed loads change the refractive index of the specimen in the crack-tip vicinity. Additionally, the Poisson effect produces non-uniform

thickness changes. A combination of these, commonly known as the *elasto-optic effect*, causes the light rays to deviate from their original path as they propagate in the crack-tip vicinity. The speckle pattern is once again photographed through the specimen in the deformed state. Then a neighboring point *Q* on the target plane is recorded by the camera through point *O* on the specimen plane after deformation. Two representative photographs obtained using DGS in the unreformed and deformed states are shown in Fig. 2.3.

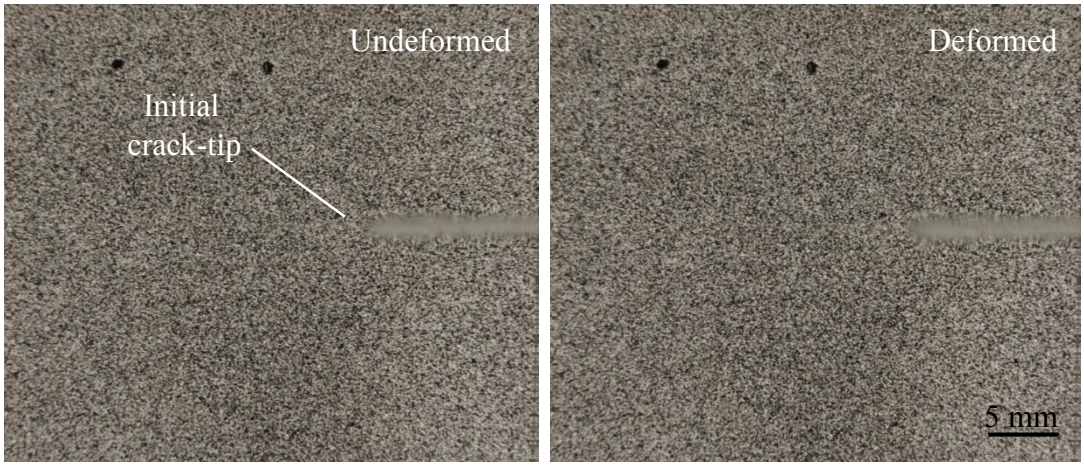

Figure 2.3: A pair of undeformed (a) and deformed (b) speckle images recorded by the digital camera through the transparent specimen near the crack-tip vicinity.

The local deviations of light rays can be quantified by correlating speckle images in the deformed and reference states to find displacement components δ_x and δ_y. The angular deflections of light rays ϕ_x and ϕ_y in two orthogonal planes (*x*-*z* and *y*-*z* planes with the *z*-axis coinciding with the optical axis of the setup and *x*-*y* being the specimen plane coordinates) can be computed using the known distance Δ. A detailed analysis carried out under paraxial conditions by Periasamy and Tippur [85] shows that the local angular deflections are related to the gradients of in-plane normal stresses as,

$$\phi_x = C_\sigma B \frac{\partial(\sigma_x + \sigma_y)}{\partial x} = C_\sigma B \frac{\partial I_1}{\partial x} \tag{2.1}$$

$$\phi_y = C_\sigma B \frac{\partial(\sigma_x + \sigma_y)}{\partial y} = -C_\sigma B \frac{\partial I_1}{\partial y} \tag{2.2}$$

where C_σ is the elasto-optic constant of the material, B is its initial thickness and $I_1 = (\sigma_x + \sigma_y)$ is the first invariant of stress *under plane stress* condition and σ_x and σ_y denote *thickness-wise* averages.

Using the Williams' asymptotic expansion for I_1 in Eq. (1.1), expressions for angular deflections in case of a mode-I statically loaded crack-tip become [86] [88],

$$\phi_x = C_\sigma B \frac{\partial I_1}{\partial x} = C_\sigma B \sum_{N=1}^{\infty} A_N \left(\frac{N}{2} - 1\right) r^{\left(\frac{N}{2}-2\right)} \cos\left(\left(\frac{N}{2} - 2\right)\theta\right) \tag{2.3}$$

$$\phi_y = -C_\sigma B \frac{\partial I_1}{\partial y} = -C_\sigma B \sum_{N=1}^{\infty} A_N \left(\frac{N}{2} - 1\right) r^{\left(\frac{N}{2}-2\right)} \sin\left(\left(\frac{N}{2} - 2\right)\theta\right) \tag{2.4}$$

Similarly, the expressions for angular deflections in case of a mixed-mode (mode-I + II) static crack-tip are [57],

$$\phi_x = C_\sigma B \frac{\partial I_1}{\partial x} = C_\sigma B \sum_{N=1}^{\infty} \left\{ \begin{array}{l} A_N \left(\frac{N}{2} - 1\right) r^{\left(\frac{N}{2}-2\right)} \cos\left(\left(\frac{N}{2} - 2\right)\theta\right) \\ + D_N \left(\frac{N}{2} - 1\right) r^{\left(\frac{N}{2}-2\right)} \sin\left(\left(\frac{N}{2} - 2\right)\theta\right) \end{array} \right\} \tag{2.5}$$

$$\phi_y = -C_\sigma B \frac{\partial I_1}{\partial y} = -C_\sigma B \sum_{N=1}^{\infty} \left\{ \begin{array}{l} A_N \left(\frac{N}{2} - 1 \right) r^{\left(\frac{N}{2} - 2 \right)} \sin\left(\left(\frac{N}{2} - 2 \right) \theta \right) \\ -D_N \left(\frac{N}{2} - 1 \right) r^{\left(\frac{N}{2} - 2 \right)} \cos\left(\left(\frac{N}{2} - 2 \right) \theta \right) \end{array} \right\} \tag{2.6}$$

where (r, θ) denote the crack-tip polar coordinates, $A_1 = K_I \sqrt{\frac{2}{\pi}}$ with K_I being mode-I stress intensity factor and $D_1 = K_{II} \sqrt{\frac{2}{\pi}}$ with K_{II} being mode-II stress intensity factor. Using the above analytical expressions (2.3)-(2.6) with N = 1, the angular deflection contours are plotted as shown in Fig. 2.3 for a mode-I and a mixed-mode case. The tri-lobed contours with 120° symmetry (based on the leading terms in the asymptotic expansion) relative to the crack axis for ϕ_x and asymmetry for ϕ_y in case of mode-I are shown in Fig. 2.3(a). For the mixed-mode case on the other hand, the contours rotate relative to the crack axis as shown in Fig. 2.3(b). Again, note that these contours were generated using only the *K*-dominant terms in the asymptotic expressions and hence the size of each set of lobes are identical. However, in finite specimen geometries and/or transiently varying states of stress, the size of each set of lobes could be different due to the influence of higher order terms ($N > 1$).

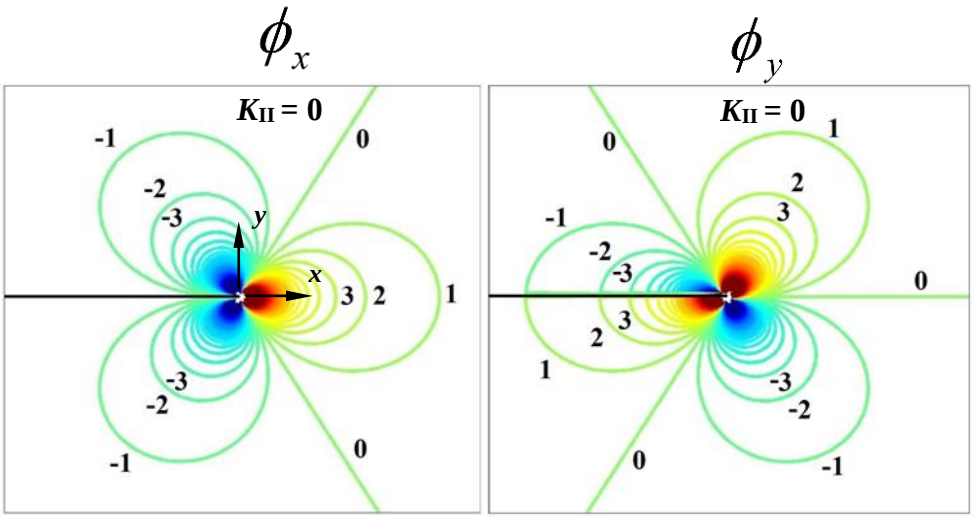

(a)

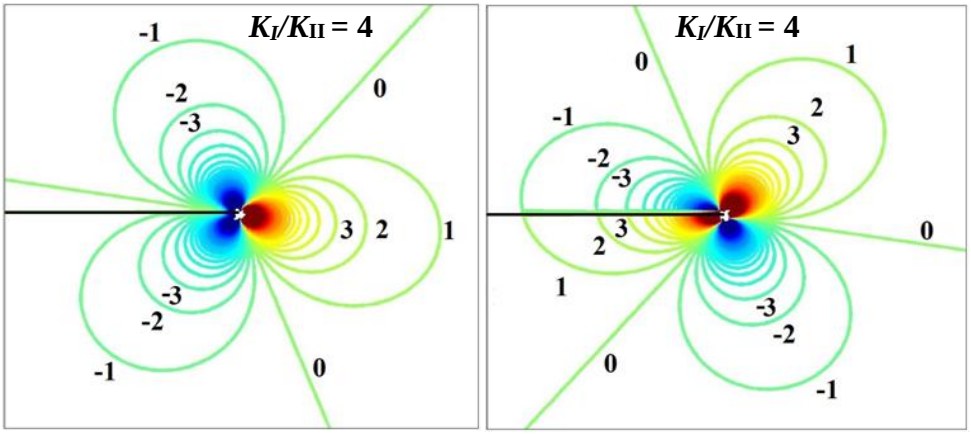

(b)

Figure 2.4 : Analytical contour plots of ϕ_x and ϕ_y for (a) $K_{II} = 0$ and (b) $K_I / K_{II} = 4$ The overlaid numerical values on the contours represent relative magnitudes and sign of DGS contours.

2.3 Quasi-static mode-I crack-tip problem

2.3.1 Specimen preparation and geometry

A 220 mm x 60 mmm rectangular SENB specimen of thickness 8.6 mm was machined out of a cast PMMA sheet as show in Fig. 2.5. Some of the relevant properties of PMMA used in this study are listed in Table 2.1. A notch of 12 mm was machined on the longer edge of the specimen using a diamond impregnated circular saw of approximately 300 μm thickness. The target plate used for DGS measurements was prepared by spraying a fine mist of black and white paints successively on a flat surface to create random speckles. Two heavy black dots were marked 10 mm apart on the target plate to relate the spatial dimensions on the image to those of the target plate and the specimen.

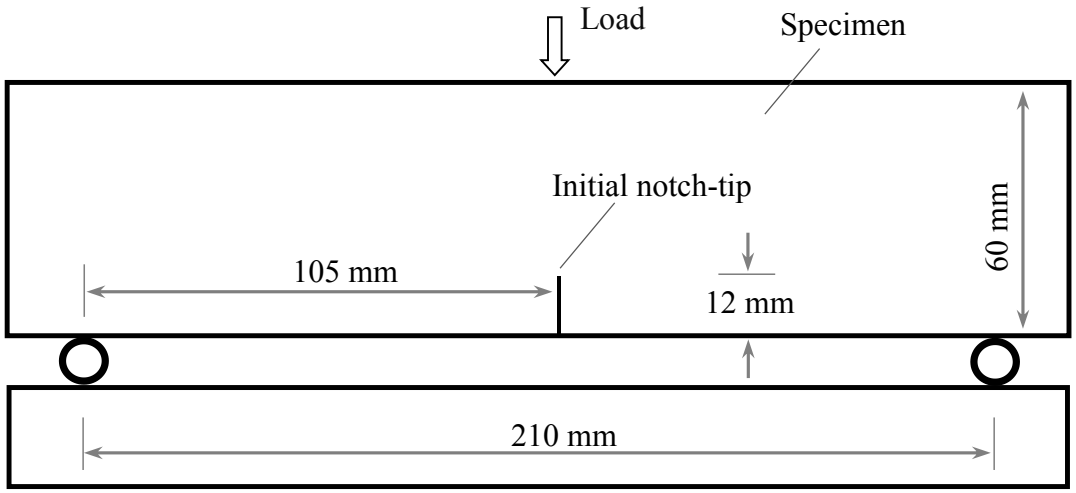

Figure 2.5: Schematic of the setup for 3-point bend test.

Parameter	Static Value	Dynamic Value
Density	1010 kg/m^3	1010 kg/m^3
Elastic modulus	3.3 GPa	5.0 GPa
Poison's ratio	0.34	0.34
Elasto-optic constant	-0.9x10^{-10} m^2/N	-1.08x10^{-10} m^2/N

Table 2.1: Some properties of cast PMMA used [85].

2.3.2 Experimental setup and procedure

An Instron 4465 universal testing machine was used for loading the specimen in tension and in displacement control mode (crosshead speed = 0.005 mm/sec). The speckled target plate was located at a distance of Δ = 34.3 mm from the specimen mid-plane and behind the specimen. A Nikon D100 digital SLR camera fitted with a 70-300 mm focal length lens (with an aperture setting of #22) and extension tube was used to record the speckles. The camera was placed in front of the specimen at a distance (L) of approximately 1400 mm with the camera focused on the target through the specimen. Both the camera and the testing machine were controlled using a computer. Two regular incandescent lamps were used to illuminate the target plate uniformly. Incandescent light source compensation setting in the image capturing software was used to account for the yellowness of the light source. During recording a camera resolution of 1504 x 1000 pixels was used to acquire 8 bit images.

A reference/undeformed image of the target plate speckles through the crack-tip vicinity was recorded in no-load (load < 1 N) condition. As the sample was loaded gradually, the perturbed speckle images of the target plate were recorded using time-lapse photography at 6 frames per minute. Two representative speckle patterns, one in the

reference state and the other in the deformed state, are shown in Fig. 2.6. The recorded images correspond to 57 mm x 38 mm region on the specimen. Using a pair of two heavy black dots (see, Fig. 2.6) marked on the target plate, the dimensions of the image in terms of number of pixels were related back to specimen/target plate dimensions (1 pixel = approx. 38 μm on the target plane). Sufficient care was also exercised to obtain a near Gaussian distribution of gray scales for each image in the mid-range of 0-255 (8 bit) scale by positioning the lamps appropriately.

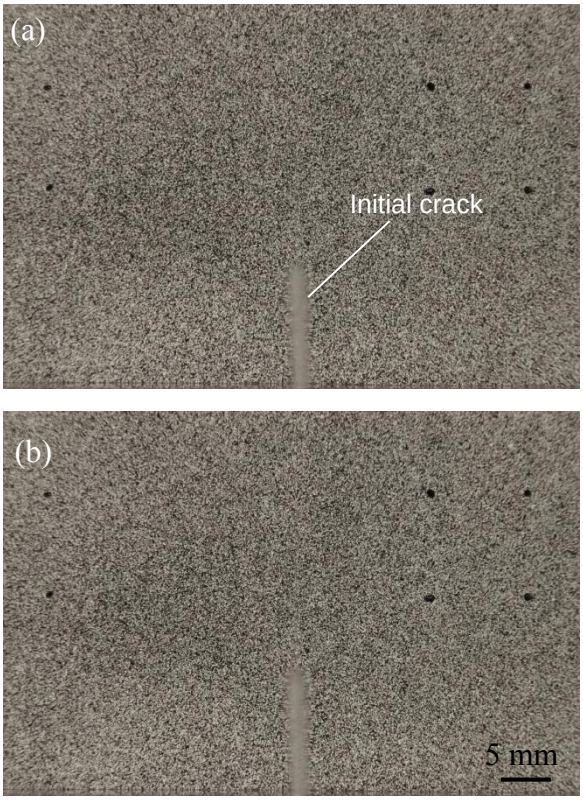

Figure 2.6: Speckle image of the target plate through the transparent edge cracked specimen at (a) no-load and (b) 575 N.

2.3.3 Image analysis

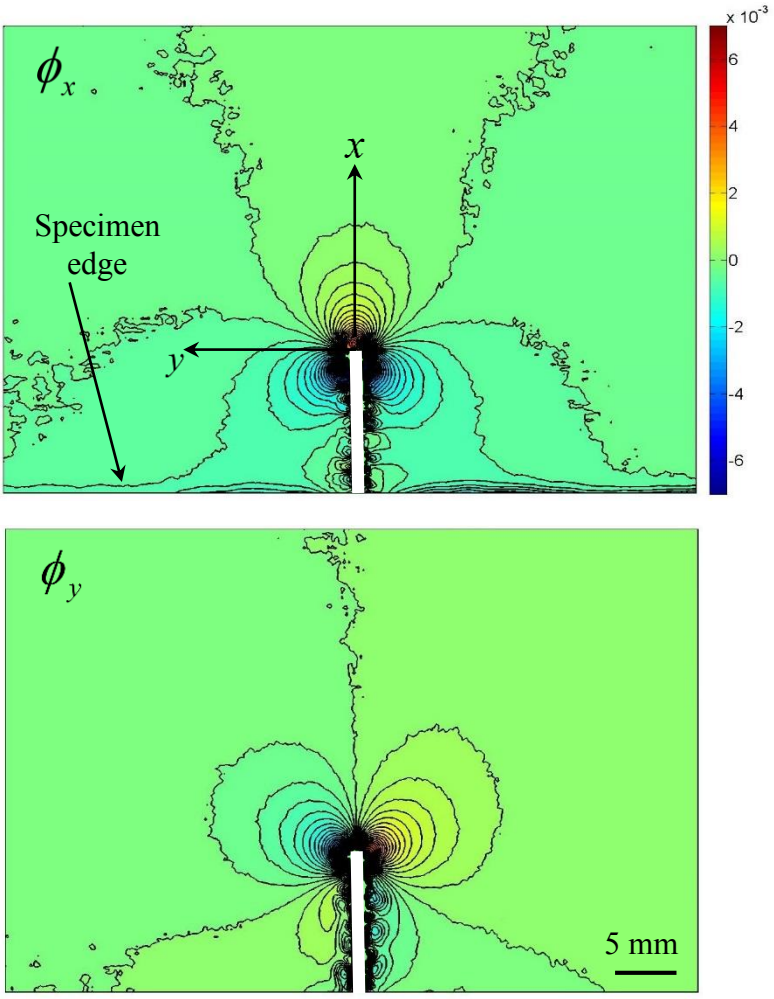

Figure 2.7: The Angular deflection contours (contour interval = $2x10^{-4}$ rad) around the mode-I crack-tip in for a representative load level of 575 N obtained from DGS. The contours on the top represent ϕ_x (in the *x*-*z* plane) and the contours on the bottom represent ϕ_y (in the *y*-*z* plane)

The 2D-DIC of images in the deformed and undeformed states was carried out using ARAMIS® software. A facet/sub-image size of 25 x 25 pixels with an overlap of 20 pixels (i.e., step size of 5 pixels) was used during speckle correlation. The resulting data

matrix of size 295 x 194 was exported to MATLAB for post-processing and the evaluation of orthogonal angular deflections in the region of interest. The angular deflection contours in the horizontal (*x*-*z*) and vertical (*y*-*z*) planes for a load of 575 N are shown in Fig. 2.7. A heavy white line is overlaid on the resulting contours to represent the edge crack. The tri-lobed crack-tip fields, as predicted by the equations for mode-I can be seen in these contour patterns. The crack flanks do show significant residual stresses and edge effects, more so in ϕ_y field than in ϕ_x field. That is, the contours adjacent to the crack flanks in ϕ_y visibly affected in Fig. 2.7. The point of convergence of these contours is useful for locating the crack-tip.

2.3.4 Evaluation of SIFs

This being a mode-I crack problem, Eqs. (2.3) and (2.4), described earlier, can be used to evaluate the SIF. In this experiment, the SIFs were evaluated using Eq. (2.3) by employing an over-deterministic regression analysis of the measured data and $N = 4$. Discrete angular deflection values around the crack-tip in the region $0.4 \le r / B \le 1.5$ and an angular extent of $-165^0 \le \theta \le 165^0$ were used in the analysis. This ensured that the data used was sufficiently close to the crack-tip yet outside the region of dominant triaxial effects near the crack-tip [89]. This also indirectly helped for minimizing the error in locating the crack-tip due to the edge effects introduced by the image correlation operation.

2.3.5 Experimental results

The variation of SIFs obtained from the regression analysis of measured data with the applied load is plotted in Fig. 2.9. The error bars correspond to the SIFs obtained by using different subsets in the $0.4 \le r/B \le 1.5$ and $165^0 \le \theta \le -165^0$ range. SIF histories were also evaluated from the analytical solution as [88],

$$K_I = \frac{F\,S}{Bw^{3/2}} \frac{3(\xi)^{1/2}\left[1.99-\xi(1-\xi)\left\{2.15-3.93(\xi)+2.7(\xi)^2\right\}\right]}{2(1+2\xi)(1-\xi)^{3/2}}, \qquad \xi = \frac{a}{w} \tag{2.7}$$

where, F is the applied load, S is the distance between the supports, B is the specimen thickness, w is the width of the specimen and a is the initial crack length. The SIFs evaluated from the boundary collocation solution is superimposed on the measured SIFs in Fig. 2.8. A good agreement between the two is clearly evident.

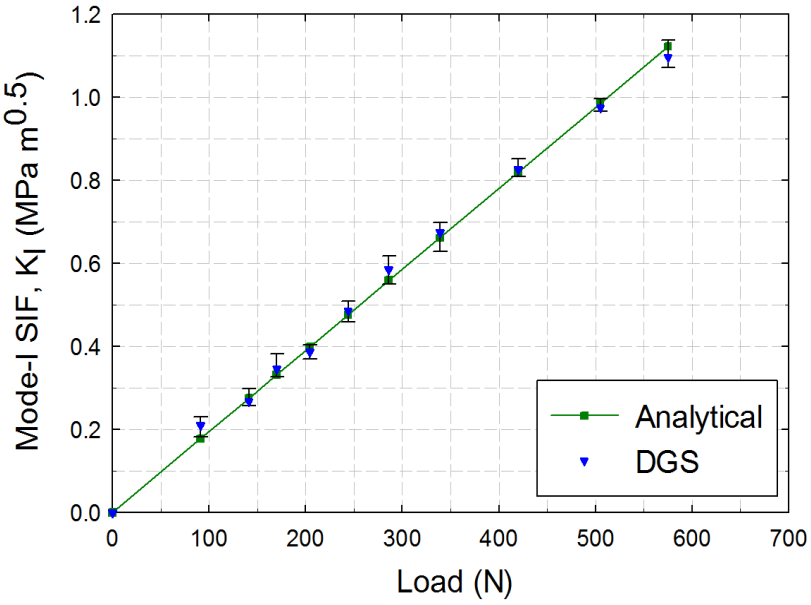

Figure 2.8: Variation of measured mode-I SIFs with applied load and comparison with analytical counterpart.

2.4 Quasi-static mixed-mode crack-tip problem

2.4.1 Specimen preparation and geometry

A 110 mm x 25.4 mm rectangular specimen of 4.5 mm thickness was machined from a cast PMMA sheet. A 45˚inclined edge notch of length 9.8 mm was introduced into the specimen as shown in Fig. 2.9 using a diamond impregnated circular saw of approximately 300 μm thickness. The target plate used for DGS measurements was prepared by spraying a fine mist of black and white paints successively on a flat surface to create random speckles. Two heavy black dots were marked 10 mm apart on the target plate to relate the spatial dimensions on the image to those on the target plate and the specimen.

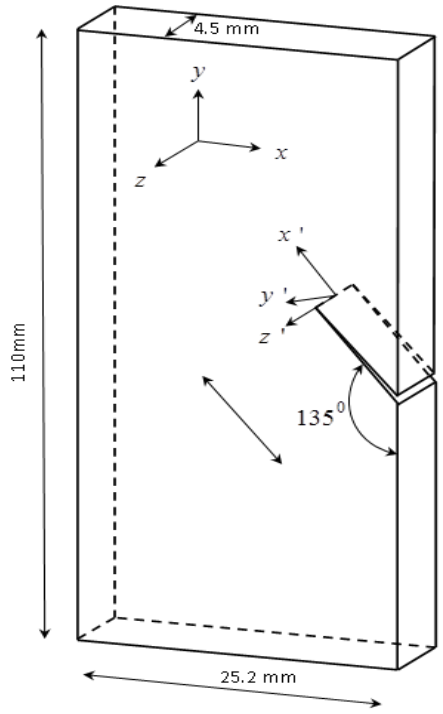

Figure 2.9: Specimen geometry used for quasi-static mixed-mode tension experiment.

2.4.2 Experimental setup and procedure

A photograph of the experimental setup used to study mixed-mode crack problems is shown in Fig. 2.10. An Instron 4465 universal testing machine was used for loading the specimen in tension and in displacement control mode (crosshead speed = 0.005 mm/sec). The experimental parameters and other details are the same as in Section 2.3.2.

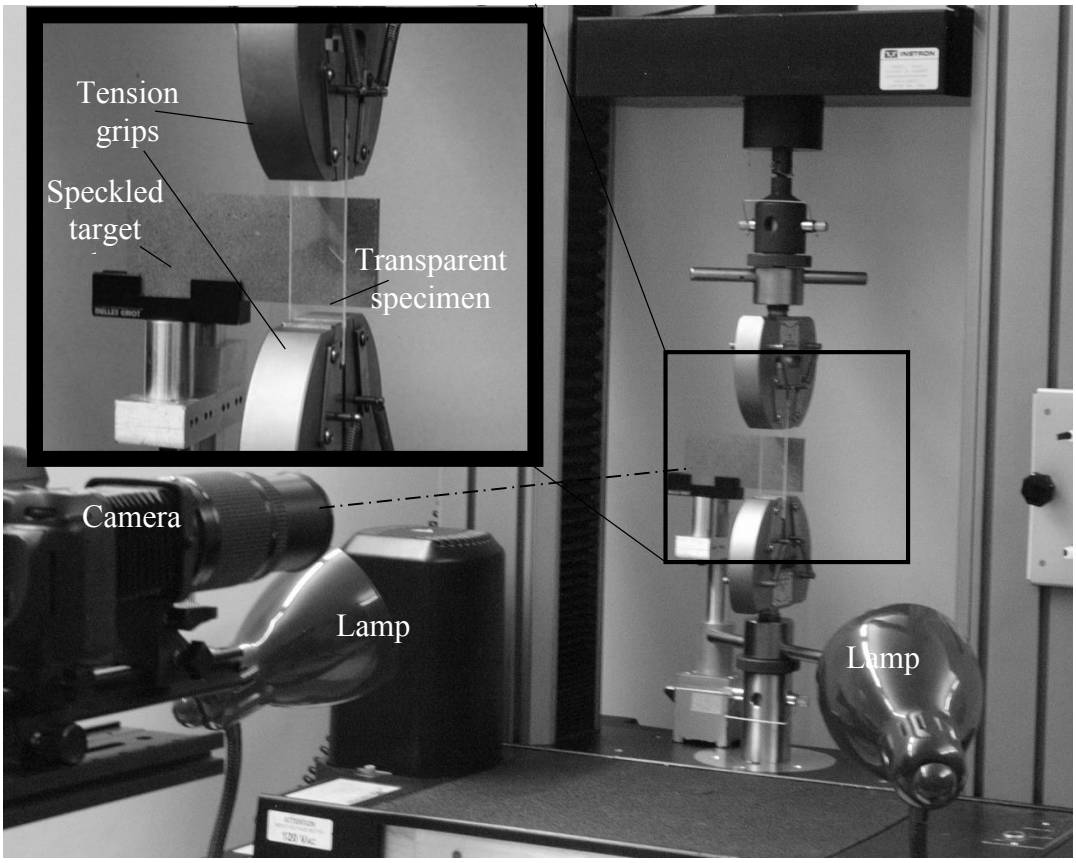

Figure 2.10: Experimental setup used for measuring mixed-mode crack-tip fields in a tensile strip using DGS. Inset shows close-up view of the edge cracked specimen and the target.

A reference/undeformed image of the target plate speckles through the crack-tip vicinity was recorded in no-load (load < 1 N) condition. As the sample was loaded

gradually, the perturbed speckle images of the target plate were recorded using time-lapse photography at 20 frames per minute. Two representative speckle patterns, one in the reference state and the other in the deformed state, are shown in Fig. 2.11. The recorded images correspond to 30 mm x 20 mm region on the specimen. Using a pair of two heavy black dots (see, Fig. 2.11) marked on the target plate, the dimensions on image in terms of pixels were related back to specimen/target plate dimensions (1 pixel = approx. 20 μm on the target plane). Sufficient care was also exercised to obtain a near Gaussian distribution of gray scales for each image in the mid-range of 0-255 (8 bit) scale by positioning the lamps appropriately. When examined carefully, it can be seen that the speckles are noticeably smeared in Fig. 2.11(b) in the vicinity of the stress concentration (particularly ahead of the crack-tip) whereas the speckles are largely unaffected in the far-field.

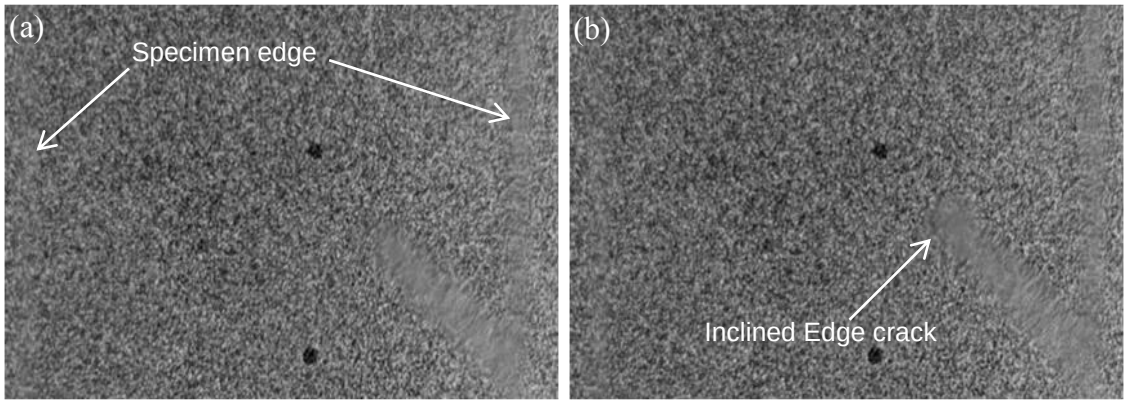

Figure 2.11. Speckle image of the target plate through the transparent edge cracked specimen at (a) no-load and (b) far-field stress $\sigma_\infty \approx 6$ MPa. The two black dots are 10 mm apart.

2.4.3 Image analysis

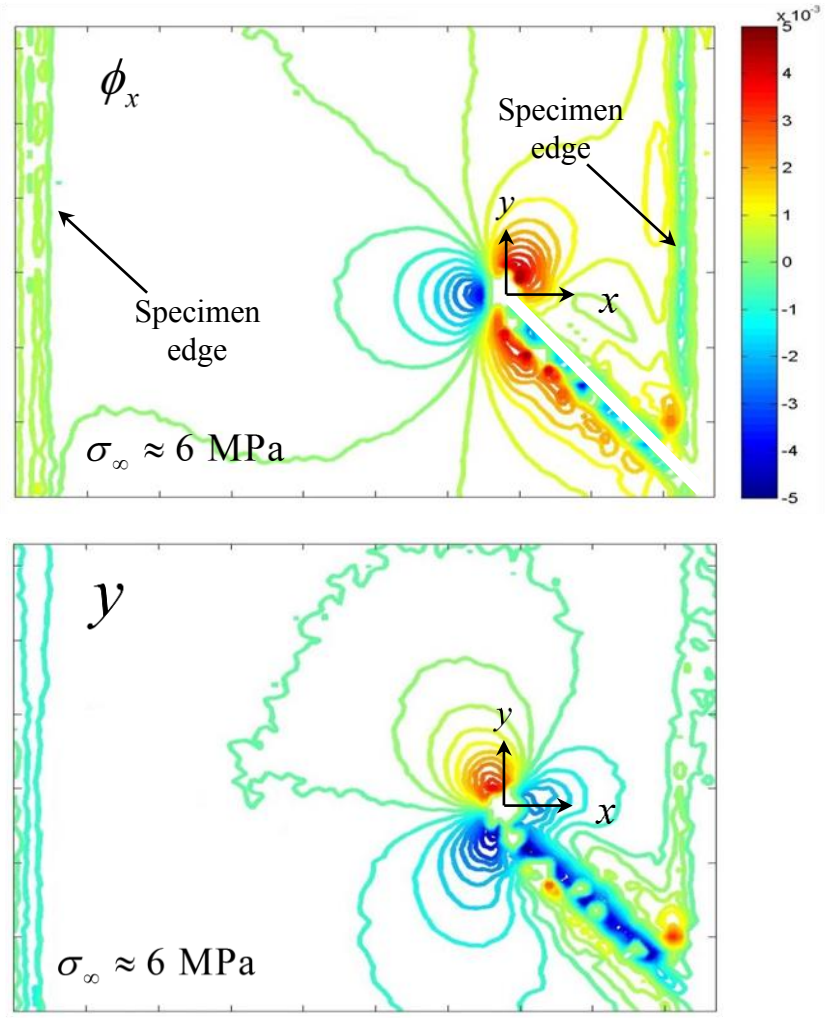

Figure 2.12: The Angular deflection contours (contour interval = 4×10^{-4} rad) around the mixed-mode crack-tip in global coordinates (*x*-*y* coordinate system) for a representative load level obtained from DGS. The contours on the top represent ϕ_x (in the *x*-*z* plane) and the contours on the bottom represent ϕ_y (in the *y*-*z* plane)

The 2D-DIC was carried out using ARAMIS® software. A facet/sub-image size of 25 x 25 pixels with an overlap of 10 pixels (i.e., step size of 15 pixels) was used during speckle correlation. The resulting data matrix of size 64 x 98 was exported to MATLAB

for post-processing including the evaluation of orthogonal angular deflections in the region of interest. The angular deflection contours in the horizontal (*x*-*z*) and vertical (*y*-*z*) planes (global coordinate system) for a select far-field uniform tension of 6 MPa is shown in Fig. 2.12. A heavy white line is overlaid on the resulting contours to represent the edge crack.

2.4.4 Evaluation of SIFs

To facilitate the analysis of DGS data in the local crack-tip coordinates (*x'* and *y'*), the corresponding angular deflections $\phi_{x'}$ and $\phi_{y'}$ were expressed in terms of ϕ_x and ϕ_y in the global coordinates (*x*, *y*) using the transformation angle α as,

$$\phi_{x'} = \phi_x \cos\alpha + \phi_y \sin\alpha \tag{2.8}$$

$$\phi_{y'} = -\phi_x \sin\alpha + \phi_y \cos\alpha \tag{2.9}$$

Now, the angular deflections for a mixed-mode static crack-tip can be expressed in the local coordinates as [90],

$$\phi_{x'} = C_\sigma B \frac{\partial I_1}{\partial x'} = C_\sigma B \sum_{N=1}^{\infty} \left\{ \begin{array}{l} A_N \left(\frac{N}{2}-1\right) r^{\left(\frac{N}{2}-2\right)} \cos\left(\left(\frac{N}{2}-2\right)\theta\right) \\ +D_N \left(\frac{N}{2}-1\right) r^{\left(\frac{N}{2}-2\right)} \sin\left(\left(\frac{N}{2}-2\right)\theta\right) \end{array} \right\} \tag{2.10}$$

$$\phi_{y'} = -C_\sigma B \frac{\partial I_1}{\partial y'} = -C_\sigma B \sum_{N=1}^{\infty} \left\{ \begin{array}{l} A_N \left(\frac{N}{2}-1\right) r^{\left(\frac{N}{2}-2\right)} \sin\left(\left(\frac{N}{2}-2\right)\theta\right) \\ -D_N \left(\frac{N}{2}-1\right) r^{\left(\frac{N}{2}-2\right)} \cos\left(\left(\frac{N}{2}-2\right)\theta\right) \end{array} \right\} \tag{2.11}$$

where $I_1 = (\sigma_x + \sigma_y) = (\sigma_{x'} + \sigma_{y'})$ is used and (r, θ) denote polar coordinates defined (relative to the local coordinates) as shown in Fig. 2.9, C_σ is the elasto-optic constant of PMMA, B = 4.5 mm is the initial thickness of the specimen, $A_1 = K_I \sqrt{\frac{2}{\pi}}$ with K_I being the mode-I stress intensity factor and $D_1 = K_{II} \sqrt{\frac{2}{\pi}}$ with K_{II} the mode-II stress intensity factor. In this experiment, the SIFs were evaluated using Eq. (2.10) by employing an over-deterministic regression analysis of the measured data and N = 4. (Alternatively, Eq. (2.11) can also be used to evaluate the SIFs; Results presented here are based on Eq. (2.10)). Discrete angular deflection values around the crack-tip in the region $0.4 \le r / B \le 1.5$ and an angular extent of $-135^0 \le \theta \le 135^0$ were used in the regression analysis. This ensured that the data used was sufficiently close to the crack-tip yet outside the region of dominant triaxial effects [89]. This also indirectly helped in minimizing the error in locating the crack-tip due to the edge effects introduced by the image correlation operation.

2.4.5 Mixed-mode FE simulation

A complimentary quasi-static finite element simulation of the mixed-mode tension experiment was carried out using ABAQUS® software. The model was discretized into 4,589 four node bilinear plane stress quadrilateral elements. The local seeding around the crack-tip was used to generate a fine mesh. Table 1 shows the material properties of PMMA

used in the simulation. The discretized model and the boundary conditions used are shown in Fig. 2.13.

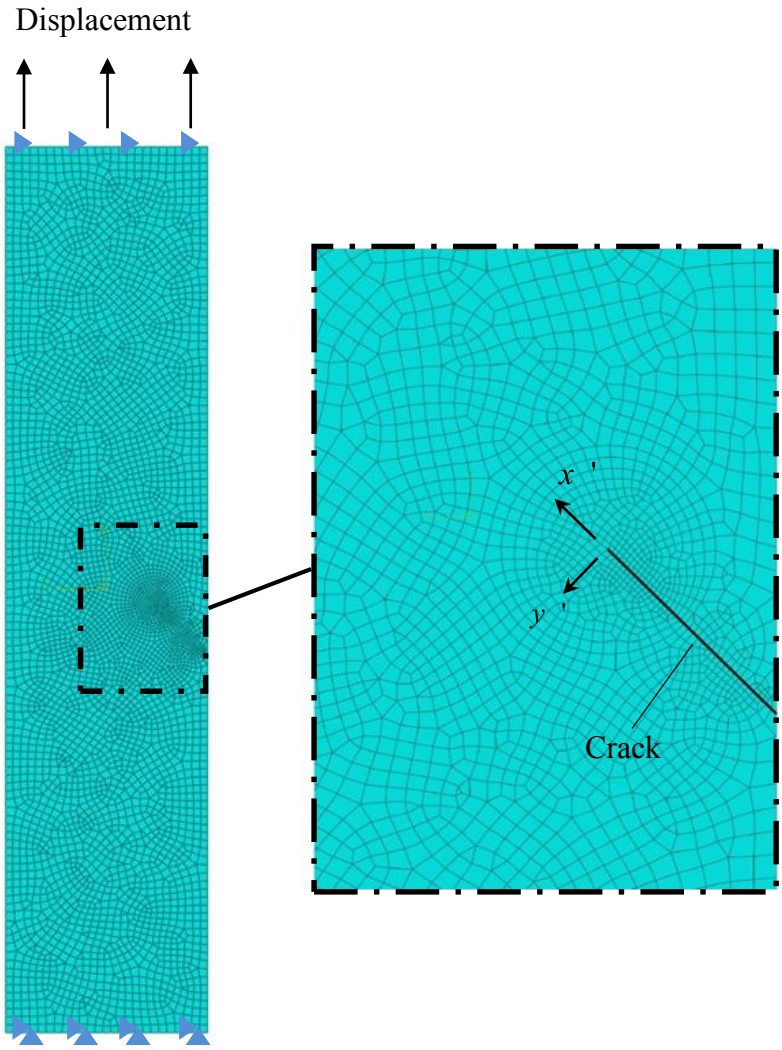

Figure 2.13: Details of numerical simulations; finite element model showing the discretization and the boundary conditions used.

From the load-displacement curve measured during the experiment, the displacements corresponding to the load at which DGS measurements were obtained. These displacements were imposed at one end of the specimen in a series of steps. A local

coordinate system aligned with the crack direction was defined for post-processing the data. The crack opening (COD) and crack sliding (CSD) displacements were extracted along the two crack faces. This was repeated for each displacement step. The *apparent* mode-I and mode-II SIFs, $(K_I)_{app}$ and $(K_{II})_{app}$ at each displacement step were computed using [90],

$$(K_I)_{app} = \frac{E\sqrt{2\pi}}{8\sqrt{r}} u_{y'}; \quad (r, \theta = \pi) \tag{2.12}$$

$$(K_{II})_{app} = \frac{E\sqrt{2\pi}}{8\sqrt{r}} u_{x'}; \quad (r, \theta = \pi) \tag{2.13}$$

where E is the elastic modulus, (r, θ) are the crack-tip polar coordinates, $u_{y'}$ is the COD and $u_{x'}$ is the CSD of the crack flanks. By extrapolating the linear portion of $(K_I)_{app}$ and $(K_{II})_{app}$ values plotted as a function of the radial distance r to the crack-tip, the true K_I and K_{II} were determined.

2.4.6 Results

Figure 2.14 shows the orthogonal angular deflection plots for a select far-field stress (σ_∞ ~ 6 MPa) in the local coordinate system (x' and y'). A heavy white line is overlaid on the resulting contours to represent the edge crack. It should be noted that the contour lines adjacent to the crack faces and specimen edges show unavoidable edge effects. It can be seen that the angular deflection contours in the local coordinate system $\phi_{x'}$ and $\phi_{y'}$ have

similarities with the analytical angular deflection contours for the mixed-mode crack shown in Fig. 2.4(b).

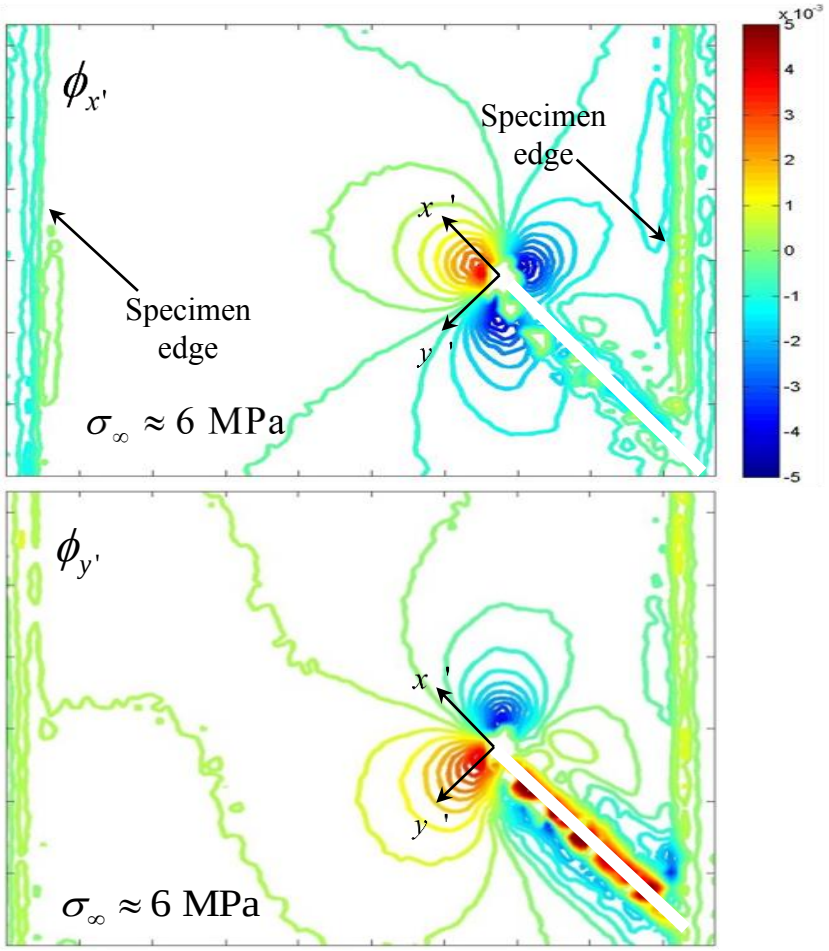

Figure 2.14: The Angular deflection contours (contour interval = $4\text{x}10^{-4}$ rad) around the mixed-mode crack-tip in local coordinate system (*x'-y'* coordinate system) for a representative load level obtained from DGS. The contours on the top represent $\phi_{x'}$ (in the *x*-*z* plane) and the contours on the bottom represent $\phi_{y'}$ (in the *y*-*z* plane).

The variation of SIFs obtained from the regression analysis of measured data with the far-field stress (σ_∞) are plotted in Fig. 2.16. The error bars correspond to the SIFs obtained by using different subsets in the $0.4 \le r/B \le 1.5$ and the $-135^0 \le \theta \le 135^0$ range.

The SIFs evaluated from the numerical simulation is superimposed on the measured SIFs in Fig. 2.15. A good agreement between the two is clearly evident.

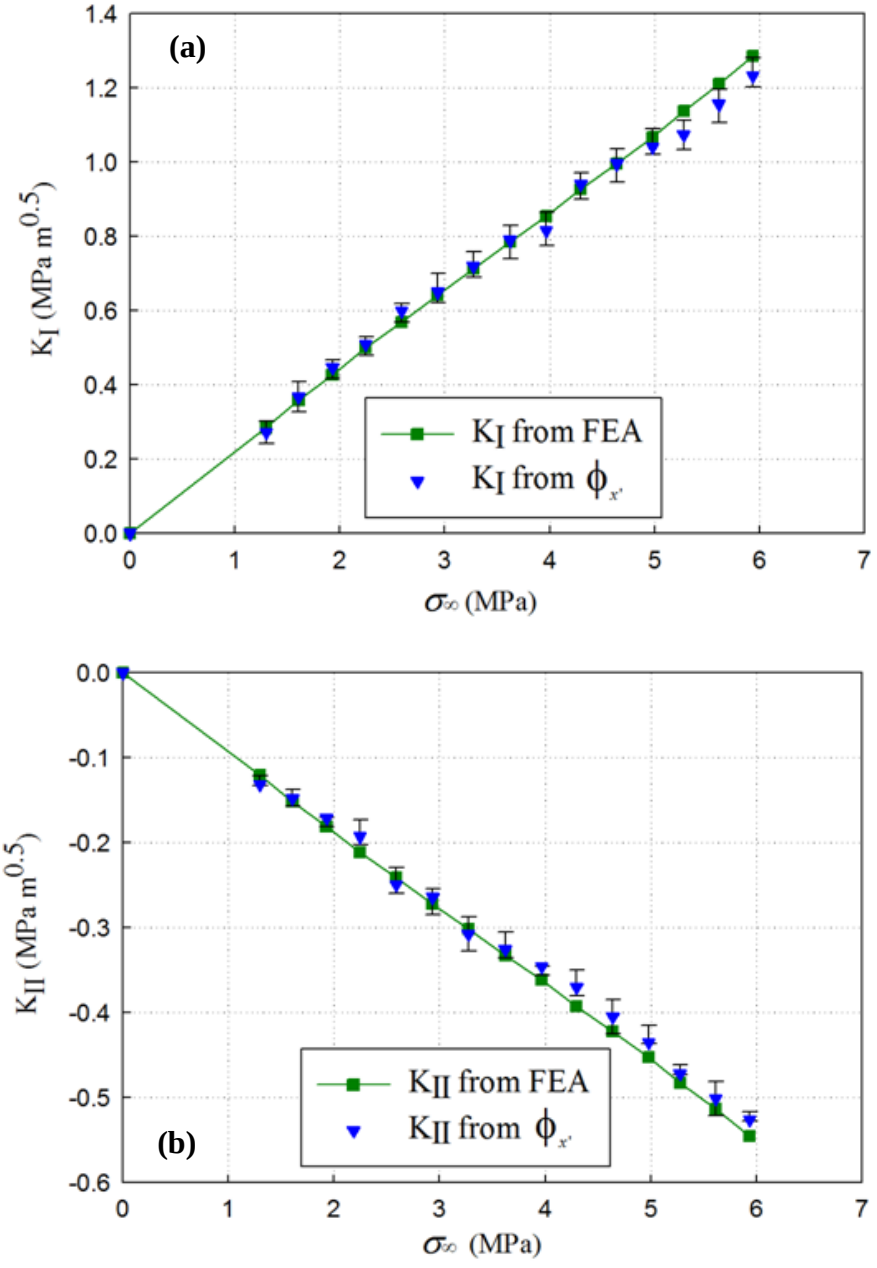

Figure 2.15: Variation of measured mixed-mode SIFs with far-field stress and comparison with FE counterparts. (a) K_I (b) K_{II}.

Chapter 3

MODE-I AND MIXED-MODE DYNAMIC FRACTURE OF PMMA AND PC

In this chapter, investigation on the mode-I and mixed-mode dynamic fracture of monolithic PMMA and PC using DGS is described. Methodology to vary the mode-mixity under dynamic loading conditions is elaborated with the help of FE simulations. Sample preparation and loading setup details are elaborated and stress intensity factor (SIF) histories along with the dynamic fracture envelopes for each material are presented. Using the maximum tangential stress (MTS) fracture criterion, the initial crack kink angles are predicted and compared with the measurements. Complimentary FE simulations of mode-I and mixed-mode cracks in PMMA are also presented

3.1. Methodology to vary mode-mixities under stress wave loading

To produce a mode-I crack initiation and self-similar crack propagation under dynamic conditions various different specimen loading configurations are used. The two that are amenable to optical measurements include a reverse impact geometry and a wedge loading geometry. In the former, a crack is cut on one of the edges of the specimen and subjected to a compressive stress pulse on the opposing edge and in line with the crack. The compressive waves upon reflection from the free surface (edge) that contains the crack turn tensile upon reflection and load the crack in mode-I conditions. In the latter, a V-notch is pre-cut into the specimen and loaded using a conforming wedge/chisel tip sending a

stress pulse. The flanks of the V-notch are loaded symmetrically by the contacting wedge driving a symmetric mode-I dynamic crack into the specimen. The schematics of the two loading configurations are shown in Fig. 3.1.

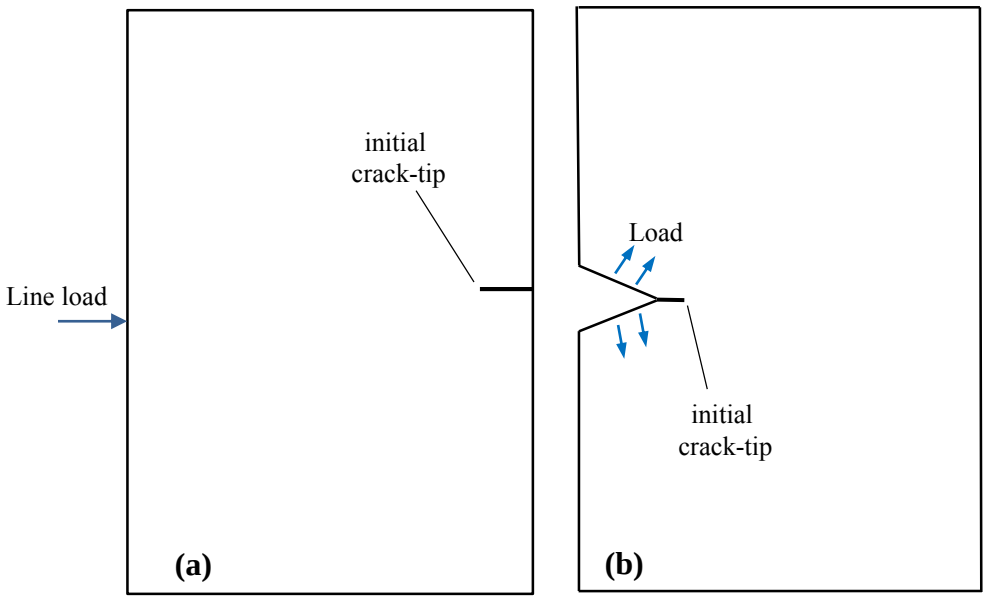

Figure 3.1 (a) Reverse impact and (b) wedge loading configurations that can be used to drive dynamic mode-I crack in a material. (c) The SIF histories for soda-lime glass specimen loaded using these two geometries.

Creating a range of mode-mixities involving combined mode-I (pure tensile) and -II (pure in-plane shear) crack-tip deformations or the so-called mixed-mode conditions leading to kinked crack growth is much more challenging under dynamic conditions. Accordingly, a specimen configuration involving a reverse impact loading of a single edge notched (SEN) geometry capable of producing a range of mode mixities is proposed here. The specimen geometry and loading configuration is shown schematically in Fig. 3.2. To understand the underlying rationale used to arrive at this specimen/loading configuration, numerical simulations were performed first. Elasto-dynamic finite element simulations

were carried out on the specimen geometry using ABAQUS®/Explicit software platform. A Hopkinson pressure bar loading an edge of a free standing cracked plate was modeled. The impact end of the long-bar was shaped into a half-cylinder to produce a line-load on the specimen edge. The specimen and the long-bar were discretized into 259,337 and 37,952 solid 3D tetrahedral elements, respectively. The discretized model overlaid with displacement contours in the *y*-direction is shown in Fig. 3.3.

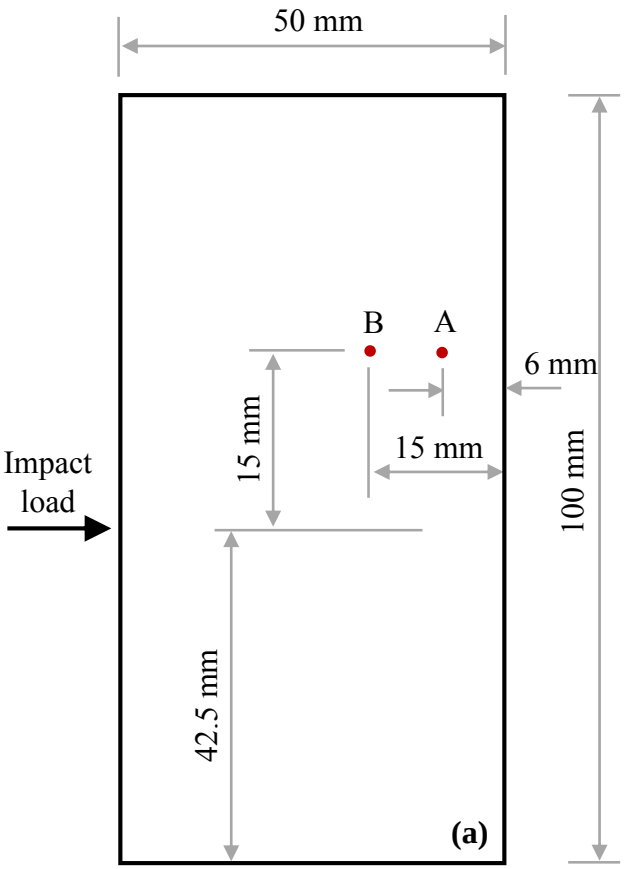

Figure 3.2: Specimen configuration used for arriving at mixed-mode crack geometries.

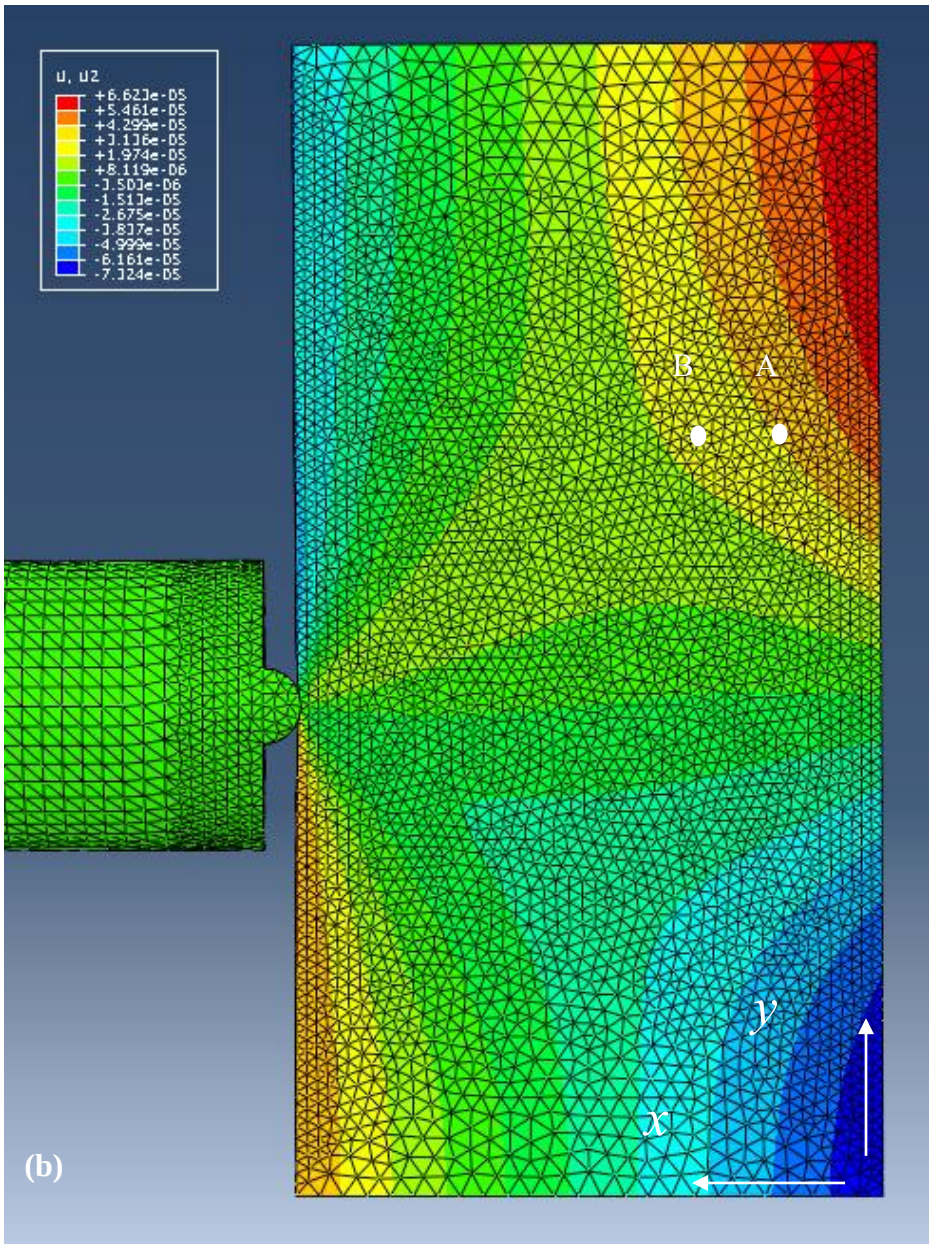

Figure 3.3: Discretized finite element model with an overlay of displacement contours in the *y*-direction from numerical simulation at an arbitrary time instant during impact (striker velocity ~ 13.5 m/sec).

Two points of interest A and B on the specimen were identified, as shown in Fig. 3.2, to monitor stress field evolution during the impact loading event. (These points

correspond to two prospective crack-tip locations in the proposed mixed-mode dynamic fracture specimen geometry.) The time steps during the elasto-dynamic analysis were allowed to be controlled automatically by the explicit integration scheme. The elastic modulus and Poisson's ratio of PMMA, obtained from an ultrasonic pulse-echo measurement of longitudinal and shear wave speeds [91], and its mass density were used in the simulations. The Hopkinson bar (or the long-bar) was modeled using the elastic properties of AL 7075-T6 used in the experiments, to be detailed later. Tables 3.1 and 3.2 list the material properties of PMMA and the AL 7075-T6 aluminum long-bar, respectively. The particle velocity ($V_p(t) = C\varepsilon(t)$ where C is the bar wave speed) history, obtained from a measured strain gauge history ($\varepsilon(t)$) on the long-bar during an actual experiment (to be detailed later), was used as the input for numerical simulations.

Dynamic Properties of AL-7075 Long-bar

Parameter	**Value**
Density	2730 kg/m^3
Elastic Modulus	71.7 GPa
Poisson's ratio	0.30
Longitudinal wave speed in bar	5700 m/s

Table 3.1: Some properties of long-bar used

Dynamic Properties of PMMA

Parameter	**Value**
Density	1010 kg/m^3
Elastic modulus	5.3 GPa
Poisson's ratio	0.34
Elasto-optic constant	-1.08 x 10^{-10} m^2/N

Table 3.2: Properties of cast PMMA used in simulations and experiments.

The normal stress (σ_{yy}) and in-plane shear stress (σ_{xy}) at points A (distance of A from the edge a = 6 mm; a/w = 0.12 from the free edge, w being the width of the plate = 50 mm) and B (distance of B from the edge a = 15 mm; a/w = 0.3 from the free edge) were monitored during the course of the loading event and are shown in Fig. 3.4(a) and (b), respectively. It can be seen that σ_{yy} at both the points are compressive between 15-45 μs ($0.8 < \frac{t}{t^*} < 2.4$ where $t^* = w/C_L$ corresponds to the excursion time for the longitudinal wave over the width of the sample and C_L the longitudinal wave speed of PMMA (~2750 m/s) as the impact induced waves travel initially from the near edge towards the far edge. The reflected tensile waves from the free edge cause a tensile stress beyond $\frac{t}{t^*} \sim 2.4$. During this time interval, at Point A, σ_{yy} increases rapidly when compared the one at point B. On the other hand, at the corresponding time instants, the magnitude of σ_{xy} increases rapidly at point B when compared to the one at point A. In the $0.8 < \frac{t}{t^*} < 2.4$ interval, shear stresses at these points are significantly higher than the corresponding σ_{yy}. In light of these, if the tip of a horizontal edge crack originating at the far (right) edge of the plate were at point A, it will experience a lower shear to tensile stress ratio $(\sigma_{xy}/\sigma_{yy})$ and hence a lower mode-mixity than a prospective crack-tip at point B. Thus, by increasing the crack length from 6 mm (Point A) to 15 mm (Point B), one could potentially increase the mode-mixity at crack initiation when all other parameters are the same.

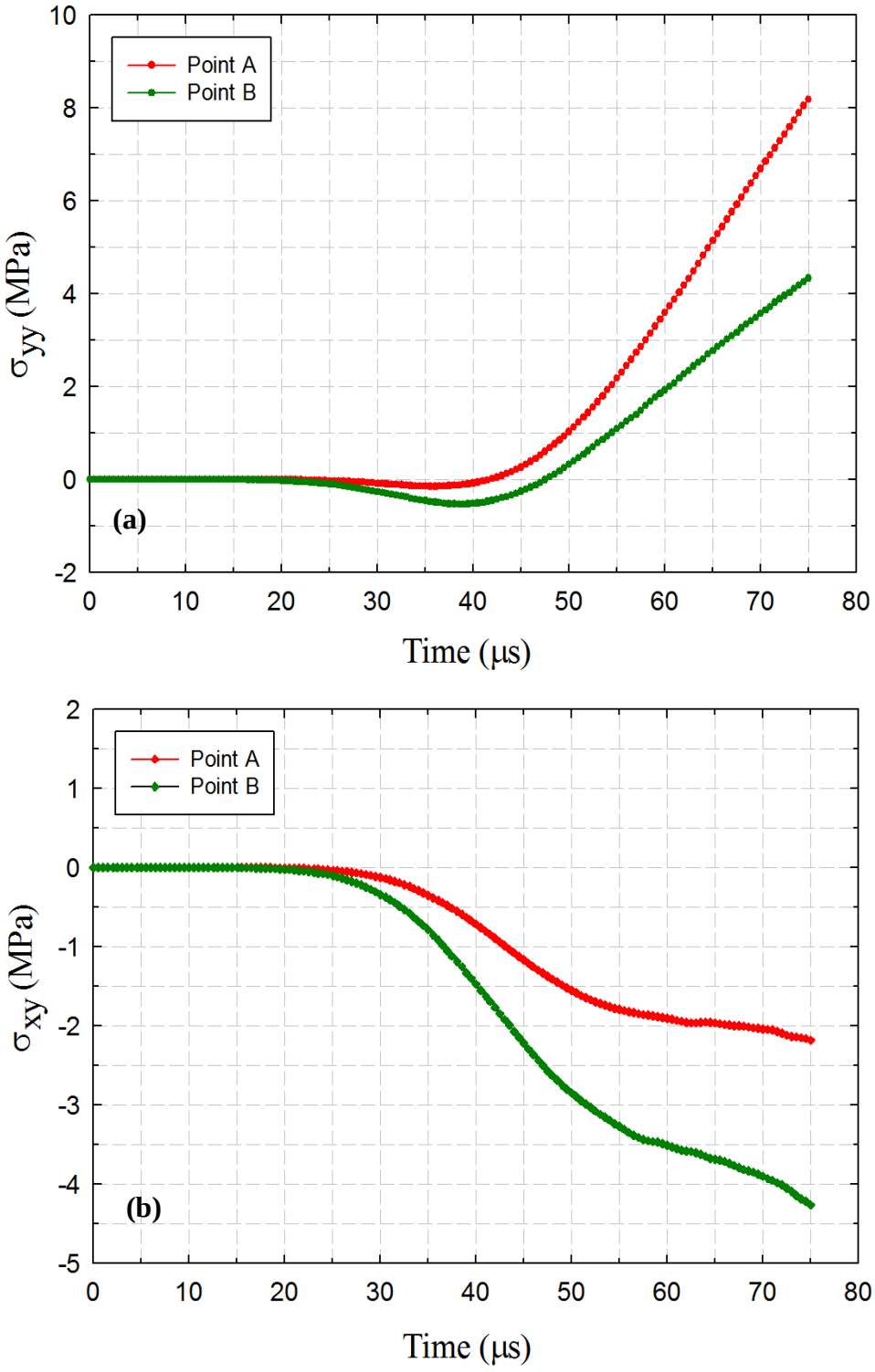

Figure 3.4: Stress field evolution at Points A and B of an uncracked specimen (see, Fig. 3.2) subjected to eccentric impact loading (striker velocity ~ 13.5 m/sec).

Another potential method for altering the mode-mixity at crack initiation in the reverse impact geometry is to vary the impact velocity between experiments while maintaining all other experimental parameters and the specimen geometry the same. That is, when the impact velocity is increased in the specimen configuration (Fig. 3.2), the normal and shear stress histories at the prospective crack-tip location (say, point B) change. The shear stresses increase and normal stresses are decrease until a certain time (~50 μs or $\frac{t}{t^*} > 2.4$ in this case). This increases the shear to tensile stress ratio at the point of interest. Hence, if a crack-tip were present at B, it would attain lower mode-I and higher mode-II stress intensity factors earlier due to the higher impact velocity and initiate at a different mode-mixity if initiation conditions are reached. This is demonstrated in Fig. 3.5(a) and (b) where σ_{yy} and σ_{xy} histories, respectively, for two different impact velocities (13.5 m/s and 16 m/s) are plotted at location B (see, Fig. 3.2). The argument is further supported by multiple experiments using a SEN specimen geometry with crack-tip at point B (a = 15 mm; e = 15 mm) subjected to impact velocities ranging from 10.5 m/s to 19 m/s. The crack initiated and kinked at significantly higher angles, from 32.6 deg. to 62.2 deg (as shown in Fig. 3.6 (a)-(e)), as the impact velocity was increased. *However, the former method of increasing the crack length is chosen for the current investigation to avoid potential loading rate effects at different velocities contaminating mixed-mode crack initiation behavior.*

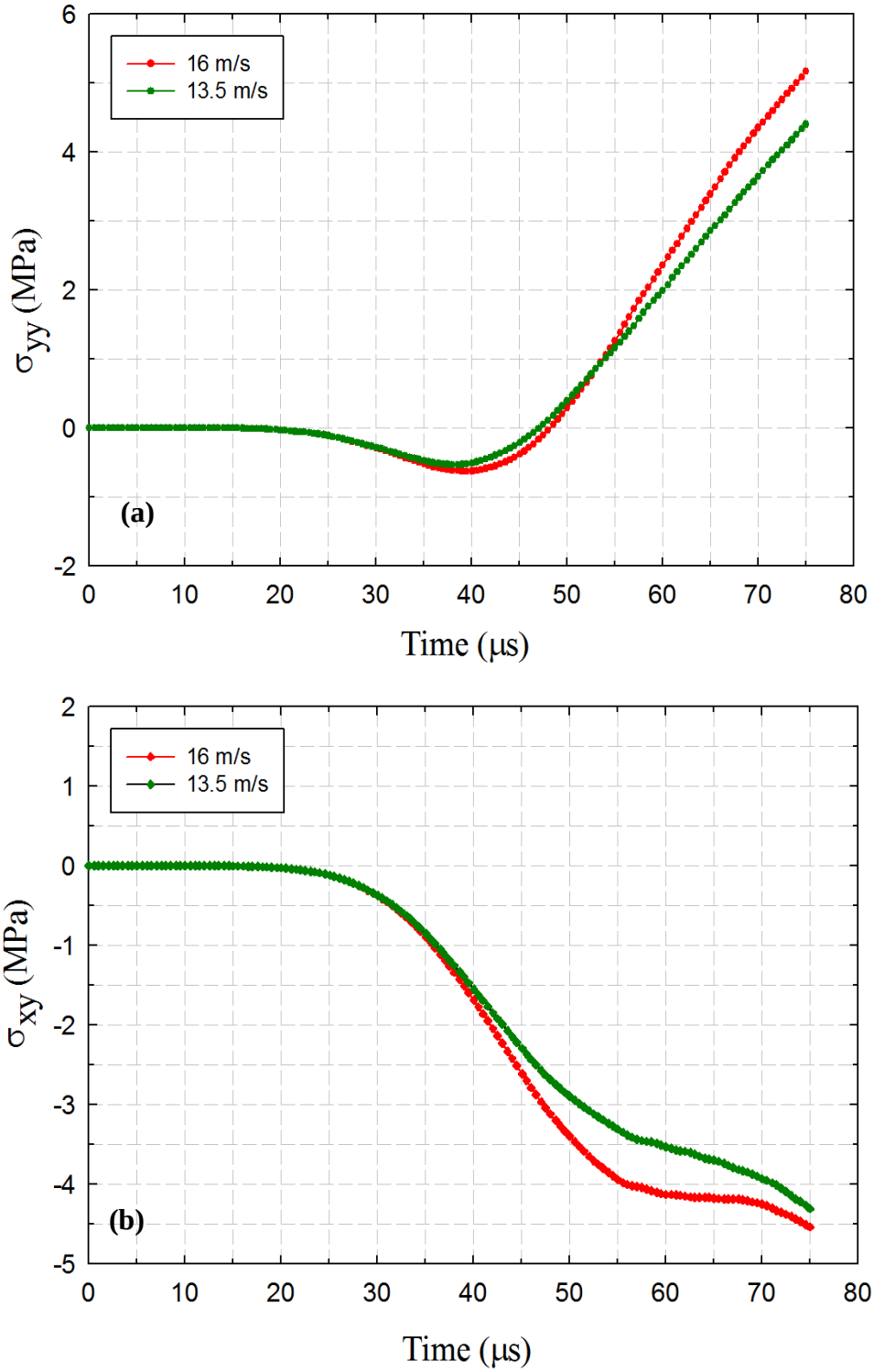

Figure 3.5: Stress field evolution at Point B for different impact velocities (striker velocity ~ 13.5 m/s and 16 m/s) on an uncracked specimen.

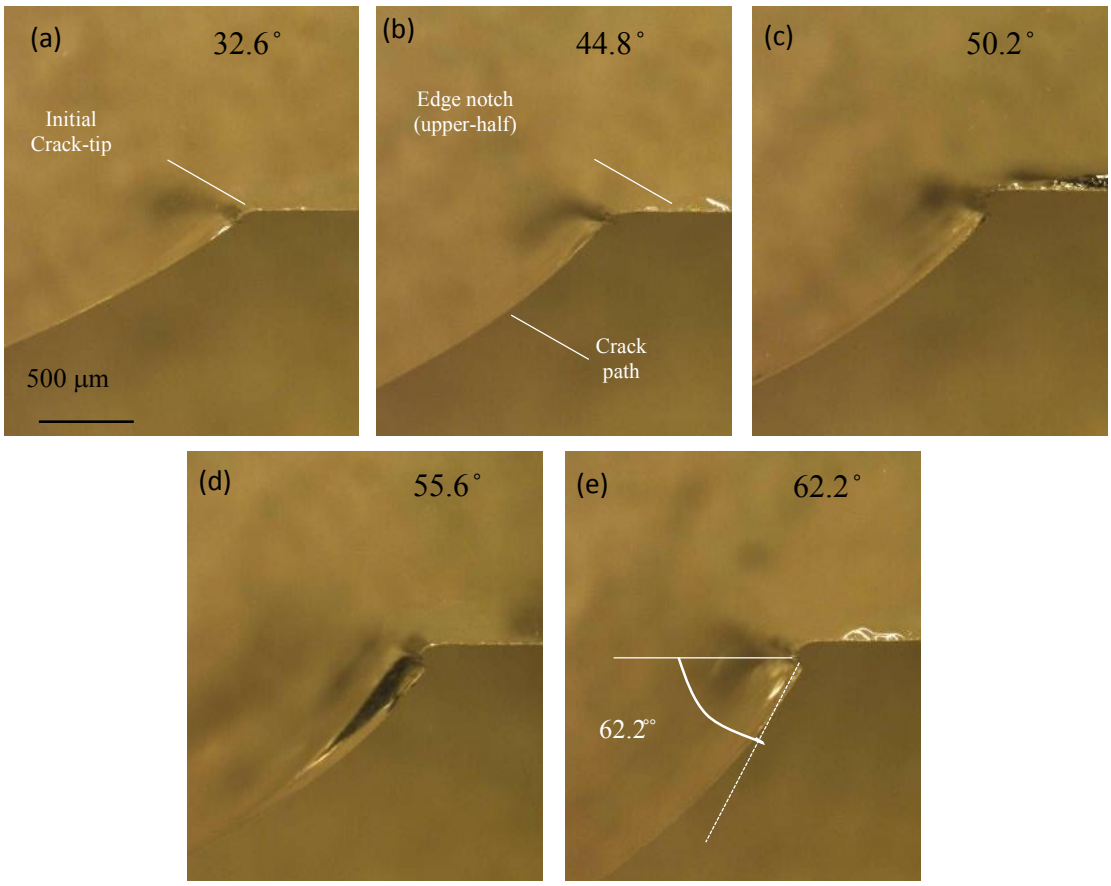

Figure 3.6: Close up images of crack initiation in PMMA specimens (a = 15mm; e = 15mm) at various impact velocities of (a) 10.5 m/s, (b) 12 m/s, (c) 13.5 m/s, (d) 16 m/s, (e) 19 m/s. The crack initiation angle relative to the initial notch orientation is shown on the right top corner of each photograph of the upper-half of the fractured specimen.

3.2. Sample preparation and geometry

SEN plate specimens were prepared to carry out dynamic fracture experiments. The specimens of 100 mm x 50 mm in-plane dimensions and thickness of 8.6 mm for PMMA and 6.15 mm for PC were machined from cast PMMA sheets (see Fig. 3.7). A notch was machined into these specimens using a 300 μm thick diamond impregnated saw. The notch length (and location of the notch tip) was varied to obtain different mode-mixities (see inset in Fig. 3.7 for details) while the eccentricity (e) between the loading point on the opposite

face and the crack location was kept constant. Five different configurations were used to produce various mode mixities at crack initiation. This included the mode-I case with an eccentricity $e = 0$. The initial notch tip in each case was sharpened using a razor blade and the resulting sharpness of the tip in case of PMMA is as shown in the inset of Fig. 3.7. Evidently, the resulting crack-tip root radius is at least an order of magnitude lower than the initial notch radius.

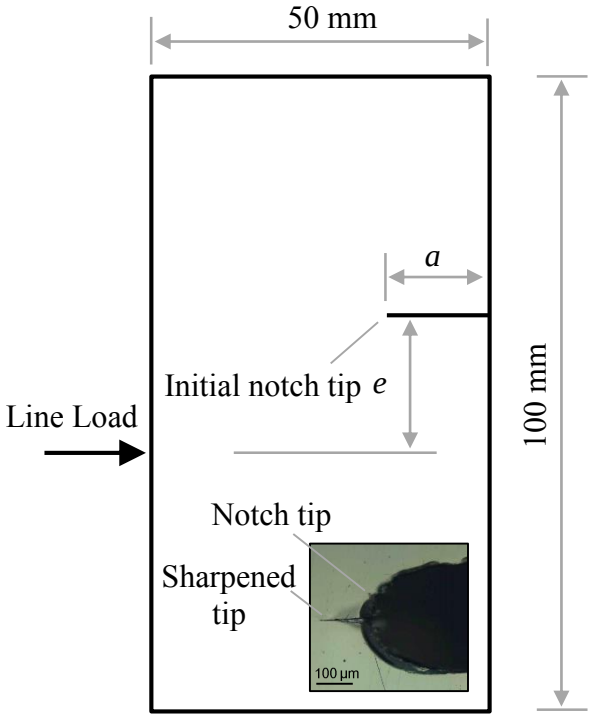

Mode-I	Config.1	$a = 6$ mm, $e = 0$ mm
Mixed-mode	Config.2	$a = 6$ mm, $e = 15$ mm
	Config.3	$a = 9$ mm, $e = 15$ mm
	Config.4	$a = 12$ mm, $e = 15$ mm
	Config.5	$a = 15$ mm, $e = 15$ mm

Figure 3.7: Specimen configuration used in mixed-mode dynamic fracture experiments. Values of a and e used are listed in the table. Inset shows the initial notch tip (PMMA) sharpened using a razor blade. (The line-load and the initial crack are equidistant relative to the horizontal axis of the specimen.)

3.3. Experimental setup

The dynamic mode-I and mixed-mode fracture in monolithic PMMA and PC specimens were studied using transmission-mode DGS in conjunction with ultrahigh-speed digital photography. The schematic of the experimental setup used is shown in Fig. 3.8. A Hopkinson pressure bar (long-bar) was used for loading the single edge pre-notched specimen. It was a 1.83 m long-bar of 25.4 mm diameter with a cylindrical end (line-load) pressed against an unconstrained plate on the edge opposite to the cracked edge (see, Fig.3.9). The sample was positioned on the platform of a micro-positioning stage using a 2 mm thick strip of soft putty between the specimen and the platform. Another identical putty strip was placed on the top edge of the specimen to ensure symmetry in terms of acoustic impedance. A 305 mm long, 25.4 mm diameter rod held in the barrel of a gas-gun was co-axially aligned with the long-bar and was used as the striker. Both the long-bar and the striker were made of AL 7075-T6 eliminating any impedance mismatch between them during impact. A striker velocity of 13.5 ± 0.5 m/s was employed uniformly in all tests for PMMA and the corresponding strain history measured off the long-bar is shown in Fig. 3.10 and was used to obtain the particle velocity input to the finite element computations discussed earlier. Whereas, a striker velocity of 17.5 m/s was used in all the experiments for polycarbonate in order to be able to initiate the crack in this relatively tough polymer.

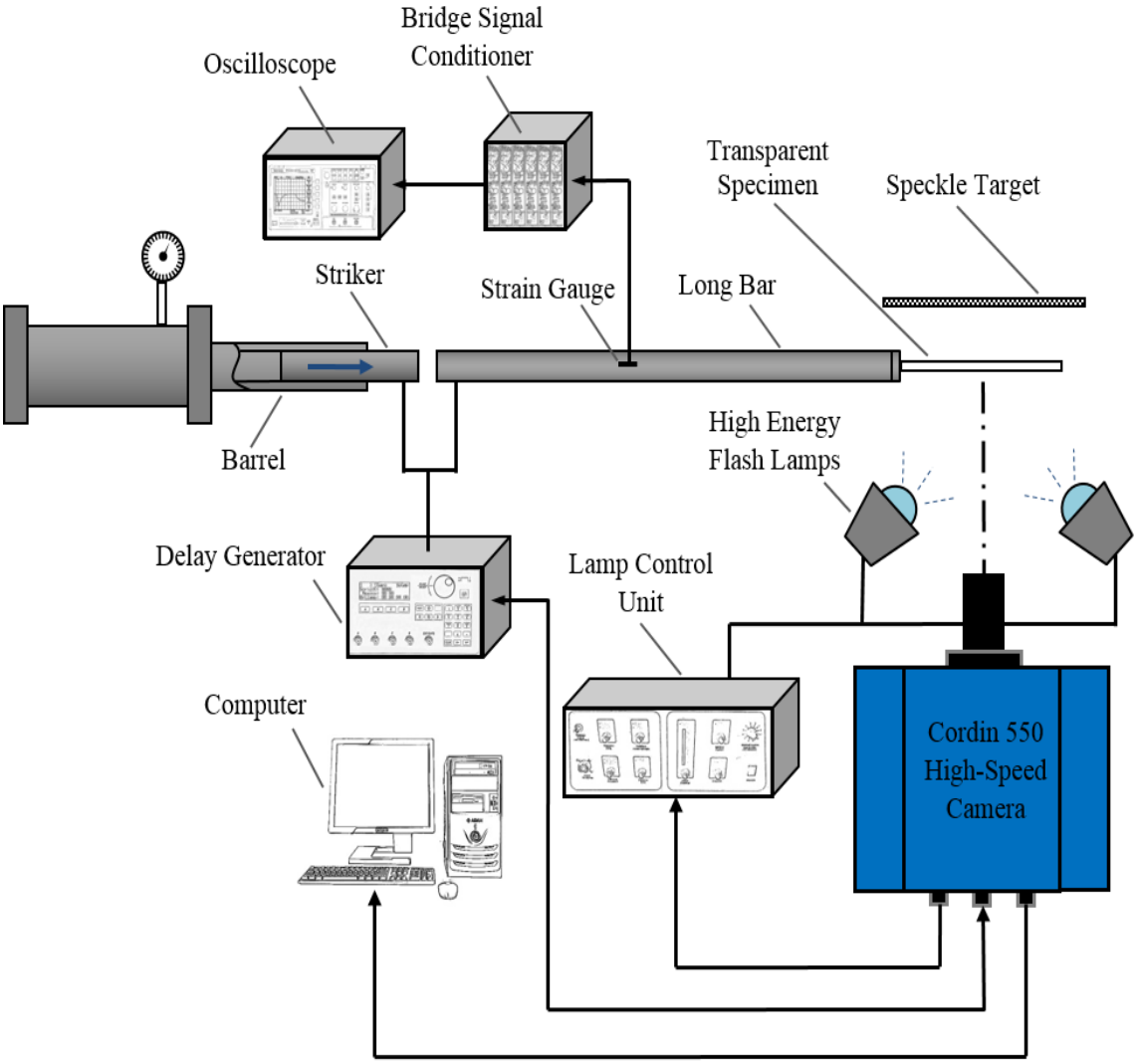

Figure 3.8: Experimental setup used for dynamic mixed-mode fracture studies.

The speckle images were acquired using a Cordin-550 ultrahigh-speed digital camera with 32 CCD sensors of 1000 × 1000 pixels spatial resolution and 8 bit grayscale resolution positioned radially around a five-facet rotating mirror. The imaging system also included two high-energy flash lamps producing broad-band white light illumination needed to capture the speckles decorating the target plane. Experimental parameters such

as the trigger delay, flash duration, framing rate, CCD gain, and data storage were controlled using a computer connected to the camera. A 28-300 mm focal length macro zoom lens mounted on an adjustable bellows was used for imaging. Further, the lens aperture was kept open as widely as possible (numerical aperture on the lens was $F^{\#}5.6$) to achieve a good exposure with minimum electronic gain during photography. The specimen was at a distance of approximately 850 mm in front of the camera. A speckled target plate was placed behind the specimen at a distance (Δ) of 29.3 mm from the mid-plane of the specimen. A pair of heavy dots (Fig. 3.11) were marked on the target plate to help relate the dimension on the image to the actual specimen/target dimensions during image analysis. The speckles covered approximately 4-5 pixels; or, the scale factors ranged between 22-24 pixels/mm.

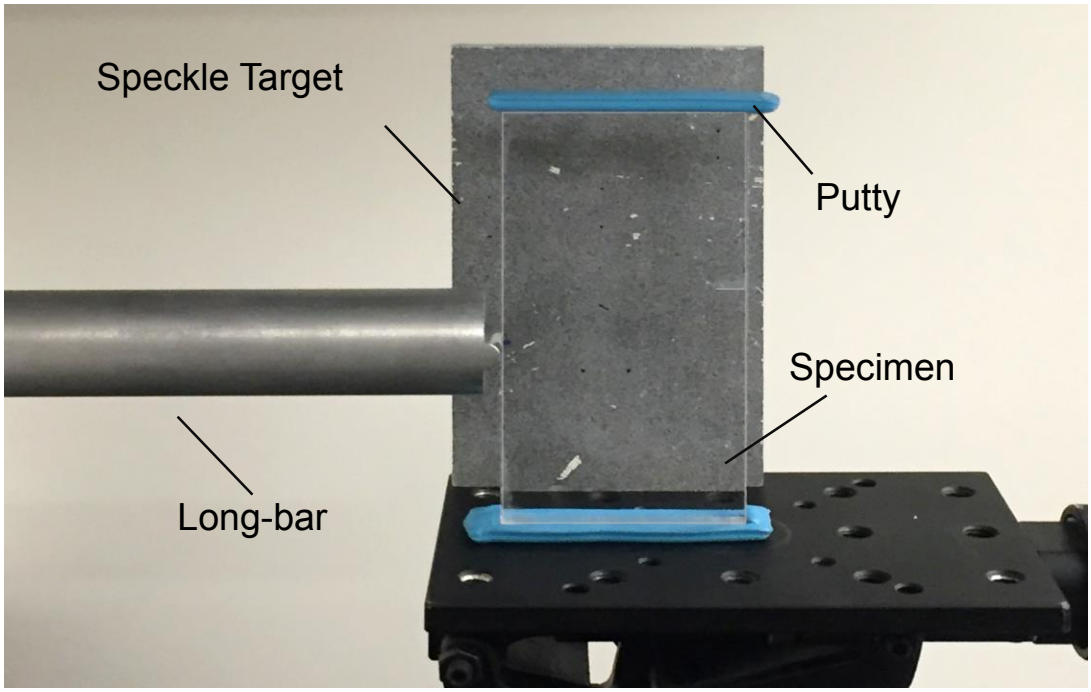

Figure 3.9: Close-up view of the specimen loading configuration used in mixed-mode fracture experiments.

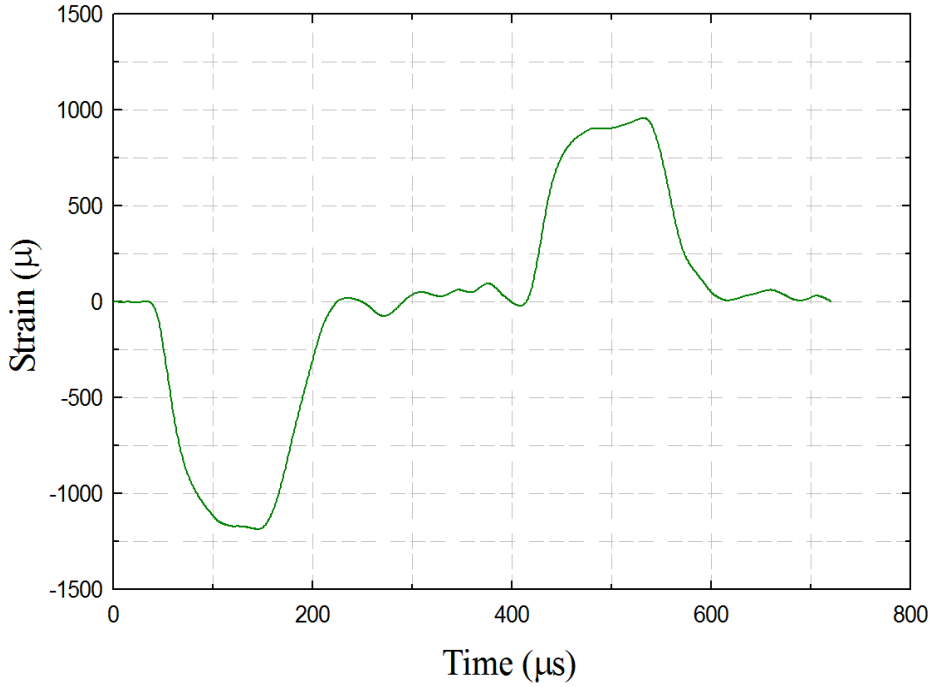

Figure 3.10: Strain history data recorded on the long-bar for a striker velocity of ~13.5 m/s

The region of interest in this study was in the neighborhood of the initial notch tip. That is, the camera recorded approx. 45 mm × 45 mm region. Prior to loading the specimen, a set of 32 speckle images were recorded in the undeformed state at 400,000 frames per second. Care was exercised to achieve a near Gaussian distribution of gray scales for each speckle image, typically in the mid-range of 0-255 gray scale by optimizing the position of the flash lamps by trial and error. Next, without altering any of the camera settings, the striker was launched towards the long-bar. When the striker contacted the long-bar, a compressive stress wave was set-off in the long-bar, which propagated over its length before compressively loading the crack-free specimen edge. The *loading phase* of the stress pulse lasted ~120 μs. As the striker contacted the long-bar, a trigger signal was generated prompting the camera to record a second set of 32 images at the same framing rate as the

specimen was loaded by stress waves. A trigger delay was used to adjust the recording window due to the fixed number of frames (32) of the camera. Thus, a total of 32 pairs of images in the deformed and undeformed (reference) states were recorded at 2.5 μs intervals between successive images. Two such speckle images in the region of interest, one in the undeformed state and the other in the deformed state with a kinked dynamically growing crack, are shown in Fig. 3.11. The corresponding two images for each sensor were paired from the undeformed and deformed sets and each of these 32 matched pairs was correlated separately.

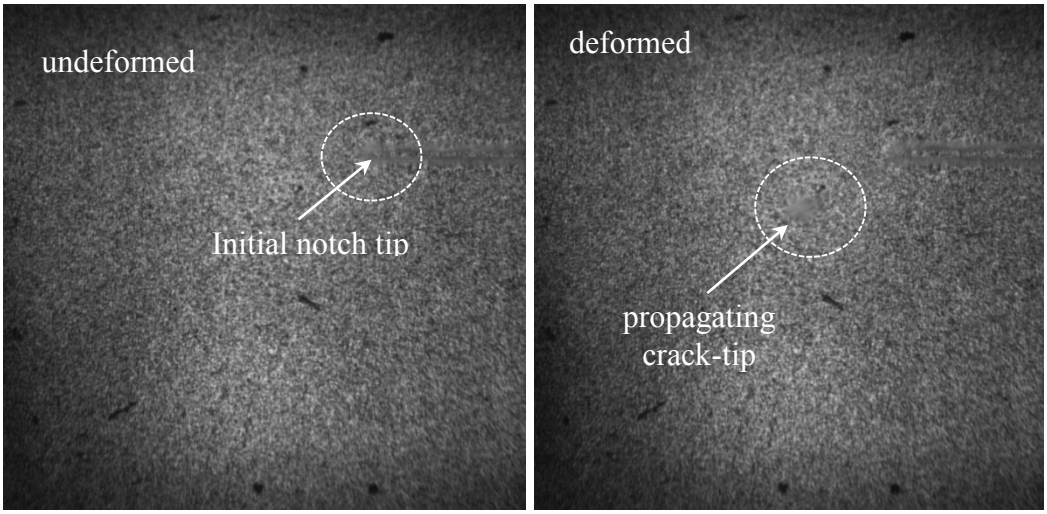

Figure 3.11: Speckle images in the undeformed (top) and deformed (bottom) states recorded by the high-speed camera though a PMMA specimen.

3.4 Image analysis

The 2D digital image correlation was carried out using the image correlation software ARAMIS®. Each image was segmented into facets/sub-images consisting of 25 ×

25 pixels. An overlap of 20 pixels (or, step size of 5 pixels) was used during image analysis. This resulted in 194 × 194 matrix of data points in the region of interest for each of the two orthogonal speckle displacement fields. The corresponding angular deflections of light rays were subsequently determined using the known distance (Δ) between the specimen and the target planes.

The position of the crack-tip in each digitized image was used to measure the instantaneous crack length. The crack extension data typically includes measurement errors. To minimize the errors, a quadratic Bézier curve [92, 93] was fitted to the crack length data at a time instant '*i*' as,

$$a_i(s) = (1-s)^2 \hat{a}_i + 2s(1-s)\hat{a}_{i+1} + s^2 \hat{a}_{i+2}, \quad 0 \le s \le 1 \tag{3.1}$$

where s, $\hat{a}$ and a are the smoothing parameter, the digitized crack length, and the smoothed crack length, respectively. In the above expression $\hat{a}_i, \hat{a}_{i+1}, \hat{a}_{i+2}$ are the control points of $\hat{a}_i(s)$. The value of *s* was 0.5 such that the smoothed data point is at the middle of the interval. Subsequently, the crack velocity (*V*) was estimated from the smoothed crack length history using backward difference method,

$$V_i = \frac{a_i - a_{i-1}}{t_i - t_{i-1}} \tag{3.2}$$

where *a* and t are crack length and time, respectively.

Using the two orthogonal angular deflection fields in the *x*- and *y*-directions, the instantaneous counterparts in the local coordinates (x', y') (x' coincided with the local

crack growth direction) for a moving crack were obtained via coordinate transformation. The mode-I and mode-II stress intensity factors were evaluated from an over-deterministic least-squares analysis of the crack-tip data in conjunction with the asymptotic equation (see [90] [94] for details),

$$\phi_{x'}(t) = \phi_x(t)\cos\theta(t) + \phi_y \sin\theta(t)$$

$$= C_\sigma B \left[\begin{array}{l} -\frac{1}{2} r_l^{\frac{-3}{2}} \left\{ \begin{array}{l} f(V;C_L;C_S) A_1(t) \cos\left(\frac{3\theta_l}{2}\right) \\ +g(V;C_L;C_S) D_1(t) \sin\left(\frac{3\theta_l}{2}\right) \end{array} \right\} \\ \sum_{N=2}^{\infty} \left\{ \begin{array}{l} A_N \left(\frac{N}{2}-1\right) r_l^{\left(\frac{N}{2}-2\right)} \cos\left(\left(\frac{N}{2}-2\right)\theta_l\right) \\ +D_N \left(\frac{N}{2}-1\right) r_l^{\left(\frac{N}{2}-2\right)} \sin\left(\left(\frac{N}{2}-2\right)\theta_l\right) \end{array} \right\} \end{array} \right] \tag{3.3}$$

where f and g are functions of instantaneous crack velocity, and (r_l, θ_l) denote the contracted crack-tip polar coordinates, C_σ is the elasto-optical constant of the material, and B is its initial thickness. Further, (r_l, θ_l) can be expressed in the local Cartesian coordinates (x', y') as, $r_l = \left\{(x')^2 + \alpha_L^2 (y')^2\right\}^{\frac{1}{2}}$ and $\theta_l = \tan^{-1}\left(\frac{\alpha_L y'}{x'}\right)$. The coefficients of $A_1(t)$ and $D_1(t)$ in the asymptotic series are related to the mode-I and mode-II stress intensity factors $K_I(t)$ and $K_{II}(t)$, respectively, as $A_1(t) = K_I\sqrt{\frac{2}{\pi}}$ and $D_1(t) = K_{II}\sqrt{\frac{2}{\pi}N}$. The functions f and g are,

$$f(V;C_L;C_S)=\left(\frac{1+\nu}{1-\nu}\right)\frac{\left(1+\alpha_S^2\right)\left(1-\alpha_L^2\right)}{4\alpha_L\alpha_S-(1+\alpha_S^2)^2}$$, and

$$g(V;C_L;C_S)=\left(\frac{1+\nu}{1-\nu}\right)\frac{\left(2\alpha_S\right)\left(1-\alpha_L^2\right)}{4\alpha_L\alpha_S-(1+\alpha_S^2)^2} \tag{3.4}$$

where $\alpha_L=\left[1-\frac{\rho(1-\nu)}{2\mu}V^2\right]^{\frac{1}{2}}$ and $\alpha_S=\left[1-\frac{\rho}{\mu}V^2\right]^{\frac{1}{2}}$ for plane stress. Here, μ and ρ are shear modulus and mass density, respectively. Data in the region ($0.35\le r/B\le 0.85$) and ($-165^0\le\theta\le 165^0$) near the crack-tip with $N=4$ was used during analysis.

3.5 Initial crack path prediction

The maximum tangential stress (MTS) criteria introduced by Erdogan and Sih [6] is one of the conditions for predicting the crack growth direction. It has been found to predict crack kink angles rather accurately in brittle solids [95, 96] and hence it is considered next. The MTS criterion postulates that the crack growth occurs in the direction of maximum tangential (hoop) stress. Thus the crack kink angle predicted by the MTS criterion can be expressed as [97],

$$\alpha_{kink}=\cos^{-1}\left(\frac{3K_{IIcr}^2\pm\sqrt{K_{Icr}^4+8K_{Icr}^2K_{IIcr}^2}}{K_{Icr}^2+9K_{IIcr}^2}\right) \tag{3.5}$$

where K_{Icr} and K_{IIcr} are critical mode -I and mode-II stress intensity factors *at crack initiation*, respectively. In this work, the crack kink angle at initiation was predicted based on SIF values just prior to initiation. Thus predicted kink angle was verified by the

observed/measured angle near the initial crack-tip. The crack kink angle in experiments was determined from fracture photographs using commercially available image editing software.

3.6 Mode-I and mixed-mode dynamic fracture of PMMA

3.6.1 Crack-tip deformations, crack initiation and growth

Photographs of five fractured samples from each of the configurations are shown in Figs. 3.12(a)-(e). The stress wave loading occurred on the left edge of the specimen evident as a small crater (whitened region) near the impact point. In these images, the crack initiates from the initial tip (near the right edge) and propagates towards the left edge as indicated by the arrowhead. In each case the path the crack took was different. In Fig. 3.12(a) the crack propagated self-similarly until it reached the free edge and deviated from its path due to a loss of in-plane constraint. In Figs. 3.12(b)-(e) the crack propagated in mixed-mode with a distinct kink at initiation in each case. Figs. 3.12(a1)-(e1) show the close-up view in the initial crack-tip vicinity and the corresponding kink angles. The crack initiation angle monotonically increased from 'config. 1' to 'config. 5' (0°, 24.8°, 36.2°, 41.4°, 52.3°). This clearly shows that the mode-mixity increased with crack length when eccentricity was constant. The crack initiation angles predicted by the MTS criterion were also evaluated and are listed in Table 3.3. Both of them show good agreement.

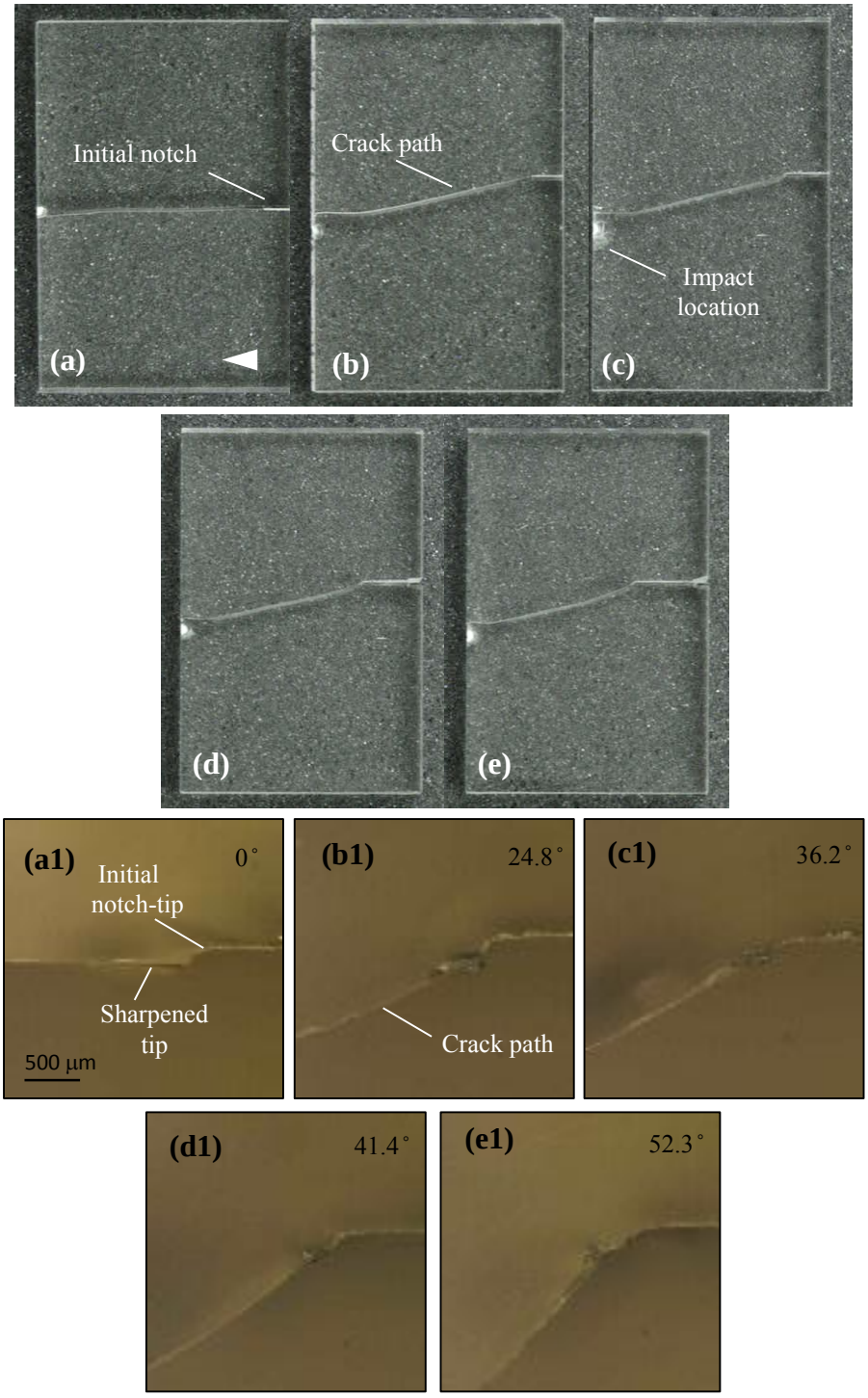

Figure 3.12: (a)-(e) Photographs of fractured PMMA specimens (upper half) with config. 1-5 in sequence. (a1)-(e1) Close-up photographs of crack initiation at initial notch tip for the respective configurations showing different crack initiation angles. (Only the upper-half of the fractured specimen is shown)

	α_{cr} (deg.)	MTS criteria (deg.)
Config. 1	0	0
Config. 2	24.8	24.4
Config. 3	36.2	37.4
Config. 4	41.4	43.9
Config. 5	52.3	53.1

Table 3.3: Measured crack initiation kink angle (error ± 0.3 deg) for PMMA compared with the MTS criteria

Plots of measured angular deflection contours ϕ_x and ϕ_y proportional to stress gradients $\left(\sigma_{xx}+\sigma_{yy}\right)_{,x}$ and $\left(\sigma_{xx}+\sigma_{yy}\right)_{,y}$ (the comma notation denotes derivatives with respect to the subscript) obtained from the image correlation for two select configurations namely, 'config.1' and 'config.5' are shown in Figs. 3.13 and 3.14, respectively. Further, note that the plots presented are only for two select time instants (one at crack initiation and another during propagation) for brevity. (The contour levels and the scale bar are shown in the first plot in each set and are applicable to the other plots as well.) In these, t = 0 μs represents the time the crack initiated at the original tip. In each figure, top and bottom rows correspond to ϕ_x and ϕ_y, respectively. Fig. 3.13 shows angular deflection contours for config.1 (a = 6 mm; e = 0 mm). The crack followed nearly a straight path during the window of observation. It can be seen that the relative size of the contours increased during propagation suggesting an increase in stress intensity factors during the observation window. Further, as expected, the crack-tip contours representing the stress

gradients $\left(\sigma_{xx}+\sigma_{yy}\right)_{,x}$ are approximately symmetric relative to the initial crack whereas $\left(\sigma_{xx}+\sigma_{yy}\right)_{,y}$ contours are clearly antisymmetric.

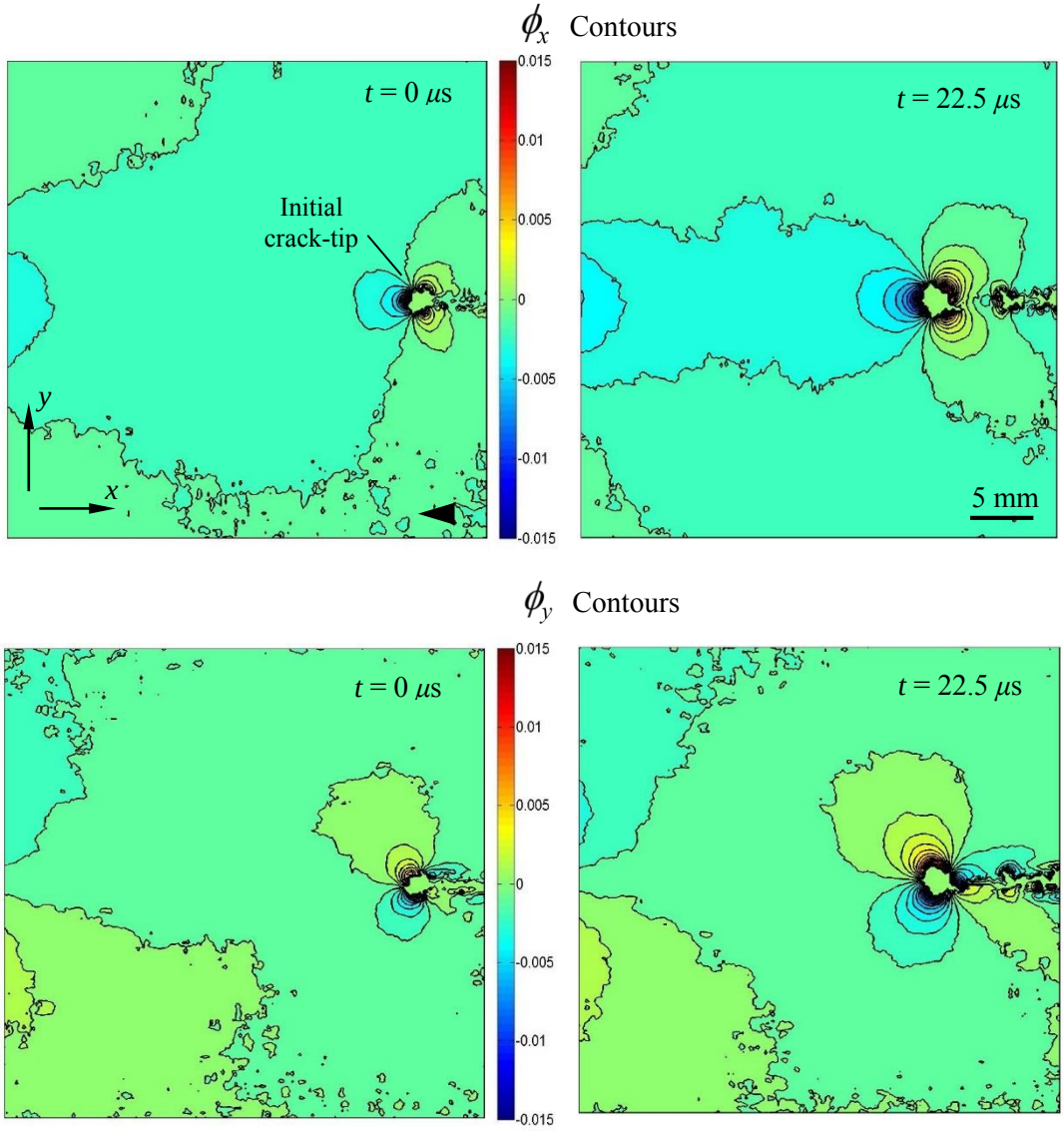

Figure 3.13: Angular deflection contour plots (contour interval = 5×10^{-4} rad) proportional to stress gradients of $\left(\sigma_{xx}+\sigma_{yy}\right)$ in the *x*- and *y*-directions for a PMMA specimen with a = 6 mm and e = 0 mm. (Note that t = 0 in these correspond to the instant at crack initiation.)

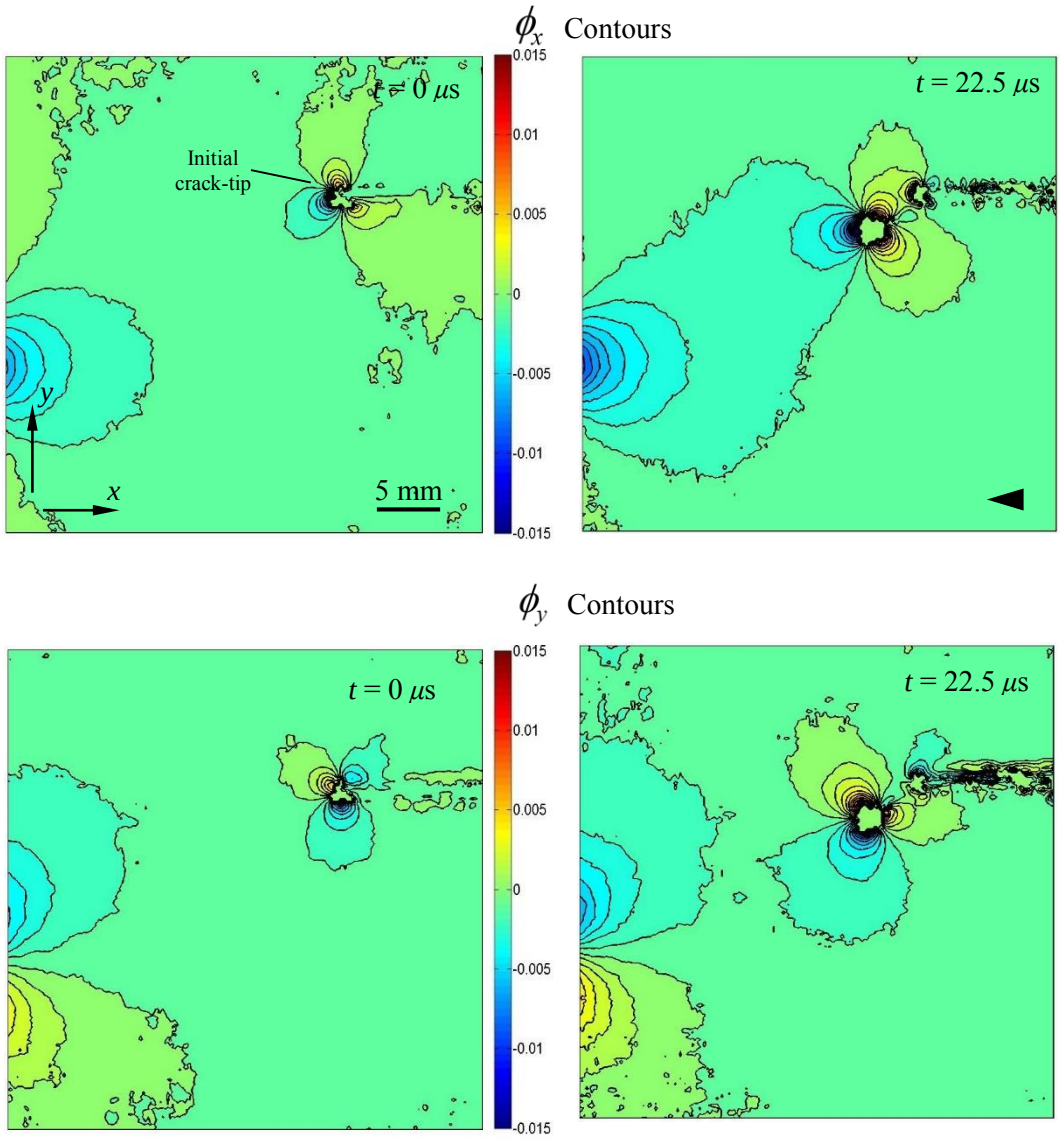

Figure 3.14: Angular deflection contour plots (contour interval = 5×10^{-4} rad) proportional to stress gradients of $\left(\sigma_{xx}+\sigma_{yy}\right)$ in the *x*- and *y*-directions for a PMMA specimen with *a* = 15 mm and *e* = 15 mm. (Note that *t* = 0 in these correspond to the instant at crack initiation).

The partially visible contours near the left edge of the region-of-interest are caused by the concentrated line-load acting on the sample. Fig. 3.14 shows the angular deflection contours for config. 5 (*a* = 15 mm; *e* = 15 mm). The measured contours of $\left(\sigma_{xx}+\sigma_{yy}\right)_{,x}$ and

$\left(\sigma_{xx}+\sigma_{yy}\right)_{,y}$ are both asymmetric throughout the loading history. The crack initiated at an angle relative to its initial orientation. At time t = 0 μs the angular deflection contours are rotated relative to the initial notch and are oriented towards the direction of crack initiation. Further, the number of contours increased with time during the observation window implying an increase in the stress intensity factors.

3.6.2 Crack speed and stress intensity factor histories

A compilation of crack velocity histories for all the configurations is shown in Fig. 3.15(a). In all the configurations the cracks rapidly accelerate soon after initiation followed by a gradual slowing down speed. At the end of the window of observation, which is t = 25 μs after crack initiation, the final (maximum) velocity monotonically increased from 267 m/s in config.1 to 347 m/s in config. 5. This suggests that the mixed-mode cracks travel faster when compared to mode-I counterpart.

A compilation of mode-I and mode-II stress intensity factor histories evaluated form DGS data for all five configurations are plotted in Fig. 3.15(b). The time axis of each experiment was shifted such that t = 0 corresponds to the instant at which the crack initiated at the initial notch tip as determined from the recorded images. First, consider one select configuration (say, config.1). In the pre-crack initiation period, a monotonic increase in the magnitude of the stress intensity factors is evident. The mode-II stress intensity factors are negative, consistent with the loading configuration employed.

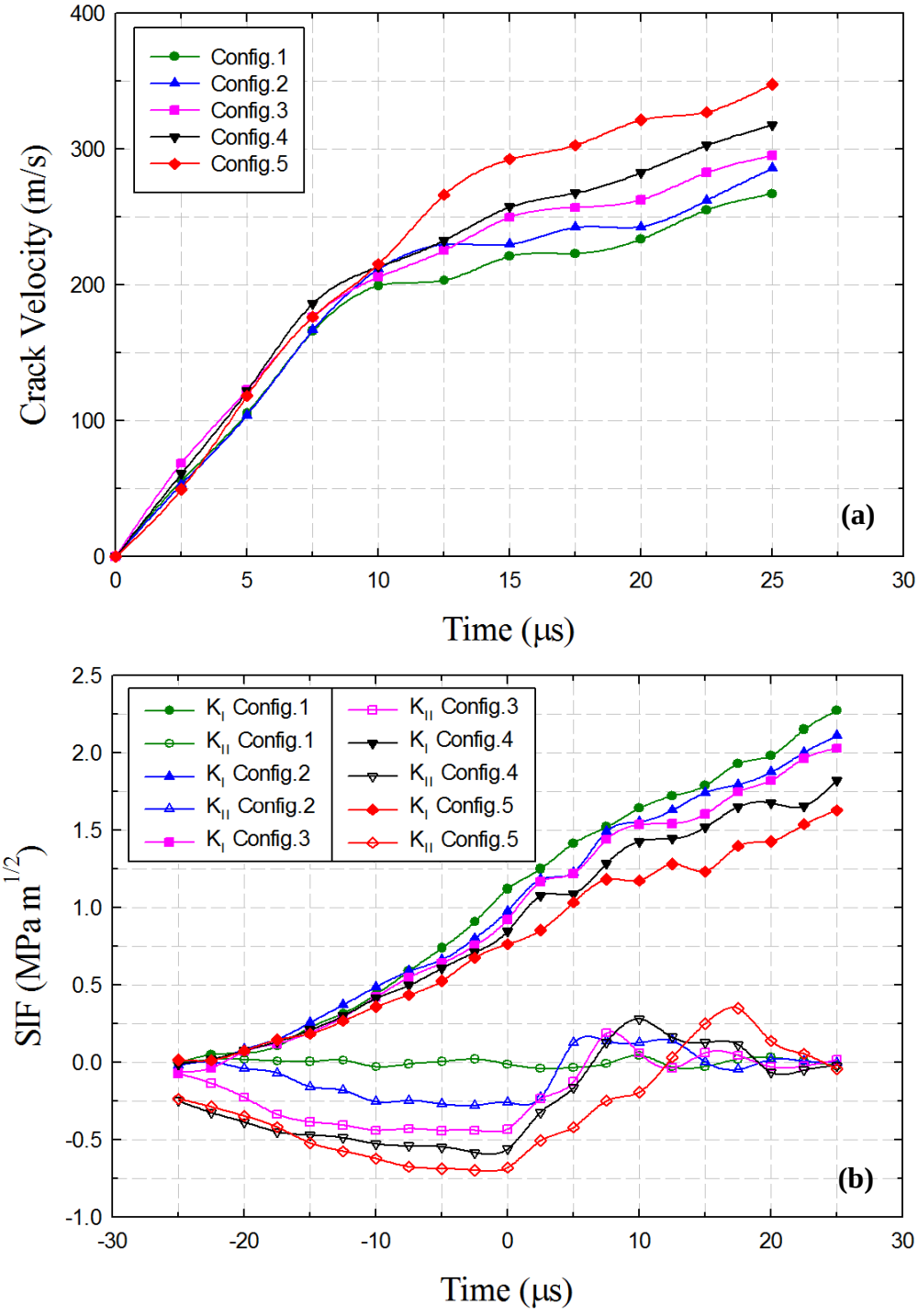

Figure 3.15: Compilation of crack velocity and stress intensity factor (SIF) histories for all PMMA configurations. (K_{II} for config. 1 should be ideally zero and the associated deviations provide an estimate of measurement errors for other configurations.)

After crack initiation, the mode-I stress intensity factors continue to increase whereas the mode-II stress intensity factors precipitously drop to zero before changing sign as the emanating stress waves from the propagating crack-tip bounce off the free edges of the sample and interfere with the crack-tip fields. Considering the SIF histories across all configurations, it can be seen that there is a monotonic reduction in its magnitude of K_I at initiation from config. 1 to config. 5. The K_{II} histories, on the other hand, show an opposite trend with a monotonic increase in magnitude of K_{II} at initiation from config. 1 to config. 5. Further, in the time window of observation, K_{II} values approximately reach a plateau prior to crack initiation. In the post-initiation period, K_I histories continue to increase while a precipitous drop in K_{II} occurs in all cases. An oscillatory decaying trend in K_{II} about zero is also evident suggesting preference of the crack to grow in mode-I condition. These are in line with predictions based on computations described in the earlier section where an increase in the shear stress and a decrease in the normal stress at the prospective crack-tip were seen when the tip was located father away from the free edge (longer crack).

3.6.3 Finite element simulations

Complimentary finite element simulations of the mode-I and mixed-mode impact tests on SEN specimen were carried out using ABAQUS®/Explicit software to extract the mixed-mode stress intensity factors independently until crack initiation [90]. Two loading configurations namely config.1 and config.5 were modeled. The long-bar in the loading setup was also modeled for this simulation. The impact end of the long-bar was cylindrical in shape (line-load). The specimen and the long-bar were discretized into 259,337 and

37,952 solid 3D tetrahedral elements respectively. The discretized model with the crack opening displacements is shown in Fig. 3.16.

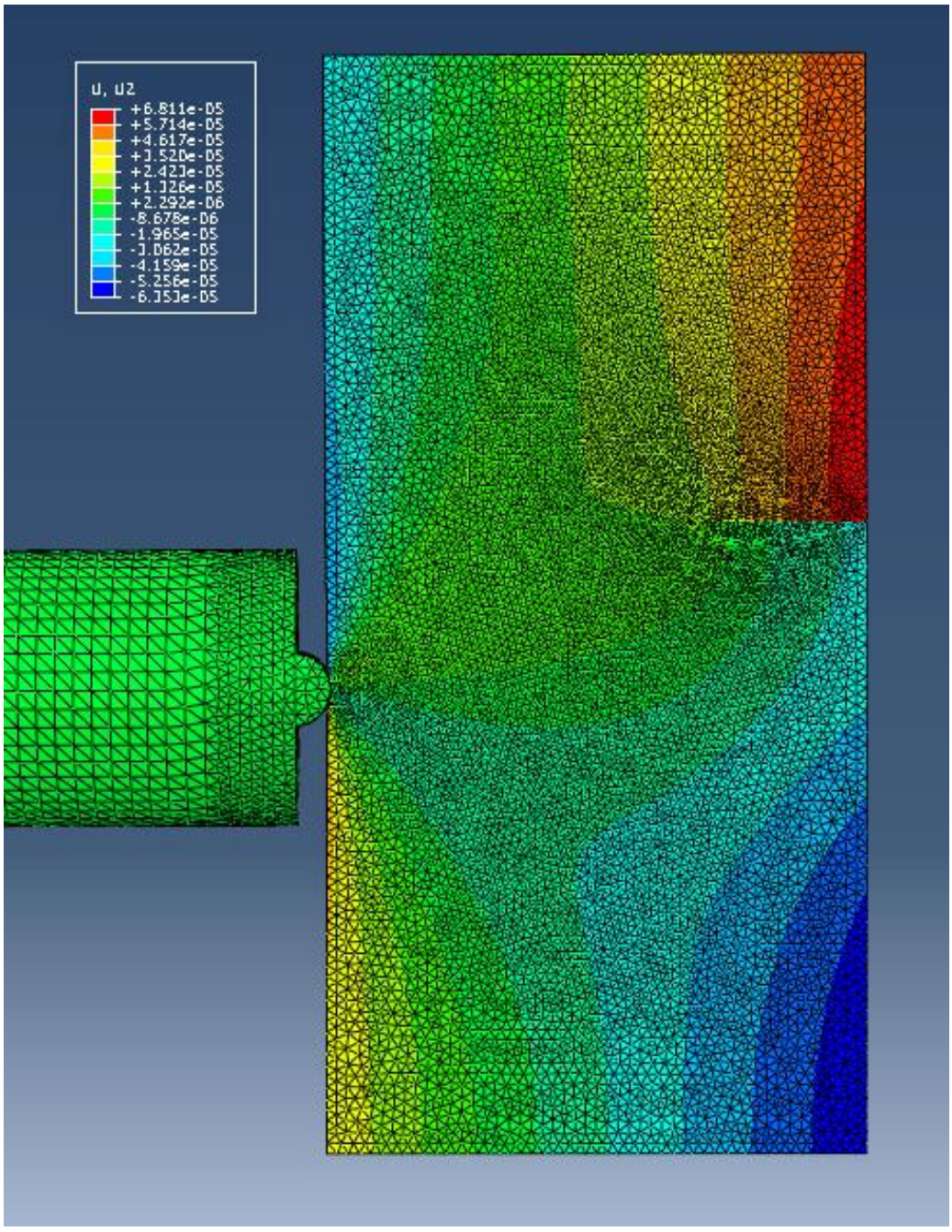

Figure 3.16: Discretized finite element model of config.5 (a = 15 mm; e = 15 mm) for PMMA with an overlay of displacement contours in the y-directions.

Local seeding was adopted around the initial crack-tip to generate finer mesh around it. The time steps during the analysis were allowed to be automatically controlled by the integration scheme. The Young's modulus and Poisson's ratio of PMMA used in this analysis were obtained from ultrasonic pulse echo technique using longitudinal and shear wave speeds [98] and its mass density. Tables 3.1 and 3.2 shows the material properties of PMMA and the AL-7075 aluminum long-bar used in the simulation, respectively. The particle velocity obtained from strain gage readings on the Hopkinson pressure bar experiment was input into the analysis. The crack opening (v) and crack sliding (u) displacements were extracted along the two crack faces. This was repeated for each displacement step. The apparent mode-I and mode-II stress intensity factors, $(K_I)_{app}$ and $(K_{II})_{app}$ at each step were computed using [99],

$$(K_{I;II})_{app} = \frac{E\sqrt{2\pi}}{8\sqrt{r}}(v;u);(r,\theta=\pi) \tag{3.6}$$

The computed mode-I stress intensity factor corresponding to the one obtained experimentally was matched at $t = 0$ as shown in Fig. 3.17. The remaining pre-initiation values for both mode-I and mode-II in Fig. 3.17 show a good match with the other experimental counterparts.

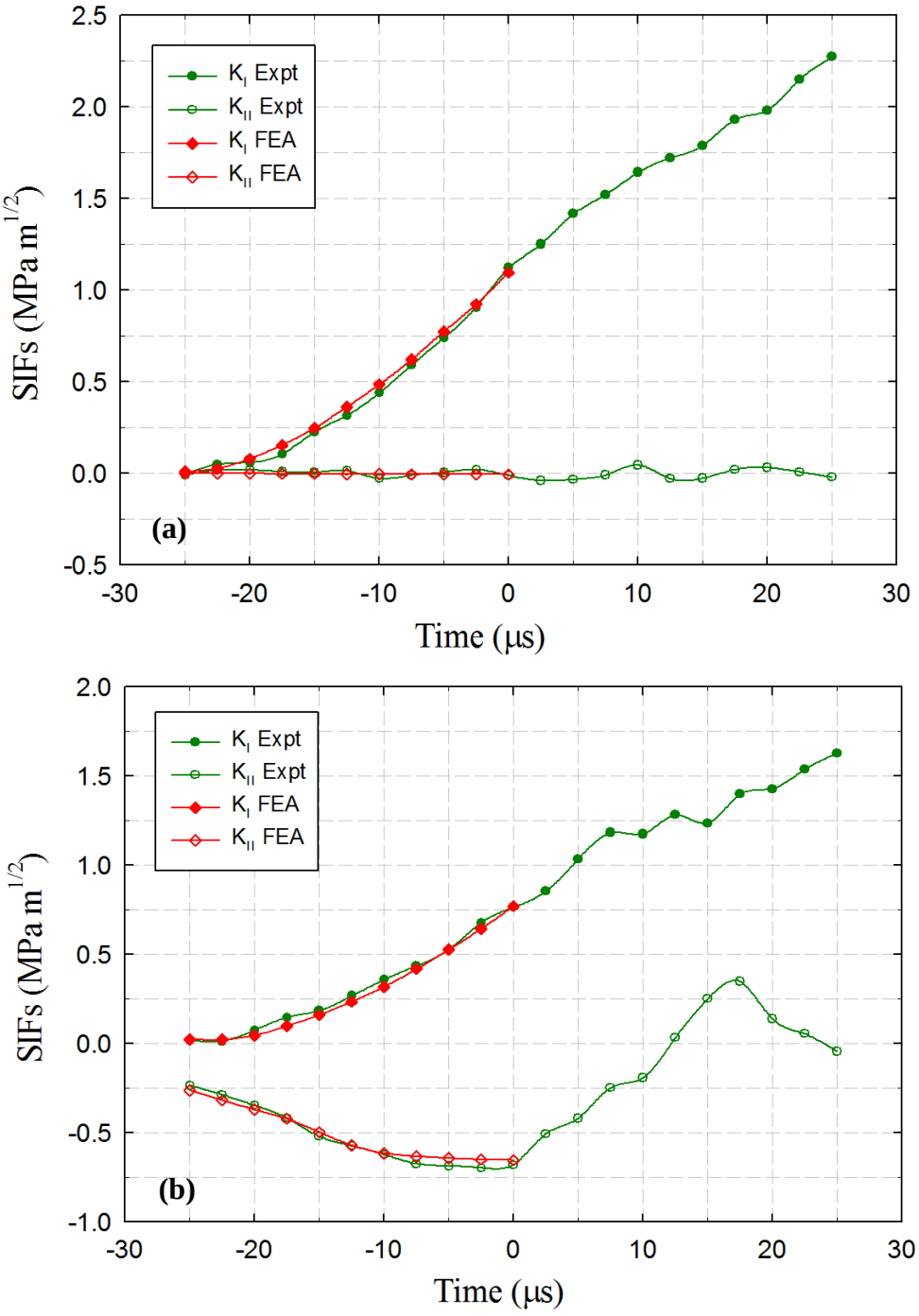

Figure 3.17:Stress intensity factors (SIFs) evaluated from experiments and finite element analysis for (a) config. 1 (a = 6 mm, e = 0 mm) and (b) config. 5 (a = 15 mm, e = 15 mm). (t = 0 corresponds to crack initiation.)

3.6.4 Experiment repeatability

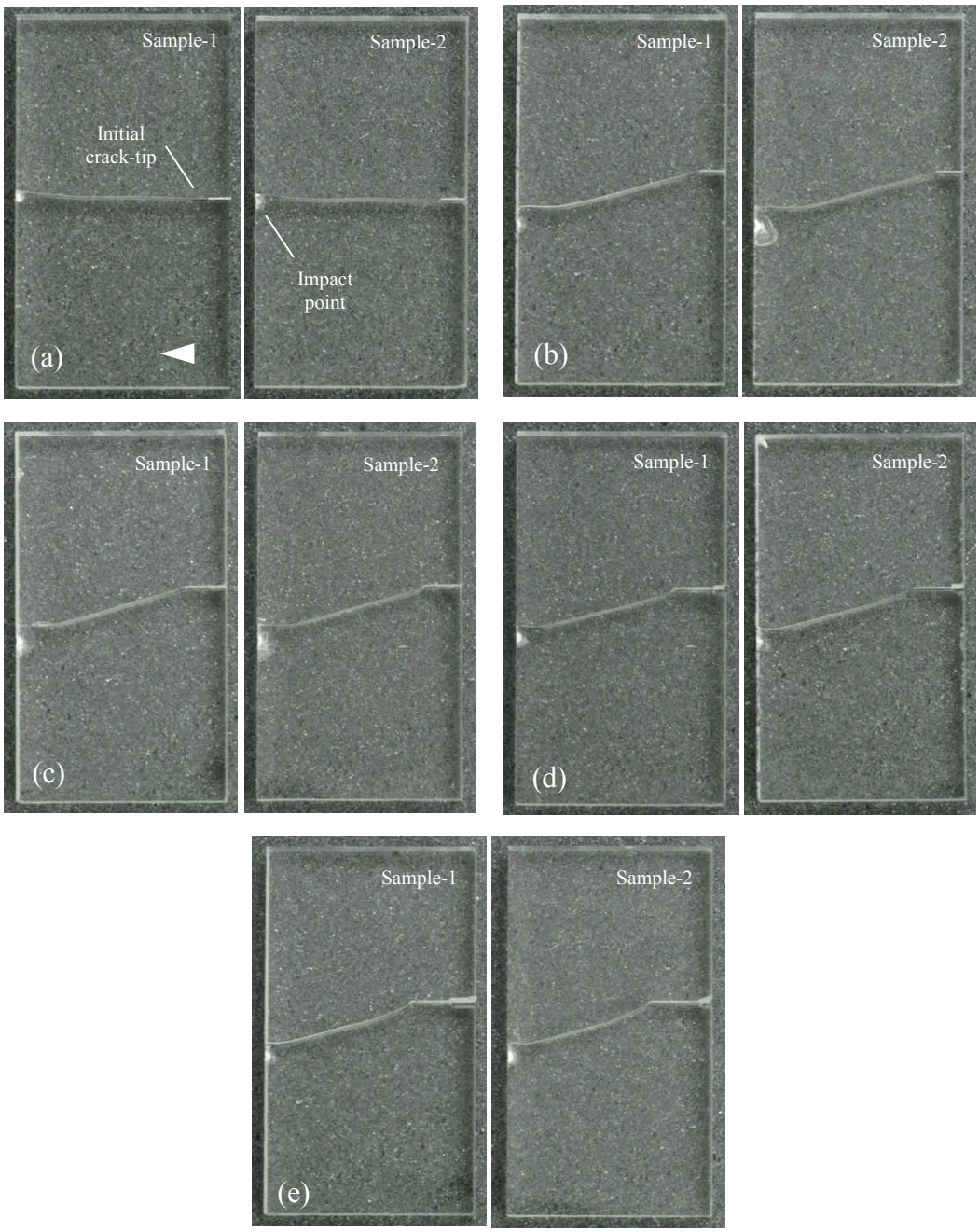

Figure 3.18: Experiment repeatability: (a)-(e) Multiple fractured samples of config. 1 to 5, respectively.

Multiple experiments were conducted to ensure repeatability in terms of dynamic fracture behavior as well as measured fracture parameters. Fig. 3.18(a)-(e) shows photographs of two fractured samples of PMMA of each configuration. A high degree of reproducibility in crack paths throughout the fracture event is clearly evident. SIF histories for two different samples of config.1 and config.5 are shown in Fig. 3.19. Again, repeatability can be readily seen in the measured values of SIFs. The slope of the graphs in the pre-initiation regime, the SIFs at crack initiation, and the slope in post initiation regime are in good agreement.

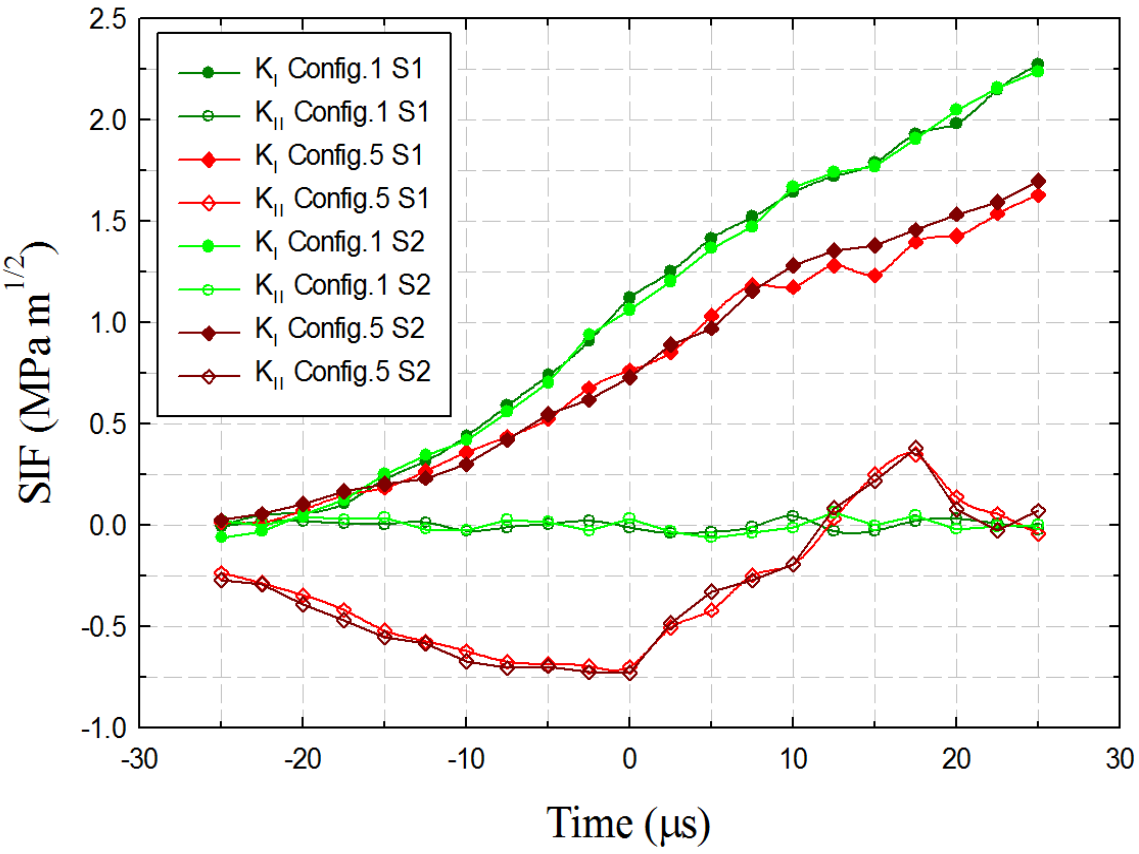

Figure 3.19: SIF histories for multiple fractured samples of each configuration showing repeatability of measurements.

3.7 Mode-I and mixed-mode dynamic fracture of polycarbonate

3.7.1 Evaluation of elasto-optic constant for polycarbonate

Elasto-optic constant of Lexan-9430 was evaluated using a specimen configuration of line-load acting on an edge of a large planar sheet approximating a classical Flamant problem. A 100 mm x 75 mm rectangular sheet of thickness 6.15 mm was placed on a flat rigid platform and subjected to load as shown in Fig. 3.20. An Instron 4465 universal testing machine was used for loading the specimen in displacement control mode (crosshead speed of 0.005 mm/sec). A target plate coated with random black and white speckles was placed behind the specimen at a distance of 28.1 mm from the mid plane of the specimen. A Nikon D100 digital SLR camera fitted with a 70-300 mm focal length lens and extension tube was used to record the speckles. The camera was placed in front of the specimen at a distance (L) of ~900 mm with the camera focused on a uniformly illuminated target plane through the specimen. A camera resolution of 1504 x 1000 pixels was used to acquire 8 bit images.

An undeformed image of the target plate through the specimen was recorded (1 pixel ~ 30 μm on the target plane) at no-load condition. As the sample was loaded, the deformed images of the target plate were recorded at 300 N, 600 N, 900N and 1200 N loads. Two representative speckle patterns, one in the no-load state and the other in the deformed state, are shown in Fig. 3.21. Sufficient care was exercised to obtain a near Gaussian distribution of gray scales for each image in the mid-range of 0-255 (8 bit) scale

by adjusting the illumination and the numerical aperture of the lens. The speckles are noticeably distorted in Fig. 3.21(b) at the top of the specimen near the concentrated load.

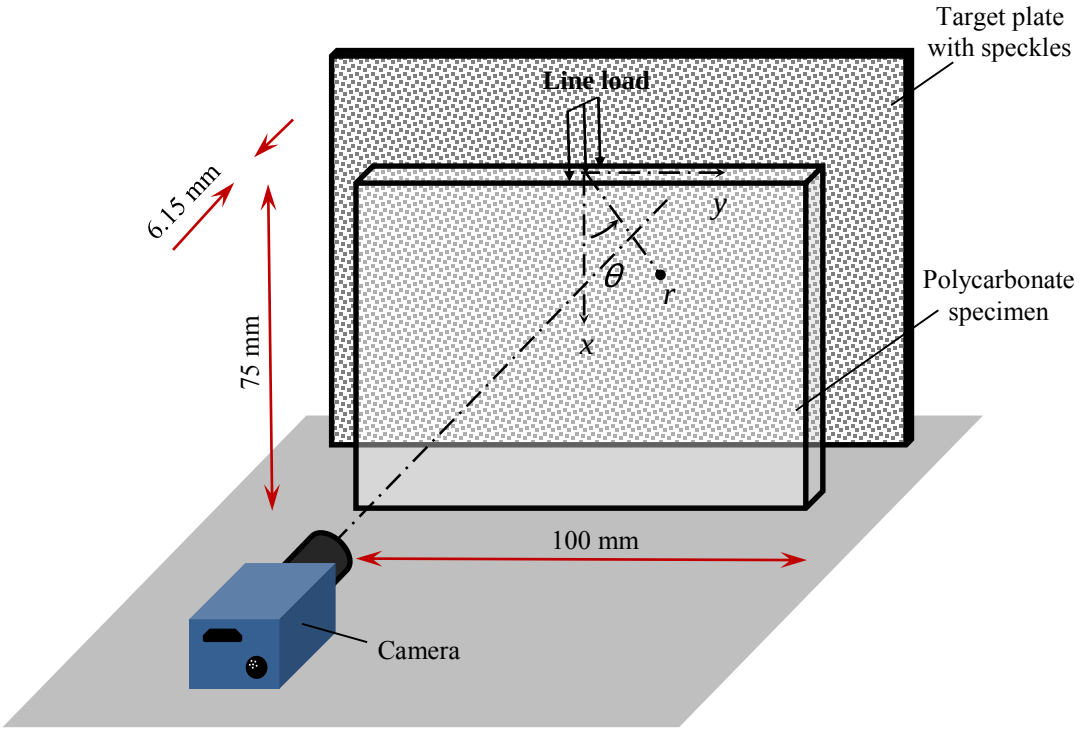

Figure 3.20: Experimental setup for line loading on a polycarbonate sheet to evaluate elasto-optic constant.

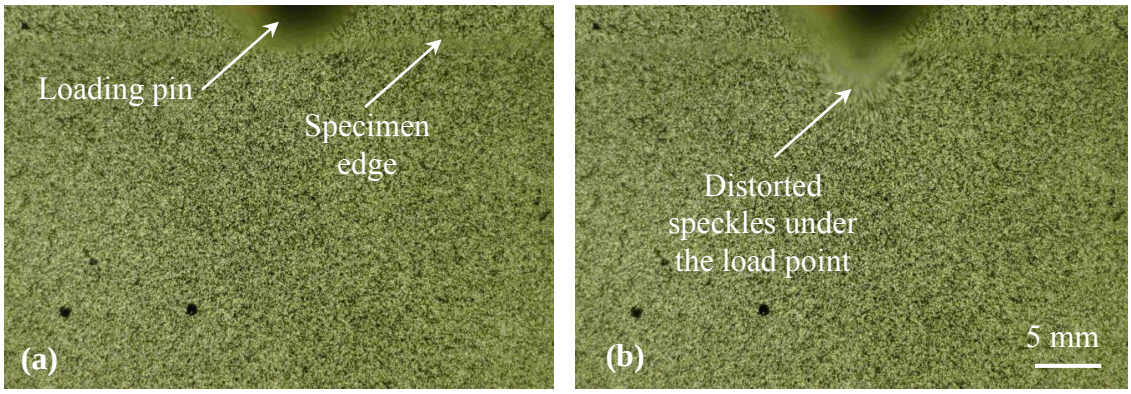

Figure 3.21: Speckle images of a polycarbonate sheet under the line-load: (a) Undeformed and (b) deformed.

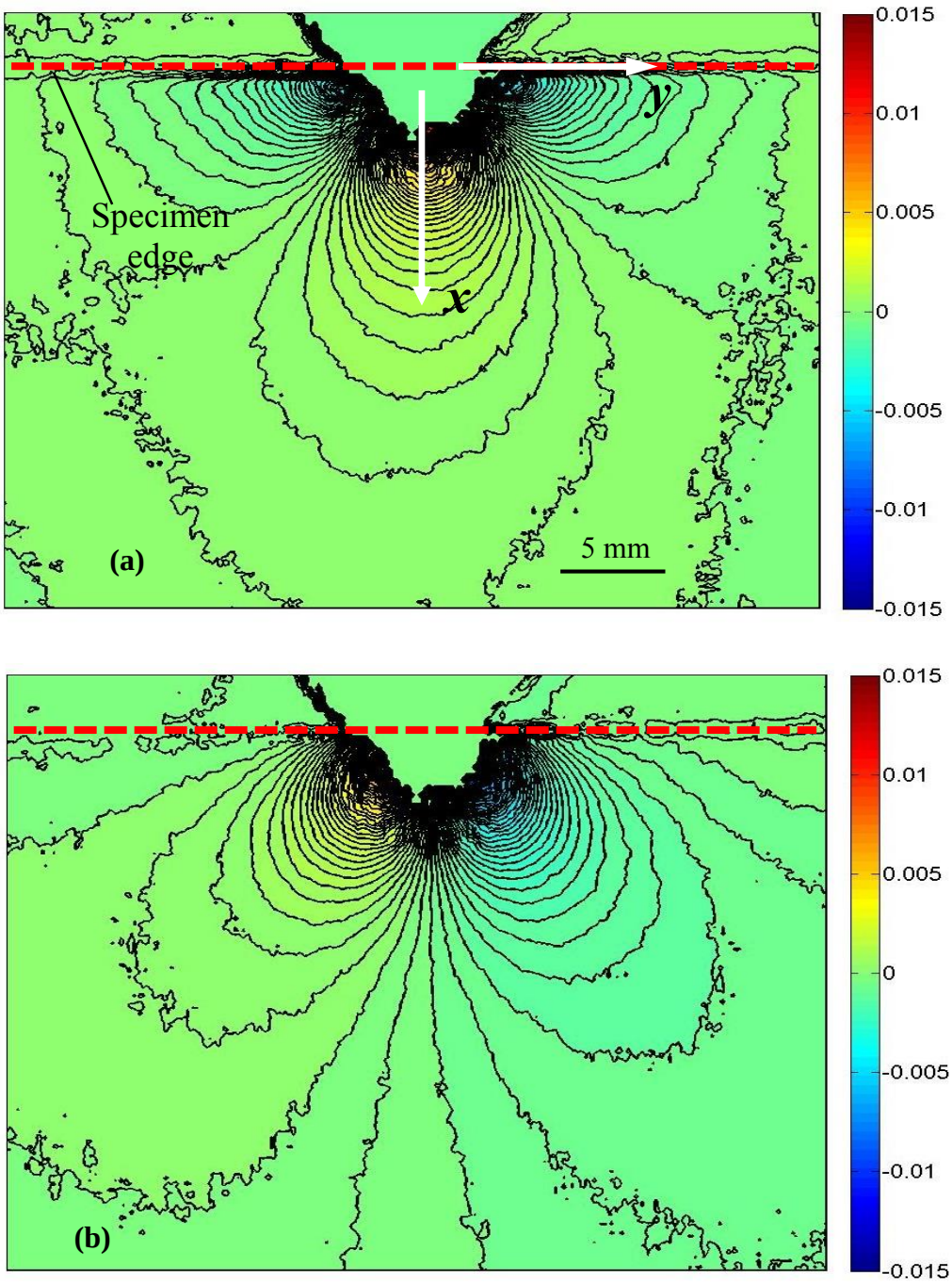

Figure 3.22: Angular deflection contour plots (contour interval = 3×10^{-4} rad) proportional to stress gradients of $(\sigma_{xx}+\sigma_{yy})$ in the (a) *x*- and, (b) *y*-directions for a polycarbonate specimen under the line-load.

The digitized speckle images (1504 x 1000 pixels) in the deformed state were correlated with the image from the undeformed state using ARAMIS®. A sub-image size of 25 x 25 pixels with an overlap of 20 pixels (i.e., step size of 5 pixels) was used during image correlation. The angular deflection contours in the horizontal (*x*-*z*) and vertical (*y*-*z*) planes (global coordinate system) for a compressive load of 1200 N is shown in Fig. 3.22.

The angular deflections measured in two in-plane orthogonal direction are related to stresses as [85],

$$\phi_x = C_\sigma \frac{2F}{\pi} \frac{\cos(2\theta)}{r^2}$$
$$\phi_y = C_\sigma \frac{2F}{\pi} \frac{\sin(2\theta)}{r^2} \tag{3.7}$$

where C_σ is the elasto-optic constant, F is the applied load, B is the specimen thickness and (r,θ) denote the polar coordinates relative to the loading point. The C_σ evaluated along $\pm 45^\circ$ for ϕ_y and 90° for ϕ_x for an applied load of 300 N is plotted against r/B ratio in Fig. 3.23. The far field values of the angular deflections were forced to be zero based on the known boundary conditions. This accounted for any potential rigid body translations that occurred while conducting experiments. It can be seen that there is a drop in the magnitude of C_σ from $0 \le r/B \le 0.5$. In the $0.5 \le r/B \le 2.0$ range it is nearly a constant, beyond which it again deviates due to far-field effects unaccounted for in eq. (3.7). Similar analyses for other loads were also carried out and the averaged value of C_σ was -1.33 ± 0.04 x 10^{-10} m^2/N.

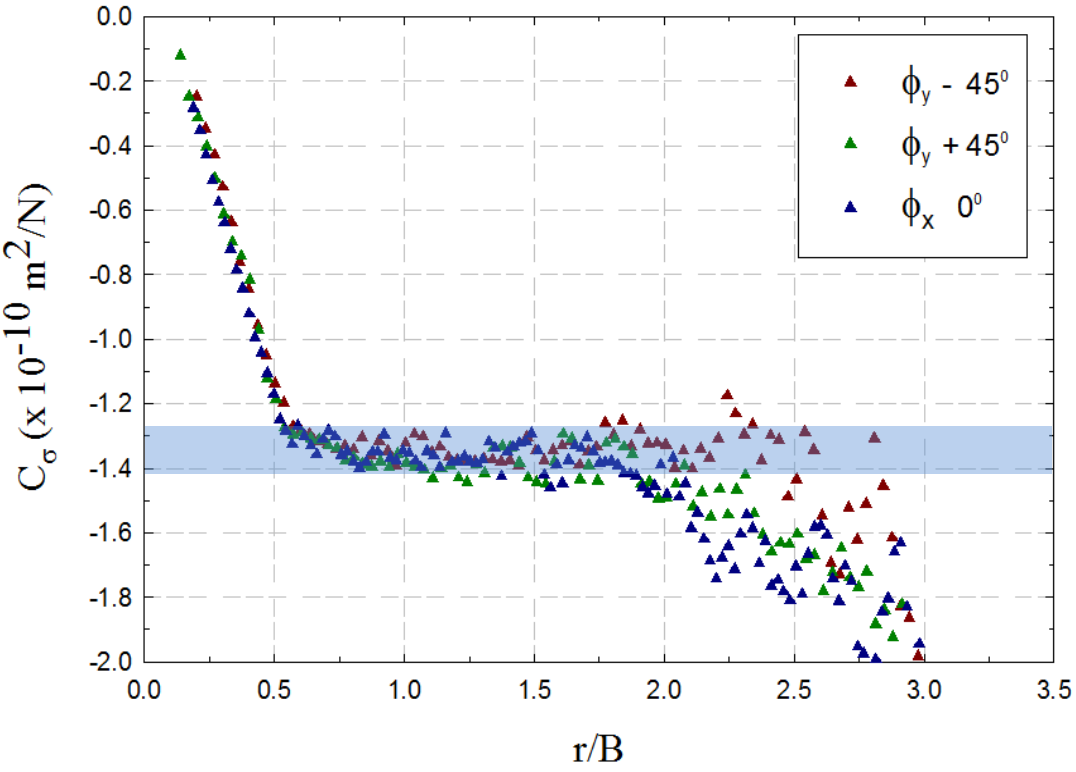

Figure 3.23 Variation of elasto-optic constant C_σ evaluated at 300 N load for polycarbonate.

3.7.2 Crack path and deformation histories

Photographs of five fractured samples from each of the configurations are shown in Figs. 3.24(a)-(e). The stress wave loading occurred at the left edge of the specimen. The crack initiated from the initial crack-tip and propagated from the right edge of the specimen towards the left as shown by the arrowhead. In each case the crack initiated and kinked at a different angle. In Fig. 3.24(a), due to symmetric loading configuration, the crack propagated in a mode-I condition throughout until it approached the free edge and deviated from its path. In Figs. 3.24(b)-(e) the crack has initiated and propagated in mixed-mode. Figs. 3.24(a1)-(e1) shows the close-up of the initial crack-tip vicinity.

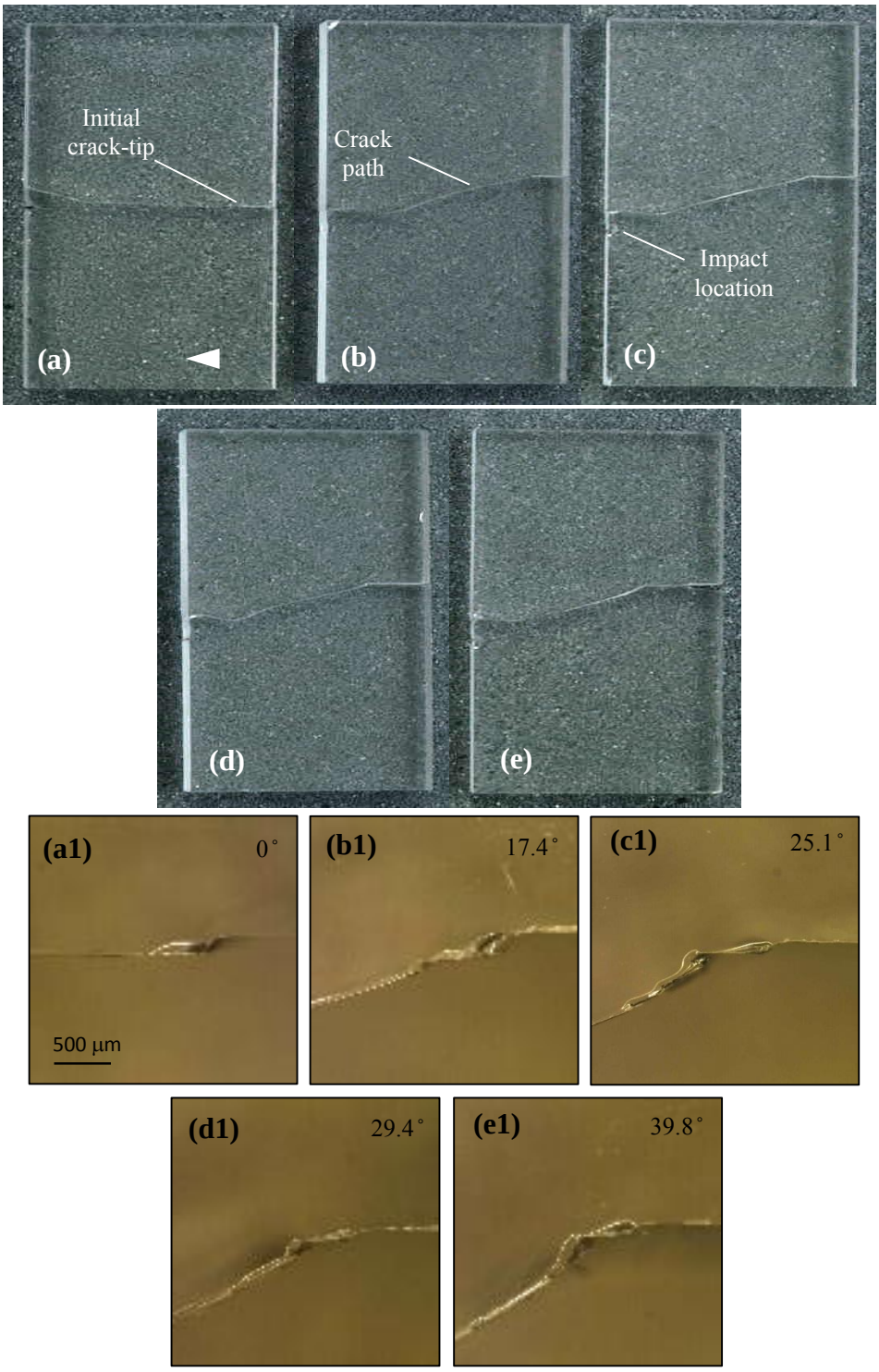

Figure 3.24: (a)-(e) Photographs of fractured polycarbonate specimens for config. 1-5 in sequence. (a1)-(e1) Close-up view (upper half) of crack initiation at the initial notch tip for the respective configurations with the measured crack initiation angle.

As in the PMMA cases, it can be seen that the crack initiation angle monotonically increases from config. 1 to config. 5 (0˚, 17.4˚, 25.1˚, 29.4˚, 39.8˚). This clearly shows that the crack initiation angle and hence mode-mixity changes with crack length. The kink angles however were not as large as in PMMA (0˚, 24.8˚, 36.2˚, 41.4˚, 52.3˚) counterparts although experiments were repeatable. Higher fracture toughness of polycarbonate relative to PMMA and the differences in crack initiation mechanics due to its ductility are potentially responsible for the differences. The crack initiation angle predicted by the MTS criterion was also evaluated and is listed in Table 3.4. There is a good agreement between the observed crack initiation angle and the MTS criterion for only config. 2 but they deviate significantly (lower) in others.

	α_{cr} (deg.)	MTS criteria (deg.)
Config. 1	0	0
Config. 2	17.4	17.8
Config. 3	25.1	34.2
Config. 4	29.4	40.1
Config. 5	39.8	46.7

Table 3.4: Measured crack initiation angles (error ± 0.3 deg.) for polycarbonate specimen compared with MTS criteria. (Larger discrepancy between the two in mixed-mode case is attributed to ductility of polycarbonate.)

Contour plots of measured angular deflection contours ϕ_x and ϕ_y proportional to orthogonal stress gradients $\left(\sigma_{xx}+\sigma_{yy}\right)_{,x}$ and $\left(\sigma_{xx}+\sigma_{yy}\right)_{,y}$ obtained from DGS for two select configurations namely, config. 1 and config. 2 are shown in Figs. 3.25 and 3.26, respectively. For brevity, plots for two select time instants, one at crack initiation and the second during propagation, are presented. (The contour levels and the scale bar are shown

in the first plot in each set and are applicable to the other plots as well.) In these $t = 0$ μs represents the time at which the crack initiated at the original sharpened tip. In each figure, top and bottom rows correspond to ϕ_x and ϕ_y, respectively.

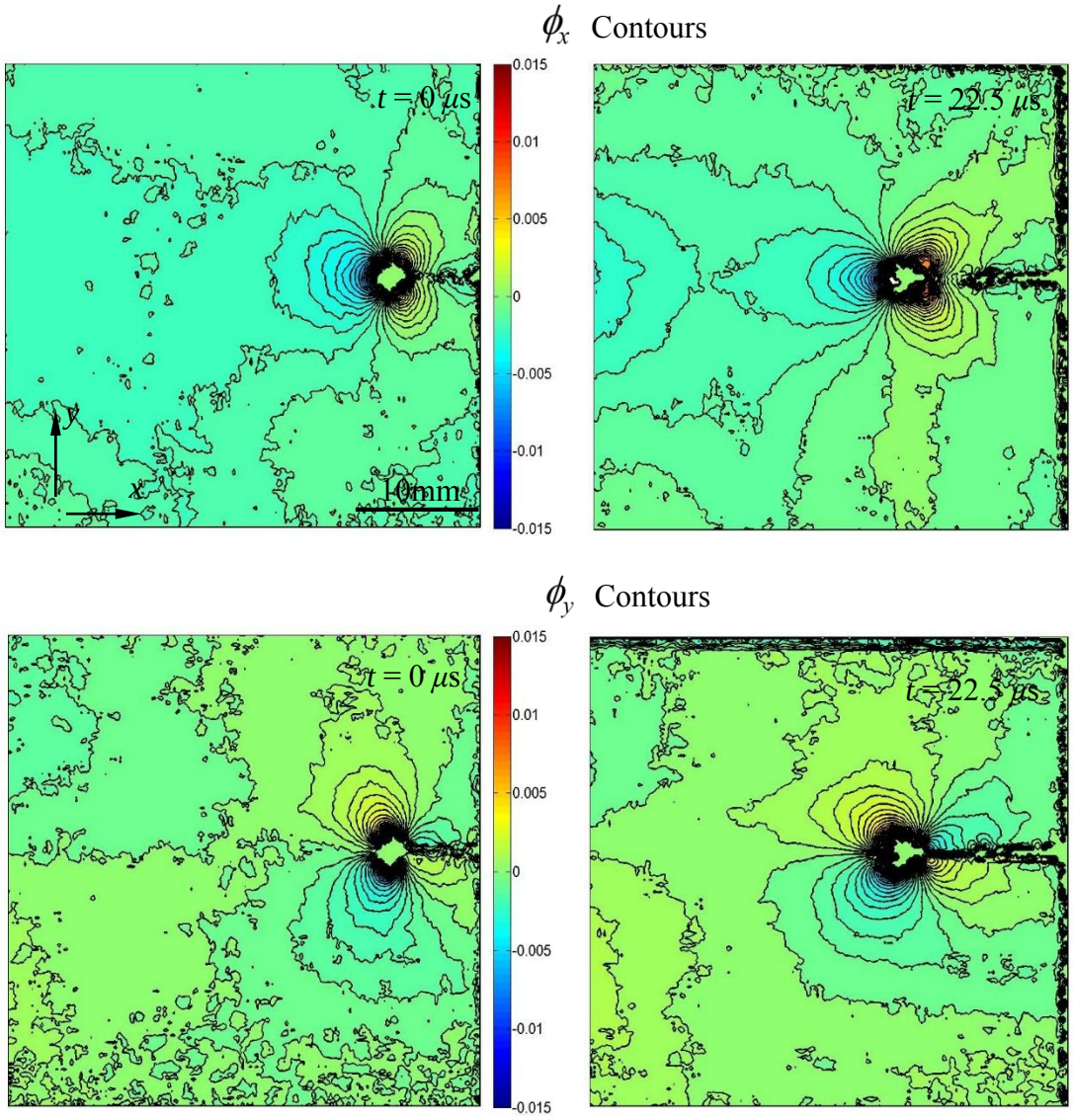

Figure 3.25: Angular deflection contour plots (contour interval = 5×10^{-4} rad) proportional to stress gradients of $(\sigma_{xx} + \sigma_{yy})$ in the *x*- and *y*-directions for a polycarbonate specimen with $a = 6$ mm and $e = 0$ mm.

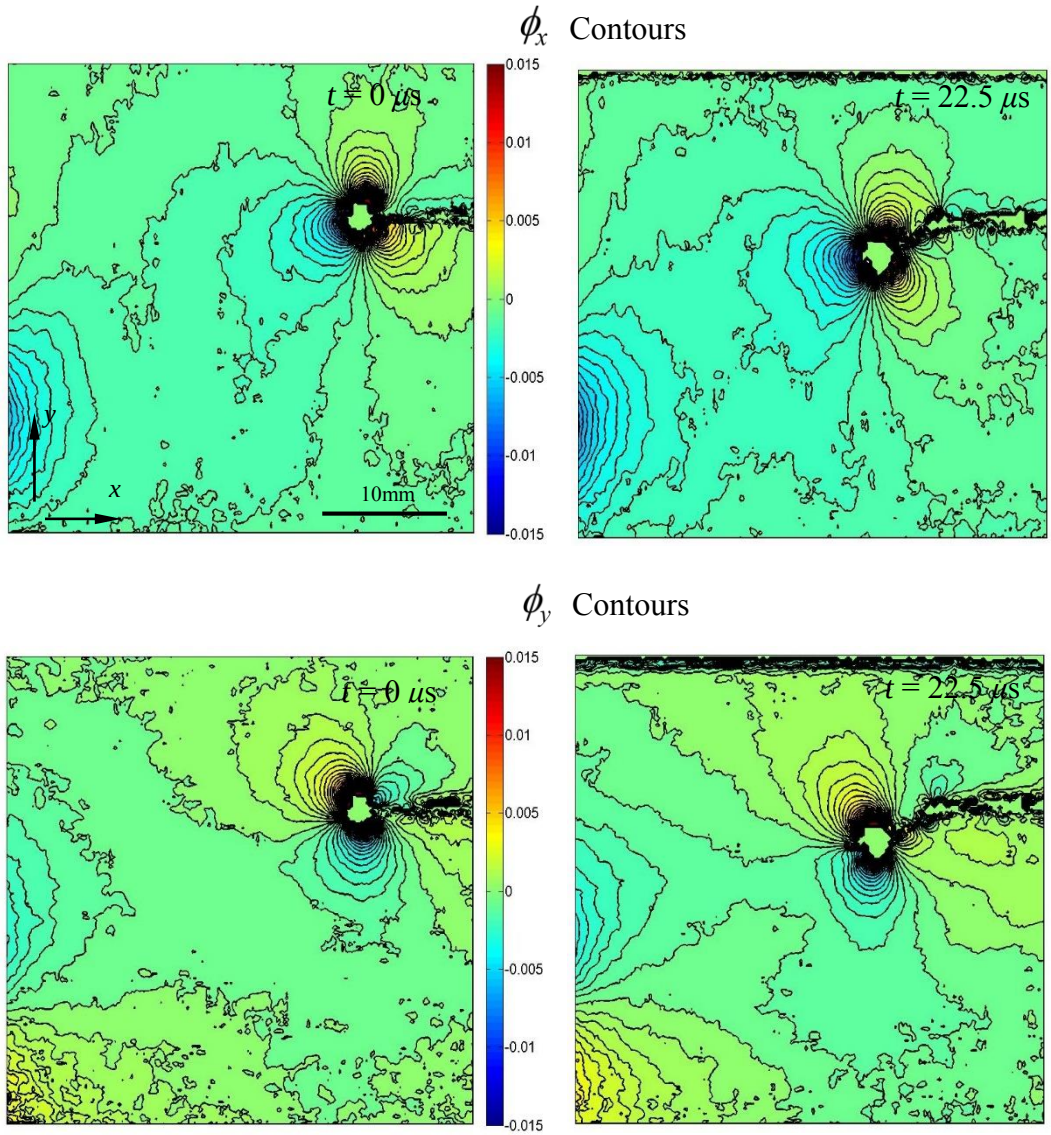

Figure 3.26: Angular deflection contour plots (contour interval = 5×10^{-4} rad) proportional to stress gradients of $(\sigma_{xx}+\sigma_{yy})$ in the x- and y-directions for a polycarbonate specimen with a = 15 mm and e = 15 mm.

Fig. 3.25 shows the angular deflection contours for config.1 (a = 6 mm; e = 0 mm). The crack followed nearly a straight path during the window of observation. It can be seen that the overall size of the contours increased during propagation suggesting an increase in

stress intensity factors. The partial contours seen on the left edge of the plot are due to the line-load from the long-bar. Fig. 3.26 shows the angular deflection contours for config. 5 (a = 15 mm; e = 15 mm). The crack initiated at an angle suggesting mode-mixity at initiation. At time t = 0 μs the angular deflection contours turned towards the direction of crack initiation. Again, the overall size of the contours increased during the observation window implying an increase in the magnitude of the effective stress intensity factors.

3.7.3 Crack velocity and Stress Intensity Factor histories

A compilation of crack velocity histories for all the configurations are shown in Fig. 3.27(a). The trends are similar to those for PMMA (Fig. 3.15(a)). At the end of the window of observation, which is t = 25 μs after crack initiation, the final velocity monotonically increased from config.1 (340 m/s) to config. 5 (458 m/s). This again reinforces the observations in case PMMA that cracks travel faster under mixed-mode conditions. Furthermore, when compared to PMMA counterparts, cracks travels faster in PC. This is attributed to higher impact velocity used for PC compared to PMMA to achieve crack initiation in PC. Both mode-I and mode-II stress intensity factor histories (K_I and K_{II}) evaluated form DGS for all configurations are plotted in Fig. 3.27(b). Time t = 0 corresponds to the instant at which the crack initiated. As in the PMMA counterparts (Fig. 3.15(b)) K_I values increased monotonically after impact until crack initiation and the values were lower for a longer notches at a given instant. The critical K_I values at crack initiation were consistently higher in each of the cases when compared to the PMMA counterparts.

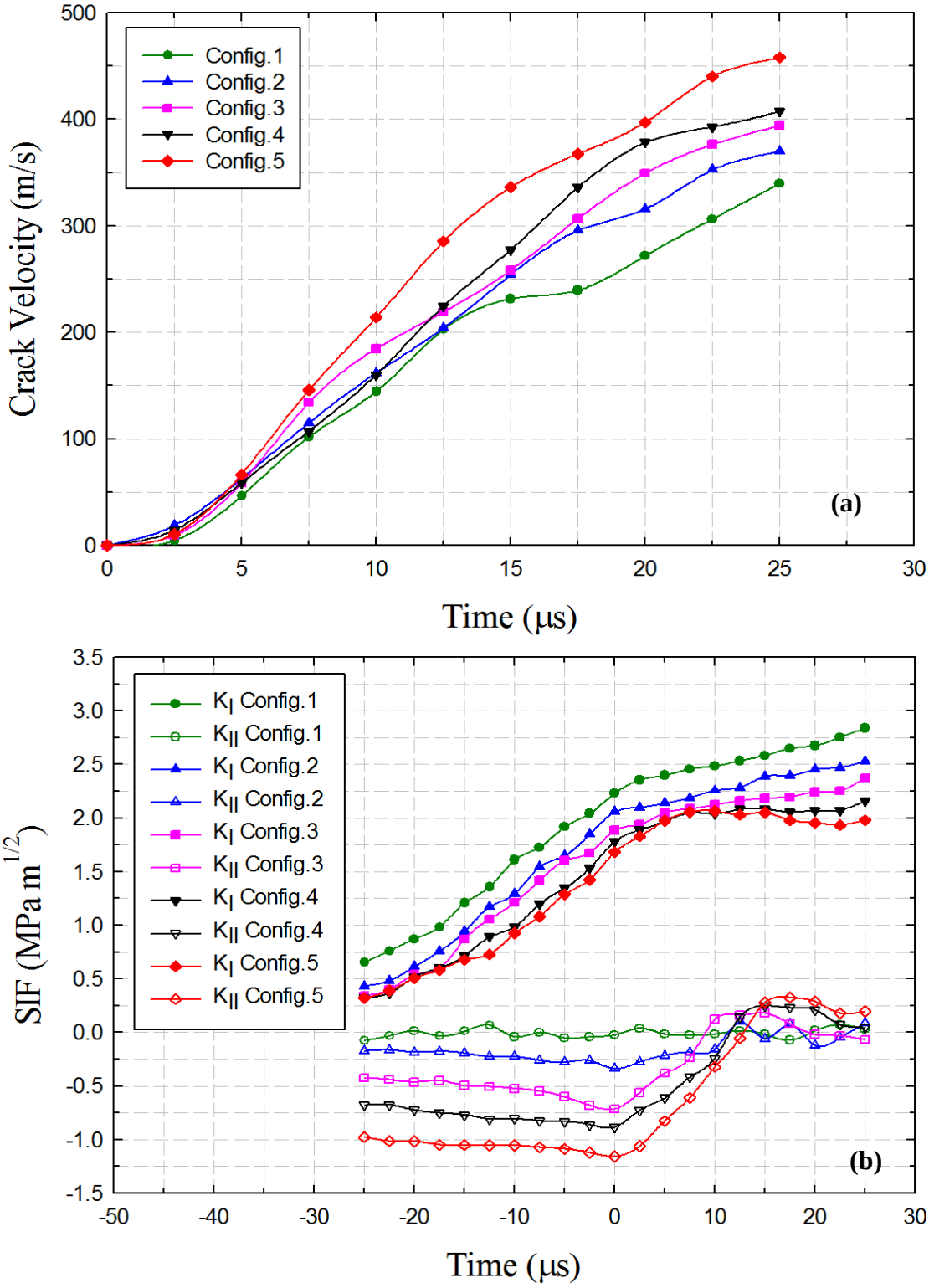

Figure 3.27: Compilation of crack velocities (a) stress intensity factors (SIFs) (b) for different configurations of polycarbonate.

Further, the critical K_I values decreased with the initial crack length (config. 1 to config. 5). The post crack initiation ($t > 0$) K_I values continued to increase but at different and lower rates in each geometry. The K_{II} histories on the other hand showed an opposite trend. Prior to crack initiation, the K_{II} values are nearly constant for each configuration, the highest magnitude corresponding to the case with the deepest initial edge crack. That is, a continuous increase in K_{II} values at initiation from config. 1 to config. 5 are evident. This trend is in line with the numerical predictions for different geometries where an increase in shear stress and a decrease in normal stress were seen at the prospective crack-tip locations of longer cracks (as described earlier). After the crack initiated ($t = 0$), a sustained drop in the magnitude of K_{II} values towards zero occurred in all cases suggesting the tendency for crack growth to occur in a mode-I fashion. As in PMMA counterparts, K_{II} histories for polycarbonate show an oscillatory behavior about zero in the post-initiation period. And, polycarbonate being tougher polymer relative to PMMA the magnitudes of both K_I and K_{II} are significantly higher.

3.7.4 Comparison between PMMA and PC fracture

The enlarged crack-tip images shown in Fig. 3.12 for different specimen configurations provide details about crack initiation and growth in PMMA. For clarity, one half (the upper half) of the fractured sample is shown. At this magnification, the dynamically grown crack edges appears relatively sharp in each of these images without any strong indication of crazing as whitened regions adjacent to the crack flanks, consistent with a brittle fracture behavior. Further, the crack initiation angles match the ones

computed using the MTS criteria. On the other hand, Fig. 3.24 shows polycarbonate counterparts in the crack-tip vicinity. When compared to PMMA, the crack flanks after initiation show visible whitening and a relatively rugged morphology indicating crazing and ductility (see Fig. 3.28 (a) for details). This characteristic is similar to the ones reported in Ref. [100] . Further, during initial crack growth, staircase/stepped patterns along the crack path are evident (see Fig. 3.28(b)) suggesting an intermittent growth/arrest mechanism at crack initiation. Considering all these toughening mechanisms, the match between the measured kink angle and the prediction based on brittle fracture criteria is rather poor.

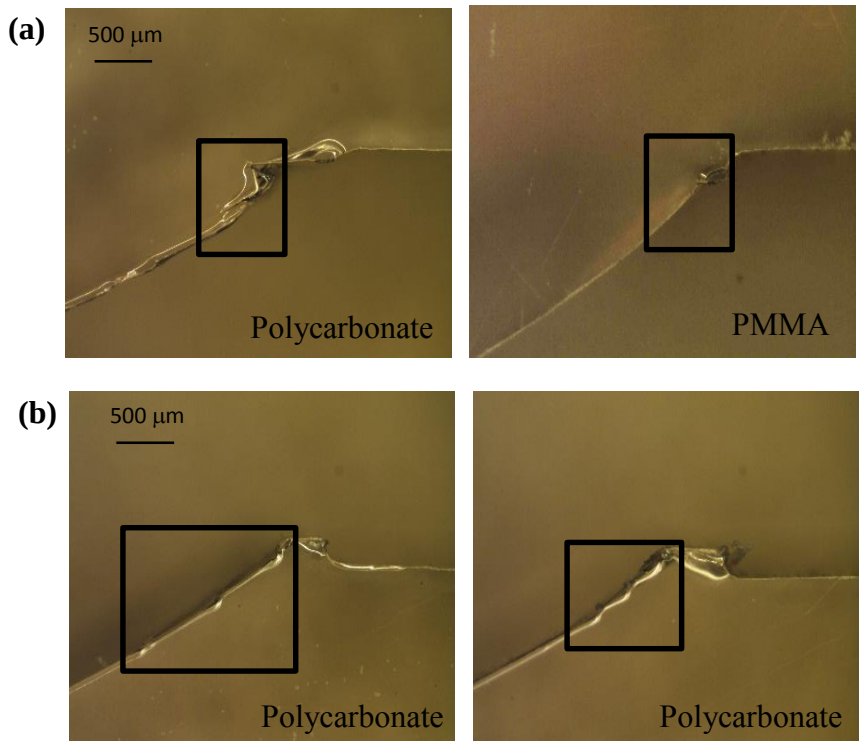

Figure 3.28: Distinct characteristics observed in polycarbonate from fractography. (a) Ductile and brittle failures observed in polycarbonate and PMMA respectively. (b) Staircase/stepped pattern at initiation observed in polycarbonate.

The critical values of stress intensity factors K_I and K_{II} were plotted as a fracture envelope of the functional form $f(K_I, K_{II}) = 0$ in Fig. 3.29. Such an envelope could be considered as an extension of the ones for quasi-static conditions with inertial effects entering the results through measured stress intensity factors [101]. At least two data points for each loading configuration are included for both PMMA and polycarbonate. The data sets were fitted with an equation of the form $\left(\frac{K_I}{K_{Icr}}\right)^2 + \left(\frac{K_{II}}{K_{IIcr}}\right)^2 = 1$ and the corresponding fits are shown in the Fig. 3.29. The K_{Icr} for mode-I crack initiation in case of polycarbonate reported here (2.25 MPa√m) is in agreement with the sharpest crack case reported in [102].

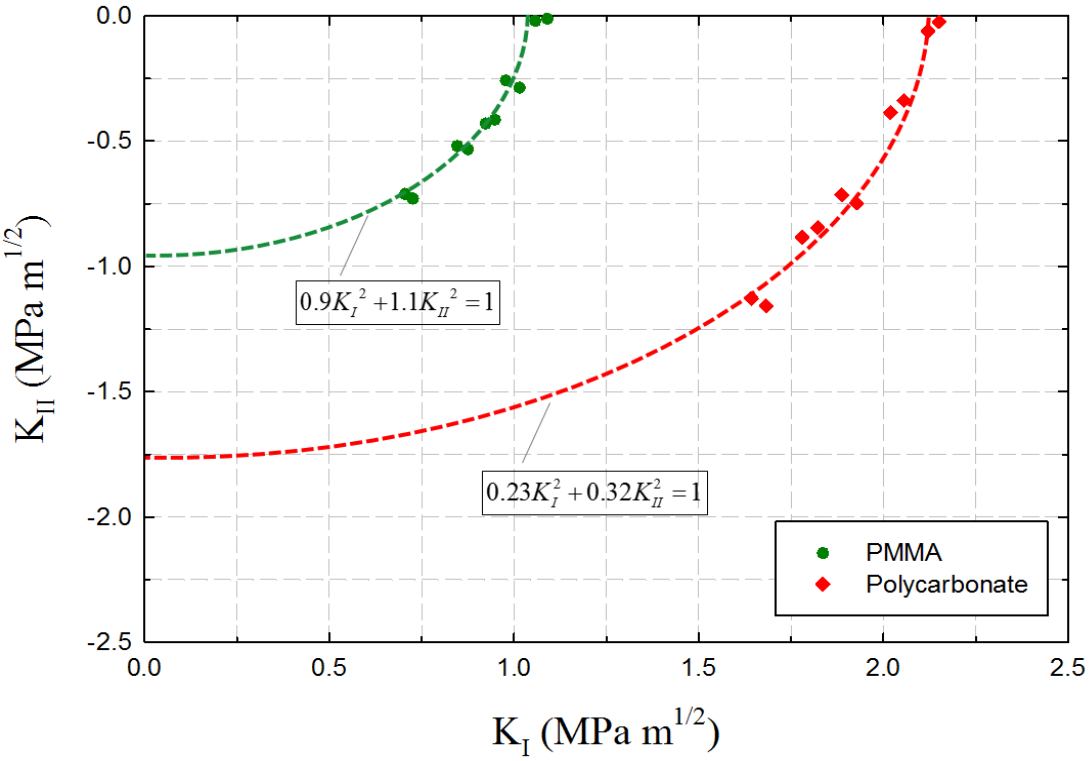

Figure 3.29: Fracture envelopes for PMMA and polycarbonate.

Chapter 4

DYNAMIC CRACK INTERACTION WITH AN INTERFACE IN PMMA BILAYERS

In this chapter, the interactions of a dynamically growing crack approaching a weak interface oriented normally to the incoming crack are described. The bilayers considered include two PMMA plates bonded using an acrylic adhesive forming an interface oriented normally to the initial crack propagation direction. Interfaces are characterized as 'strong' and 'weak' based on their crack initiation toughness. The dynamic fracture behavior of monolithic PMMA is also studied in the same configuration for comparison. The crack growth and fracture parameter histories of propagating cracks are evaluated and the underlying fracture mechanics is explained.

4.1 Specimen geometry and preparation

Two different specimen geometries were used in this study and are shown in Fig. 4.1. One of the geometries is for a monolithic specimen whereas the other is for a bilayer. The bilayer was prepared by bonding two PMMA plates (152 mm x 50.8 mm of thickness 8.6 mm) using a commercially available acrylic adhesive, Weldon 16, whereas the monolithic specimen was a single PMMA plate (152.4 mm x 101.6 mm of thickness 8.6 mm). In case of layered configurations, bond surfaces of the constituent layers underwent additional surface preparation. They were first sanded using 400-grit sandpaper in the

direction perpendicular to the thickness of the specimen and then cleaned using lint free cloth soaked in isopropyl alcohol to remove any debris.

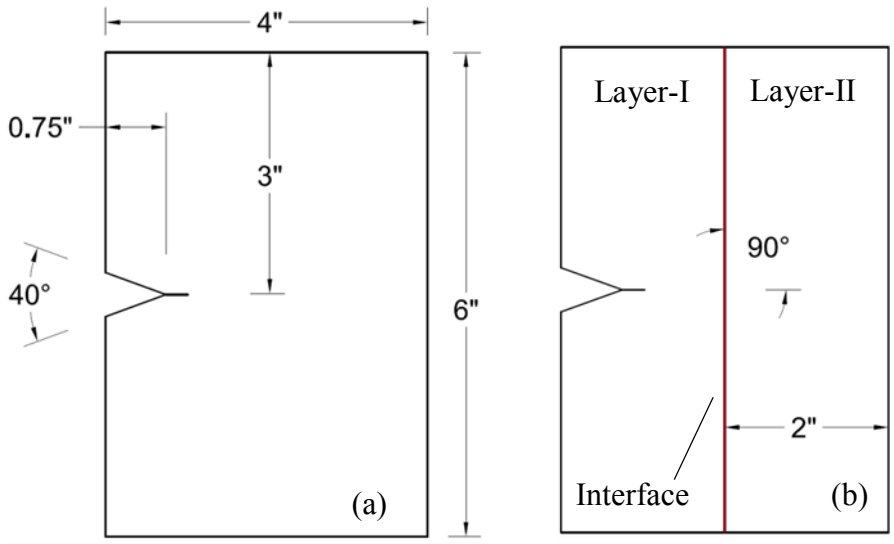

Figure 4.1: Specimen configurations studied. (a) Monolithic (b) Bi-layered

The schematic of the steps involved layered material preparation is shown in Fig. 4.2. The two plates to be bonded were placed on the bed of a drill press vise. The adhesive was applied to one of the two surfaces to be bonded and then both were squeezed against each other using the jaws of the vise. Two steel spacers (shims) of required thickness were placed between the two layers to control the resulting interface thickness. The joint was cured at room temperature for 24 hrs before experimentation. The adhesive characteristics and properties are shown in Table 4. 1. A 40˚V-notch was machined on one long edge of both monolithic and bilayer specimens and was subsequently extended into the specimen by 2 mm. The extended notch was sharpened by scoring it with a sharp razor blade. The wedge shaped end of the long impactor bar (Hopkinson bar) (see Fig. 4.12) matched the

V-notch of each of these specimens. The overall dimensions of both the monolithic and layered specimens were same.

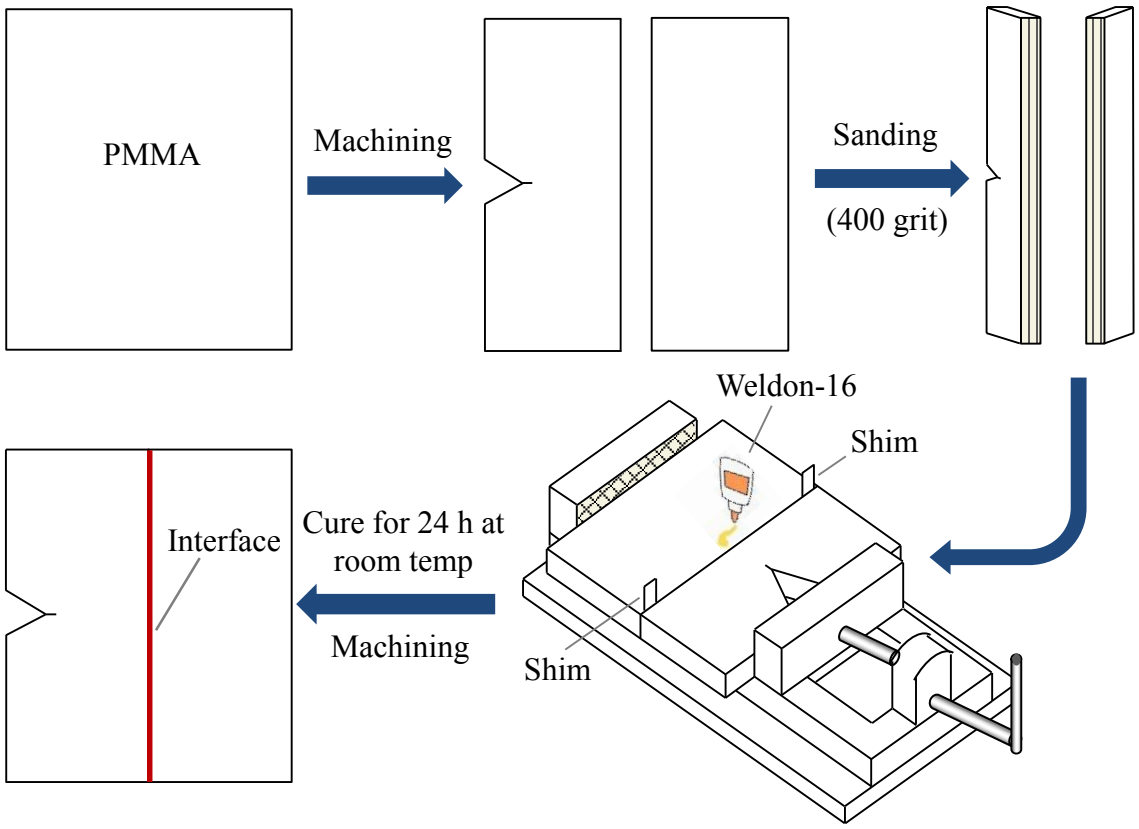

Figure 4.2: Schematic of the steps involved in bi-layered material preparation.

Adhesive Properties and Characteristics	
Parameter	**Value**
Color	clear
Viscosity	800 cps
Working time	2-3 minutes
Fixure time	5-6 minutes
80% Strength	16 hours
Specific gravity	1.02 ± 0.04

Table 4.1: Characteristics of Weldon 16 acrylic adhesive

4.2 Interface characterization

4.2.1 Interface fracture toughness

The interface was initially characterized using its mode-I quasi-static crack initiation toughness. Three-point bend tests on edge cracked geometries were used for this purpose. It consisted of two rectangular PMMA pieces of 70 mm x 15 mm and thickness of 8.6 mm joined together as shown in Fig. 4.3. The bond surfaces (8.6 mm x 15 mm) were prepared similar to the one used for making dynamic fracture specimens. Bilayer sheets with various bond layer thicknesses from 25 μm to 1.3 mm were prepared and were used to make multiple fracture specimens from each sheet to measure interfacial crack initiation toughness. A 3 mm long disbond was introduced along the interface of each sample during preparation. The specimen was left in the vise for 24 h before performing the fracture tests.

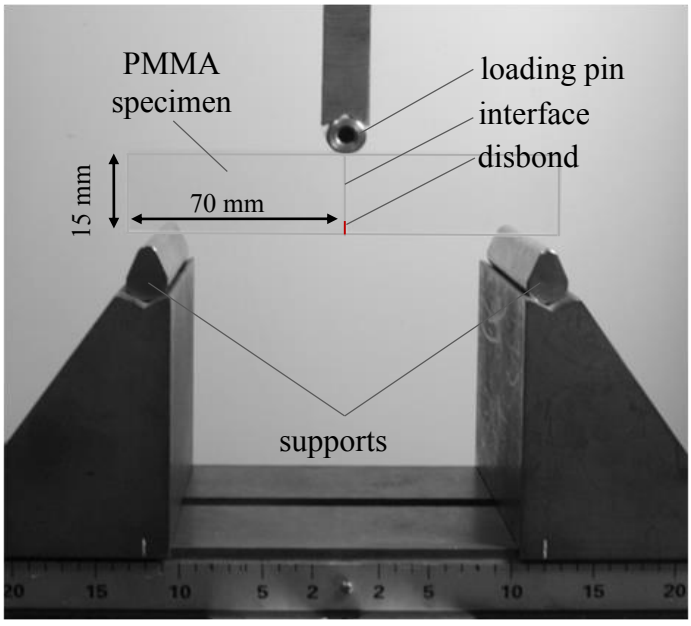

Figure 4.3: Photograph of the experimental setup used to characterize interface fracture toughness.

An Instron 4465 loading machine was used to perform symmetric 3-point bend tests. The specimen was loaded in displacement control mode with a crosshead speed of 0.005 mm/sec. The load was applied on the interface of the edge cracked beam samples (span = 120 mm) as shown in Fig. 4.3. The applied load history was recorded up to fracture. Representative load deflection plots for two select interface thicknesses are shown in Fig. 4.4(a). The samples fractured in a brittle fashion as evident from an abrupt drop in the load at fracture. Using the measured peak load and the specimen geometry, the crack initiation toughness was evaluated as [90],

$$K_I = \frac{F\,S}{Bw^{3/2}} \frac{3(\xi)^{1/2}\left[1.99-\xi(1-\xi)\left\{2.15-3.93(\xi)+2.7(\xi)^2\right\}\right]}{2(1+2\xi)(1-\xi)^{3/2}}, \qquad \xi = \frac{a}{w} \tag{4.1}$$

This was repeated for various interface thicknesses to quantify the dependence of crack initiation toughness on adhesive layer thickness. The results thus obtained are plotted in Fig. 4.4(b) for different interface thicknesses. It can be seen that the crack initiation toughness decreases with the interface thickness. Two cases, one with an interface thickness of 25 μm and another with 100 μm were chosen as the 'strong' and 'weak' interfaces, respectively. The critical static mode-I SIF for neat (virgin) PMMA was also measured using symmetric 3-point bend tests and was recorded as 1.31 ± 0.07 MPa√m (dotted line in Fig. 4.4(b)) which is *higher than the crack initiation toughness of both interface thicknesses studied*. That is, the 'weak' and 'strong' interface crack initiation toughness were ~52% and ~77% , respectively, of virgin PMMA.

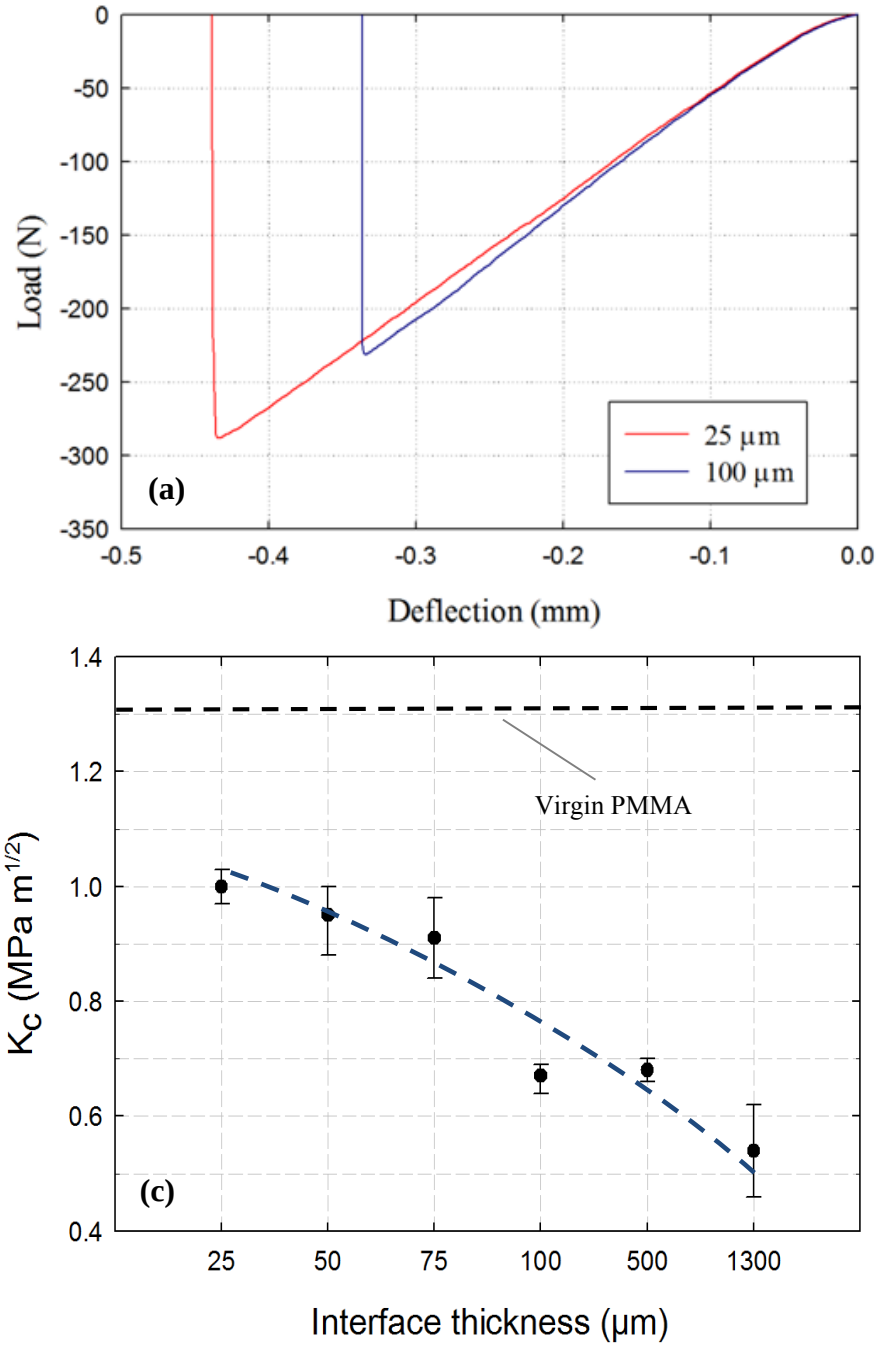

Figure 4.4: (a) Measured load-deflection response for fracture specimens with 25 µm and 100 µm interface thicknesses. (b) Variation of crack initiation toughness with interface thickness. (Note that all interfaces have lower crack initiation toughness than virgin PMMA).

4.2.2 Interfacial crack initiation toughness under mixed-mode conditions

The 100 μm interface was characterized for its mixed-mode fracture toughness using asymmetric four-point bending shear tests [103] [104]. The loading configuration was as shown in Fig 4.5(a). The specimen was made by machining 16 mm wide rectangular strips (W = 16 mm) from the specimens used for performing dynamic crack growth tests (inclusive of the interface; see Fig. 4.1(b)). A notch of 4 mm was machined along the interface using diamond impregnated saw to form SENB specimen. A razor blade was used to sharpen the notch tip. An Instron 4465 universal testing machine was used for loading the specimen in the displacement-control mode (crosshead speed = 0.005 mm/sec). Multiple tests were carried out by varying experimental parameters C and D. From the failure load, mode-I and -II SIFs, effective SIF and mode-mixity were evaluated using [104],

$$K_I = \frac{P}{BW}\left[\frac{C-D}{C+D}\right]\left(\left(\frac{6s}{W}\right)f_1\right)\sqrt{a}\ ,\ K_{II} = \frac{P}{BW}\left[\frac{C-D}{C+D}\right]f_2\sqrt{a}\ ,$$

$$K_{eff} = \sqrt{K_I^2(t)+K_{II}^2(t)}\ \text{, and}\ \psi = \tan^{-1}\left(\left(\frac{f_2}{f_1}\right)\left(\frac{W}{6s}\right)\right) \tag{4.2}$$

The variables in the above equation are described in Fig 4.5(a). Various values of s (0 mm, 2 mm, 5 mm and 10 mm) were used to obtain different mode mixities. The values of geometric constants f_1 and f_2 were 1.29 and 1.86 based on the plots reported in Ref. [104]. The plot of K_{eff} vs. mode-mixity is shown in Fig 4.5(b). Data point for zero mode-mixity obtained from mode-I tests has been included in this plot for completeness. It can

be seen that the interface crack initiation toughness increases with the increase in mode mixity.

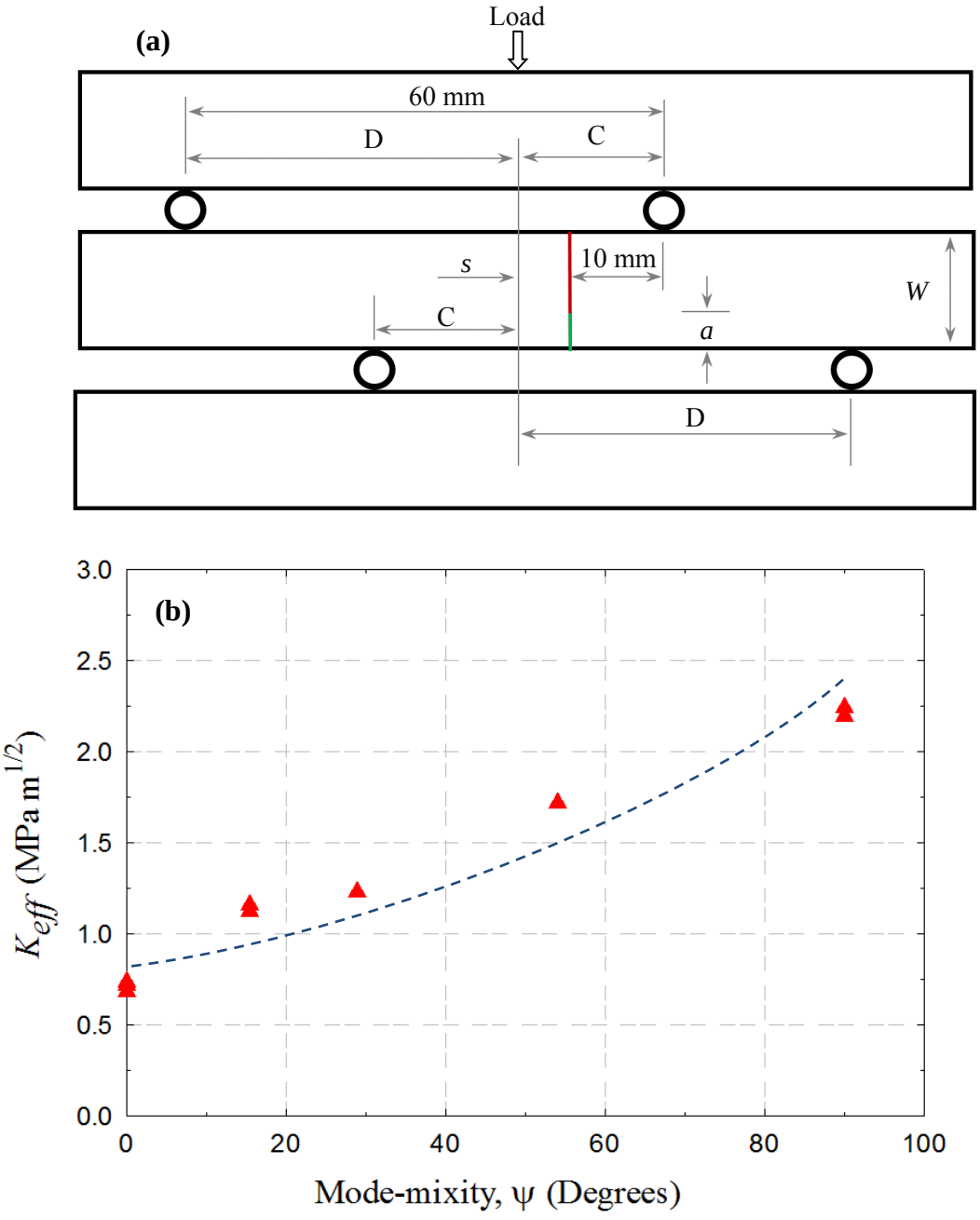

Figure 4.5: Asymmetric four-point-bend tests: (a) Loading configuration and geometry, (b) Effective SIF vs. mode-mixity plot.

4.2.3 Interface tensile strength

To measure the quasi-static tensile strength of the interface, tension tests were carried out. The experimental setup is shown in Fig 4.6 (inset). The specimen was prepared by bonding two PMMA sheets using Weldon 16 adhesive with an interface thickness of 100 μm. The glued sheets were machined to tension specimen (dog-bone) geometry, as shown. An Instron 4465 universal testing machine was used for loading the specimen in displacement-control mode (crosshead speed = 0.005 mm/sec). Multiple tests were carried out. The load-deflection plot obtained for two such experiments are shown in Fig. 4.6. From the failure load and area of cross-section (8.6 mm × 5 mm), the tensile strength of the interface was evaluated as 23 ± 0.3 MPa.

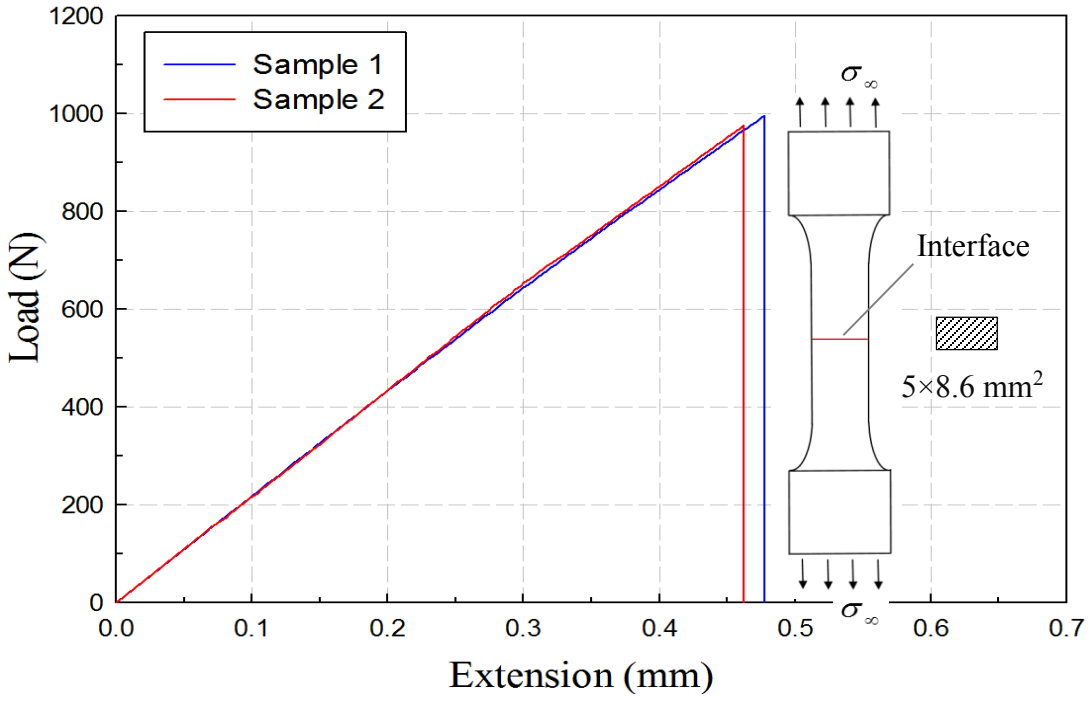

Figure 4.6: Load-deflection plots for two tension tests (gage section = 5 mm × 8.6 mm). Inset shows the dog-bone specimen geometry with interface

4.2.4 Interface shear strength

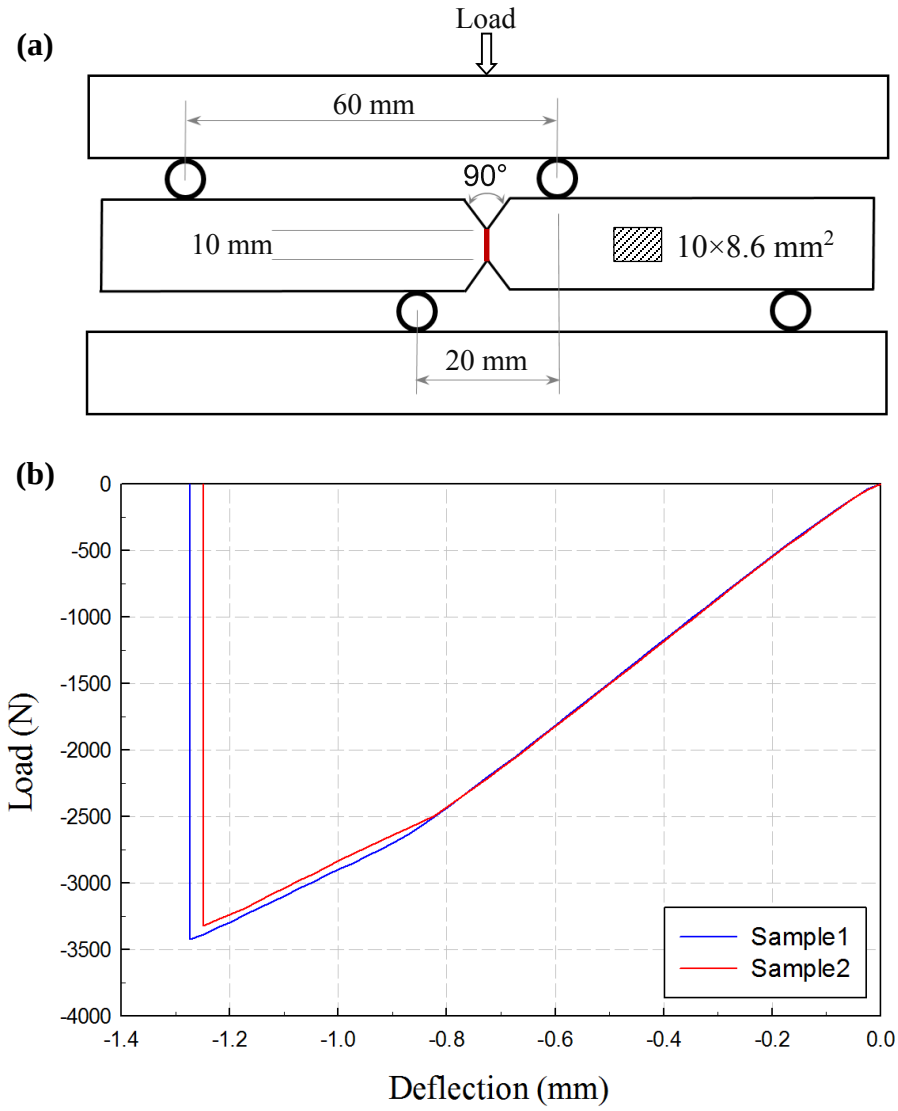

Figure 4.7: Asymmetric four-point-bend tests: (a) Loading configuration and geometry, (b) Representative load-deflection plots.

To measure the shear strength of the interface, asymmetric four-point bending shear tests [103] were carried out. The loading configuration is shown in Fig. 4.7(a). Again, the specimen was prepared by bonding two PMMA sheets using the acrylic adhesive Weldon

16 with an interface thickness of 100 μm. The glued sheets were machined to the final specimen geometry and dimensions, as shown. An Instron 4465 universal testing machine was used for loading the specimen in the displacement-control mode (crosshead speed = 0.05 mm/sec). Multiple tests were carried out. The load-deflection plot obtained for two such experiments are shown in Fig. 4.7(b). From the failure load and area of cross-section (8.6 mm × 10 mm), the shear strength was evaluated. The quasi-static shear strength was found to be 26 ± 0.5 MPa.

4.2.5 Elastic modulus of the adhesive

Due to the difficulty in making bulk samples directly from the adhesive Weldon 16, conventional techniques could not be employed to measure its elastic modulus to ensure that the bilayers are indeed elastically homogeneous. The nano-indentation technique was utilized to measure the elastic modulus of the adhesive along with PMMA for comparison. A 25 mm x 25 mm rectangular piece of PMMA with thickness 8.6 mm was used as the substrate on to which a hemispherical dent of 3 mm was created using a drill. The dent was cleared of debris, following which the adhesive was poured into and cured for 24 hours. Subsequently, the surface was prepared for nano-indentation test by sanding it step by step to #1200 grit sand paper followed by further polishing and buffing. The test was performed using Hysitron TI 950 TriboIndenter with a Berkovich diamond indentor tip. The nano-indentation was carried out at two locations each on the adhesive as well as on PMMA substrate. The load displacement response of both adhesive and PMMA are shown in Fig.4.8.

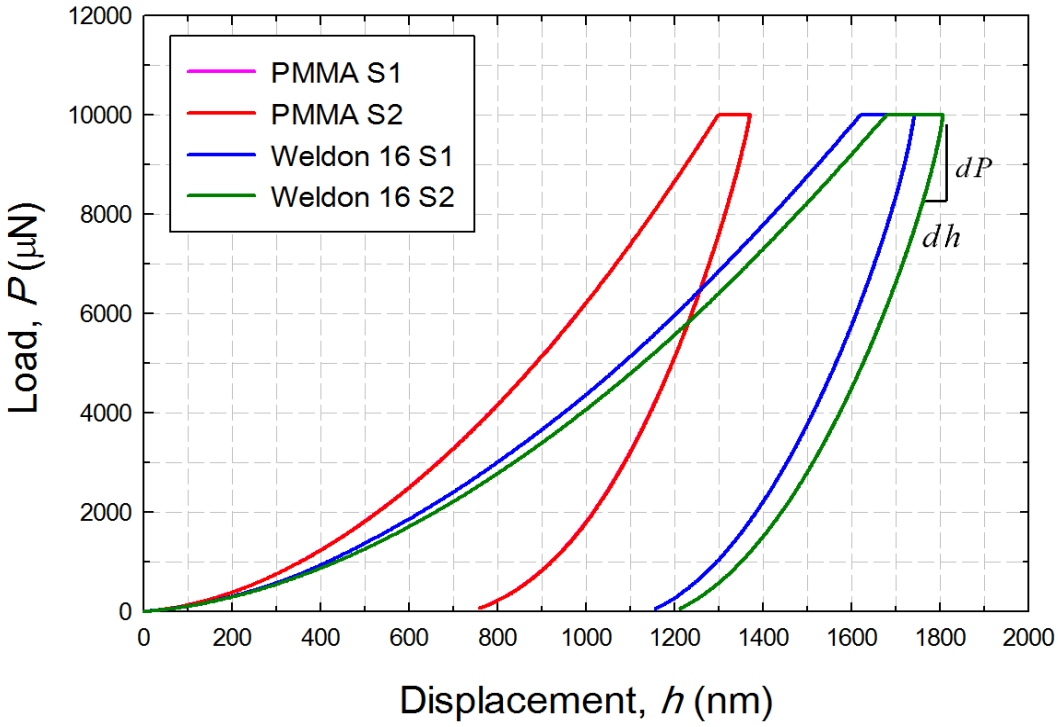

Figure 4.8: Load vs. displacement plot obtained from the nano-indentation test for the adhesive (Weldon 16) and PMMA. (Note the two specimens of PMMA have their plots overlapping each other)

From the slope of the unloading region, the unloading stiffness was measured as [105] [106],

$$S = \frac{dP}{dh} = \frac{2\beta\sqrt{A}}{\sqrt{\pi}} E_r \text{ or } E_r = \frac{\sqrt{\pi}S}{2\beta\sqrt{A}} \tag{4.3}$$

where, $\frac{dP}{dh}$ is the slope of the upper portion of the unloading curve during the initial stages of unloading (contact stiffness), A is the projected contact area at maximum load, $\beta \approx 1$ is the geometric factor for the chosen indentor tip and E_r is the reduced modulus. Using E_r, the elastic modulus was obtained as [105],

$$E = \frac{1-\nu^2}{\left[\frac{1}{E_r}\right] - \left[\frac{1-\nu_i^2}{E_i}\right]} \tag{4.4}$$

where, ν is the Poisson's ratio of the material, E_i and ν_i are the elastic modulus (1140 GPa) and Poisson's ratio (0.07) of the indentor, respectively. The Poisson's ratio of the adhesive was assumed to be that of PMMA ($\nu = 0.35$) as it is an acrylic based adhesive. The average elastic modulus of the adhesive and PMMA were measured as 2.85 ± 0.12 GPa and 3.35 ± 0.04 GPa. Thus, the elastic modulus of the adhesive being nearly same (within ~15%) as the one for the substrate, it was reasonable to assume that the bilayers to be elastically homogeneous.

4.2.6 Dynamic interface fracture toughness

The dynamic interface fracture toughness was evaluated for the interface using the Hopkinson pressure bar loading and measurements were made using DGS in conjunction with high-speed photography. Two interface thicknesses of 25 μm and 100 μm ('strong' and 'weak' interfaces respectively) were studied. The specimen geometry and loading configuration is shown in Fig. 4.9. The specimen preparation, experimental procedure, image analysis and evaluation of fracture parameters are same as the descriptions in Sections 4.1, 4.3, 4.4, and 4.5, respectively. The test setup used was similar to the one described in Chapter 3 (see Fig. 3.7) except for the wedge shaped impactor as shown in Fig. 4.12 inset.

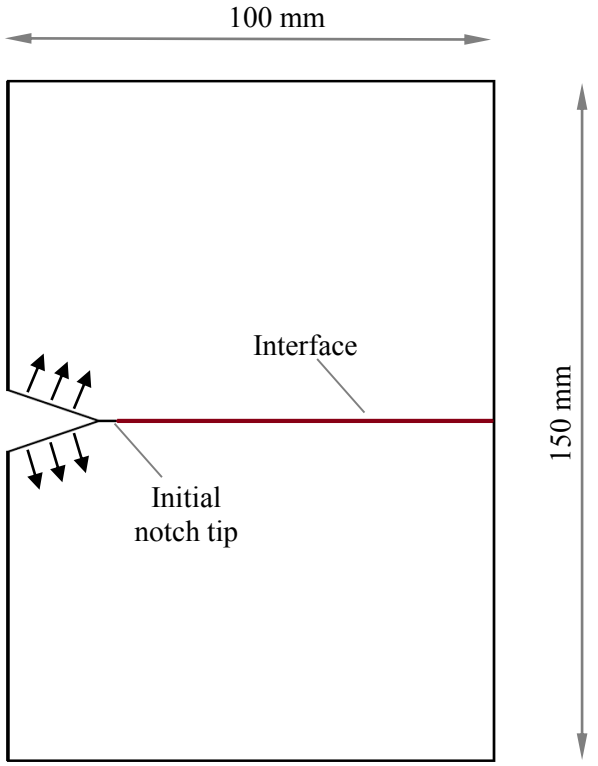

Figure 4.9: Specimen geometry and loading configuration used for measuring dynamic fracture toughness of the interface.

The in-plane orthogonal angular deflection measurements at two time instants for a 'strong' interface are shown in Fig. 4.10. The velocity histories and the SIF histories for both the interface thicknesses are plotted in Fig. 4.11(a) and (b), respectively. The crack speeds reached up to 800 and 600 m/s in the 'weak' and 'strong' interface cases. They both are substantially higher than the corresponding ones in a monolithic sheet, typically in the 250-300 m/s range [90]. It can be seen that the fracture toughness of the 'strong' interface (0.94 MPa√m) is higher than that of the 'weak' interface (0.72 MPa√m). When compared with the dynamic fracture toughness of PMMA (1.12 MPa√m) [99], the fracture toughness of 'strong' and 'weak' interfaces were 84% and 64%, respectively.

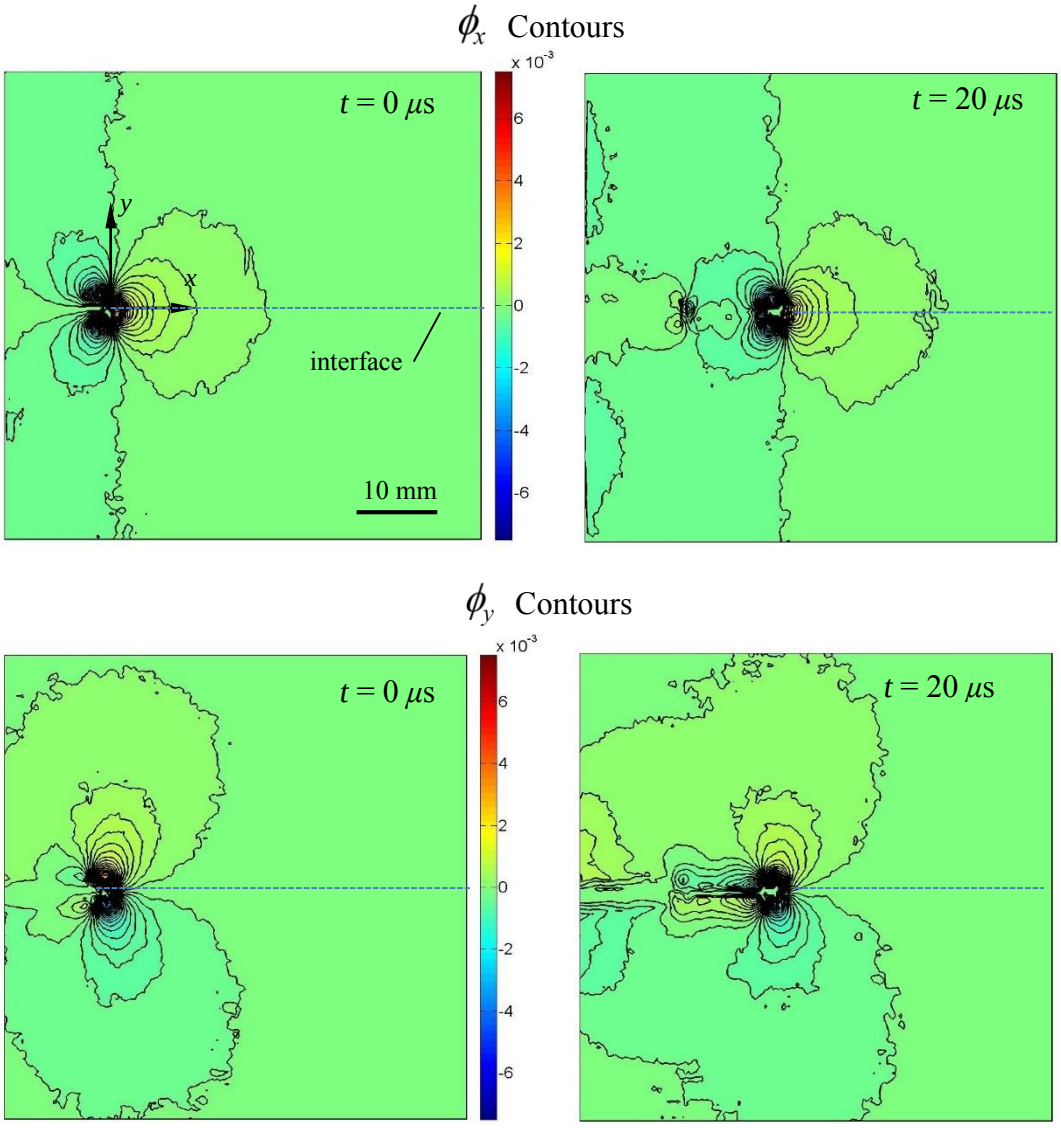

Figure 4.10: Angular deflection contour plots (contour interval = 2×10^{-4} rad) proportional to stress gradients of $(\sigma_{xx}+\sigma_{yy})$ in the *x*- and *y*-directions for a 25 μm interface. (*t* = 0 corresponds to crack initiation)

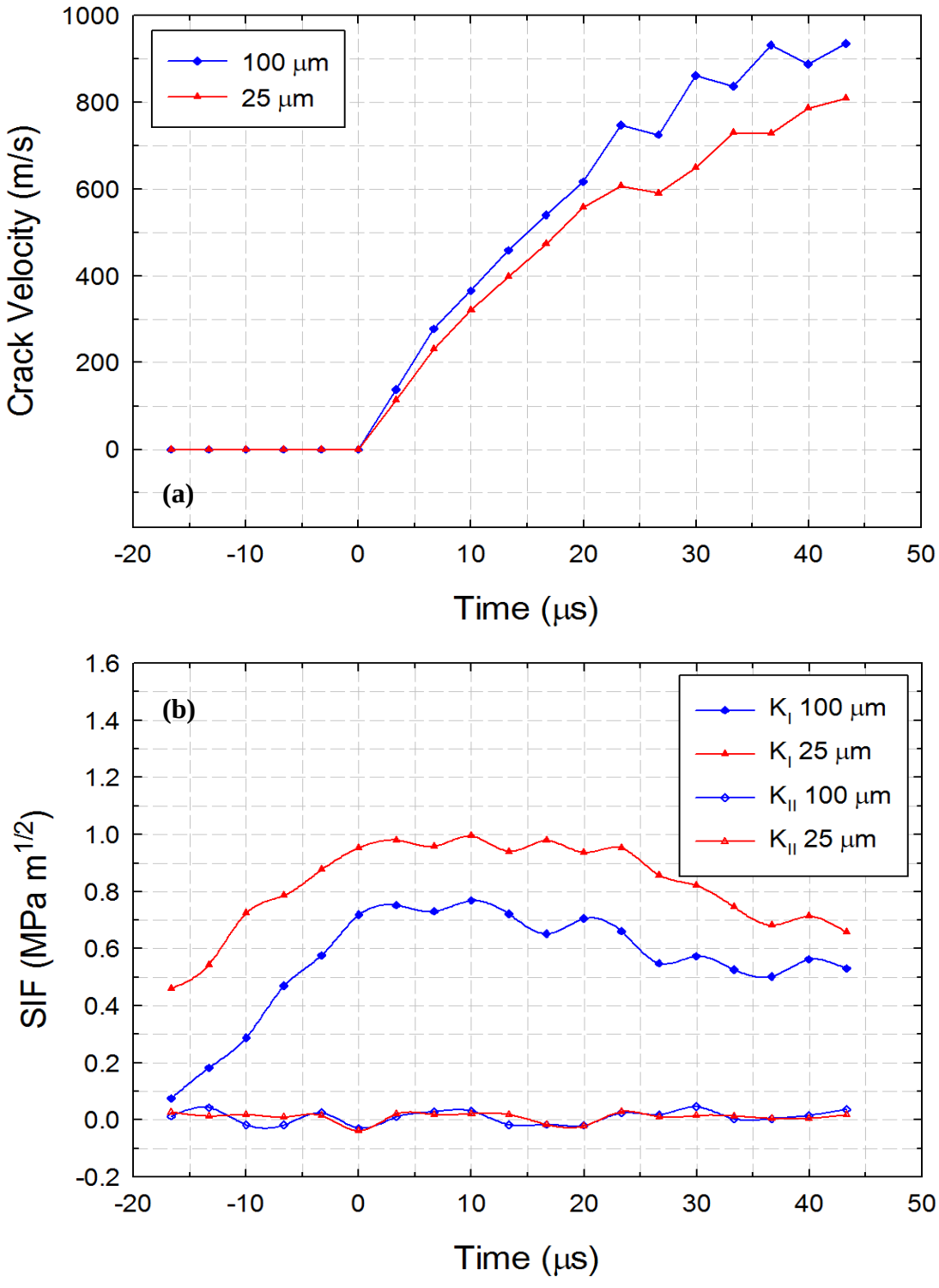

Figure 4.11: Dynamic fracture parameter histories for 25 μm and 100 μm interfaces (a) Crack-tip velocity histories, and (b) SIF histories

4.3 Experimental setup and procedure

Dynamic fracture study of monolithic and layered PMMA specimens was carried out in conjunction with DGS technique and ultrahigh-speed digital photography. The schematic of the experimental setup used is similar to the one described in Chapter 3 (see Fig. 3.7), except for the impactor with a wedge tip used here. The long-bar with a polished wedge shaped tip (see, Fig. 4.12 inset) was held against the unconstrained specimen with an identical wedge shaped V-notch.

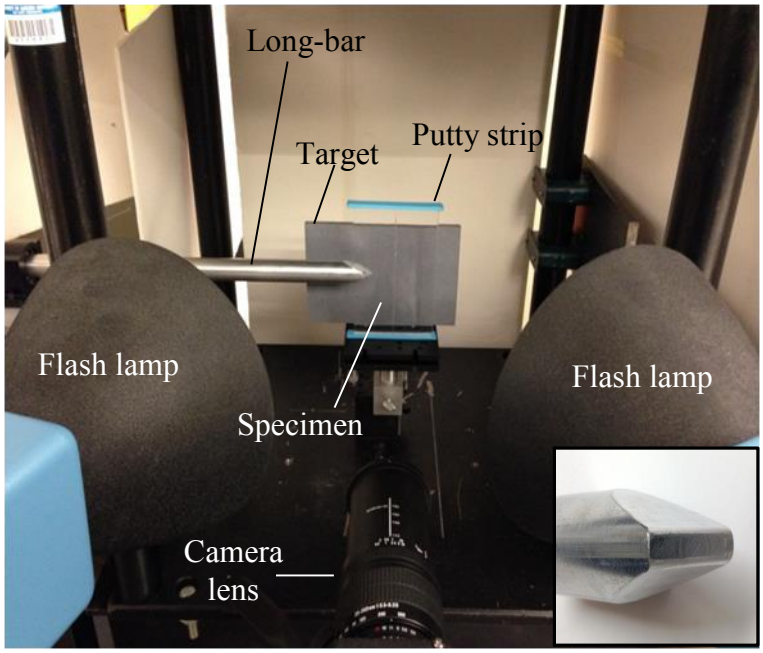

Figure 4.12: Photograph of the close-up view of the experimental setup used in dynamic fracture experiments. Inset shows the wedge shaped long bar impactor head.

The specimen was at a distance of approximately 900 mm in front of the camera. The specimen was placed on a flat adjustable platform with a layer of putty along the top and bottom edges of the specimen, as shown in Fig. 4.12. The putty was placed to achieve

approximately ‘free’ boundary conditions. A target plate with random black and white speckles was placed behind the specimen at a fixed distance of $\Delta = 29.3$ mm away from the mid-plane of the specimen to perform DGS measurements. A couple of heavy black dots (see Fig. 4.13) were marked on the target plate to relate the dimension on the image to the actual specimen/target dimensions. The vertical long edge of the specimen containing the V-notch was held against the wedge shaped tip of the long-bar.

The region of interest in this study was around the interface; hence the camera was focused on a square region of 52 mm x 52 mm in the vicinity of the vertical interface and on both of its sides. Prior to loading, a set of 32 images of the target plate through the specimen in the undeformed state were recorded at 200,000 frames per second and stored. Sufficient care was also exercised to obtain an approximately Gaussian distribution of gray scales for each image, typically in the mid-range of 0-255 (8 bit) scale by positioning the lamps appropriately. Without changing the camera settings, the striker was launched towards the long-bar using the gas-gun at a velocity of ~14 m/s. When the striker contacted the long-bar, a compressive stress wave was generated in the long-bar, which propagated along its length before loading the specimen along the two inclined faces of the V-notch. The duration of the loading phase of stress wave pulse generated was ~120 μs. When the striker contacted the long-bar, a trigger signal was also generated. This initiated recording of a second set of 32 images (deformed state) at the same framing rate at a preset trigger delay of 445 μs. Thus, a total of 32 pairs of images in the deformed and undeformed states were recorded at 5 μs intervals between successive images. Two representative speckle images recorded through the specimen in the region of interest, one in the undeformed state

and the other in deformed state for a layered specimen configuration, is shown in Fig. 4.13. It can be seen that the speckles in the deformed image are noticeably smeared in the vicinity of the propagating crack-tip whereas they seem unaffected in the far-field. The interface appears as a translucent vertical line at the center of each image. The corresponding two images for each sensor were paired from the undeformed and deformed sets and each of these 32 matched pairs was correlated individually.

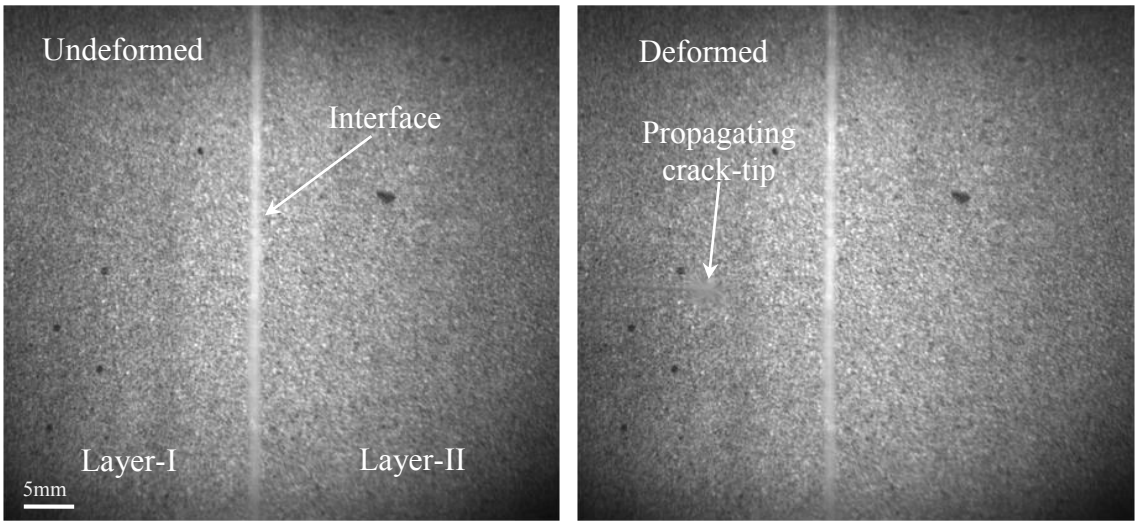

Figure 4.13: Speckle images in the undeformed (top) and deformed (bottom) states recorded by the high-speed camera though the bi-layered PMMA specimen.

4.4 Image Analysis

The 2D-DIC was again carried out using the image analysis software ARAMIS®. The recorded image corresponds to approximately 52 x 52 mm^2 region on the specimen. During analysis, each image was segmented into facets/sub-images consisting of 25 x 25 pixels. An overlap of 20 pixels (i.e., step size of 5 pixels) was used during image correlation. This resulted in 194 x 194 matrix of data points in the region of interest for

each of the two orthogonal angular deflection fields. Using MATLAB, in-plane orthogonal deflections were evaluated using the known distance Δ between the specimen and the target planes.

4.5 Evaluation of crack velocity and stress intensity factors

The position of the crack-tip in each digitized image was used to measure the instantaneous crack length. Using the crack length history, crack velocity *V was* evaluated using backward difference computations. The asymptotic crack-tip fields are the same as described in Chapter 3 (see Eqn. 3.3). To evaluate SIF histories, the angular deflection fields were digitized by identifying the current crack-tip location and crack direction. Subsequently the local Cartesian and polar coordinates were established. A number of discrete data points (orthogonal angular deflection values) around the crack-tip in the region $0.25 \le r/B \le 0.75$ and an angular extent $-135^0 \le \theta \le 135^0$ were collected and stored. This ensured that data close to the crack-tip where triaxial effects are dominant and the data near the crack faces influenced by edge effects are largely excluded from the analysis [108]. At each data point the angular deflection components in global coordinate system as well as their location were stored. These digitized data and angle of rotation of the crack at that time instant were used to perform an over-deterministic least-squares analysis to estimate both mode-I and mode-II SIFs. This process was repeated for all 32 pairs of images and for each time step to generate SIF histories. Since the crack growth occurred in mixed-mode conditions, the SIFs were used to evaluate strain energy release rate, *G*, and mode-mixity, ψ , as [109],

$$G(t) = \frac{K_I^2(t) + K_{II}^2(t)}{E} \quad ; \; \psi(t) = \tan^{-1}\left(\frac{K_{II}(t)}{K_I(t)}\right) \tag{4.5}$$

where E is the elastic modulus.

4.6 Crack path selection and angular deformation histories

Photographs of three fractured samples from each configuration representing monolithic and two layered specimens with 'weak' and 'strong' interfaces are shown in Fig. 4.14. The impact loading occurred along the V-notch faces of each image and crack propagation direction is from the left to right, as indicated by the arrowhead. In each case it is evident that the crack propagated self-similarly under mode-I conditions until it reached the interface vicinity. Differences in crack paths occurred subsequently for layered configurations whereas for the monolithic specimen, the crack continued to grow in a self-similar path until it reached the final third of the uncracked ligament beyond which it deviated from its initial path due to a loss of in-plane constraint [110] as it approached the free edge. Fig. 4.14(a) shows the crack path for a monolithic specimen. Figs. 4.14(b) and (c) show crack paths for 'weak' and 'strong' interfaces, respectively. In these, more complex fracture patterns involving interfacial crack growth and mixed-mode crack branching in layer–II are evident. Thus, the interface caused a single mode-I crack in layer-I to branch into two nearly symmetric interface cracks before emerging as two mixed-mode daughter cracks in layer-II. This clearly shows that the introduction of the interface has greatly perturbed crack growth causing the crack to branch and create greater surface area. In the specimen with a 'weak' interface, the trapped interface cracks traveled for a longer

distance (~12 mm) along the interface when compared to the specimen with a 'strong' interface (~4 mm). Further, the angle of emergence of the two daughter cracks in layer-II is higher in case of the strong interface (~28^0) when compared to the weak counterpart (~18^0) as the crack emerged into layer-II.

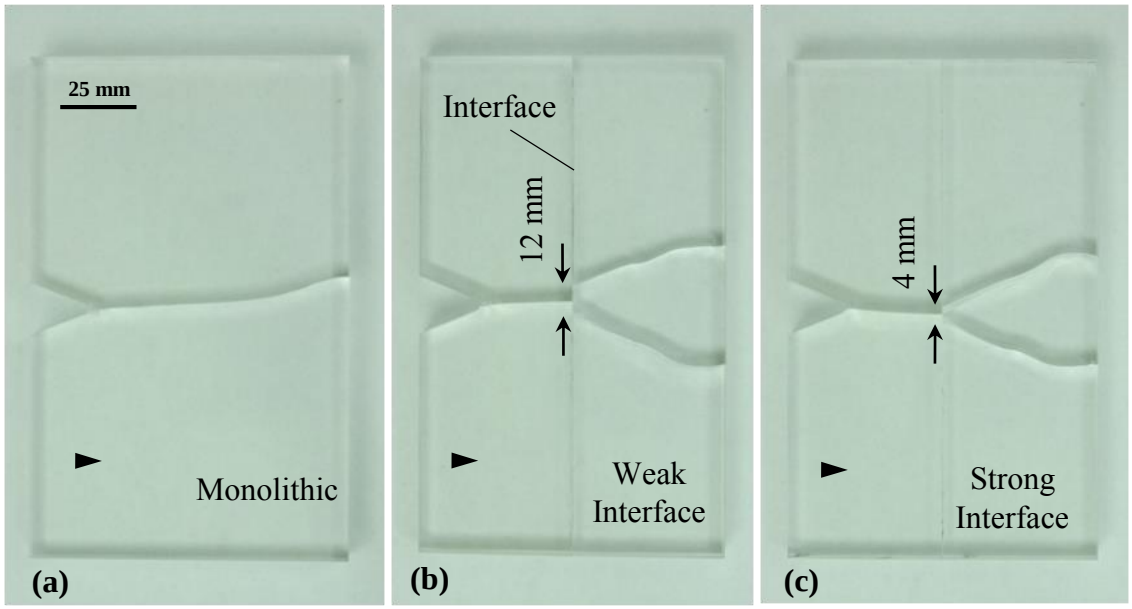

Figure 4.14. Photographs of fractured specimens showing crack path selection in (a) Monolithic (b) 'Weak' 90° layered configuration (c) 'Strong' 90° layered configuration. Arrowhead indicates crack growth direction.

Plots of angular deflection contours from the image correlation data are shown in Figs. 4.15-4.17. Note that plots presented here are only for four select time instants for the sake of brevity. (The angular deflection contours, the contour levels and the scale bar are shown in the first plot in each set and are applicable to the other plots as well.) In these, t = 0 μs represents the time at which the crack initiated at the original sharpened notch tip. In each figure, sets (a) and (b) correspond to ϕ_x and ϕ_y contours, respectively.

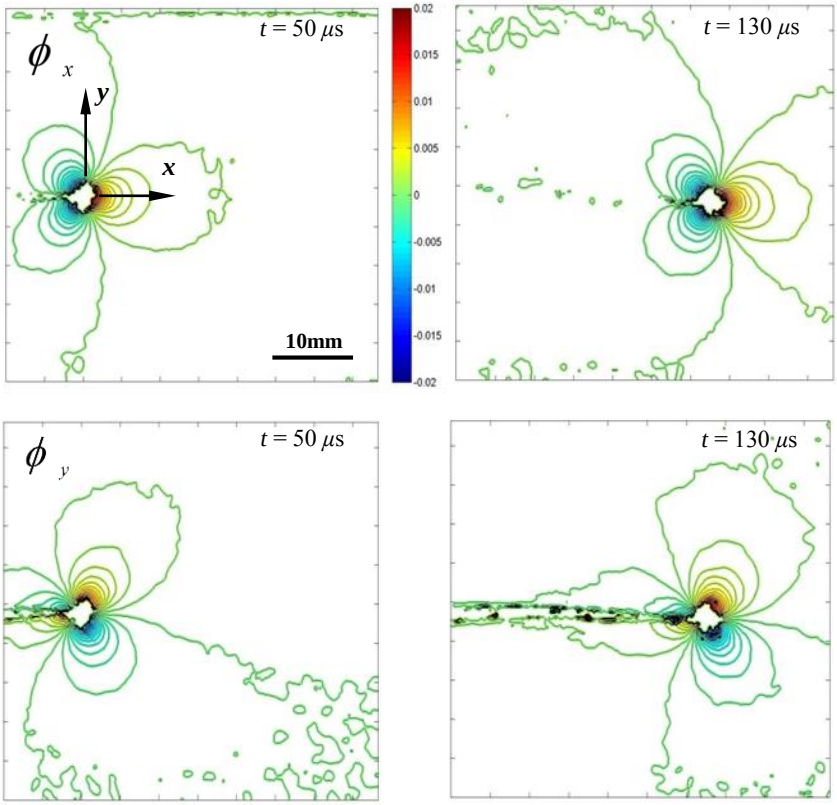

Figure 4.15: Angular deflection contour plots (contour interval = 8 x10^{-4} rad) proportional to stress-gradients in the *x*- and *y*-directions for a monolithic specimen. (Crack growth from left to right)

Figure 4.15 shows angular deflection contours for a monolithic specimen. The crack followed a nearly straight path during the time window of interest suggesting a predominantly mode-I fracture behavior. The overall size of contours remained approximately unchanged during crack growth suggesting a constant stress intensity factors in the window of observation. It should also be noted that ϕ_x contours are symmetric in shape and magnitude with respect to the growing crack whereas ϕ_y contours are only symmetric in shape but antisymmetric in magnitude.

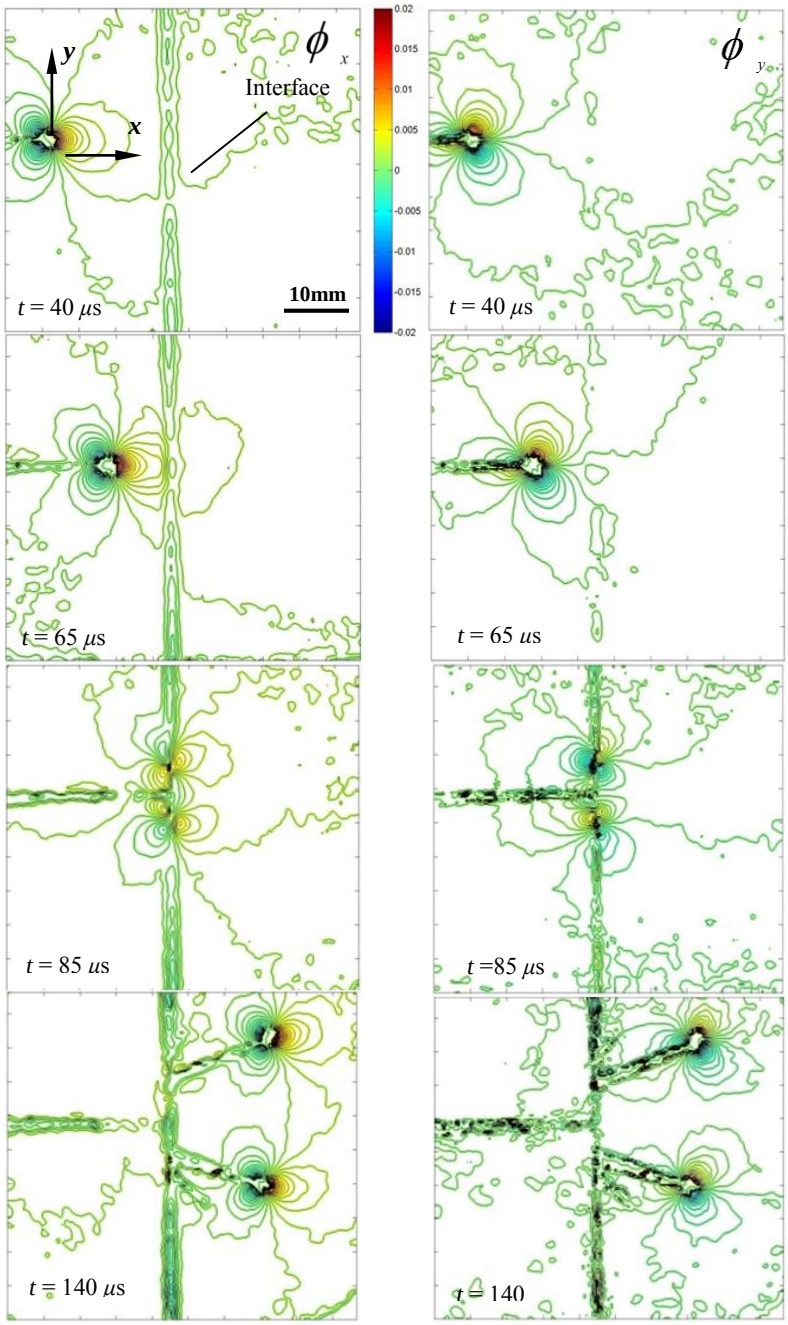

Figure 4.16: Angular deflection contour plots (contour interval = 8×10^{-4} rad), ϕ_x on the left and ϕ_y on the right, proportional to stress-gradients in the *x*- and *y*-directions for a bi-layered specimen with 'weak' interface.

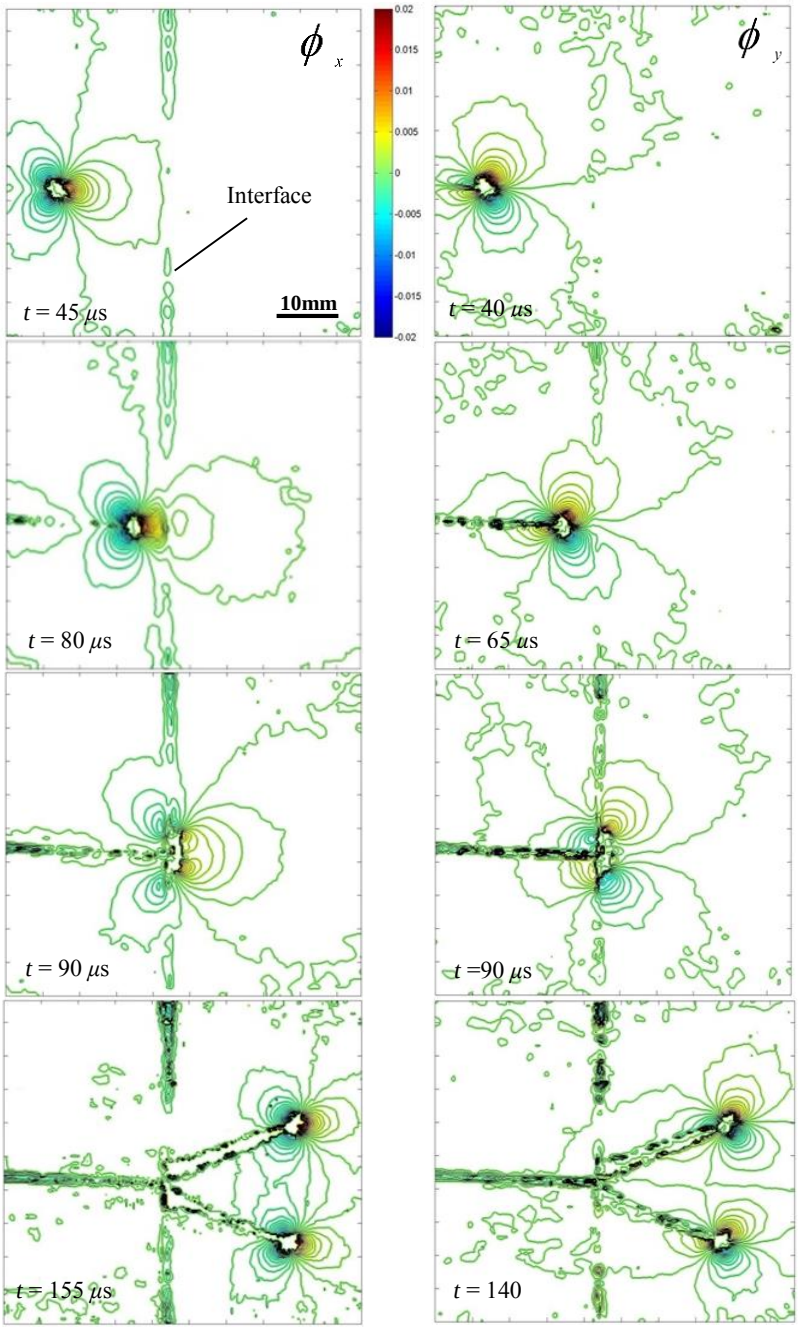

Figure 4.17: Angular deflection contour plots (contour interval = $4\text{x}10^{-4}$ rad) ϕ_x on the left and ϕ_y on the right, proportional to stress-gradients in the *x*- and *y*-directions for a bi-layered specimen with 'strong' interface.

Figure 4.16 shows angular deflection contours in a layered material with a 'weak' interface. Initially the crack travels self-similarly in layer-I as in the monolithic specimen. When it approaches the interface, a perturbation in the lobes ahead of the crack-tip for ϕ_x contours are evident while no significant perturbation is observed in the corresponding ϕ_y contours. Later it can be seen that the interface causes the crack to branch into two symmetric (with respect to the *x*-direction) daughter cracks propagating along the interface in mixed-mode condition as evident from asymmetric (relative to crack growth direction) tri-lobed structures typical of crack-tip stress gradient fields [59] [107]. Subsequently, two daughter cracks emerge from the interface into layer-II and propagate nearly symmetrically, again under mixed-mode conditions. Interaction between these two daughter cracks can also be observed as some of the contours of the upper branch are linked with those of the lower branch.

The same distinct features at various time instants can be observed in the angular deflection contours for the specimen with a 'strong' interface in Fig. 4.17. Major differences here include the extent of crack growth along the interface and angle of emergence of the two daughter cracks into layer-II.

4.7 Crack growth histories

Figures 4.18(a) and (b) show the plots of crack length and velocity histories, respectively, for all the three configurations. It should be noted that $t = 0$ μs represents the time at which the crack initiates at the original notch tip. Five distinct regions in the velocity histories can be seen for bilayer specimens relative to the monolithic counterpart.

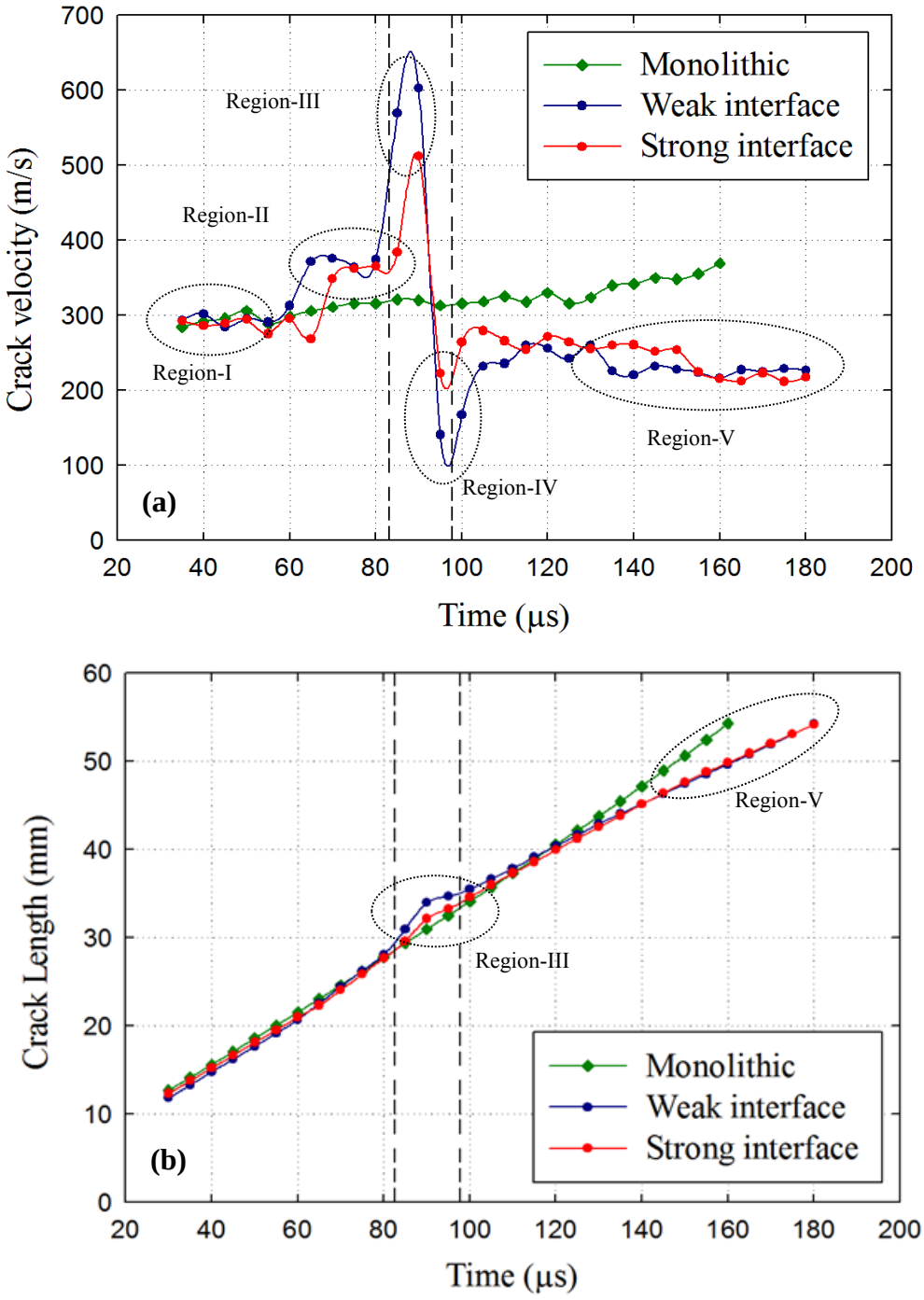

Figure 4.18: Crack growth histories: (a) Crack velocity histories and (b) Crack length histories, for specimens with 'strong' and 'weak' interfaces and a monolithic specimen. The region between the vertical broken lines qualitatively represents the interface vicinity.

A pair of vertical broken lines is used to *qualitatively* demarcate the time instants at which the crack-tip is in the interface vicinity. In region-I, following crack initiation, a constant crack velocity trend for propagation in layer–I under mode-I conditions can be seen. The crack velocities of specimens with interfaces are similar to that of the monolithic specimen in this region. In region-II, a step increase in crack velocity for the two bilayer cases is observed as the crack-tip approaches the interface. This suggests an increase in crack-tip driving force as stress waves reflect off the interface, communicating to the crack-tip the presence of a region of weakness (relative to the monolithic material) ahead. In region-III, a rapid increase in crack velocity (and crack length) is observed as the crack propagates along the interface in the form of *two* trapped interfacial crack-tips. The computed crack velocity in case of a specimen with a 'weak' interface is generally higher when compared to the 'strong' counterpart. This is in agreement with the higher travel distance for the crack along the interface in case of a specimen with the 'weak' interface as compared to the 'strong' interface. In region-IV a rapid deceleration of the two daughter cracks[1] can be seen as the crack is about to exit the interface and penetrate layer-II. This is because of the resistance offered by layer-II for the crack propagation as compared to the interface. It can be seen that for a specimen with a 'weak' interface, the dip in crack velocity is greater when compared to the one with a 'strong' interface, which is to be expected. Region-V shows crack velocities (and crack length) in layer-II for bilayer specimens to be much lower relative to the monolithic counterpart.

[1] Note that data for only one of the two cracks are shown in Fig. 4.18.

4.8 SIF, strain energy release rate, and mode-mixity histories

The stress intensity factor histories for all the configurations evaluated from the angular deflection fields and the least-squares analysis discussed earlier is plotted in Fig. 4.19. The set of vertical broken lines qualitatively suggests the interface 'vicinity.' Figure 19(a) shows SIF histories of a specimen with a 'weak' interface relative to a monolithic specimen. It can be seen that K_I for a monolithic specimen is nearly constant and K_{II} is oscillatory about zero for the duration of crack growth in the observation window. This behavior is to be expected since crack growth occurred in the monolithic case predominantly under mode-I condition. (It should be noted that oscillations seen in the K_{II} values about zero provides information on the accuracy of the least-squares analysis undertaken in this work.) Initially, K_I for the specimen with a weak interface is same as that for the monolithic case but as the crack approaches the interface, K_I increases gradually to a peak value of 1.62 MPa√m whereas K_{II} remains nearly zero until it reaches the interface. Further, as the crack enters the interface, K_I drops while K_{II} increases rapidly suggesting a significant increase in the shear component and hence the mode-mixity as the trapped cracks propagates along the interface. When cracks penetrate layer-II, K_I increases to values above that in the monolithic configuration before decreasing gradually whereas K_{II} attains a peak value of 0.41 MPa√m just as it emerges from the interface before dropping off precipitously. (*It is worth noting that the values of* K_I *and*

K_{II} *in the interface and layer-II are shown for only one crack-tip* (*upper branch*) *in these plots and in reality there are two daughter cracks to consider*.)

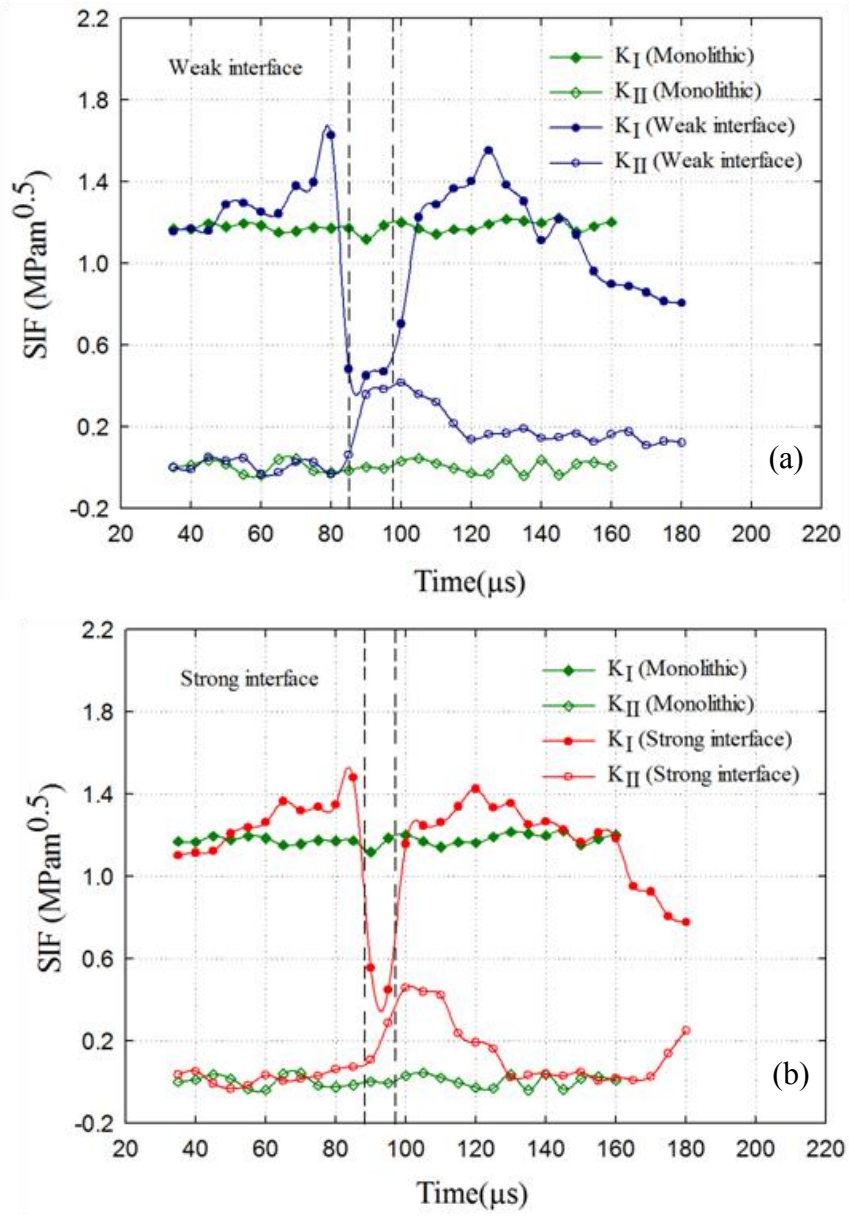

Figure 4.19: Stress intensity factor (SIF) histories for a bi-layered specimen with (a) weak interface and (b) strong interface and their comparison with those for a monolithic counterpart.

It can be seen that the final K_I for the specimen with a 'weak' interface is much lower than that of the monolithic case whereas K_{II} is marginally higher suggesting a reduction in the final crack driving force. Figure 4.19(b) shows the SIF histories of a specimen with a 'strong' interface relative to those of the monolithic counterpart. The sample with a 'strong' interface also shows similar distinct characteristics; a peak K_I value of 1.51 MPa√m and a peak K_{II} of 0.49 MPa√m. Final K_I values towards the end of the observation window (with a substantially lower K_{II}) for bilayer specimens are much lower relative to the monolithic case demonstrating that the introduction of an interface reduces the stress intensity factors significantly as more energy is expended in the formation of two daughter cracks and new surfaces. It can also be seen that, throughout crack propagation, K_I and K_{II} for the specimen with a 'weak' interface is higher than the specimen with a 'strong' interface suggesting that more energy was dissipated in the former.

The strain energy release rate (G) and mode-mixity (ψ) histories evaluated using K_I and K_{II} data are shown in Fig. 4.20. Similar to the earlier discussion on SIFs, the same distinct features can be seen in the G histories. The final G for specimens with an interface (both 'strong' and 'weak' cases) is much lower (~130 N-m^{-1}) than that of the monolithic counterpart (~280 N-m^{-1}), shown in Fig. 20(a1) and (b1), which is about 54% reduction without altering the weight to the structure. (*As noted earlier, the values of G in case of bilayer specimens, along the interface and in layer-II, are shown only for one crack-tip, the upper branch in these plots, and in reality there are two daughter cracks to consider.*)

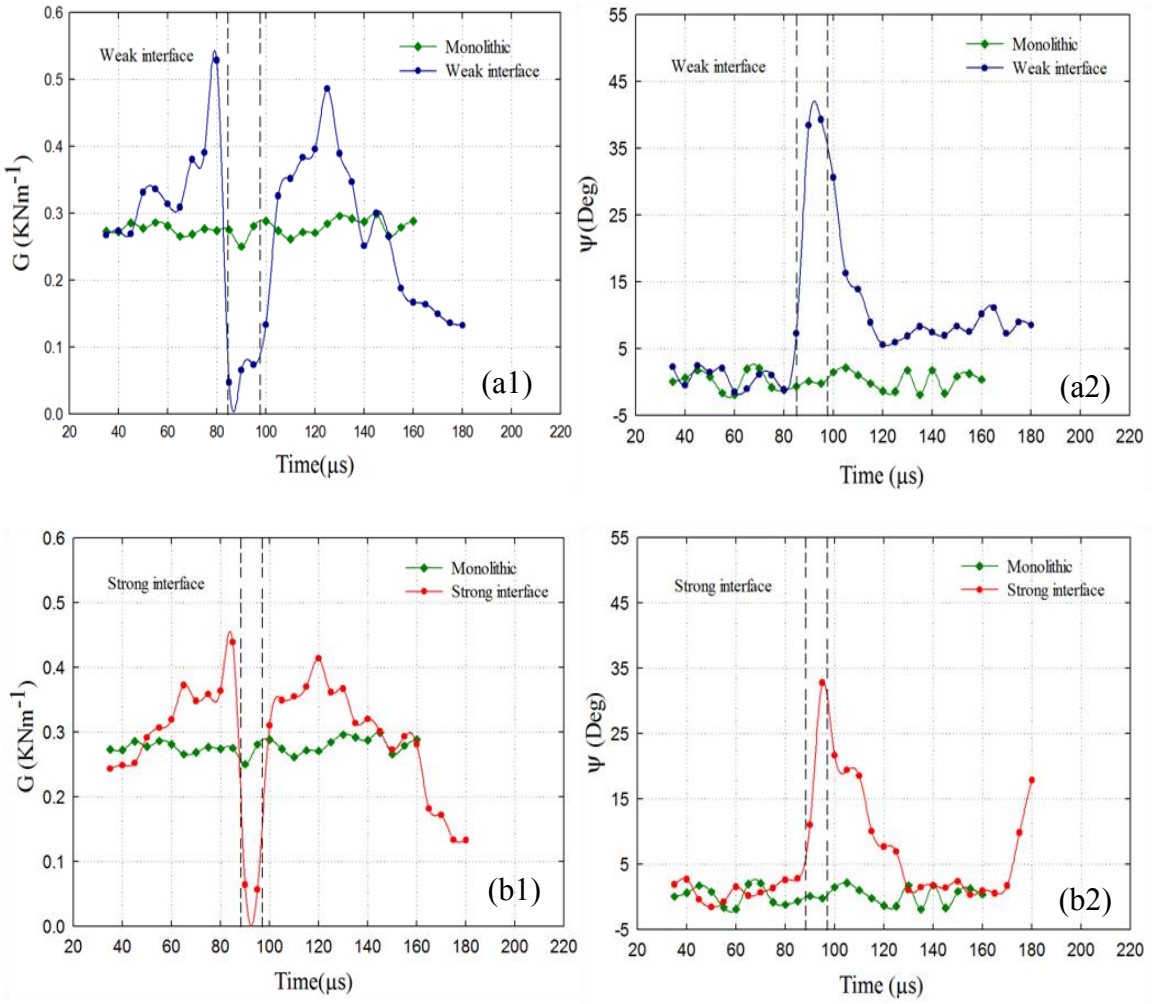

Figure 4.20: Strain energy release rate (G) and mode-mixity (ψ) histories for a bi-layered -specimen with (a) weak interface and (b) strong interface and their comparison with those of a monolithic counterpart.

Referring to the mode-mixity plots, the specimen with a 'weak' interface compared to the monolithic specimen, shown in Fig. 4.20(a2), an oscillatory mode-mixity about zero can be seen until the crack reaches the interface vicinity. As the crack enters the interface, the mode-mixity increases rapidly to a maximum value of ~39^0. Subsequently, as the crack emerges from the interface the mode-mixity decrease gradually to ~8^0. In case of a specimen with a 'strong' interface, shown in Fig. 4.20(b2), similar features can be seen as

well. The peak mode-mixity of ~33^0 is observed when the crack travels along the interface. Further, as the crack penetrates layer-II, the mode-mixity gradually falls and as it travels further in layer-II, the mode-mixity approaches zero. (Towards the end of observation window, the mode-mixity increases, possibly a local experimental aberration.) It is observed that the mode-mixity during crack penetration into layer-II is higher (~21^0) in case of specimen with a 'strong' interface when compared to that with a 'weak' interface (~16^0). This is consistent with the earlier observation of higher angle of penetration into layer-II for the 'strong' interface case when compared to its 'weak' counterpart (see Figs. 4.20(a2) and (b2)).

4.9 Interaction between daughter cracks

As observed in the earlier sections, there are two successful daughter cracks in layer-II for both types of bilayer specimens. Also, in all the earlier plots, the SIF histories for one of the daughter cracks (top branch) were presented. In this section, SIF histories for both the top and the bottom cracks are discussed. Figs. 4.21(a) and (b) show K_I and K_{II} histories, respectively, for both the daughter cracks. The crack-tip fields show interaction with each other as noted earlier (Figs. 4.16-4.17) and the resulting intertwined pattern of K_I histories is evident in Fig. 4.21(a). Interestingly, K_I of the top crack is higher than that for the bottom crack at an instant whereas the values reverse in the next. This behavior can be observed rather consistently throughout the observation window in layer-II and are highlighted by a pair of opposing arrows in Fig. 4.21(a) at a few time instants.

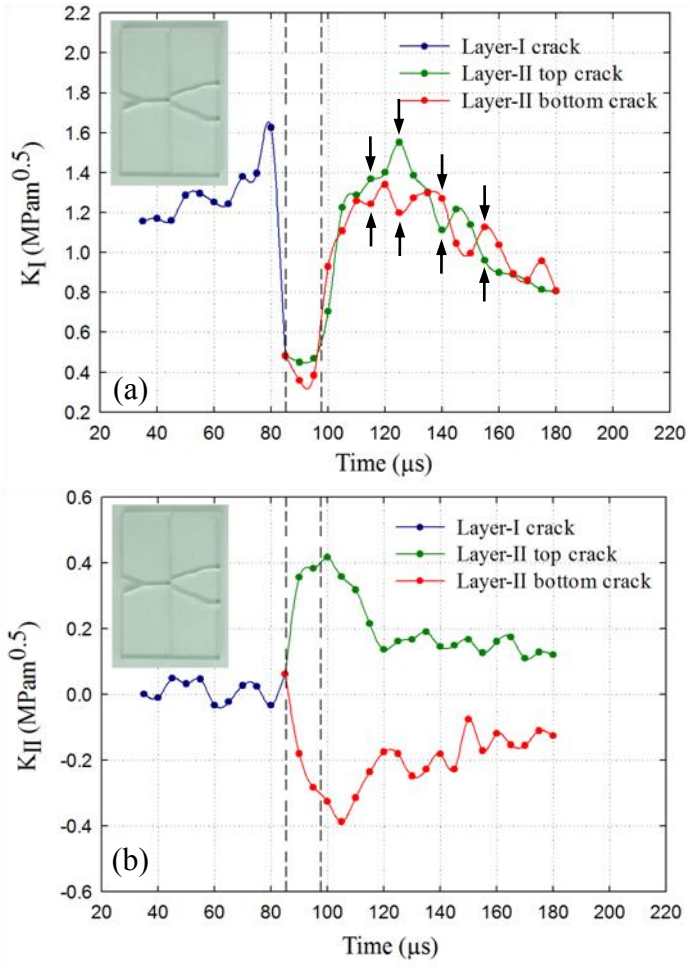

Figure 4.21: Interaction between branched cracks: (a) Mode-I, and (b) mode-II SIF histories for the two daughter cracks in layer-II for bi-layered specimen with a weak interface. Out-of-phase oscillations in K_I values for the two daughter cracks are evident during propagation in layer-II.

That is, when one tip is experiencing a high value, the other is at a low value. At the same time instants, the K_{II} values (Fig. 4.21(b)) for the two daughter cracks are comparable in magnitudes but are opposite in sign. That is, the upper crack is experiencing a positive shear and a positive K_{II} whereas the lower is experiencing a negative shear and a negative K_{II}.

4.10 Experiment repeatability

Multiple experiments were conducted for monolithic and bilayer configurations (both ‘weak’ and ‘strong’ interface cases) to ensure repeatability in terms of dynamic fracture behavior as well as fracture parameters. Fig. 4.22(a) shows photographs of two fractured samples of monolithic specimen whereas Fig. 4.22(b) and (c) show two fractured samples of specimens with ‘strong’ and ‘weak’ interface, respectively. A high degree of reproducibility in crack paths throughout the fracture event (well past the interface) is clearly evident in Figs. 4.22(b) and (c). Figs. 4.23(a) and (b) show SIF histories for two different samples with a ‘weak’ and a ‘strong’ interface, respectively. Again, repeatability can be readily seen in the measured values of SIF histories also. That is, the SIF histories of multiple samples closely agree with each other before the crack reaches the interface. After the crack penetrates the second layer there are only marginal differences between the two SIF histories. Despite the highly transient nature of the problem, and the possibility of potential variations in material and interface characteristics, a rather high degree of reproducibility is evident.

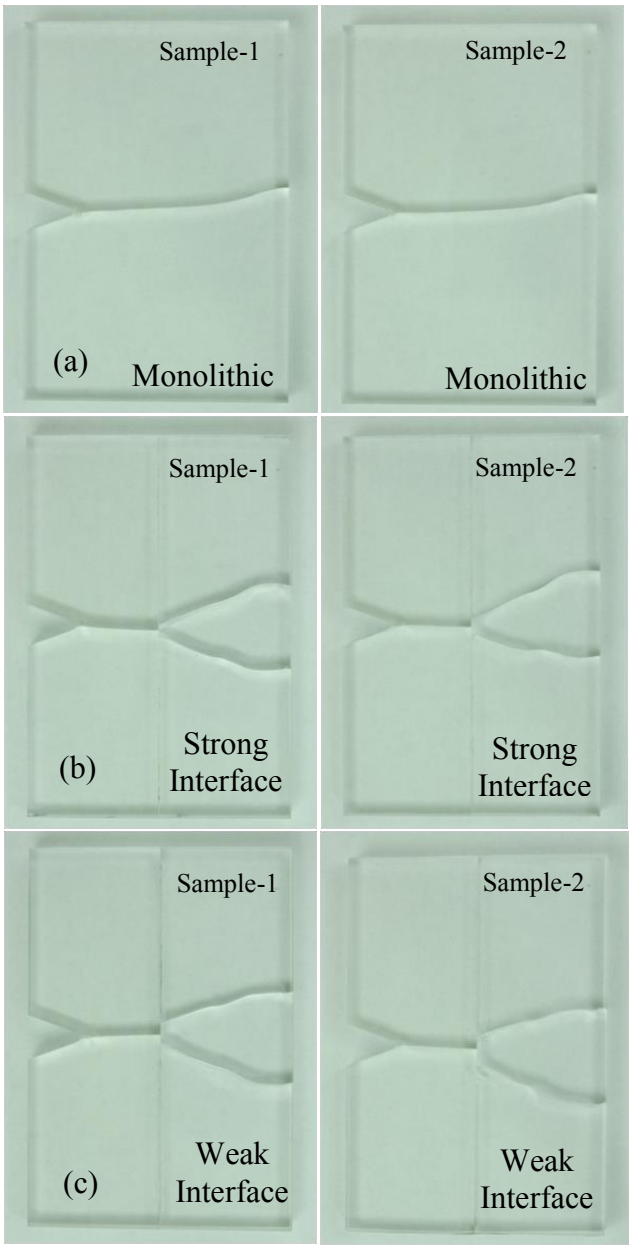

Figure 4.22: Multiple fractured samples of each configuration.

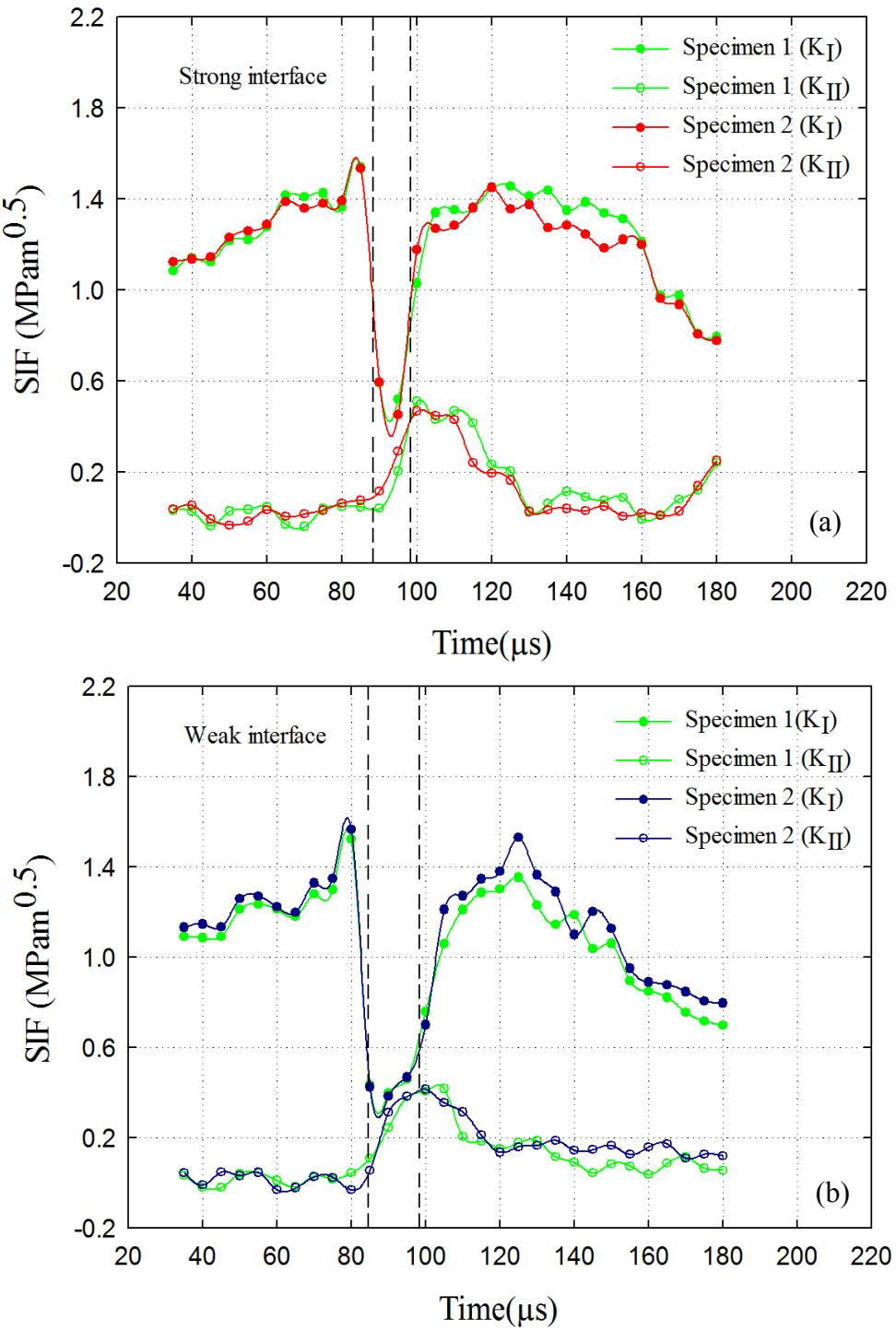

Figure 4.23: SIF histories for multiple fractured samples of each configuration. The vertical broken lines denote the crack-tip vicinity.

Chapter 5

MECHANICS OF CRACK PENETRATION VS. BRANCHING IN BILAYERS

In this chapter, the effect of interface location within the same external geometry of PMMA bilayers is studied. The dynamic crack-interface interactions and the related mechanics of crack penetration vs. branching at a weak interface (relative to the substrates) are described. The material preparation, various specimen configurations and loading setup are described first. The experimental results namely the crack-tip velocity and stress intensity factor histories are reported next. An empirical observation based on measured crack-tip parameters for crack penetration and branching is also presented.

5.1 Specimen preparation and geometry

Two cast PMMA plates 170 mm tall, 8.6 mm thick and of different widths were joined along 170 mm × 8.6 mm faces using an acrylic adhesive to form bilayer specimens. The bonding surfaces were sanded using 400 grit sandpaper and then cleaned to remove any residue before joining. The cured specimens were machined to their final dimensions of 150 mm × 100 mm × 8.6 mm (see Fig. 5.1). The adhesive used was Weldon 16, a transparent acrylic adhesive, to produce plates that were elastically homogeneous but had a discrete plane of weakness (see Chapter 4 for details). An interface thickness of 100 μm was maintained in all specimens using shims (spacers) while bonding the plates. The crack initiation toughness for the joint was ~50% of the virgin PMMA. A 40º V-notch was

machined at the mid-span of the first layer. The notch was extended into the plate by 2 mm using a 300 μm thick diamond impregnated circular saw resulting in a total notch length '*a*' of 21 mm. The extended notch tip was subsequently sharpened by scoring it with a razor blade. The bilayer specimens had an interface at four different distances (designated by '*d*' in Fig. 5.1), 7 mm, 17 mm, 28 mm and 42 mm from the sharpened tip. These correspond to *d*/*a* ratios of 0.33, 0.80, 1.33, and 2.0, respectively.

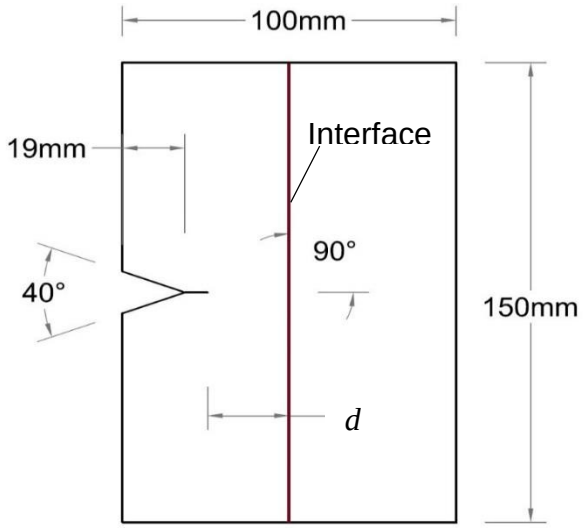

Figure 5.1: Specimen configurations studied. Values of *d* used are 7 mm, 17 mm, 28 mm and 42 mm (or, *d*/*a* ratios of 0.33, 0.80, 1.33, and 2.0, respectively).

5.2 Experimental details

The schematic of the experimental setup used is similar to the one in Chapter 3 (see Fig. 3.7), except for the wedge shaped impactor used here as in Chapter 4. The speckle images were acquired using a Cordin-550 ultrahigh-speed digital camera with a sensor resolution of 1000 × 1000 pixels and 32 independent CCD sensors positioned radially around a five-facet rotating mirror. The imaging system also included two high-energy

flash lamps producing broad-band white light illumination. Experimental parameters such as the trigger delay, flash duration, framing rate, CCD gain, and data storage were controlled using a computer connected to the camera. A 28-300 mm focal length macro zoom lens mounted on an adjustable bellows was used for imaging the dynamic event. Further, the lens aperture was kept open as widely as possible (numerical aperture $F^{\#}5.6$) to achieve a good exposure with minimum electronic gain setting during photography. The specimen was at a distance of approximately 850 mm in front of the camera. (Each speckle covered approximately 4-5 pixels; or, the scale factor was 22-24 pixels/mm were used.) The specimen was placed on an adjustable platform with a 2 mm thick strip of putty pressed on the top and bottom edges of the specimen. The putty strips helped to achieve symmetric, approximately free surface boundary conditions at the top and bottom edges. A target plate decorated with random black and white speckles was placed behind the specimen at a distance $\Delta = 29.3$ mm from the mid-plane of the specimen. A pair of heavy dots (Fig. 5.2) was marked on the target plate to help relate the dimension on the image to the actual specimen/target dimensions during image analysis. The region of interest in this study was in the neighborhood of the interface. Accordingly, the camera was focused on a 45 mm × 45 mm square region on either side of the (vertical) interface. Prior to loading, a set of 32 images of the speckles were recorded in the undeformed state at 200,000 frames per second. (The choice of the framing rate was to balance information gathering over the entire event covering crack growth in layer-I, along the interface, and in layer-II with good spatial as well as temporal detail, within the capabilities of the camera). Sufficient care was exercised to achieve an approximately Gaussian distribution of gray scales for each image, typically

in the mid-range of 0-255 (8 bit) gray scale by adjusting the flash lamps. Next, without altering any of the camera settings, the striker was launched towards the long-bar at a velocity of ~14 m/s.

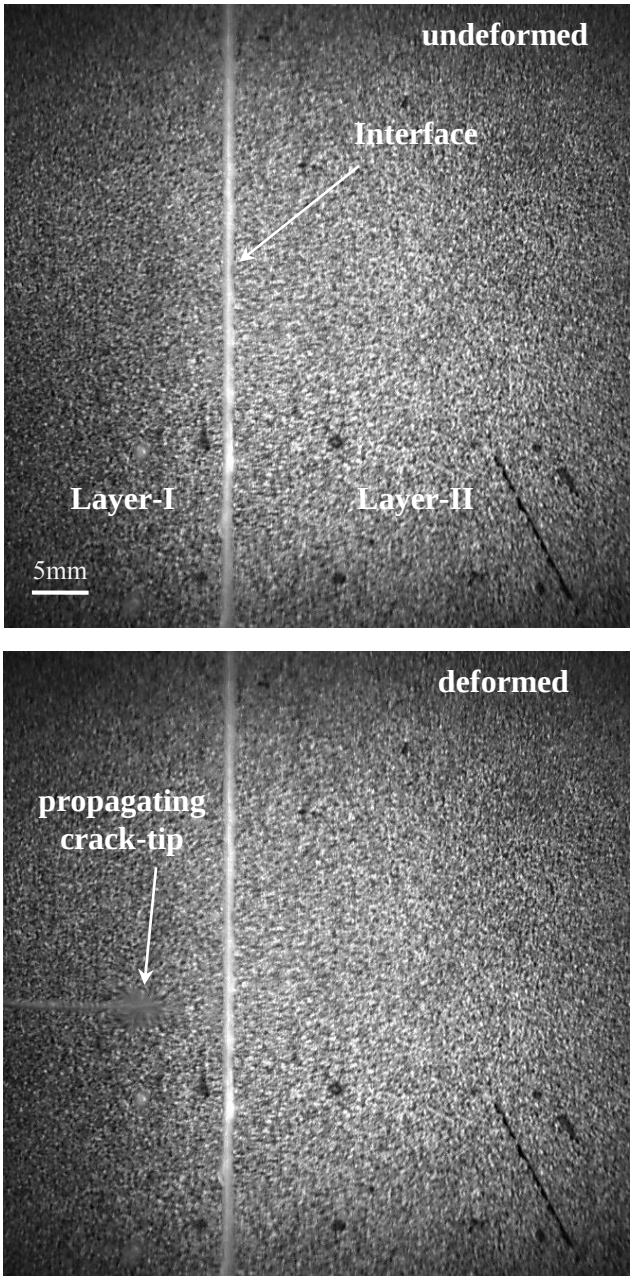

Figure 5.2: Speckle images in the undeformed (top) and deformed (bottom) states recorded by the high-speed camera though a PMMA bilayer.

When the striker contacted the long-bar, a compressive stress wave was set-off in the long-bar, which propagated over its length before loading the specimen along the two inclined faces of the V-notch. The duration of the loading phase of the stress pulse generated was ~120 μs. When the striker contacted the long-bar, a trigger signal was also produced. This started the camera to record a second set of 32 images in the deformed state at the same framing rate. A trigger delay, different for each interface configuration, was used to adjust the time window due to the fixed number of frames (32) that could be recorded by the camera. Thus, a total of 32 pairs of images in the deformed and undeformed (reference) states were recorded at 5 μs intervals between successive images. Two representative speckle images in the region of interest, one in the undeformed state and the other in the deformed state are shown in Fig. 5.2 for a layered specimen configuration. It can be seen that the speckles are noticeably distorted in the vicinity of the propagating crack-tip (in the deformed image) whereas they are largely unaffected in the far-field. The interface is evident as a translucent vertical line at the center of each image. The corresponding two images for each sensor were paired from the undeformed and deformed sets and each of these 32 matched pairs was correlated separately. The image analysis was performed and crack-tip parameters were extracted similar to that described in Chapter 4. Since mixed-mode crack growth occurred in some cases, the SIFs were used to evaluate the *effective* SIF (K_{eff}) and mode-mixity (ψ) using,

$$K_{eff}(t) = \sqrt{K_I^2(t) + K_{II}^2(t)} \text{ , and } \psi(t) = \tan^{-1}\left(\frac{K_{II}(t)}{K_I(t)}\right) \tag{5.1}$$

5.3 Crack path and deformation histories

Photographs of four fractured samples, one from each configuration (interface at d = 7 mm, 17 mm, 28 mm, and 42 mm from the initial tip), are shown in Fig. 5.3. The stress wave loading occurred near the left edge of the specimen on the faces of the V-notch and the crack propagation direction was from left to right, as shown by the arrowhead. In each case it is evident that the crack propagated self-similarly until it reached the interface vicinity. The differences in crack paths occurred subsequently.

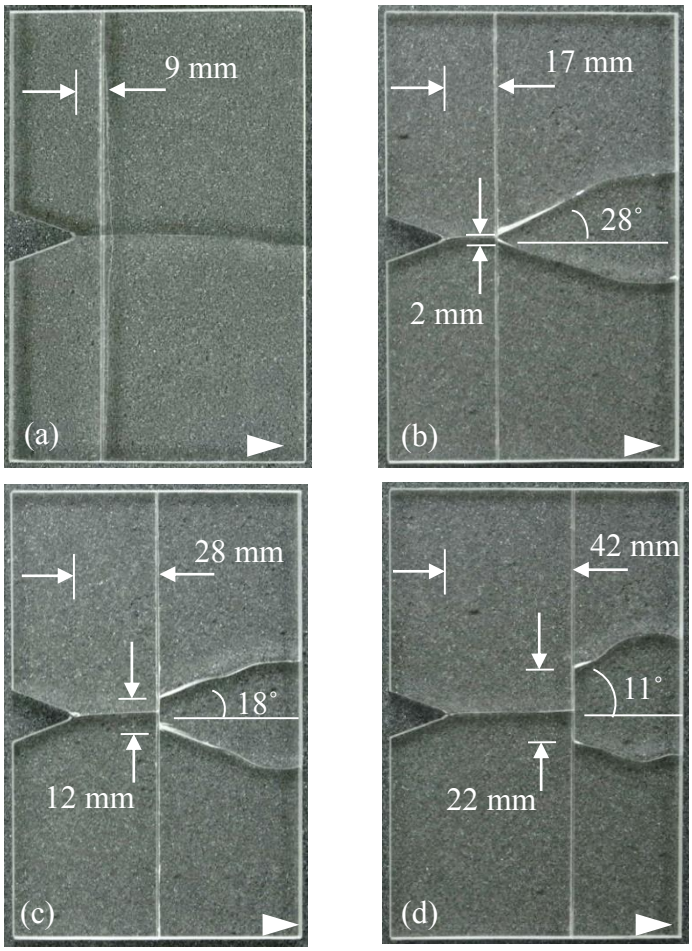

Figure 5.3: Photographs of fractured specimens showing crack path selection in d = (a) 9 mm, (b) 17mm, (c) 28 mm, and (d) 42 mm configurations, respectively. Arrowheads indicate crack growth direction.

For all configurations except the one where the interface was the nearest to the initial tip, the mode-I crack in the first layer arrived at the interface, lodged into the interface, bifurcated into two interface crack-tips, one propagated upwards and the other downwards, and then both penetrated the second layer simultaneously after some amount of interfacial crack growth. The extent of interfacial crack growth and the angle of emergence of the crack into the second layer varied with the position of the interface from the initial crack-tip. Fig. 5.3(a) shows the crack path for the d = 7 mm configuration and Figs. 5.3(b)-(d) for d = 17 mm, 28 mm, and 42 mm configurations, respectively. For an interface location of d = 7 mm, the mode-I crack propagated towards the interface and then grew past the interface into the second layer in a self-similar fashion without any visible branching until it reached the final third of the specimen. Beyond that, it modestly deviated from its initial path due to a loss of in-plane constraint [111] as it approached the free edge. In Figs. 5.3(b)-(d), more nuanced fracture patterns involving mixed-mode interfacial crack growth and crack penetration into layer–II are evident. That is, the location of the interface dictated the crack path selection and the fracture behavior. This clearly shows that the introduction of the interface does not always produce crack branching but the location of the interface within the given geometry and the associated differences in crack-tip parameters determine the creation of new surfaces. Further, in d = 17 mm, 28 mm, and 42 mm configurations, the trapped interface cracks traveled over distances of approximately 2 mm, 12 mm, 16 mm, respectively, along the interface, a monotonic increase, before emerging into the second layer as two daughter cracks at angles ±28°, ±18°, ±11° with respect to the initial tip direction, a monotonic decrease.

Multiple experiments were conducted for all the four configurations to ensure repeatability in terms of dynamic fracture behavior as well as the measured fracture parameters. Figs. 5.4(a)-(d) shows photographs of two fractured samples each for all the four configurations. A high degree of reproducibility in terms of crack paths during the fracture event is clearly evident from these photographs. (The repeatability of fracture parameters for such PMMA bilayers has already been discussed in Chapter 4) Despite the highly transient nature of the problem, and potential variations in material and interface characteristics, a rather high degree of reproducibility of results is evident.

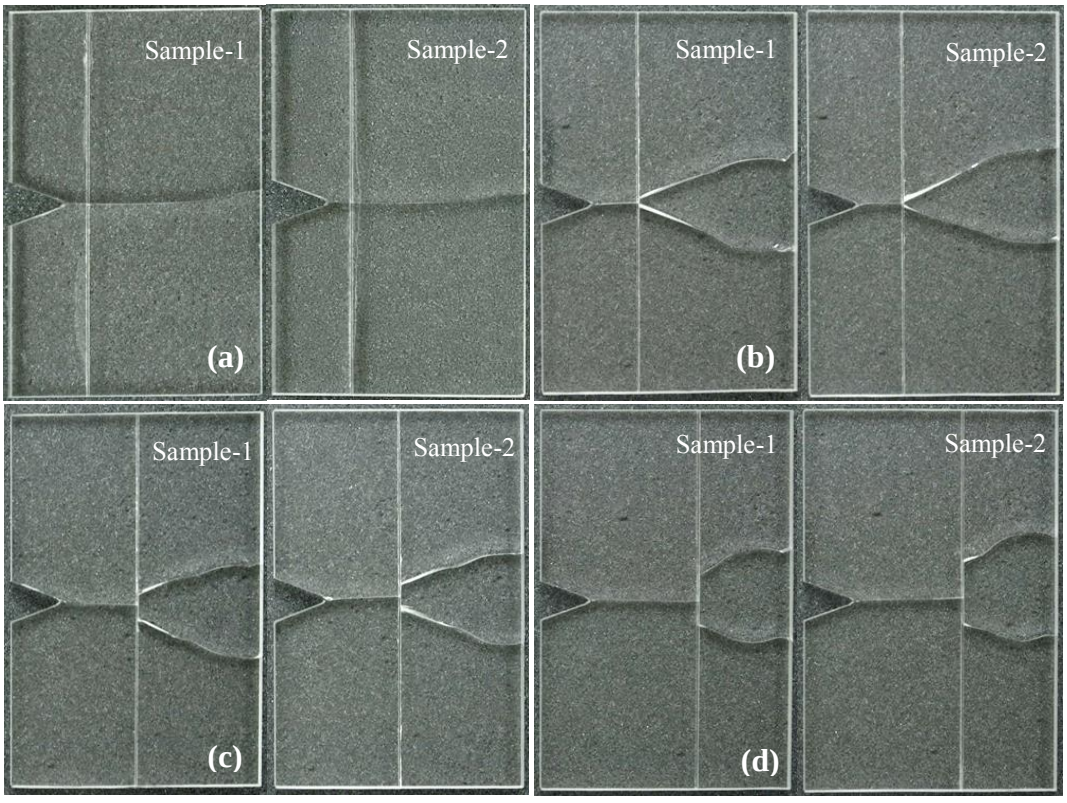

Figure 5.4: Multiple fractured samples of each configuration, namely (a) d = 7 mm, (b) d = 17 mm, (c) d = 28 mm, and (d) d = 42 mm, showing repeatability of the experiment in terms of crack path and fracture behavior.

Plots of measured angular deflection contours ϕ_x and ϕ_y proportional to orthogonal stress gradients $\left(\sigma_x + \sigma_y\right)_{,x}$ and $\left(\sigma_x + \sigma_y\right)_{,y}$ (the comma notation denotes derivatives with respect to the subscript) obtained from the image correlation for two select configurations namely, d = 7 mm and 17 mm are shown in Figs. 5.5 and 5.6, respectively. Further, note that the plots presented are only for three select time instants for the sake of brevity. (The angular deflection contours, the contour levels and the scale bar are shown in the first plot in each set and are applicable to the other plots as well.) In these t = 0 μs represents the time at which the crack initiated at the original notch tip[2]. In each figure, sets (a) and (b) correspond to contours of ϕ_x and ϕ_y, respectively.

Fig. 5.5 shows angular deflection contours for d = 7 mm configuration. The crack followed a nearly straight path during the time window of interest, both in layer-I and -II without detectable propagation along the interface. This behavior is similar to the monolithic specimen described in Chapter 4 and suggests that there was little effect of the interface on the crack trajectory. The overall size of the contours changed during crack growth implying a variation of stress intensity factors during the window of observation. (It should also be noted that ϕ_x contours are symmetric in shape and magnitude with respect to the growing crack path whereas ϕ_y contours are only symmetric in shape but antisymmetric in magnitude.)

[2] Separate experiments were carried out in which the region of interest was around the initial crack-tip to determine the time at which crack initiated and this data was used to compile the fracture histories of various configurations into a single timeline. Details are suppressed for brevity.

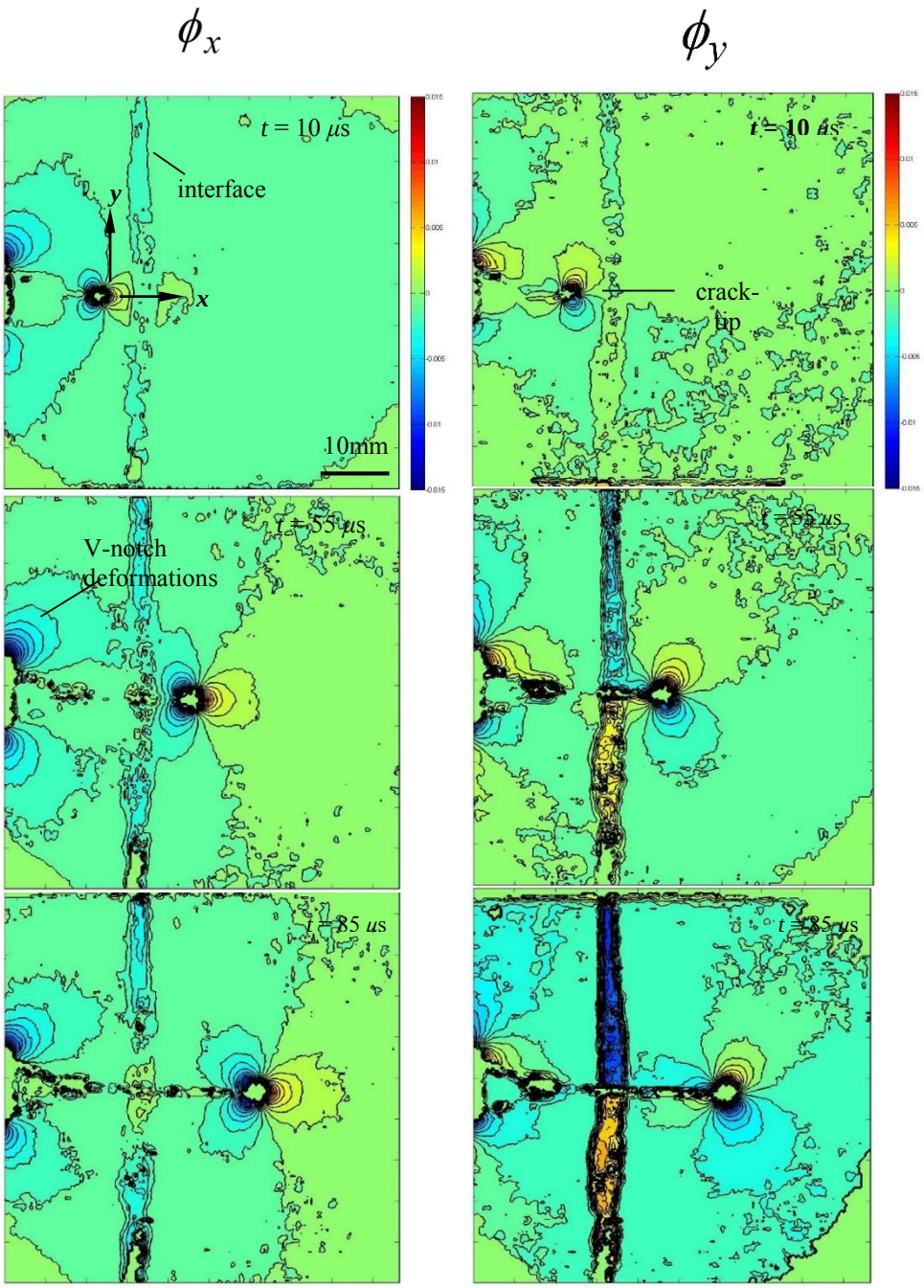

Figure 5.5: Angular deflection contour plots (contour interval = 1×10^{-3} rad) proportional to stress gradients of $\left(\sigma_x+\sigma_y\right)$ in the *x*- and *y*-directions for a d = 7 mm configuration. (Time t = 0 corresponds to crack initiation at the original notch tip.)

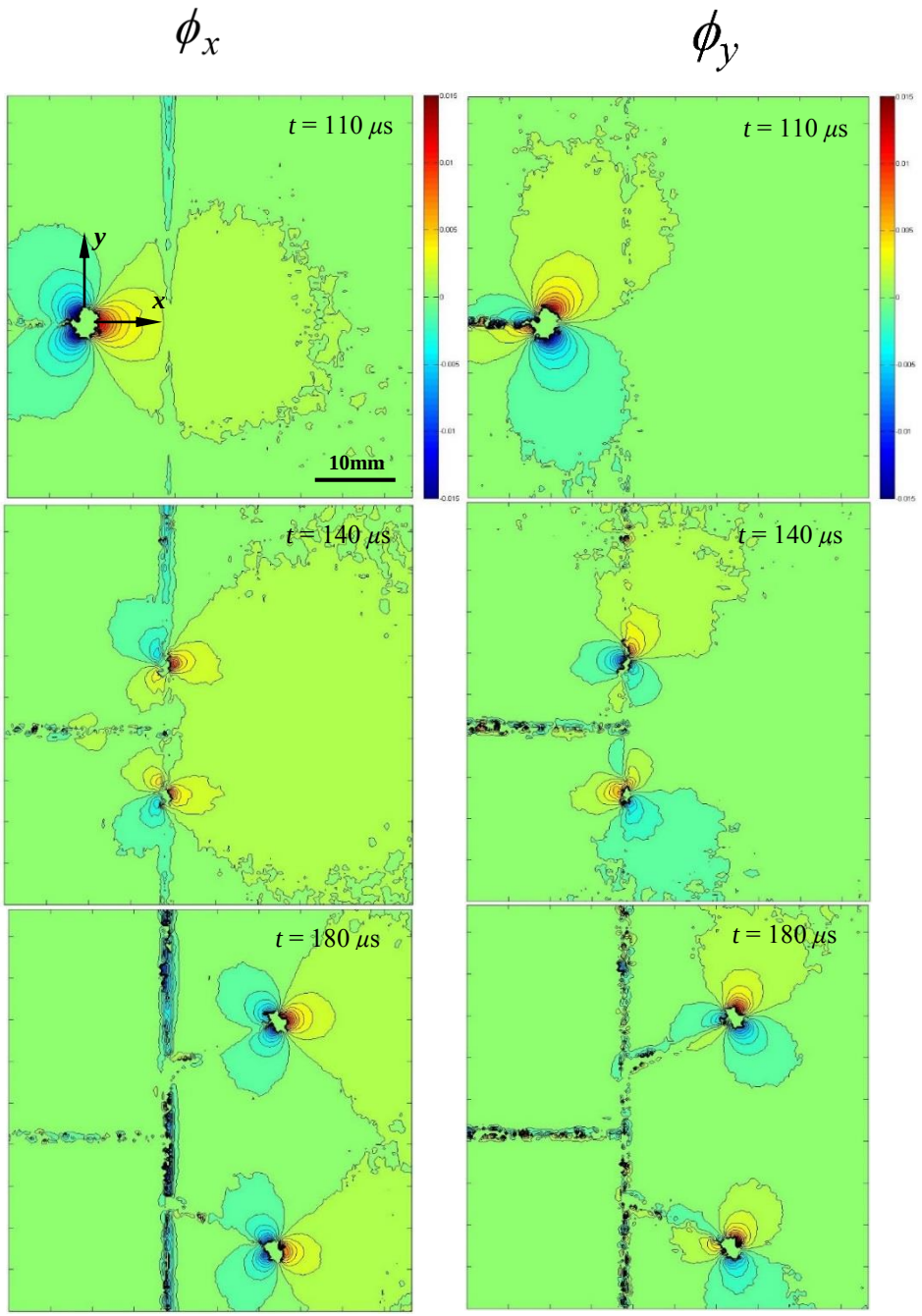

Figure 5.6 : Angular deflection contour plots (contour interval = 1×10^{-3} rad) proportional to stress gradients of $\left(\sigma_x + \sigma_y\right)$ in the *x*- and *y*-directions for a d = 42 mm configuration. (Time t = 0 corresponds to crack initiation at the original notch tip.)

Fig. 5.6 shows angular deflection contours for d = 42 mm configuration. Initially the crack traveled self-similarly in layer-I as in d = 7 mm configuration. When it neared the interface, however, perturbations in the outer contours ahead of the crack-tip for ϕ_x are evident. At a later instant, it can be seen that the crack is propagating along the interface as two globally symmetric (with respect to the initial crack growth or the x-direction) daughter cracks which are about to kink into layer-II. Subsequently, the two daughter cracks emerge from the interface into layer-II and propagate nearly symmetrically, but in mixed-mode condition as evident from asymmetric (relative to crack growth direction), tri-lobed contours typical of crack-tip stress gradient fields [56]. Similar features at various time instants were observed in the angular deflection contours for d = 17 mm and 28 mm configurations as well but are not shown for the sake of brevity. Major differences were the extent of crack growth along the interface and angle of emergence of the two daughter cracks into layer-II.

5.4 Crack velocity histories

Fig. 5.7 shows plots of crack velocity histories for all the four configurations. (Note that these histories correspond to the upper branch of the branched crack configurations; the lower branches show similar history in each case, see section 4.9). It should be noted that t = 0 μs represents the time at which the crack initiated at the original notch tip. The solid-line circle marked on each of these plots represents the value at an instant before the crack enters the interface and the dotted-line circle represents the instant at which the crack

emerges from the interface. (For d = 7 mm, 17 mm, 28 mm, and 42 mm cases[3], the crack velocities upon the arrival at the interface were approximately 265 m/s, 326 m/s, 370 m/s, 441 m/s, respectively.) From the figure it can be seen that the velocity histories for d = 17 mm, 28 mm and 42 mm configurations all follow a similar pattern whereas d = 7 mm configuration has a distinctively different behavior. In the former cases, the crack velocity transitioned from a lower to a higher value as the tip approached the interface. When it entered the interface and transitioned from being a single mode-I crack to bifurcated interfacial cracks, the velocity increased rapidly to a (different) peak value in each case. These peak velocities attained during interfacial propagation increased monotonically with the interface distance d from the initial crack-tip. The peak velocities were approximately 440 m/s, 528 m/s and 824 m/s for d = 17 mm, 28 mm and 42 mm configurations, respectively. Following the rapid increase in velocity, an equally steep drop, generally close to or below the value corresponding to the one at the entrance to the interface occurred. Subsequently, these crack-tips broke out of the interface simultaneously and into layer-II as mixed-mode cracks at speeds lower than the corresponding initial velocities. Further, it can be seen from Fig. 5.7 that the crack velocity for d = 42 mm configuration towards the end of the event (after t ~220 μs) was as low as ~170 m/s. In contrast to these cases, in d = 7 mm configuration it can be observed that the velocity increased when the crack approached the interface but it continued to gain speed rather smoothly as it propagated past the interface without interfacial growth, eventually attaining a maximum

[3] The crack velocity upon arrival at the interface for an interface distance of d = 28 mm and a higher interface toughness (K_{Icr} = 1.02 MPa√m) reported in Section 4.7 was ~365 m/s.

velocity of ~394 m/s before slowing down as it propagated further into layer-II to a final velocity of ~283 m/s during the observation window.

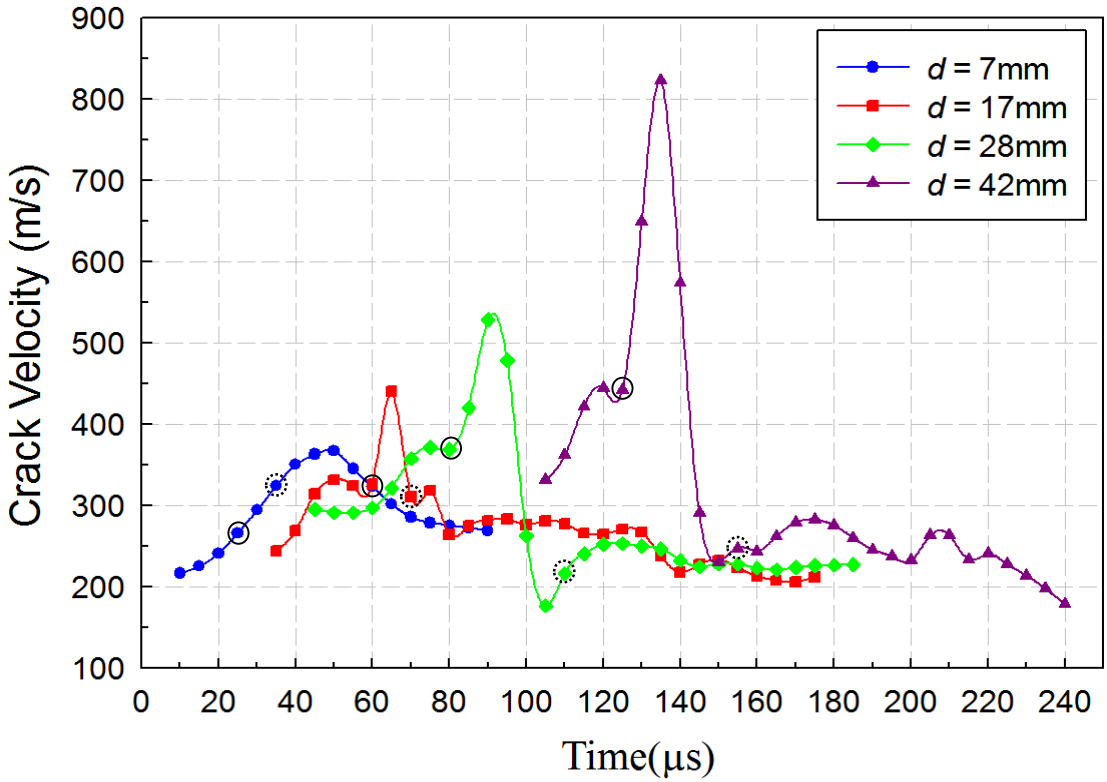

Figure 5.7: Crack velocity histories for all the four configurations investigated. The solid-line circles represent the instant before the crack enters the interface and the dotted-line circles represent the instant at which crack emerges from the interface. (Time $t = 0$ corresponds to crack initiation at the original notch tip.)

5.5 Stress intensity factor histories

The effective SIF histories (K_{eff}) and the corresponding mode-mixity (ψ) variations evaluated from DGS for all configurations are plotted in Fig. 5.8(a) and (b), respectively. Similar to the velocity histories, the effective SIF histories of the three branched configurations, namely, d = 17 mm, 28 mm and 42 mm, showed similarities whereas it was distinctively different in case of the unbranched (d = 7 mm) configuration.

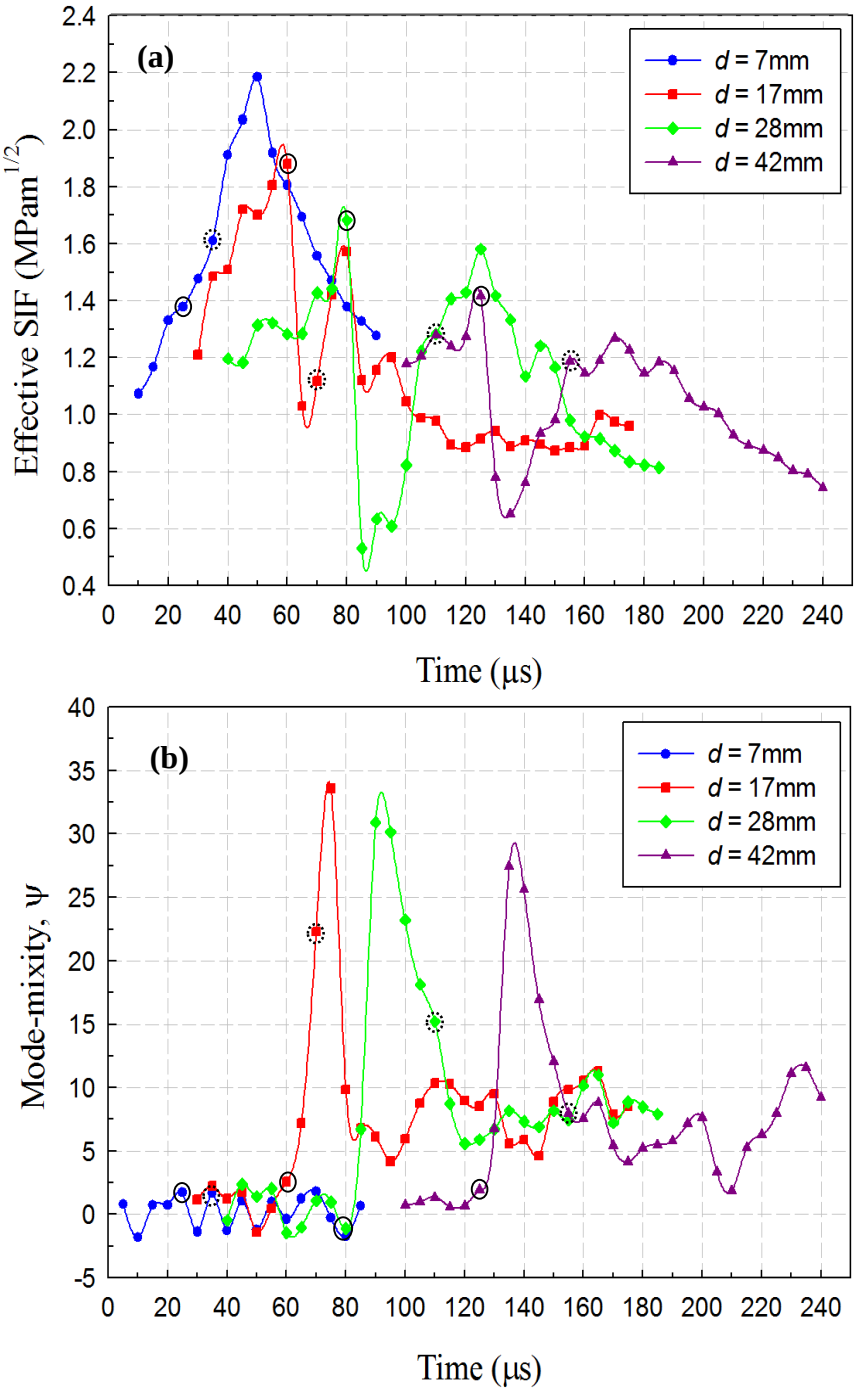

Figure 5.8: Time history of crack-tip parameters (Time t = 0 corresponds to crack initiation at the original notch tip) for all the four configurations investigated: (a) Effective stress intensity factor histories and (b) mode-mixity histories. The solid-line circles represent the instant before the crack enters the interface and the dotted-line circles represent the instant at which crack emerges from the interface; note that there is greater uncertainty with crack kinking out of the interface.

Again, these histories correspond to the upper branch of the bifurcated cracks. In each of these cases, K_{eff} values increased as the mode-I crack approached the interface, reaching a maximum when it was about to enter the interface. As the interfacial debonding and bifurcated crack growth ensued along the interface, a steep drop in K_{eff} occurred in each of these cases. Following a gradual recovery from this low value after the steep drop, the interface crack kinked into layer-II at a K_{eff} value lower than the one at the entrance to the interface. As the mixed-mode crack growth in layer-II continued, a steady drop in the K_{eff} values, sometimes below the nominal crack initiation toughness values of the virgin material, were seen. On the contrary, in the unbranched case (d = 7 mm), K_{eff} increased monotonically as the crack reached the interface, penetrated the interface and then layer-II. The peak value of K_{eff} occurred when the crack-tip had grown past the interface and into layer-II before dropping steadily at later stages.

In all of the three branched crack configurations[4], it can be seen that the peak value of K_{eff} occurred right before the crack entered the interface and there is a successive reduction in the peak value as the interface is moved farther from the initial crack-tip, i.e., 1.88 MPa√m, 1.57 MPa√m and 1.41 MPa√m, respectively (solid-line circles). It can also be seen that there is a decrease in the final value of K_{eff} in layer-II as the interface is positioned farther from the initial crack-tip, i.e., 0.95 MPa√m, 0.81 MPa√m and 0.73 MPa√m, respectively. In the unbranched specimen configuration, the effective SIF

[4] The measured effective SIF for the crack upon its arrival at the interface for an interface distance of d = 28 mm and a higher interface toughness (K_{Icr} = 1.02 MPa√m) reported in Section 4.8 was ~1.48 MPa√m.

increased gradually from 1.07 MPa√m (at ~10 μs after initiation) as it propagated in layer-I. When the crack propagated past the interface into layer-II the effective SIF continued to gradually increase reaching a peak value of 2.38 MPa√m and then dropped back to 1.35 MPa√m at the end of the observation window.

The mode-mixity ψ (Fig. 5.8(b)) for the three branched cases show similar variation whereas the one for the unbranched configuration is nearly zero in the observation window. In the former three cases, as the crack transitioned from layer-I into the interface, a steep increase in ψ occurred due to increased mode-II SIF. The mode-mixity values when the cracks kinked into layer-II vary, the highest being for d = 17 mm configuration and the lowest for d = 42 mm case. This pattern is consistent with the measured angles of crack emergence noted in Fig. 5.3.

5.6 Crack penetration vs. branching mechanism

The observed crack penetration or branching at an interface was examined using measured fracture parameters, namely, the instantaneous crack velocity V and SIF K_I for each of the configurations. This was done by evaluating stresses at a point directly ahead of the propagating crack-tip but situated on the interface. The position of the crack-tip in each image was used to measure the instantaneous distance of the point interest on the interface (r_i). Knowing $\theta = \theta_i = 0$ at the point of interest, the stresses were evaluated using K-dominant expressions [3],

$$\sigma_{ij} = \frac{K_I(t)}{\sqrt{2\pi r_i}} \sum_{ij}(\theta = 0, V), \quad i, j = x, y \tag{5.2}$$

where,

$$\sum_{xx} = \frac{1}{D}\left\{\frac{\left(1+\alpha_S^2\right)\left(1+2\alpha_L^2-\alpha_S^2\right)}{\sqrt{\gamma_L}}\cos\left(\frac{\theta_L}{2}\right) - \frac{4\alpha_S\alpha_L}{\sqrt{\gamma_S}}\cos\left(\frac{\theta_S}{2}\right)\right\}$$

$$\sum_{yy} = -\frac{1}{D}\left\{\frac{\left(1+\alpha_S^2\right)^2}{\sqrt{\gamma_L}}\cos\left(\frac{\theta_L}{2}\right) - \frac{4\alpha_S\alpha_L}{\sqrt{\gamma_S}}\cos\left(\frac{\theta_S}{2}\right)\right\},$$

$$\sum_{xy} = \frac{2\alpha_L\left(1+\alpha_S^2\right)}{D}\left\{\frac{1}{\sqrt{\gamma_L}}\sin\left(\frac{\theta_L}{2}\right) - \frac{1}{\sqrt{\gamma_S}}\sin\left(\frac{\theta_S}{2}\right)\right\},$$

$$D = 4\alpha_S\alpha_L - \left(1+\alpha_S^2\right)^2, \quad \alpha_{S;L} = \sqrt{1-\left(\frac{V}{C_{S;L}}\right)^2},$$

$$\gamma_{S;L} = \sqrt{1-\left(\frac{V\sin\theta}{C_{S;L}}\right)^2}, \quad \tan\theta_{S;L} = \alpha_{S;L}\tan\theta.$$

In the above, $K_I(t)$ is the instantaneous mode-I SIF, C_S and C_L are the shear and longitudinal wave speeds, and V is the crack velocity. Figs. 5.9(a)-(d) show plots of instantaneous normal stress biaxiality $\left(\frac{\sigma_x}{\sigma_y}\right)_i$, $\left(\tau_{\max}^{2D}\right)\left(=\left|\frac{\sigma_x-\sigma_y}{2}\right|_i\right)$, $\left(\tau_{\max}^{3D}\right)\left(=\left|\frac{\sigma_x}{2}\right|_i\right)$ and $\left(\sigma_x\right)_i$ histories at the interface, directly ahead of the moving crack-tip until the crack arrives at the interface. (Note that double subscripts *xx* = *x*, *yy* = *y* are dropped henceforth for simplicity.) All these stresses increase rapidly at the point of interest as the growing crack-tip approaches it (see Figs. 5.9, 5.10(a1)-(a2)).

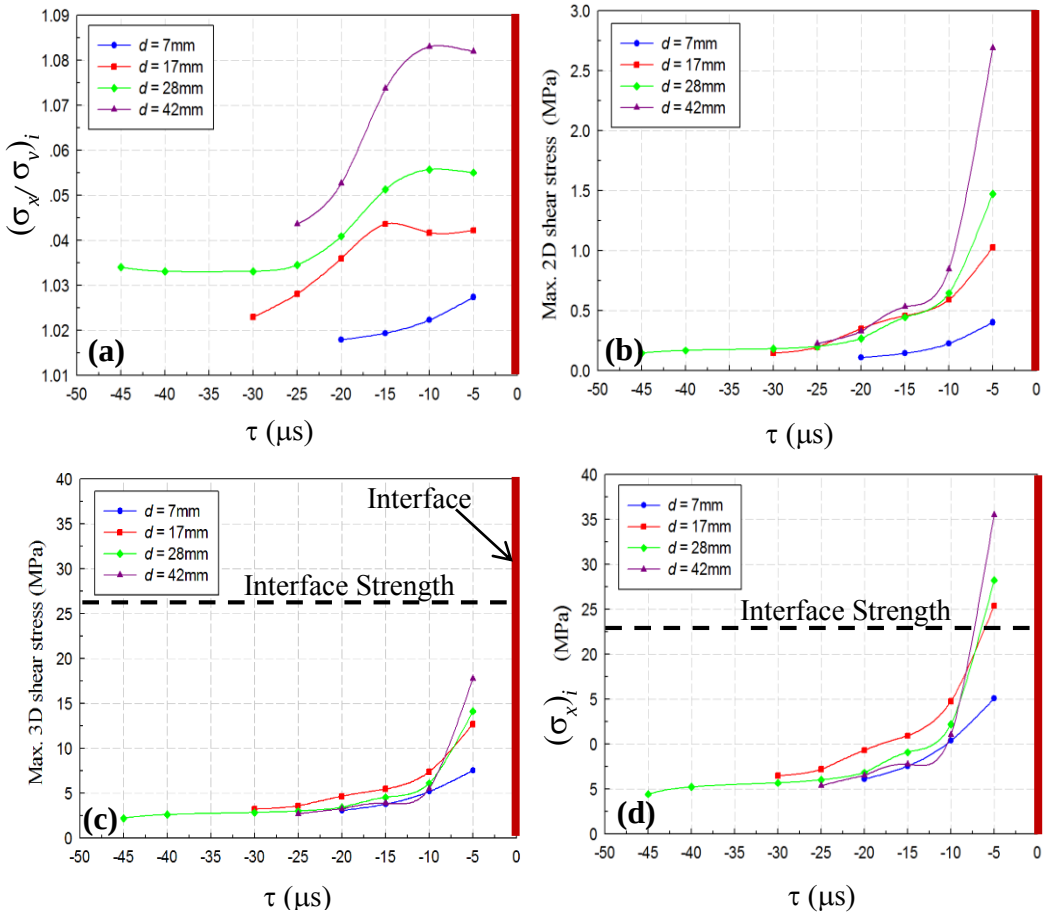

Figure 5.9: Temporal evolution of stresses at a point on the interface directly ahead of the mode-I mother crack: (a) Ratio of in-plane normal stresses, (b) Maximum in-plane shear stresses, (c) Maximum shear stress, and (d) In-plane normal stresses in the crack growth direction. ($\tau = 0$ μs *corresponds to crack reaching the interface indicated by the heavy red line.*)

From these plots one could hypothesize a failure mechanism that involves nucleation of a (micro scale) debond at the point of interest on the interface due to one of these stresses exceeding the strength of the interface (see Fig. 5.10(b1)). Based on the magnitude of $\left(\tau_{\max}^{2D}\right)_i$ relative to $\left(\tau_{\max}^{3D}\right)_i$ (Fig. 5.9(a) and (b)) one could safely assume that $\left(\tau_{\max}^{3D}\right)_i$ or $\left(\sigma_x\right)_i$ likely to cause debond nucleation. By extrapolating these plots, $\left(\tau_{\max}^{3D}\right)_i$

and $(\sigma_x)_i$ values as the crack-tip arrives at the interface were estimated; they were approximately (9, 17, 22 and 30 MPa) and (18, 34, 44 and 60 MPa), respectively, for d = 7 mm, 17 mm, 28 mm, and 42 mm configurations. The strength of the interface was also measured independently using asymmetric four-point-bend [103] and direct tension experiments for the interface, as detailed in Sections 4.2.4 and 4.2.3, respectively.

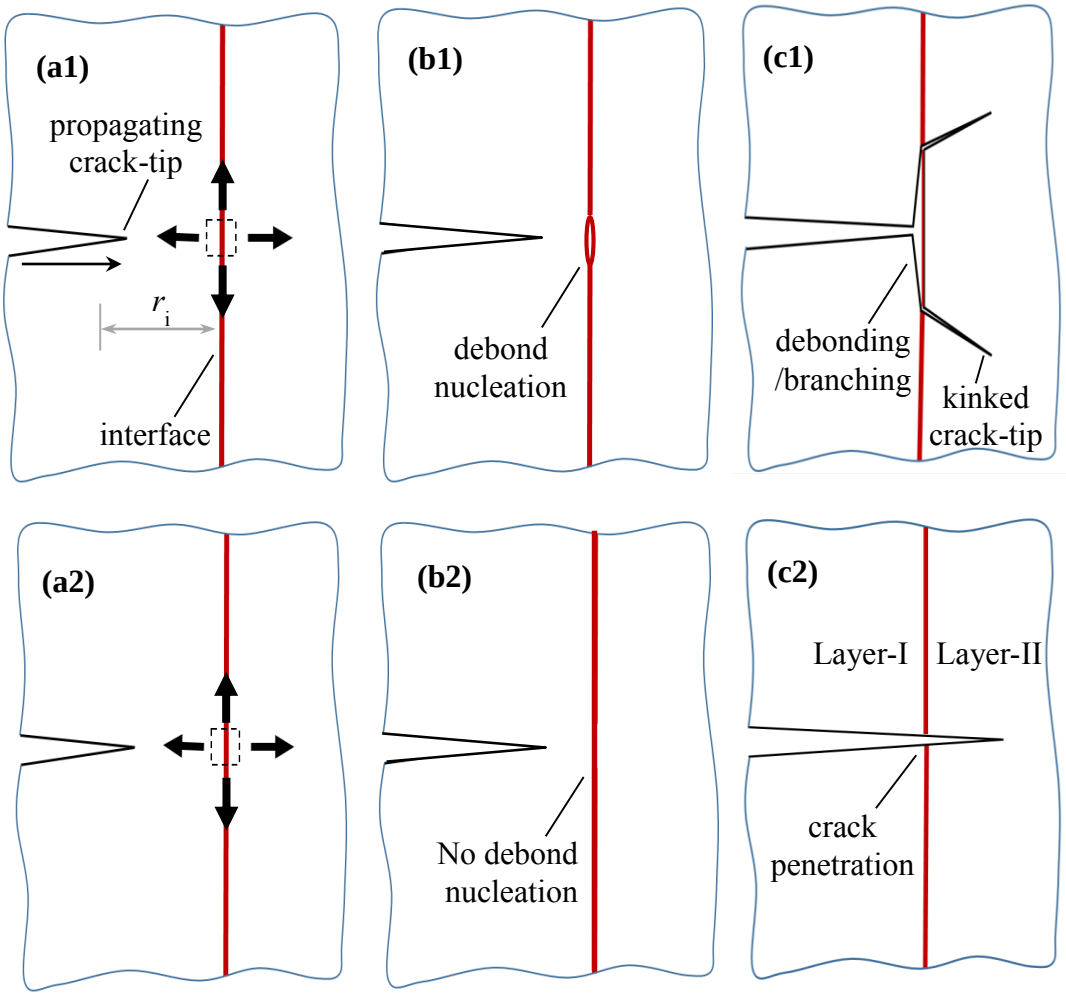

Figure 5.10: Crack penetration vs. branching mechanism: (a1),(a2) State of stress at a point on the interface ahead of an approaching mode-I crack in layer-I. (b1) Nucleation of interfacial debond that facilitates (c1) crack branching, interfacial growth and crack kinking. (b2) Unsuccessful nucleation of debond facilitates (c2) crack penetration into layer-II.

The measured shear and tensile strengths of the interface were found to be 26 ± 0.5 MPa and 23 ± 0.3 MPa, respectively. The comparison between the strength and the induced interfacial stress as the crack-tip approached the interface suggests a tension $\left(\sigma_x\right)_i$ induced debond nucleation at the interface in the d = 17 mm, 28 mm, and 42 mm cases and not a shear induced debond nucleation because the shear stress $\left(\tau_{\max}^{3D}\right)_i$ experienced by the interface is consistently lower than its shear strength (see Fig. 5.9(c) and (d)). As the crack approaches the interface, the *debond* – visualized as a crack with two equidistant singularities from the point of incidence – led to the unzipping of the interface in two opposite (upward and downward) directions over some length until it becomes energetically favorable for the crack to kink into and penetrate layer-II (see Fig. 5.10(c1)). In the d = 7 mm case, however, the stresses were below the interfacial tensile strength and hence debond did not nucleate (see Fig. 5.10(b2)), thereby allowing a successful penetration of the interface and layer-II by the incident mode-I crack without branching (see Fig. 5.10(c2)). The experimental evidence to support the occurrence of debonding ahead of propagating crack-tip is reported in Section 5.7.

In the branched crack cases, the kinking of the interface crack into layer-II was examined using the critical value of SIFs $\left(K_{eff}\right)_i \left(=\left(\sqrt{K_I^2 + K_{II}^2}\right)_i\right)$ for the 100 μm thick interface at different mode-mixities (see Section 4.2.2) and mixed-mode dynamic crack initiation toughness data for PMMA obtained from Chapter 3. The measured K_I and K_{II} at the instant the crack kinks or penetrates layer-II for the four different interface locations

are plotted as green solid diamonds overlaid on the fracture envelop for PMMA in Fig. 5.11.

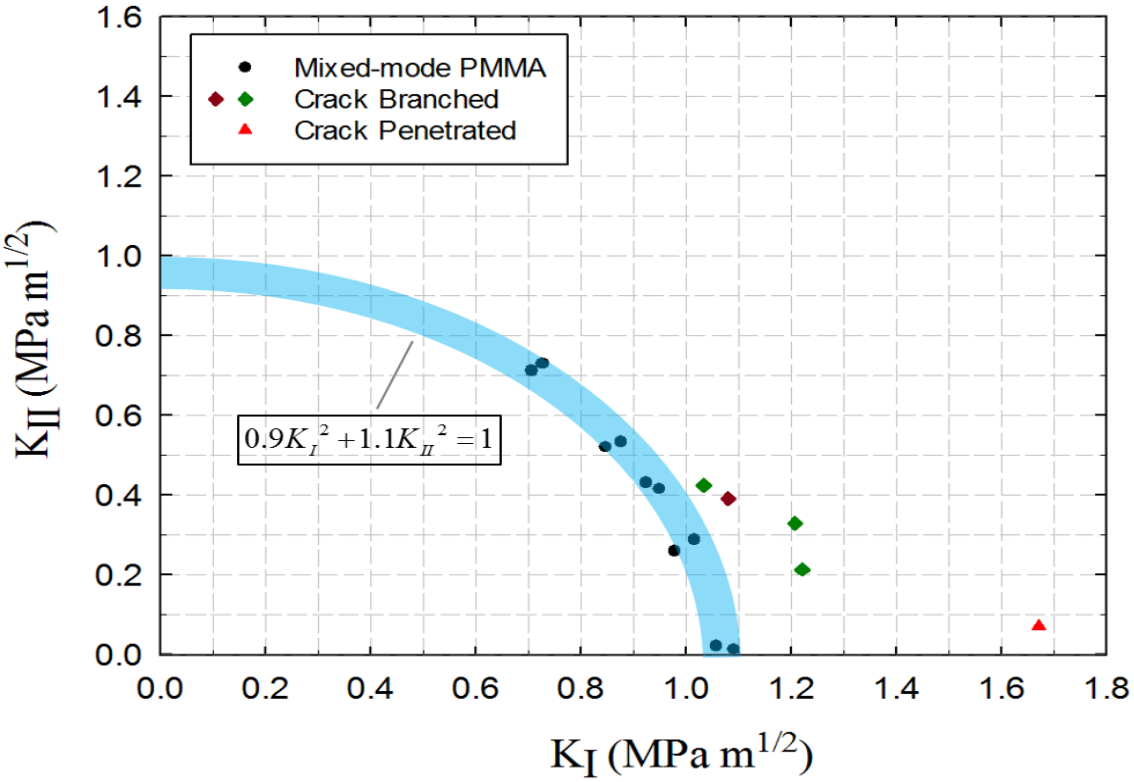

Figure 5.11: Dynamic fracture envelope for PMMA.

Also included in this plot is the data point (brown solid diamond) from Chapter 4 for the branched crack case for a 'strong' interface (25 μm thickness and interface fracture toughness of ~75% that of virgin PMMA) compared to the 'weak' interface studied in this work. A reasonably good agreement between the fracture envelope for PMMA and the solid diamonds corresponding to crack branching is notable despite the differences in the experimental conditions. On the other hand, the data point corresponding to direct penetration of layer-II without branching (red solid triangle) is clearly outside the fracture envelope, which is expected. Further, the tendency of the crack to kink out of the interface

instead of continue propagating along the weak interface can be explained by the increasing critical *effective* SIF of the interface $\left(K_{eff}\right)_i$ with mode-mixity (see Section 4.2.2) making it favorable for the daughter cracks to enter layer-II.

5.7 Interface debonding: Empirical evidence

Experiments to obtain optical evidence for deboning of the interface ahead of crack-tip arrival at the interface were attempted. The configuration with d = 42 mm was used for this purpose. The experimental details were similar to that in this Chapter. The only exception was the imaging system and region of interest (ROI) used in these experiments. A Kirana-05M high-speed camera operating at much higher framing rates (1 Mfps) than Cordin-550 in conjunction with DGS was used to make the optical measurements using DGS. The camera was focused on the speckle target through the region on the specimen where a mode-I crack was expected to arrive at the interface. The ROI was ~ 30 mm x 24 mm. The images were recorded at 1 million frames per second and analyzed using ARAMIS®. Fig. 5.12 shows the recorded images along with the angular deflection contours at three select time instants during the nucleation of a debond. It can be seen from the ϕ_y contours that there are three distinct crack-tips in the field of view simultaneously. It should be noted that the growing mother crack in layer-I is yet to arrive at the interface, yet there are two additional daughter crack-tips which have bubbled up on the interface, one above and another below the mother crack line. This provides the experimental evidence for the hypothesis of nucleation of debond along the interface due to incoming crack.

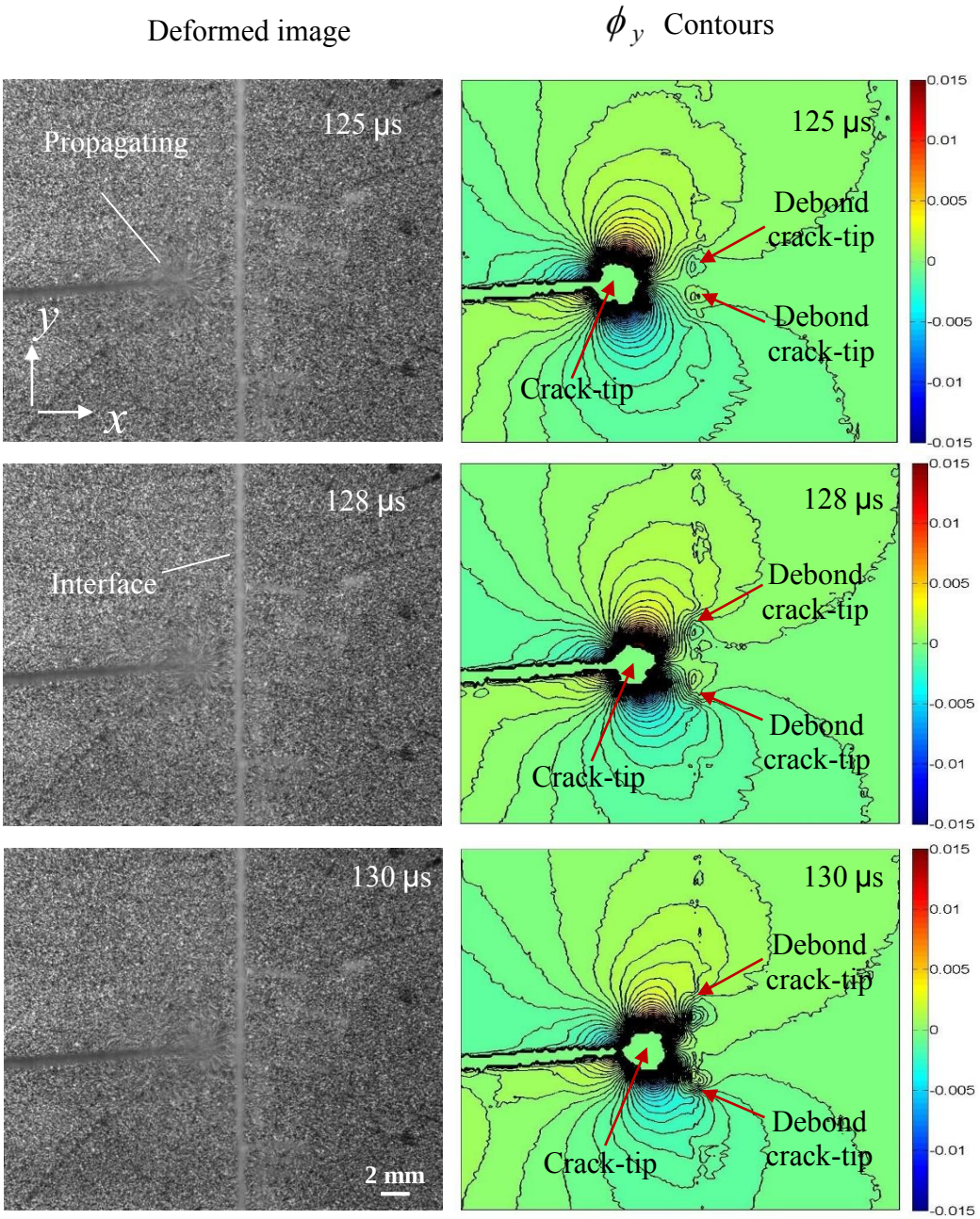

Figure 5.12: The column on the left represent the deformed images recorded at select time instant and the right column represent the corresponding angular deflection contour plots (contour interval = 4×10^{-4} rad) in *y*-direction. The red arrows point to the location of current crack-tips.

5.8 Another empirical observation

As evident from Figs. 5.7 and 5.8, the crack velocity V and the effective SIF K_{eff} histories affect the penetration vs. branching phenomenon. That is, the crack velocities monotonically increased whereas the effective SIFs monotonically decreased when the crack-tip was about to enter the interface in the branched cases as the distance between the initial tip and the interface was increased while keeping all other experimental parameters unchanged. Based on the prevailing understanding of the mechanics of dynamic crack growth in brittle monolithic solids, the crack velocity is the parameter responsible for crack branching [3, 23]. Other mode-I dynamic fracture investigations have suggested [18] K_I - V plots for a dynamically growing crack in a monolithic brittle solid as a material characteristic. However, suitable explanations for crack penetration vs. branching seen in this work do not exist. Further, the discussion in the previous section on tensile stress induced disbond nucleation suggests that the stress intensity factor also plays a significant role in this branching/penetration mechanism as $\left(\sigma_x\right)_i$ was evaluated from the SIFs. Taking these into consideration, possible existence of other quantifiable parameters involving crack velocity and effective SIF were examined. Among those considered the quantity $K_{eff} \times V$ showed a rather interesting behavior noted below:

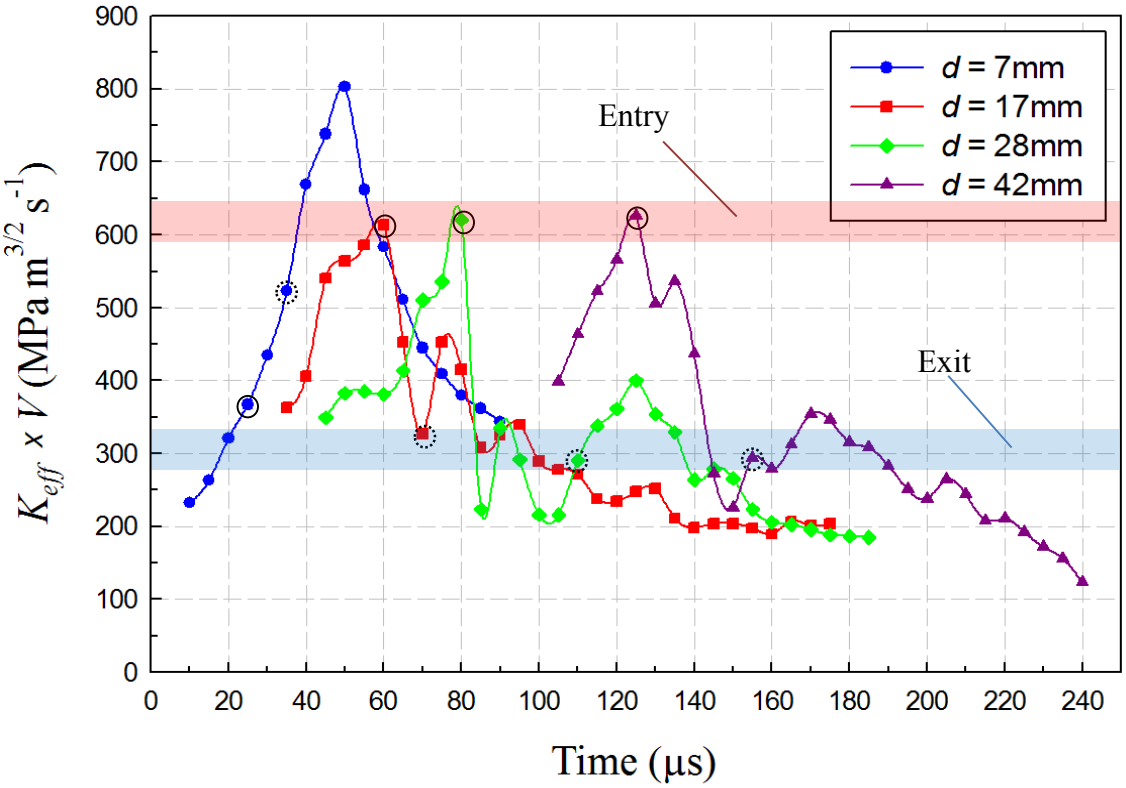

Figure 5.13: $K_{eff} \times V$ histories for all four bilayer configurations. The closed circle represents the instant before the crack entered the interface and the open circles represent the instant at which crack emerged from the interface. Crack-tip data corresponding to before and after the interface fall into two distinct bands for branched cracks and the former is approx. twice that of the latter.

A plot of $K_{eff} \times V$ histories for all configurations is shown in Fig. 5.13. The continuous circles represent the values of this parameter just before the crack entered the interface and the broken-line circles represent those just after the crack exited the interface. It can be seen that values of $K_{eff} \times V$ before the crack entered the interface (the continuous circles) in d = 17 mm, 28 mm, and 42 mm cases fall within a narrow band highlighted by the blue shaded strip at ~600 ± 25 MPa m$^{3/2}$ s^{-1} whereas after exiting the interface (the broken circles) fall within yet another narrow band highlighted by the red shaded rectangle at 300 ± 25 MPa m$^{3/2}$ s^{-1}). From the previous study on a monolithic specimen of the same

geometry in Chapter 4, $K_{eff} \times V$ was evaluated as ~340 MPa $m^{3/2}$ s^{-1} during propagation. Further, recognizing that there are *two* branched cracks in layer-II in these cases, each having $K_{eff} \times V$ of ~300 MPa $m^{3/2}$ s^{-1}, is approximately one half of the corresponding value before the crack entered the interface from layer-I[5]. Although no mechanistic explanation for this observation is readily evident, it certainly is an interesting empirical observation that deserves scrutiny. Further, the values of $K_{eff} \times V$ for the case when the crack did not branch but simply penetrated the interface and layer-II as a mode-I crack do not follow these trends.

5.9 Effect of striker impact velocity

The effect of striker impact velocity on a crack branching vs. penetration behavior is presented in this section. Three different striker impact velocities of 13.5 m/s, 16 m/s and 22 m/s were studied. The configuration with a 'weak' interface located at a distance tip d = 7 mm from the initial notch was chosen for this study as the mother crack had directly penetrated the interface without branching. The experiment details are same as that reported earlier in this Chapter. The strain history recorded on the long-bar for these three different impact velocities is shown in Fig. 5.14. From the incident and reflected regions of the strain history it can be seen that that with increase in impact velocity of the striker, more energy is transmitted into the specimen. The photographs of the fractured specimen are shown in Fig. 5.15(a)-(c). It can be seen that when the striker velocity increased from

[5] The $K_{eff} \times V$ for the crack-tip upon arrival at the interface for an interface distance of d = 28 mm and a higher interface toughness (K_{Icr} = 1.02 MPa$\sqrt{m}$) reported in chapter 4 was ~580 MPa $m^{3/2}$ s^{-1} and ~285 MPa $m^{3/2}$ s^{-1} after penetrating the interface. These fall into the two data bands for branched cracks in Fig. 5.13.

13.5 m/s to 16 m/s, the crack growth behavior at the interface changes from a direct penetration into layer-II to interface debonding followed by crack branching into layer-II.

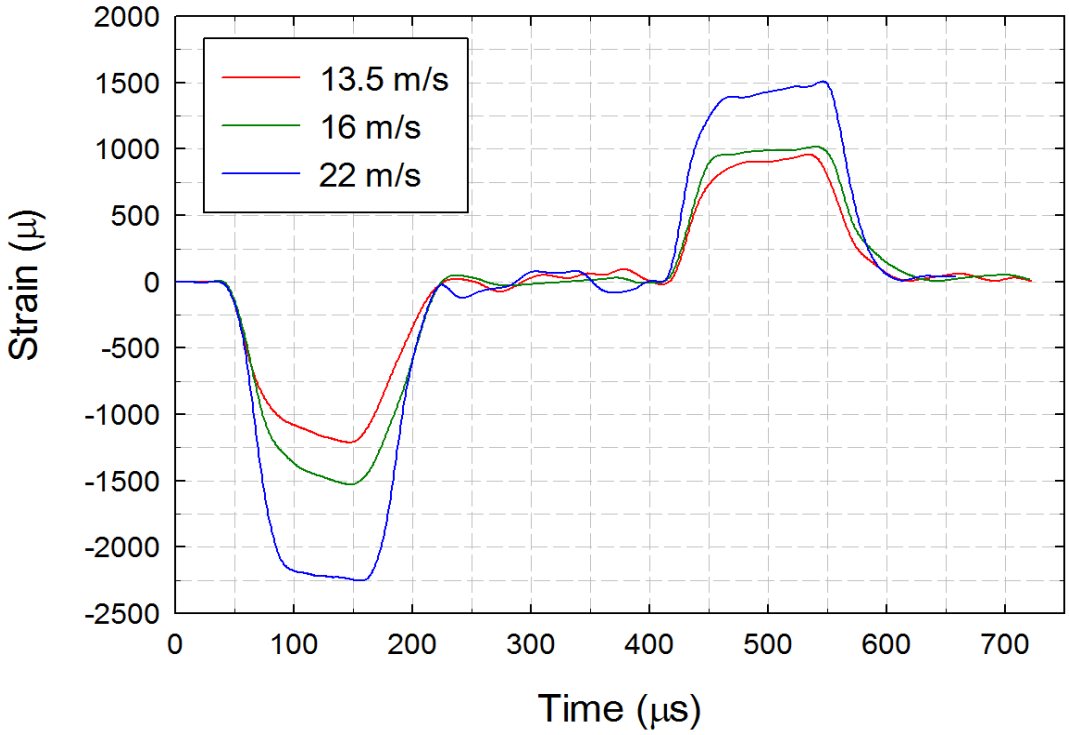

Figure 5.14: Measured strain histories on the long-bar for various striker impact velocities.

Further increase in the striker velocity did not produce significant change. The interface crack traveled a distance of 10 mm and 8 mm, with crack emergence angles of 22˚and 21˚as the impact velocity increased from 16 to 22 m/s, respectively. This marginal decrease in the interface crack length may be attributed to the increase in mode-I stress intensity factor of the crack-tip which makes the combination of critical SIFs (the data point outside the dynamic fracture envelope of PMMA, Fig. 5.11) attain conditions favorable for PMMA to fail as the two daughter cracks kink into layer-II. The decrease in the angle of emergence can also be attributed by the significant increase in mode-I SIF

leading to a decrease in mode-mixity during the initial phase of propagation in layer-II. When the crack neared the free surface, unstable growth is observed. Further, there seems to be limit for the distance traveled by the crack along the interface. This can be attributed to the SIFs reached the critical value favorable for the crack to kink into layer-II. Thus, increase in impact velocity promoted crack branching.

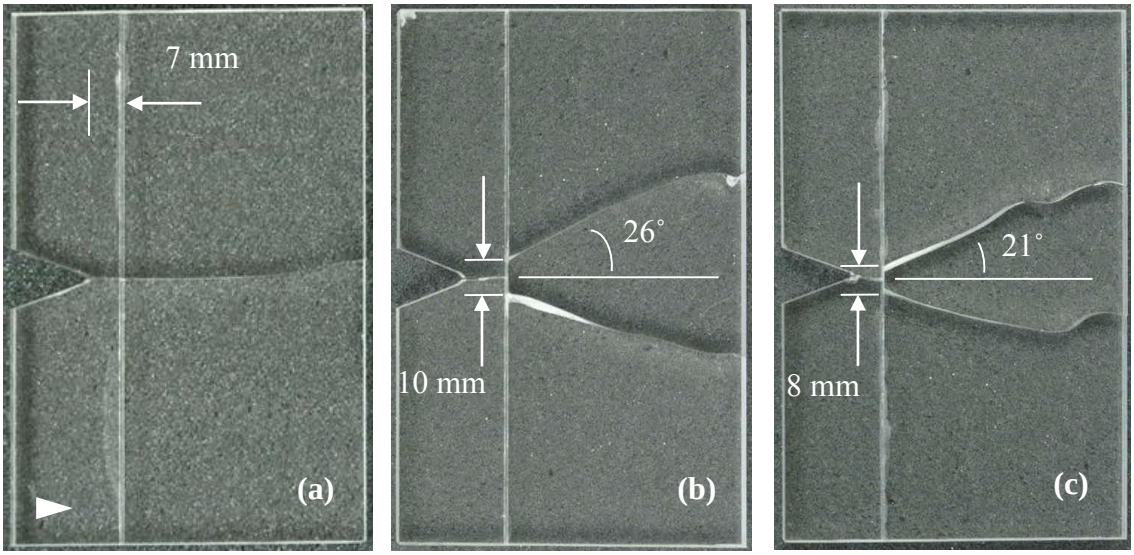

Figure 5.15: Photographs of fractured specimen with striker impact velocity of (a) 13.5 m/s, (b) 16 m/s, and (c) 22 m/s.

Figure 5.16 show the crack velocity histories for the three configurations. As seen previously, the two impact velocities that produced crack branching show similar trends whereas the unbranched case stands out. The crack velocity as the crack approached the interface is higher in case where branching occurred. This is in line with observation made earlier. It can also be seen that the duration the crack was trapped in the interface decreased with impact velocity.

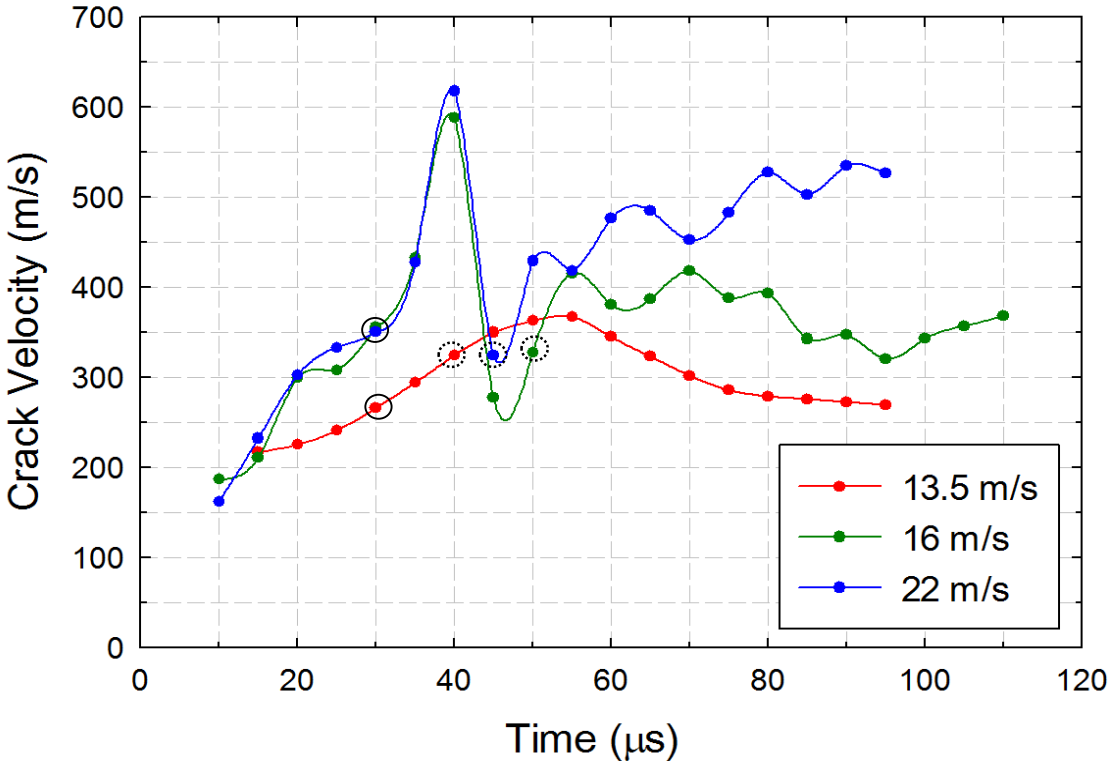

Figure 5.16: Crack velocity histories for all three impact velocities for a fixed interface distance from the initial notch tip (d = 7 mm).

The effective SIF histories and mode-mixity histories are shown in Fig. 5.17(a)-(b). In the SIF histories shown in Fig. 5.16(a), the effective SIF of the crack-tip just before reaching the interface increases with increase in impact velocity and their values are significantly higher for the case when crack branching occurred. For the two impact velocities 16 m/s and 22 m/s, as the two crack-tips exit the interface, the values of effective SIF are nearly the same. This implies that once a critical value of effective SIF is attained, the crack kinks into layer-II. This can be seen in experiments in the previous section (see Fig. 5.8(a)). In the plots shown in Fig. 5.17(b), the mode-mixity when crack kinks into layer-II for an impact velocity of 22 m/s is marginally less than that of 16 m/s supporting the observation of lower crack emergence angle in the former.

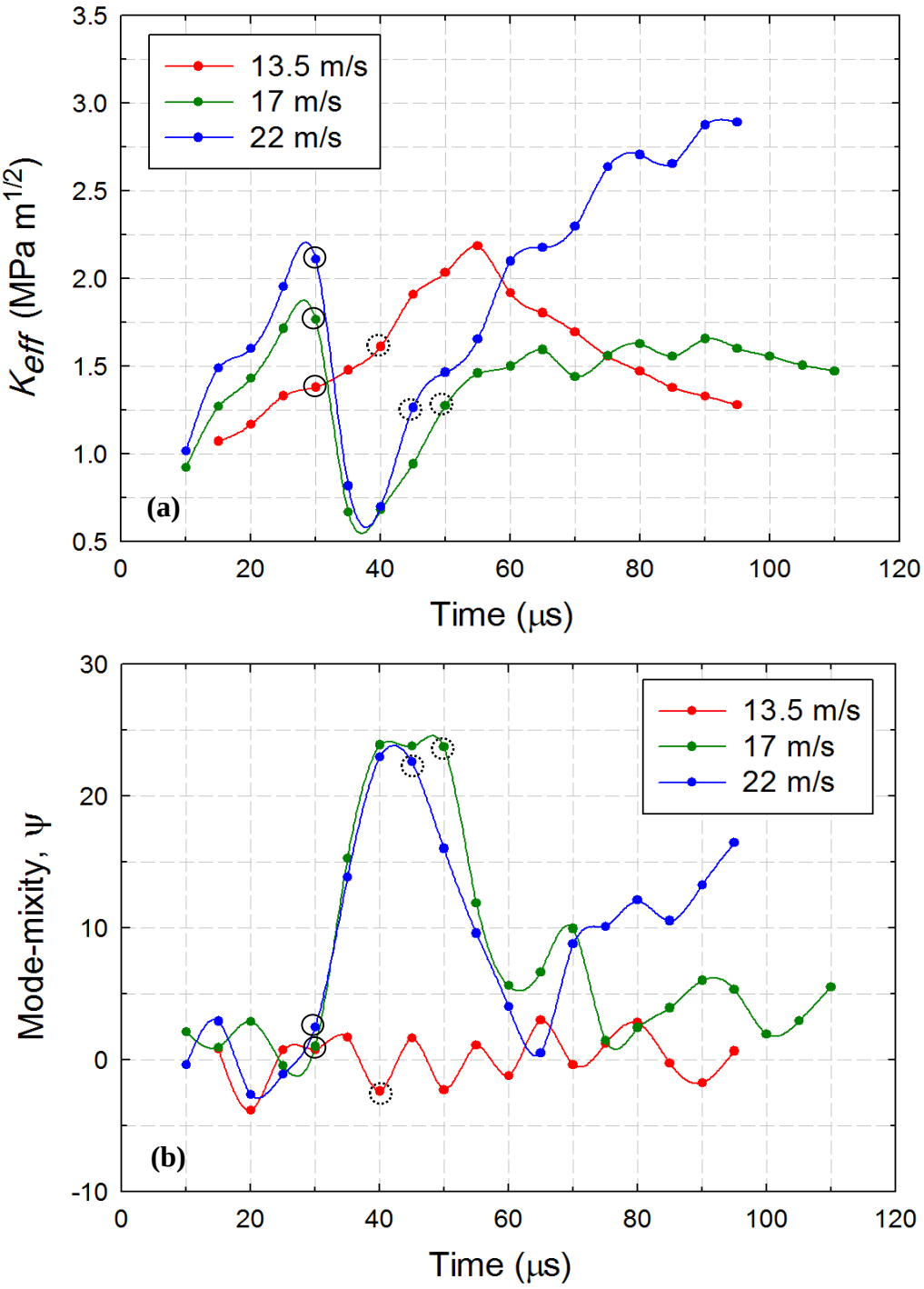

Figure 5.17: History of crack-tip parameters (Time $t = 0$ corresponds to crack initiation at the original notch tip) for all the three impact velocity investigated: (a) effective stress intensity factor histories, and (b) mode-mixity histories. The solid-line circles represent the instant before the crack enters the interface and the dotted-line circles represent the instant at which crack emerges from the interface

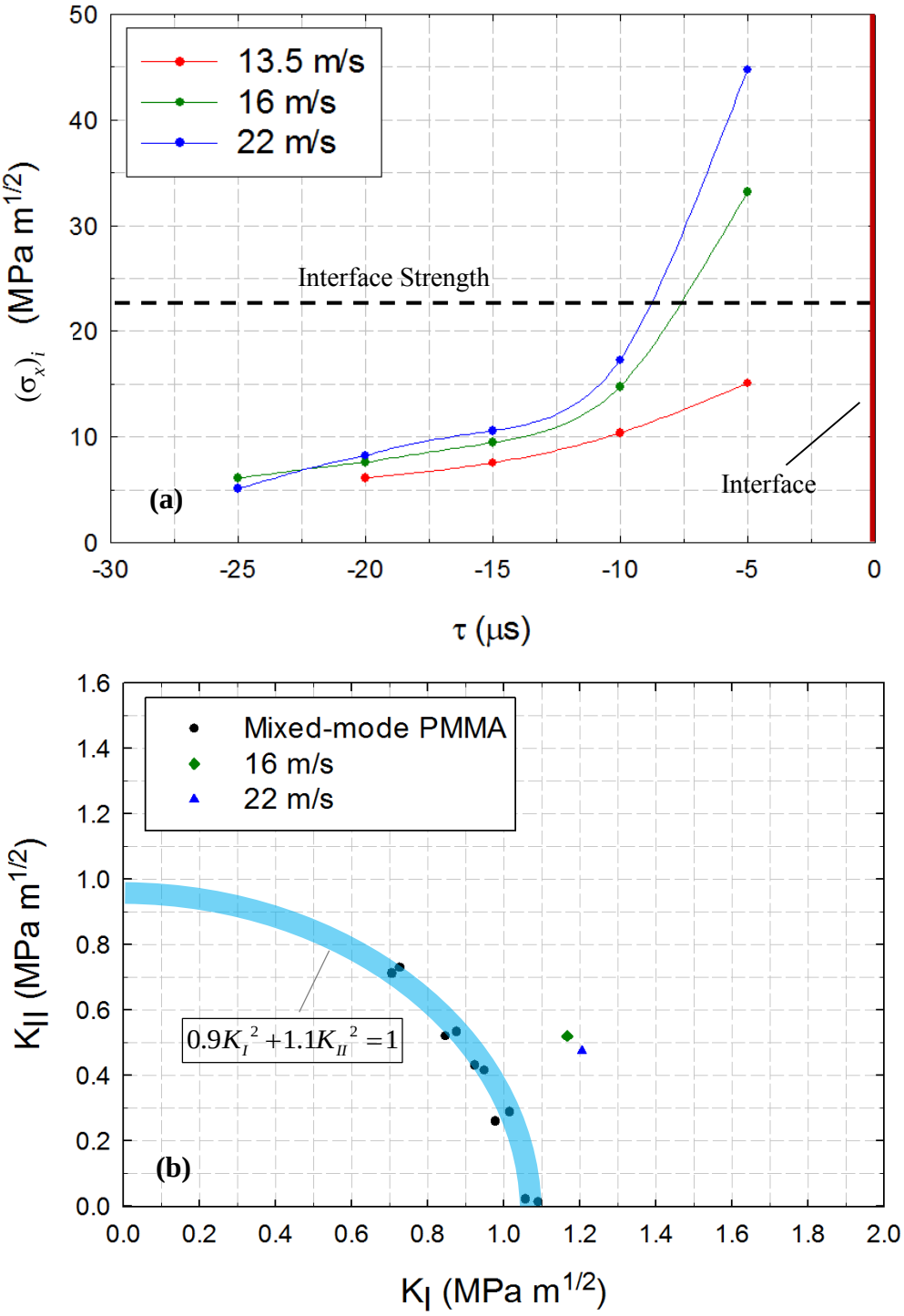

Figure 5.18: Temporal evolution of in-plane normal stress at a point on the interface directly ahead of the mode-I mother crack ($\tau = 0$ μs *corresponds to crack reaching the interface indicated by the heavy red line*), and (b) dynamic fracture envelope for PMMA

It should also be noted that the mode-mixity of ~24^{o} and 23° observed for impact velocities 16 m/s and 22 m/s, respectively, when kinking occurs at the interface is in line with the threshold value of mode-mixity for crack kinking evident from the interface fracture toughness plot for various mode mixities (Section 4.2.2). As in case of bilayers with different interface locations relative to the initial notch tip, the tensile stress induced by the growing crack at a point directly ahead of it and on the interface (σ_{xx}) is shown in Fig. 5.18(a) for the bilayer with a fixed interface distance (d = 7 mm) subjected to three different striker velocities. The interface experiences a tensile stress higher than its strength in 16 m/s and 22 m/s cases prior to the arrival of the mother crack supporting the hypothesis of debond nucleation put forward earlier. In Fig. 5.18(b) the values of SIF as the crack kinks into layer-II is plotted on the dynamic fracture envelope of PMMA. It can be seen that the two data points corresponding to impact velocities of 16 m/s and 22 m/s are outside the fracture envelope.

Similar observations regarding the effect of striker velocity can be seen on bilayers with a stronger interface case. Photographs of fractured specimens for a 'strong' interface situated at d = 7 mm and subjected to impact loading using three different striker velocities is shown in Fig. 5.19. It can be seen that as the impact velocity is increased from 13.5 m/s to 16 m/s, the crack penetration into layer-II is maintained whereas when the impact velocity was further increased to 22 m/s, the crack penetration changed to crack branching. Thus crack branching was promoted by the increase in impact velocity which caused the crack to grow faster with a higher SIF. This in turn generated higher tensile stresses on the interface ahead of the growing crack resulting in debond nucleation at the interface and

subsequent crack bifurcation, interfacial trapping, and kinking of two daughter crack into layer-II. Photograph of the fractured specimens for a 'weak' interface at $d = 7$ mm subjected to the same three striker velocities are shown in Fig. 5.20 to contrast the behavior with the 'strong' interface counterparts.

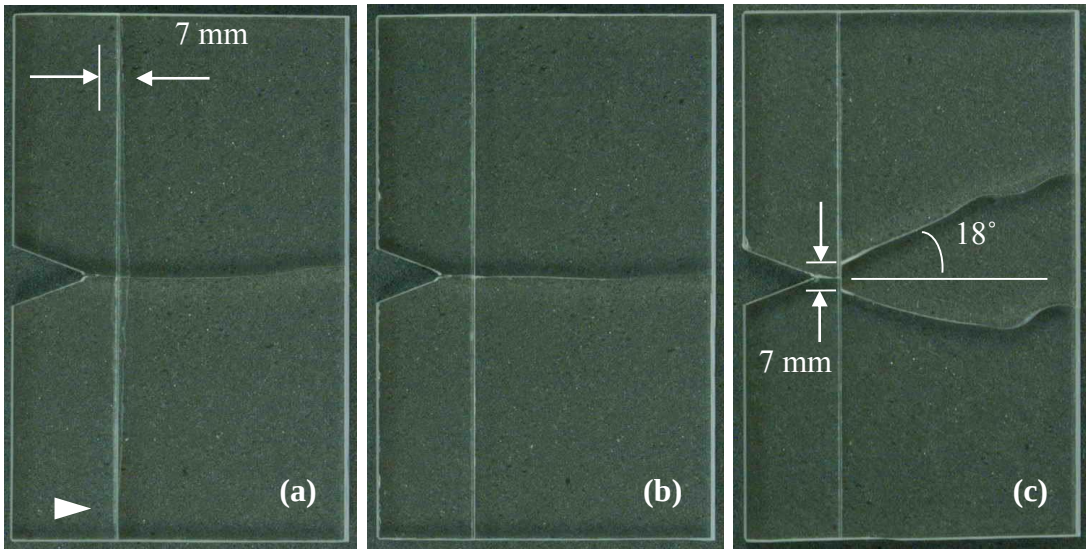

Figure 5.19: Photographs of fractured specimen with $d = 7$ mm and 'strong interface' for striker impact velocity of (a) 13.5 m/s, (b) 16 m/s, and (c) 22 m/s.

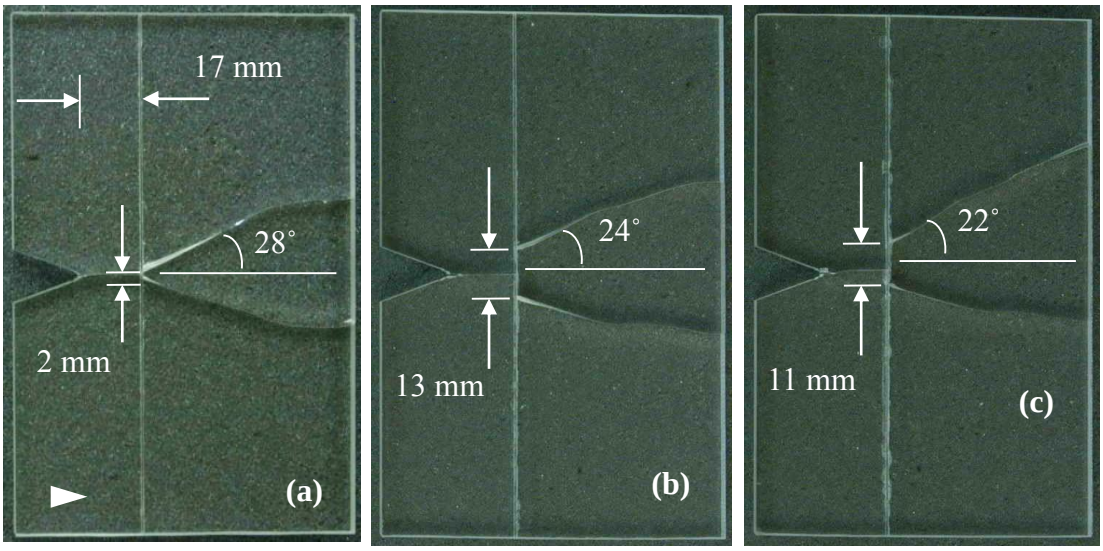

Figure 5.20: Photographs of fractured specimen with $d = 17$mm and 'weak' interface striker impact velocity of (a) 13.5 m/s, (b) 16 m/s, and (c) 22 m/s.

Chapter 6

FRACTURE OF SODA-LIME GLASS

In this chapter, the feasibility of Digital Gradient Sensing (DGS) method to measure crack-tip and impact induced deformations in soda-lime glass is described. First, the feasibility of 2D DIC and its limitation to study fracture mechanics in soda-lime glass are elaborated. The method of ultrahigh-speed photography (> 1 million frames per sec) employed conjunction with DGS is detailed. Both static and dynamic problems associated with impact induced deformations, and deformations near dynamically loaded stationary and growing cracks, are presented. The experimental details, image analysis, and results are described. The comparison for experimental results with those from finite element simulations and/or boundary collocation method is provided. Numerical integration of the measured optical data to obtain stress fields $\left(\sigma_x + \sigma_y\right)$ near both stationary and dynamically growing cracks are also included.

6.1 Why not use 2D DIC to study fracture of soda-lime glass?

Aided by advances in digital photography, image processing algorithms, and abundance of inexpensive computational power, the digital image correlation (DIC) method has emerged as a popular optical metrology tool [112] in recent years. Easy specimen preparation, ordinary white light illumination, and availability of measurements

in the digital form have added to its popularity. Accordingly, the possibility of using DIC to study fast fractures [113] in glass and other brittle ceramics was considered first to address the stated question. An experiment was performed on a soda-lime glass specimen using 2D-DIC. The geometry and loading configuration of soda-lime glass plate specimen that was used is shown in Fig. 6.11(a).

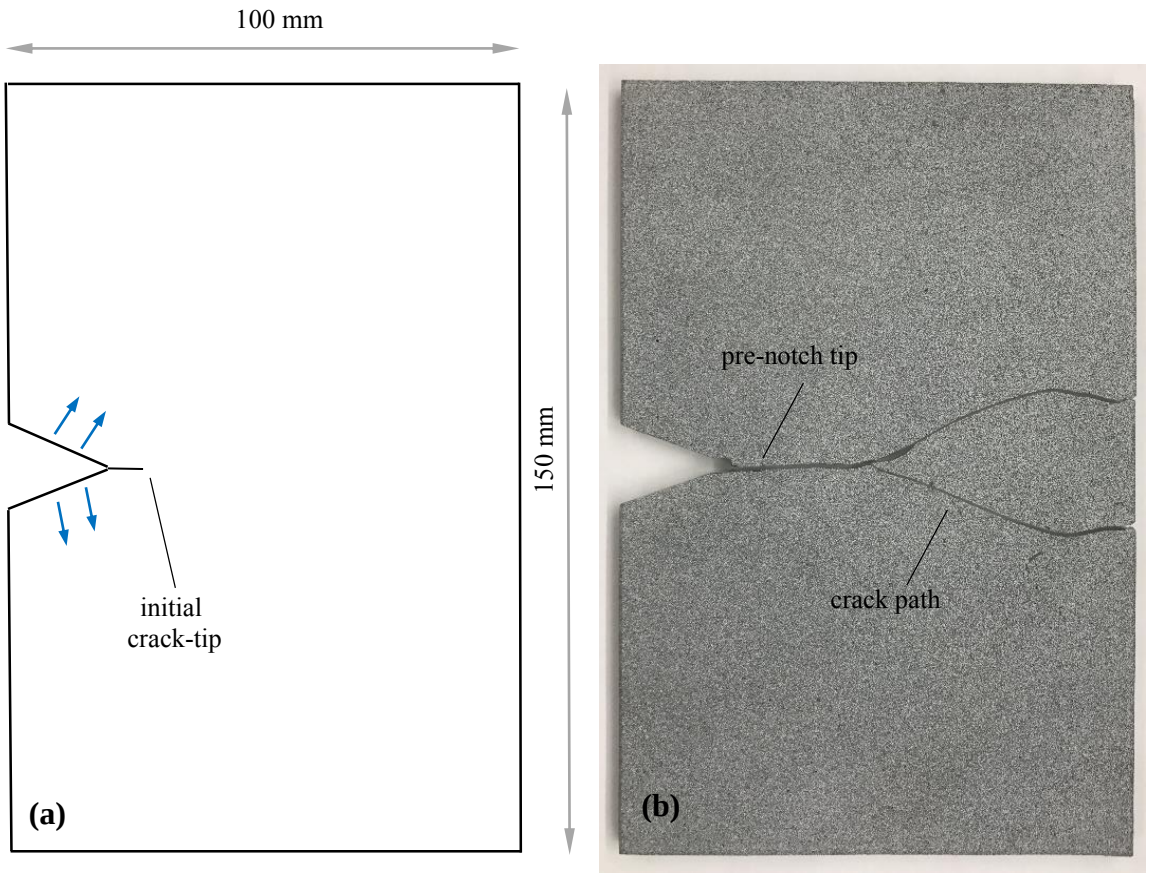

Figure 6.1: (a) Specimen geometry and loading configuration used in the study of soda-lime glass fracture using 2D-DIC, (b) the photograph of the fractured specimen.

The specimen surface was sprayed with random black and white speckles. It was dynamically loaded using a Hopkinson pressure bar having a wedge shaped tip placed into the corresponding V-notch made in the specimen. A photograph of the fractured specimen

is shown in Fig. 6.1(b). As expected, the crack initiated at the pre-notch tip and propagated under dominant mode-I conditions before bifurcating into two globally symmetric daughter cracks approximately in the middle of the specimen. The highly dynamic event was recorded using a single sensor Kirana-05M ultrahigh-speed camera (924 x 768 pixels; scale factor = 0.072 mm/pixel[6]) at 1 million frames per second. The fracture event produced a hairline crack emanating from the pre-notch tip but could not be discerned directly from the recorded speckle images. This is unlike the polymeric and fiber reinforced composite material counterparts previously studied by the authors [114, 115] where this difficulty had not been as severe. Using the image analysis software ARAMIS, deformed and undeformed images were correlated and in-plane deformations were obtained. Two typical sub-image sizes of 25 x 25 pixels and 15 x 15 pixels with step size of 5 pixels were used while analyzing the images. The resulting displacement contours in the vertical direction (along the y-axis) at a time instant $t \sim 24$ μs after crack initiation are plotted using three different contour increments in Figs. 6.2(a)-(b). It can be seen that as the magnitude of contour increments was decreased for visualization purposes, the probable location (based on displacement jump in front of the instantaneous crack-tip) of the crack-tip varied significantly between Figs. 6.22(a1) and (a2) and quite drastically between Figs. 6.22(a2) and (a3). In fact, the first two indicate a single (growing) crack-tip and the last one indicates a fully bifurcated crack with two branched crack-tips.

[6] The magnification selected was dictated by the need for observing a sufficiently large region on the specimen to capture crack initiation, growth and branching events.

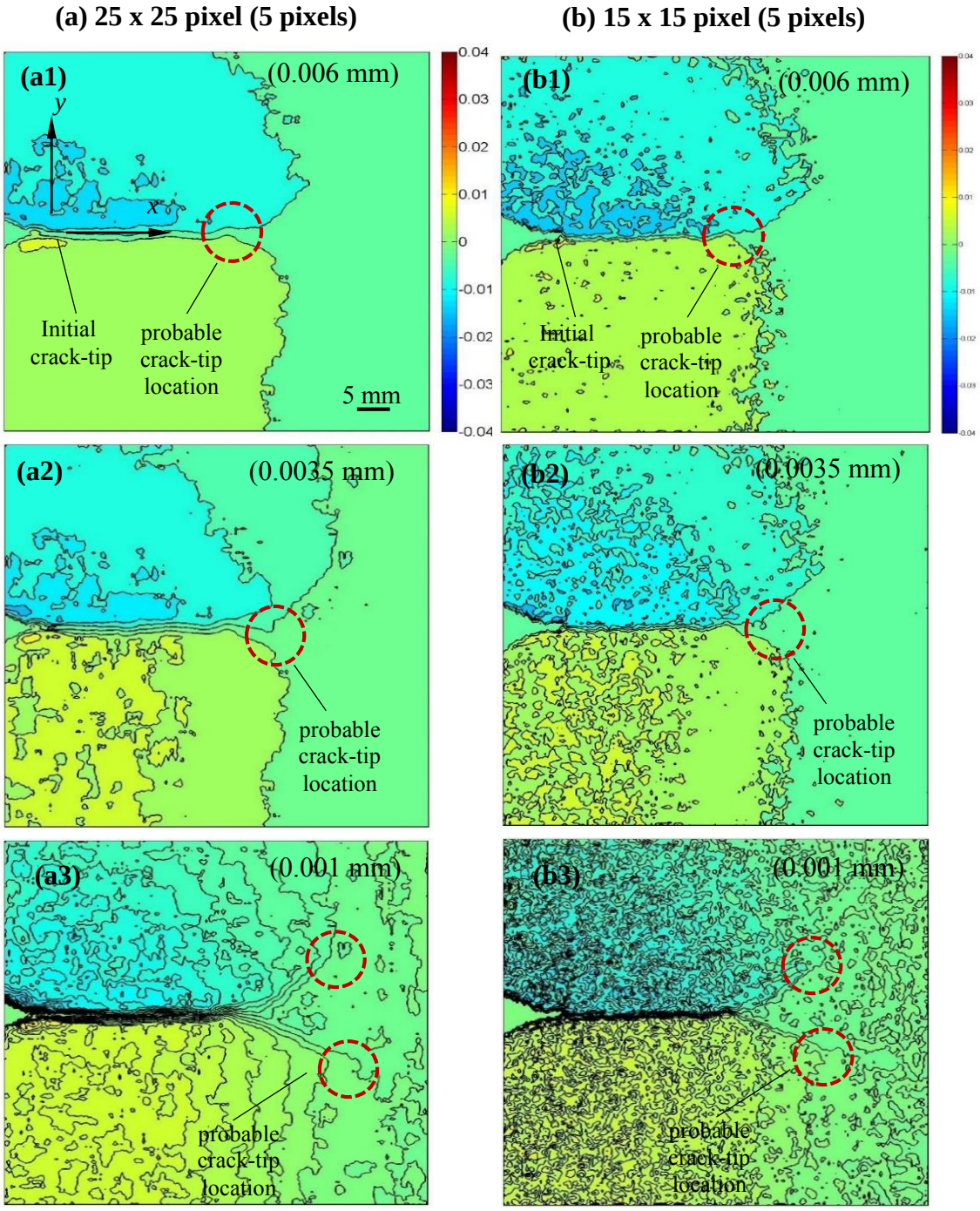

Figure 6.2: Displacement contours on soda-lime glass specimen surface along the vertical direction (normal to the crack) from DIC at a time instant of ~24 μs after crack initiation at the original tip using sub-image size of 25 x 25 pixel, and (b) 15 x 15 pixel with step size of 5 pixels with contour increments of 0.006 mm,0.0035 mm, and 0.001 mm ((a1)-(a3) and (b1)-(b3) respectively).

Similar observation can be noted for Figs. 6.22(b1)-(b3) as well. Thus, locating the crack-tip could be quite challenging in this brittle material where crack flank displacements are very small compared to polymers and fiber reinforced composites. If the crack-tip is located wrongly, the fracture parameters (velocity and stress intensity factor) thus evaluated would be incorrect. This difficulty could be alleviated to some extent if a higher magnification is used. However, it would require substantial compromise in terms of the region of observation being investigated, possibly missing different fracture mode transition features and mechanisms that occur during highly transient events in this material.

6.2 Extension of DGS

DGS was used in conjunction with ultrahigh-speed photography (>1 mfps) to make optical measurements in this study. DGS is a full-field optical method that measures angular deflections of light rays propagating through a transparent specimen. These angular deflections of light rays are due to the state of stress in the specimen and represent the gradients of stresses in their respective directions. Further details are in Chapter 1.

As described in Chapter 1, while recording images the camera was focused on the 'target' (and speckles) through the transparent sheet. Yet, the analysis requires mechanical fields described on the specimen plane, situated at a distance '*L'* from the target. That is, a point O(x, y) on the specimen corresponds to a point P(x_0, y_0) on the target plane as shown in the 2D schematic (see, Fig. 6.3). This can be accomplished using a pin-hole camera approximation for which a mapping function between the specimen and the target planes

can be deduced. In Fig. 6.3, $\tan\theta = \frac{\delta_s}{L} = \frac{\delta_t}{L+\Delta}$, where δ_s and δ_t are on the specimen and target planes. This can be rewritten as $\delta_s = \left(\frac{L}{L+\Delta}\right)\delta_t$. (A similar mapping function for the horizontal plane is understood.) Glass being a very brittle, low toughness material, the angular deflections are extremely small (a few micro-radians). Hence, Δ had to be increased significantly to accommodate for this, making the assumption of $\Delta << L$ unsuitable as in earlier chapters and necessitates accounting for the *perspective effect* during analysis.

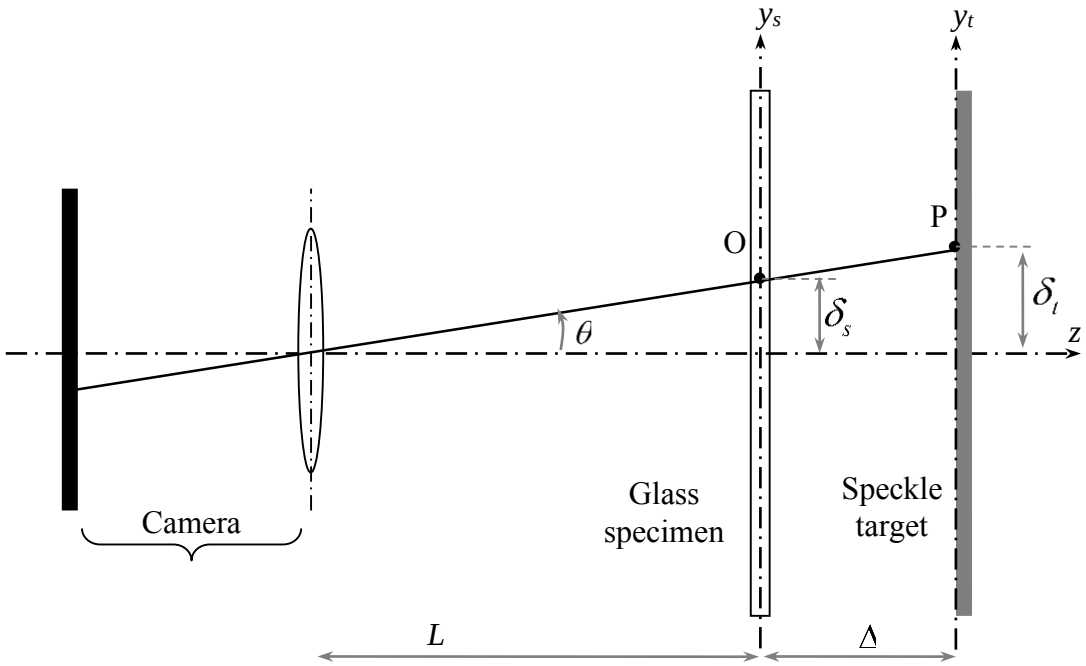

Figure 6.3: 2D Schematic for mapping target pane coordinates to the specimen plane coordinates.

6.3 Quasi-static line-load on the edge of a glass plate

6.3.1 Experimental details

A quasi-statically applied line-load on the edge of a large planar glass plate was first studied. A 100 × 75 mm^2 rectangular specimen cut from commercially procured plate glass/soda-lime glass sheet (elastic modulus ~70 GPa, Poisson's ratio 0.22 and C_σ - 0.027×10^{-10} m^2/N) [116] of thickness 4.65 mm was used. The schematic of the experimental setup is shown in Fig. 6.4.

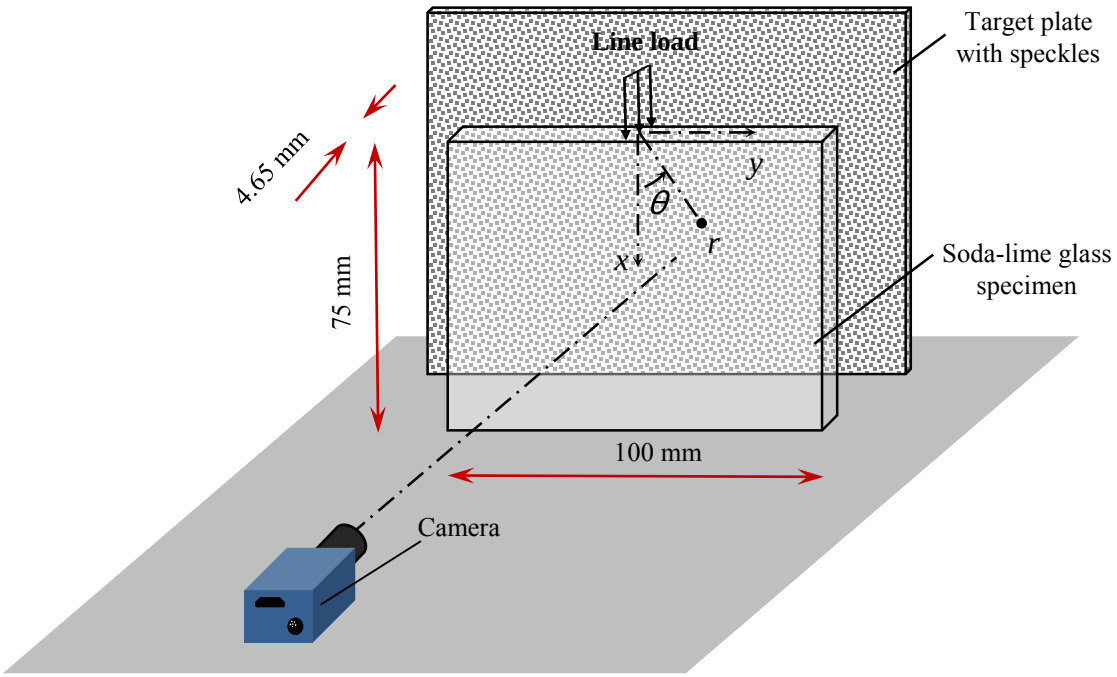

Figure 6.4:. Schematic for quasi-static line loading on a soda-lime glass sheet used in DGS.

The specimen was placed on a hardened steel platform and subjected to line-load using a cylindrical steel pin (diameter 5 mm attached to a Instron 4465 crosshead) in displacement control mode (crosshead speed ~0.005 mm/sec). A target plate painted with

random black and white speckles was placed at a distance of 712 mm away from the specimen mid-plane. A couple of heavy black dots (see, Fig. 6.5) were marked on the speckle plane to relate the image dimensions to the actual target and subsequently the specimen dimensions. A Point Grey Grasshopper3 digital camera with an 18–108 mm focal length zoom lens ($F^{\#}$ 5.6) was used to record speckles through the specimen in the load point vicinity. The camera was situated at a distance (L) of approximately 445 mm from the specimen.

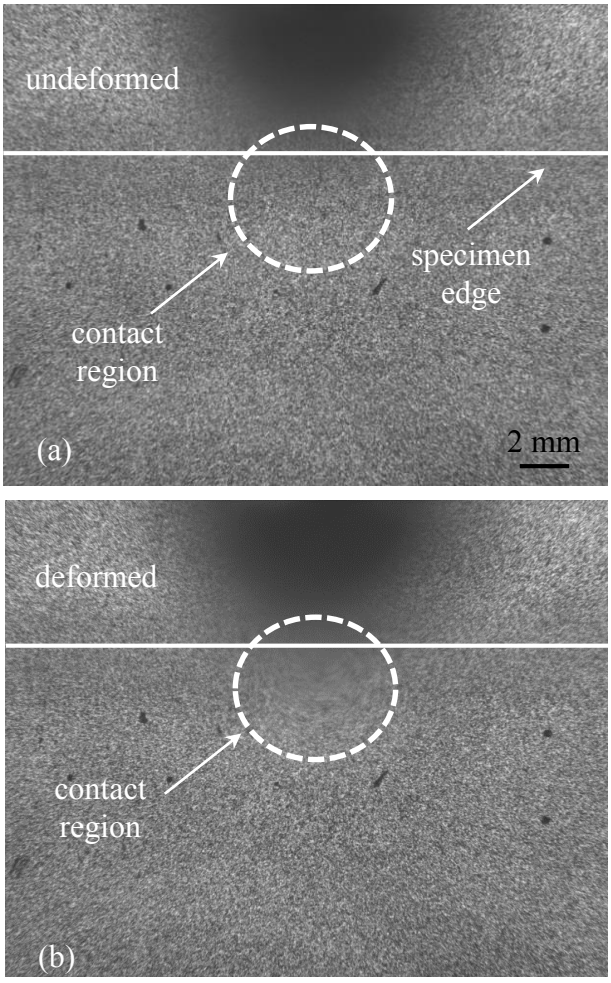

Figure 6.5: Speckle images in the undeformed (top) and deformed (bottom) states recorded through the soda-lime glass specimen subjected to line-load.

A reference image of the target was recorded through the transparent specimen in the region of interest at a small load (< 5 N). As the load increased, the speckle images were recorded using time-lapse photography (15 frames per minute). Speckle images in the loading point vicinity corresponding to the undeformed and a select deformed (3000 N) state are shown in Fig. 6.5. The recorded images correspond to 63 mm x 58 mm region on the target plate which translates to approximately 24 mm x 22 mm on the specimen. It shows that due to deformation of the specimen, the speckles appear noticeably smeared close to the loading point whereas they seem relatively unaffected at far-away locations. The digitized speckle images (1184 × 1100 pixels) recorded at different load levels were correlated with the one corresponding to the reference condition using image analysis software ARAMIS®. As described previously, an array of in-plane speckle displacements on the target plane (and hence the specimen plane) was evaluated and converted into angular deflections of light rays ϕ_x and ϕ_y. A facet/sub-image size of 25×25 pixels (1 pixel ≈ 53 μm on the target plane) with an overlap of 20 pixels was used for image analysis to extract displacement components.

6.3.2 Load history

The equation for ϕ_x and ϕ_y in terms of the applied load is described using the classical Flamant solution as [85],

$$\phi_{x;y} = C_\sigma \frac{2F}{\pi} \frac{\left[\cos(2\theta); \sin(2\theta)\right]}{r^2} \tag{6.1}$$

where C_σ is the elasto-optic constant, F is the applied load and (r,θ) denote polar coordinates defined as shown in Fig. 6.4. The *perspective effect* described in the previous section was taken into consideration during analysis. It is important to note that, accounting for rigid body translations, electronic noise and enforcement of boundary conditions of the problem to quantify the contour levels for further analysis is needed for static conditions. This can be done by forcing symmetry and far-field conditions as in Ref. [85]. The same can be accomplished by adding constant terms to the Eq. (6.1) as,

$$\phi_{x;y} = C_\sigma \frac{2F}{\pi} \frac{\left[\cos(2\theta);\sin(2\theta)\right]}{r^2} + C_{x;y} \tag{6.2}$$

where $C_{x;y}$ denote constants. In this experiment, F was evaluated using over-deterministic regression analysis of the measured field ϕ_x. Alternatively, ϕ_y can also be used to evaluate F. The discrete angular deflection values around the loading point in the region $1 \le r/B \le 2$ along with angular extent of $-80^0 \le \theta \le -50^0$, $-40^0 \le \theta \le -40^0$ and $50^0 \le \theta \le 80^0$ were used in the regression analysis. This ensured avoiding the region of dominant stress triaxiality along the free edges and regions adjacent to zones where angular deflections are nearly zero. This also helped to deal with the lack of data in the close vicinity of the loading point due to finite numerical aperture of the camera. The measured DGS contours (on the specimen plane) of angular deflections ϕ_x and ϕ_y for a select load of 3000 N are shown in Fig. 6.6. The load history from the load cell was also recorded in addition to that evaluated from DGS. A plot of both load histories is plotted in Fig. 6.7 and the two are in good agreement.

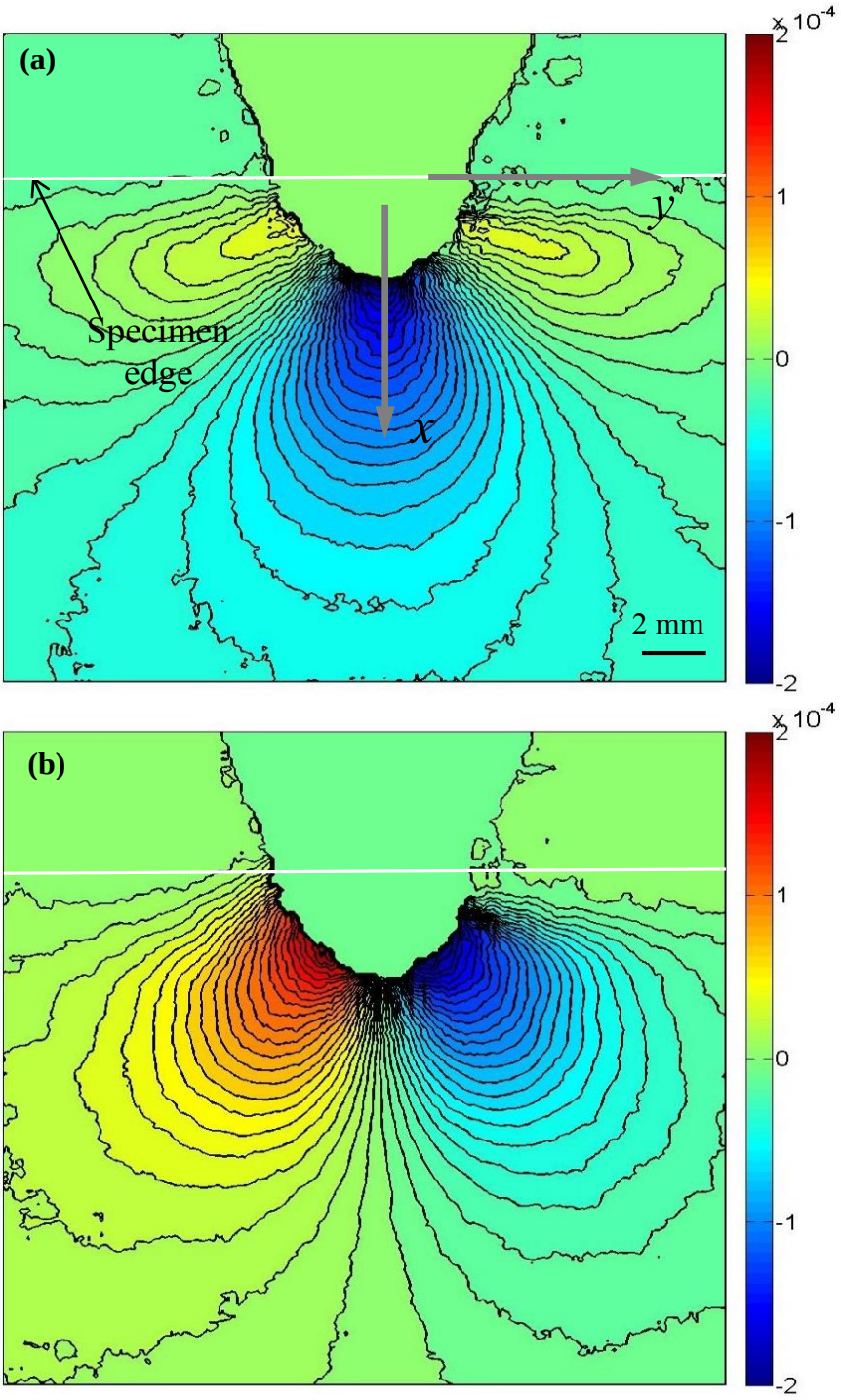

Figure 6.6: Angular deflection contour plots (contour interval = 8×10^{-6} rad) proportional to stress gradients of $(\sigma_x + \sigma_y)$ in the (a) *x*- and, (b) *y*-directions for a soda-lime glass specimen under static line-load on its edge.

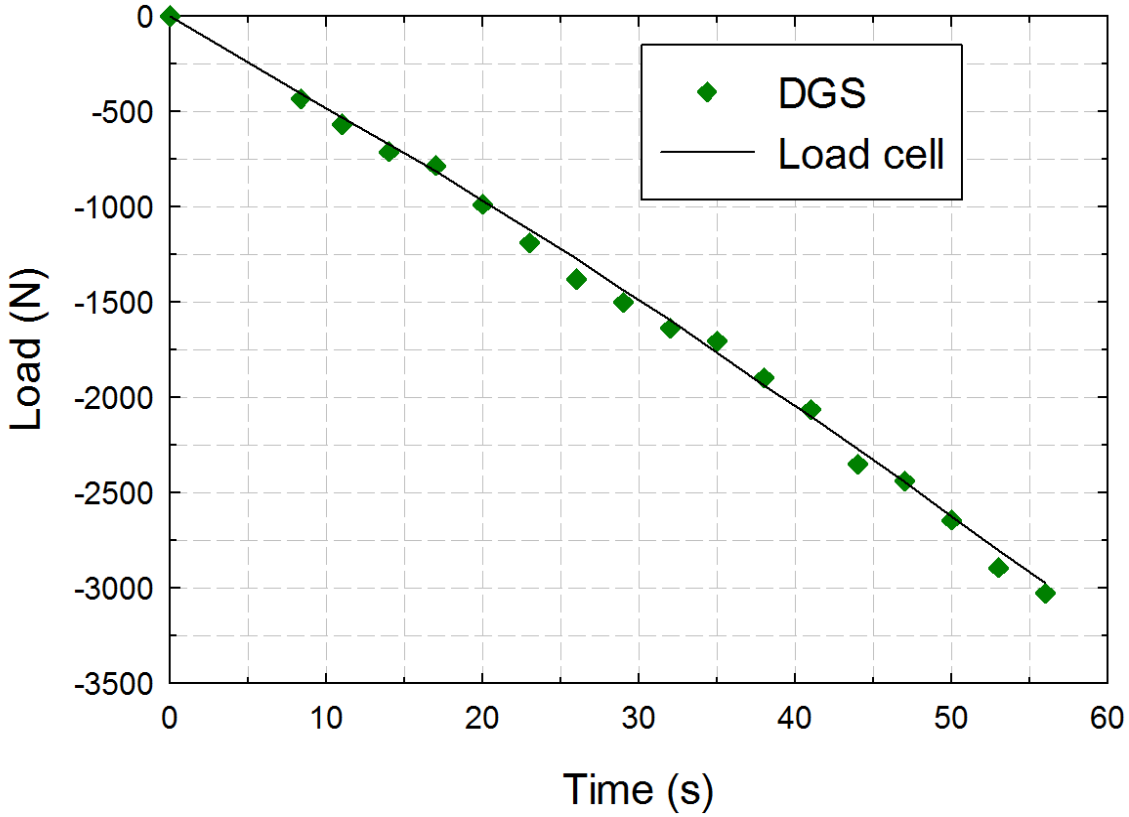

Figure 6.7: Load history obtained form (a) DGS data and (b) load cell of the testing machine.

6.4 Crack-tip deformations: Quasi-static loading

6.4.1 Experimental details

Quasi-static crack-tip deformations were measured next. A soda-lime glass sheet of 4.65 mm thickness was cut to obtain 130 mm x 50 mm SENB specimens. A 10 mm long notch was machined into it using a band saw of 2 mm thickness. Initial notch was intentionally kept wide to avoid premature specimen failure at low load levels. The specimen was placed on two anvils (120 mm apart) symmetrically relative to the notch cut along the bottom edge and the loading pin pressing down on the top edge. A symmetric 3-

point-bend test was performed on these specimens using Instron 4465 testing machine in displacement controlled mode (crosshead speed of 0.005 mm/s). The schematic of the experimental setup used is shown in Fig. 6.8.

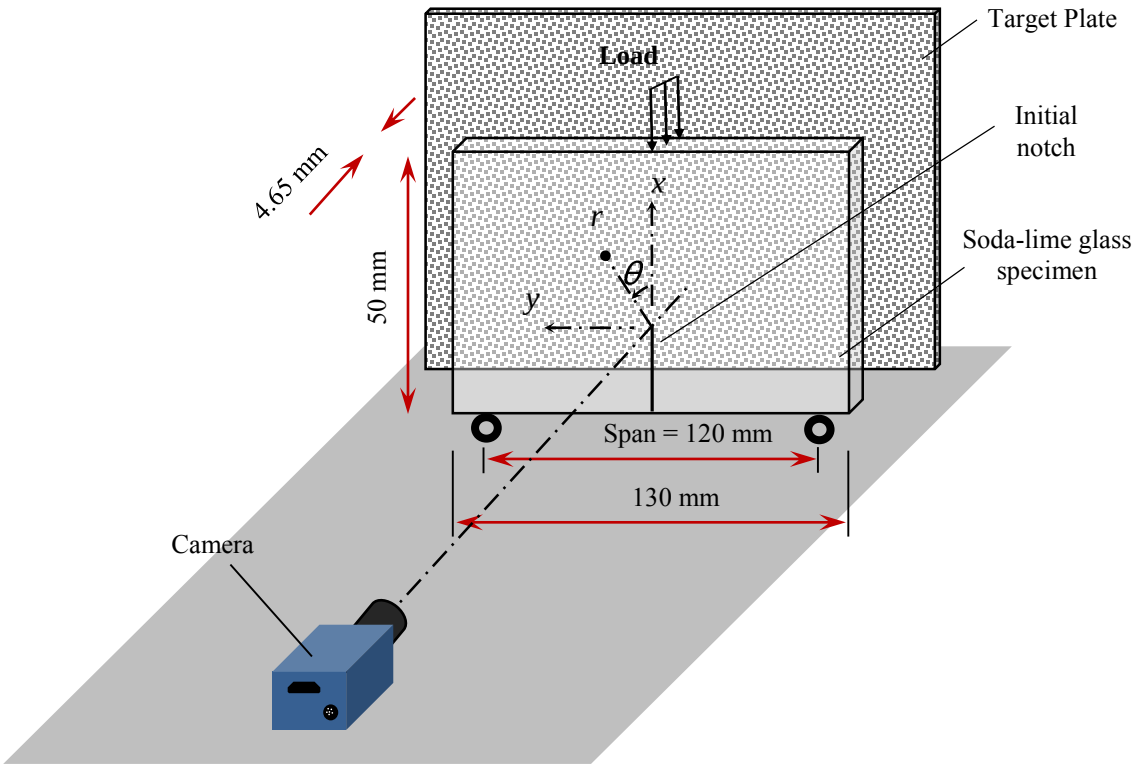

Figure 6.8: Loading configuration for quasi-static 3-point bending of an edge notched soda-lime glass plate.

The speckled target plate was placed behind the specimen at a distance of $\Delta = 712$ mm from the specimen mid-plane. A Point Grey Grasshopper3 digital camera fitted with a zoom lens of 18-108 mm focal length ($F^{\#}$ 5.6) was used to record speckles on the target plate. The camera was placed in front of the specimen at a distance (L) of approximately 445 mm with the camera focused on the target plate through the specimen. Two CFL lamps were used to illuminate the target plate uniformly.

A reference speckle image of the target plate was recorded through the crack-tip vicinity at approx. no-load (load < 5 N) condition. As the load was increased gradually, the perturbed images of the speckles on the target plate were recorded using time-lapse photography at 15 frames per minute. Two representative images, one in the reference state and the other in the deformed state, are shown in Fig. 6.9. The recorded images correspond to 63 mm x 58 mm region on the target plate which translates to approximately 24 mm x 22 mm on the specimen. Using a pair of reference dots (see, Fig. 6.9) marked on the target plate, the dimensions on the image in terms of pixels were related back to target plate dimensions (1 pixel = approx. 53 μm on the target plane) and then to the specimen dimensions (1 pixel = approx. 21 μm on the specimen plane). Sufficient care was also exercised to obtain a near Gaussian distribution of gray scales for each image in the mid-range of the gray scale by positioning the lamps appropriately. When looked carefully, it can be seen that the speckles are noticeably smeared in Fig. 6.9(b) around the notch-tip whereas the speckles seem largely unaffected away from it. The images were again correlated using ARAMIS® software. A facet/sub-image size of 25 x 25 pixels with an overlap of 20 pixels (i.e., step size of 5 pixels) was used during speckle correlation. The resulting data matrix was exported to MATLAB for post-processing including the evaluation of orthogonal angular deflections in the region of interest.

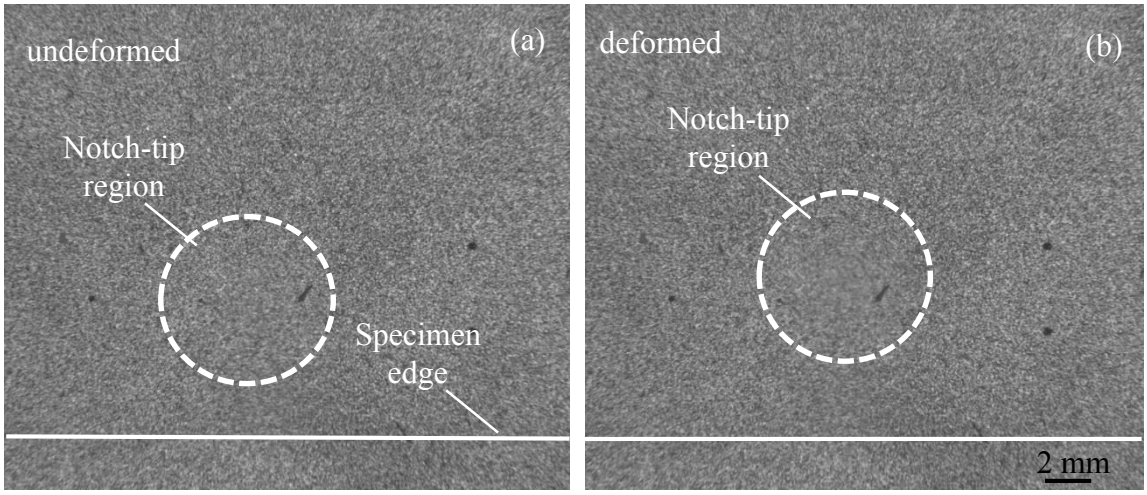

Figure 6.9: Speckle images in the undeformed (top) and deformed (bottom) states near the initial notch-tip recorded by the camera through the soda-lime glass specimen. (The notch is not in focus)

6.4.2 Stress Intensity Factors (SIFs)

Williams' asymptotic stress fields for angular deflections near a statically loaded mode-I crack-tip become [86, 90] ,

$$\phi_x = C_\sigma B \frac{\partial\left(\sigma_x + \sigma_y\right)}{\partial x} = C_\sigma B \sum_{N=1}^{\infty} A_N \left(\frac{N}{2} - 1\right) r^{\left(\frac{N}{2}-2\right)} \cos\left(\left(\frac{N}{2} - 2\right)\theta\right) \tag{6.3}$$

$$\phi_y = -C_\sigma B \frac{\partial\left(\sigma_x + \sigma_y\right)}{\partial x} = -C_\sigma B \sum_{N=1}^{\infty} A_N \left(\frac{N}{2} - 1\right) r^{\left(\frac{N}{2}-2\right)} \sin\left(\left(\frac{N}{2} - 2\right)\theta\right) \tag{6.4}$$

where (r, θ) denote the crack-tip polar coordinates, $A_1 = K_I \sqrt{\frac{2}{\pi}}$ with K_I being the mode-I stress intensity factor. (It should be noted that the dominant or the leading term of the crack-tip stress fields for $(\sigma_x + \sigma_y)$ remain unaffected in the classical Creager's solution [117] that takes into account the finite root radius.) In this experiment, the SIFs were evaluated using Eq. (6.3) by employing an over-deterministic regression analysis of the

measured data and $N = 4$. Discrete angular deflection values around the notch-tip in the region $0.5 \le r/B \le 1.5$ along with the angular extent of $-170^0 \le \theta \le -130^0$, $-110^0 \le \theta \le 110^0$ and $130^0 \le \theta \le 170^0$ were used in the regression analysis. This ensured that the data used was sufficiently close to the tip yet outside the region of significant stress triaxiality. This also indirectly helped to minimize the error while locating the crack-tip due to potential edge effects during image correlation. It should be noted that the *perspective effect* described in Section 6.3 was accounted for during the analysis. Error bars were obtained as a result of uncertainty in locating the crack-tip and by using various subsets of the region described above.

The angular deflection contours on the specimen plane in the two in-plane orthogonal directions at a select load of 880 N are shown in Fig 6.10. A heavy white line is overlaid on the resulting contours to represent the notch. The mode-I SIFs obtained from the regression analysis of measured data at different imposed load levels is plotted in Fig. 6.11. The mode-I SIFs evaluated from the load-cell measurements and the sample geometry [90],

$$K_I = \frac{F\,S}{Bw^{3/2}} \frac{3(\xi)^{1/2}\left[1.99 - \xi(1-\xi)\left\{2.15 - 3.93(\xi) + 2.7(\xi)^2\right\}\right]}{2(1+2\xi)(1-\xi)^{3/2}}, \qquad \xi = \frac{a}{w} \tag{6.5}$$

where F is the applied load, S is the span, B is the thickness of the specimen, w is the width of the specimen and a is the initial crack length are also plotted alongside the ones from DGS in Fig. 6.11. Evidently, there is a good agreement between the two.

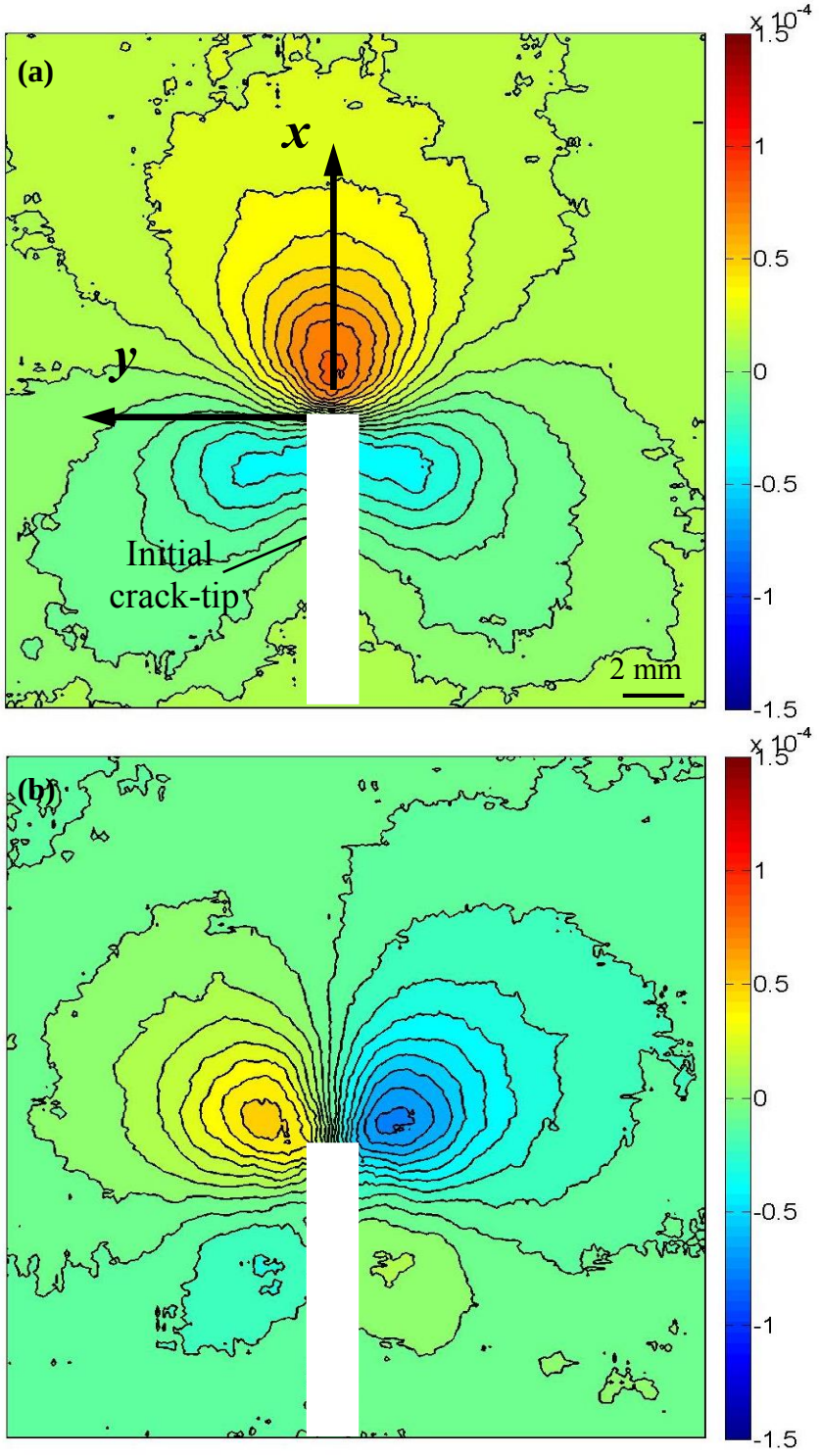

Figure 6.10: Angular deflection contour plots (contour interval = 8×10^{-6} rad) proportional to stress gradients of $(\sigma_x + \sigma_y)$ in the (a) *x*- and, (b) *y*-directions near the notch-tip for a soda-lime glass specimen under quasi-static 3-point bending load.

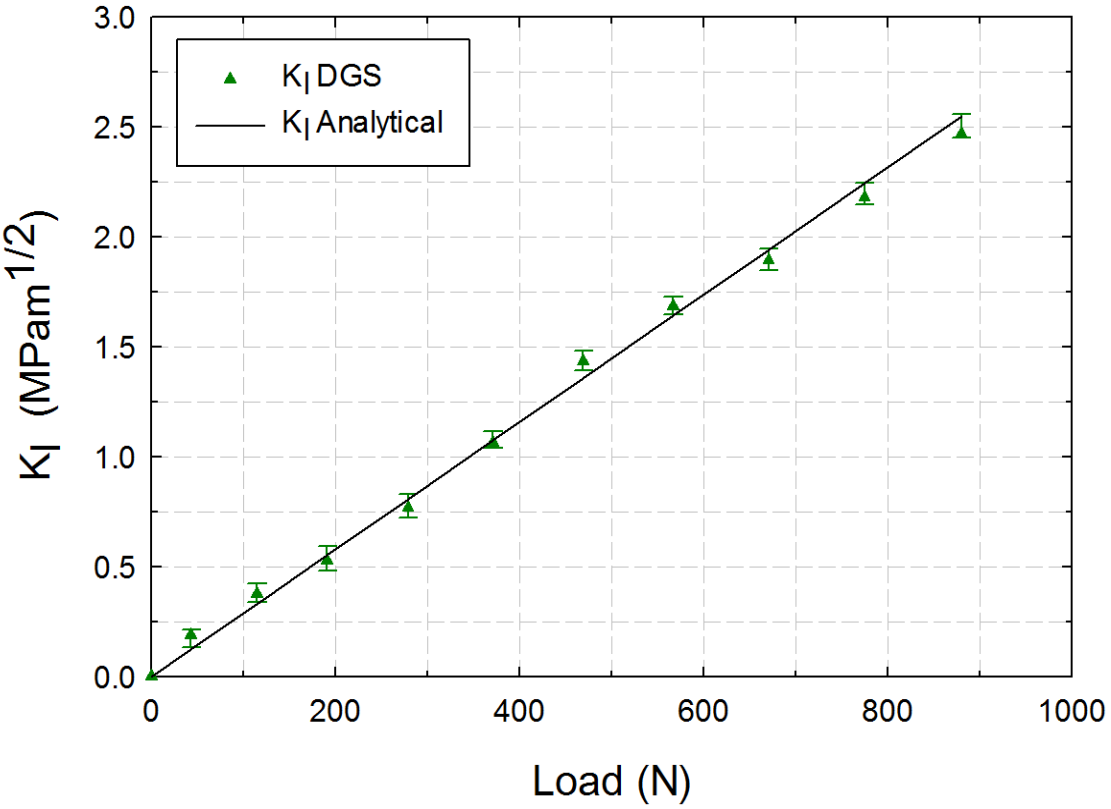

Figure 6.11: Comparison of mode-I stress intensity factors from DGS data and analytical expression.

6.5 Dynamic line-load on an edge of a plate

6.5.1 Experimental details

Next, the contact stresses due to a dynamically applied line-load on the edge of a planar glass sheet were studied using DGS. The schematic of the experimental setup is same as the one in Chapter 3. A 75 × 100 mm^2 rectangular sheet of glass specimen of thickness 5.65 mm was used for this experiment. The specimen was subjected to dynamic line-load using a Hopkinson pressure bar as shown in Fig. 6.12.

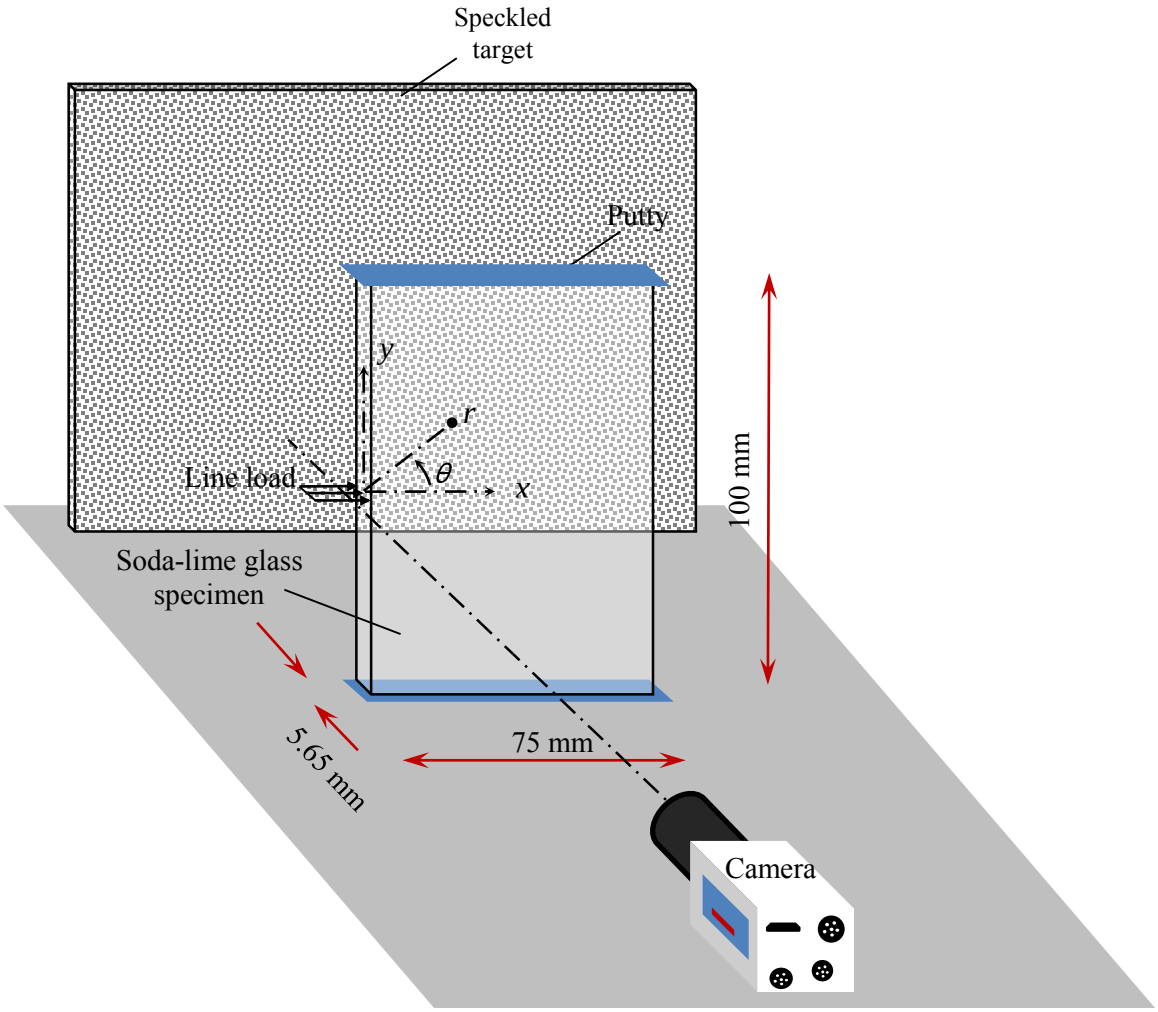

Figure 6.12: Schematic of the specimen loading configuration used to measure deformations due to dynamically imposed line-load on the edge of a soda-lime glass specimen (using a Hopkinson bar).

A Kirana model-05M ultrahigh-speed digital camera equipped with a single sensor of 924 x 768 pixels capable of storing 180 images in its on-board memory was used for recording the dynamic event. The speckles on the target plane were illuminated using two high-energy flash lamps (Cordin model 659). Other experimental parameters such as the trigger delay, flash duration, framing rate and image storage were all controlled using a standalone computer. A Nikkor 80-400 mm focal length macro zoom lens along with a

focal length doubler (2X teleconverter) and an adjustable bellows was used for imaging the speckles from a distance. Further, an aperture setting of $F^{\#}11$ was used to achieve a good exposure and a sharp focus during high-speed imaging. The camera was placed at a distance of 2362 mm in front of the specimen. A target plate coated with random black and white speckles was situated 1222 mm behind the specimen from the mid-plane of the specimen. As in the quasi-static experiments, a couple of black dots (see Fig. 6.5) were marked on the target plate to relate the image to the actual target dimensions. The region of interest in this study was around the contact region between the long-bar and specimen. Hence the camera was focused on a rectangular region of 125 mm x 102 mm (on the target plate or approx. 82 x 67 mm^2 region on the specimen plane) in the vicinity of the contact area. Care was exercised to achieve a near-Gaussian distribution of gray scales by adjusting the flash lamp location iteratively. The loading event was initiated by discharging compressed air in the gas-gun cylinder using a solenoid value to propel the striker placed inside the barrel. When the moving striker impacted the long-bar, it initiated a compressive stress wave that traveled the length of the bar before imparting a transient line-load to the specimen. The duration of the loading phase of the pulse generated was ~120 μs (see Fig. 6.14 inset). Also, a trigger pulse was generated when the striker contacted the long-bar which initiated recording of the speckles by the camera at 1 million frames per second with a 320 μs delay (selected based on the excursion time for the stress waves to travel the length the long-bar before loading the sample). The trigger pulse also operated the flash lamps. A strain gage affixed to the long-bar was used to measure the strain history and subsequently calculate the contact force history on the specimen. The delay started the camera to record

images well in in advance of the start of the loading event. This ensured capturing a reference image (image where there is no deformation in the specimen at all) to be used during image correlation step to be performed later on. Thus, a total of 180 images were recorded at 1 μs intervals between successive images with about 10-20 images before the loading phase of the specimen started. Using one of these images as the reference image, the entire series of deformed images were correlated to obtain the angular deflections in the region of interest.

As in the static experiments, the images were correlated using ARAMIS®. Each image was segmented into facets/sub-images consisting of 25 x 25 pixels during analysis. An overlap of 20 pixels (i.e., step size of 5 pixels) was used during image analysis. This resulted in a matrix of 146 x 177 data points in the region of interest for each of the two orthogonal angular deflection fields. The in-plane orthogonal deflections were subsequently evaluated using the known distance Δ between the specimen and the target planes.

6.5.2 Load history

This problem was approximated as a line-load imposed on the edge of an infinitely large plate. The assumption allowed using Flamant-like stress field (Eq. 6.2) to analyze the optical measurements. The instantaneous force, $F(t)$ in Eq. 6.2 was evaluated using over-deterministic least-squares analysis of the measured $\phi_x(t)$ fields. As described in the quasi-static counterpart, discrete angular deflection values around the loading point in the region $1 \le r/B \le 2$ along with angular extent of $-80^0 \le \theta \le -50^0$, $-40^0 \le \theta \le 40^0$ and

$50^0 \le \theta \le 80^0$ were used in the least-squares analysis. This ensured the elimination of regions of dominant stress triaxiality near the loading point. This also helped to avoid data along the free edges and zones where angular deflections are nearly zero. The load history was also evaluated from the strain gage measurements on the long-bar, $F(t) = E_b A_b \left(\varepsilon_I(t) + \varepsilon_R(t)\right)$ [85] where E_b (~72 GPa) and A_b (506.7 mm^2) are the elastic modulus and cross-section area of the long-bar, respectively, and ε_I and ε_R denote incident and reflected strain signals (see Fig. 6.14 inset).

The measured DGS contours (on the specimen plane) of angular deflections ϕ_x and ϕ_y for three select time instants are shown in Fig. 6.13. It should be noted that the contours near the free edge of the specimen show unavoidable edge effects due to finite sub-image size. Fig. 6.14 shows the plot of measured load histories from the strain gage along with the ones from optical data analysis. The load history extracted from DGS measurements is in good agreement with the load history obtained from the strain gage.

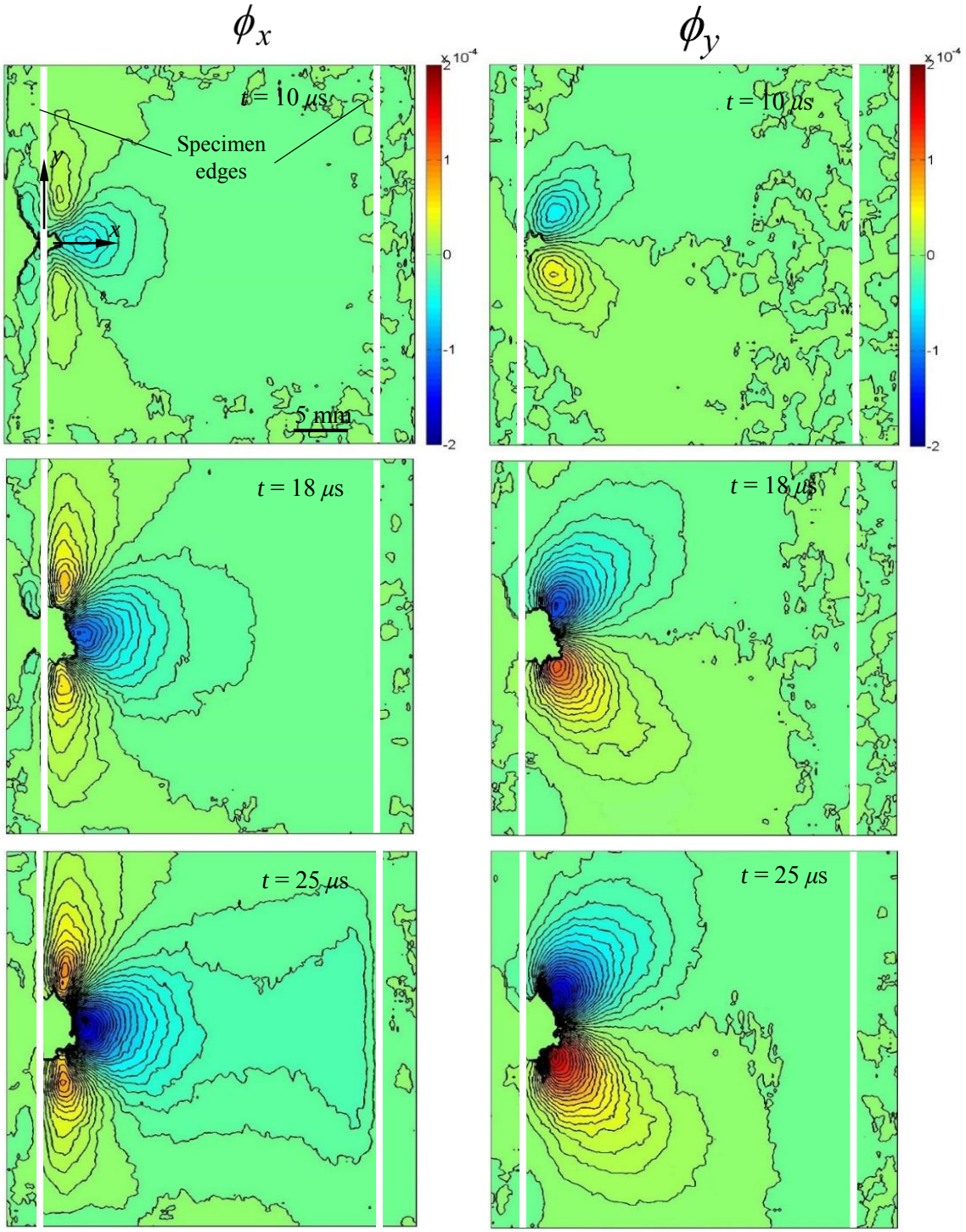

Figure 6.13: Angular deflection contour plots (contour interval = 8×10^{-6} rad) proportional to stress gradients of $(\sigma_x+\sigma_y)$ in the *x*- and *y*-directions for a soda-lime glass specimen subjected to dynamic line-load on its edge.

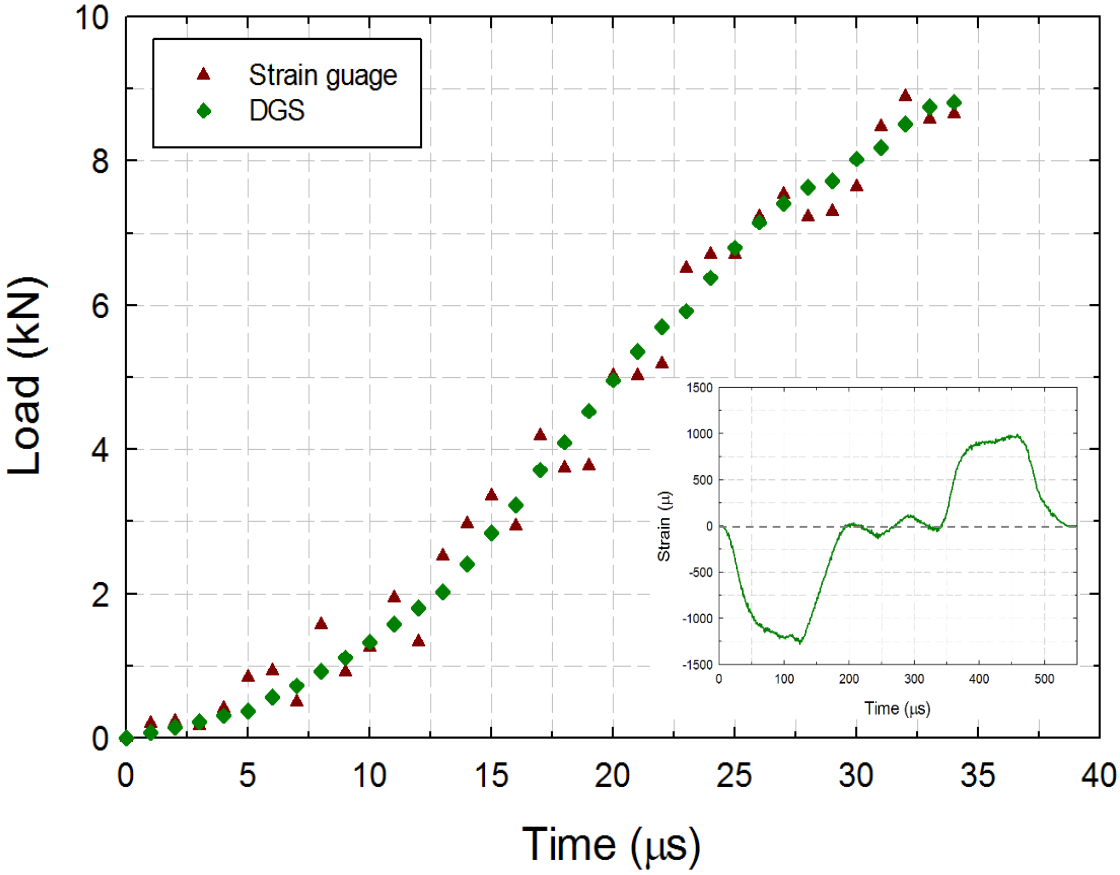

Figure 6.14: Compressive load history measured using DGS data near the impact point (green diamonds); Force history extracted from strain gage measurements on the long-bar (red triangles).

6.6 Dynamic crack-tip deformations

6.6.1 Experimental details

Next, the problem of a dynamically loaded stationary and rapidly growing mode-I crack problems were studied using DGS and ultrahigh-speed photography. The experimental setup used is same as that described in Chapter 4 except for the material of long-bar and striker bar. Both the long-bar and the striker-bar were made of maraging steel (C350) eliminating any impedance mismatch between them. The Hopkinson pressure bar

was used for loading a plate glass specimen. The plate glass sample had an initial edge notch of 12 mm length and 300 μm thickness and originated from the edge opposite to the loading edge. The sample was loaded symmetrically relative to the notch to dynamically initiate and rapidly propagate a mode-I crack. Fig. 6.15 shows the schematic of the specimen geometry and loading configuration.

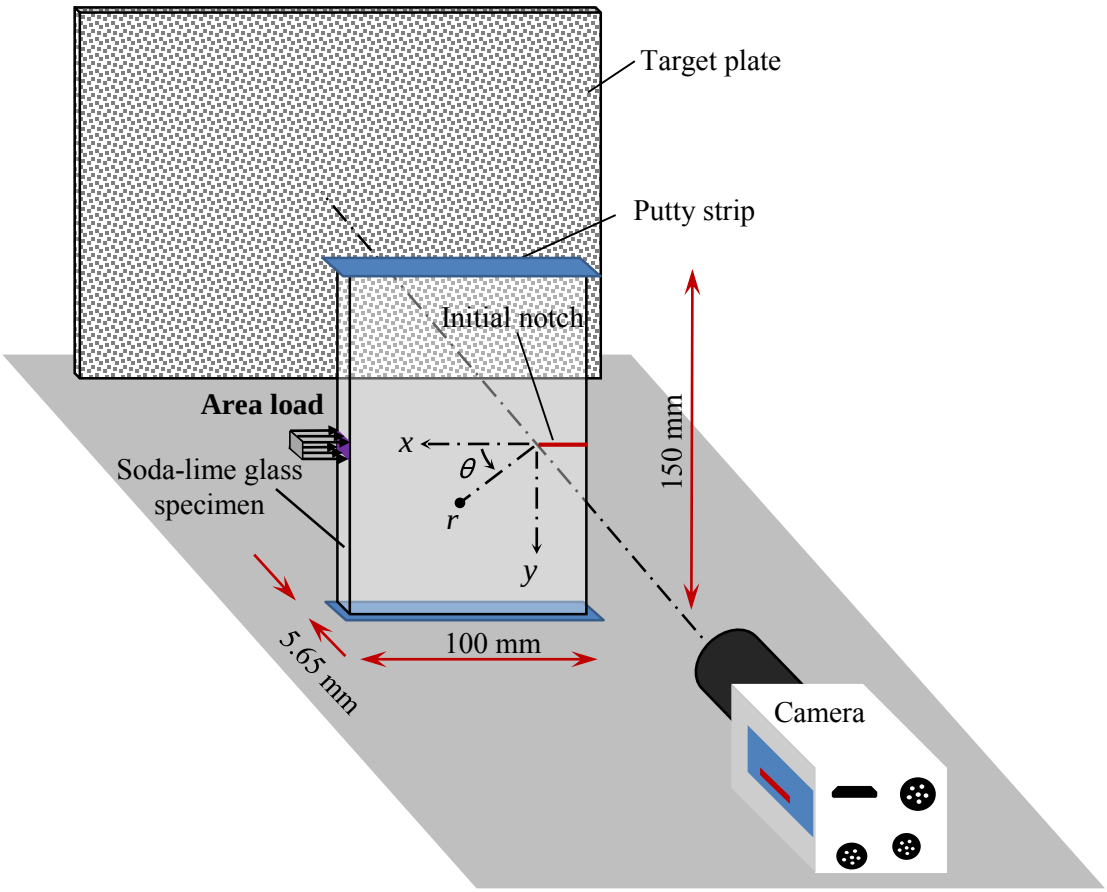

Figure 6.15: Schematic of the specimen loading configuration used in reverse impact fracture experiments on soda-lime glass. The load was imposed using a Hopkinson bar making an area contact with the specimen edge.

The recording of speckles on the target during the dynamic fracture event was done using Kirana model 05M camera assisted by a pair of high energy flash lamps to illuminate the target. The rest of the details are same as the one presented in the previous section. The region of interest in this part of the study was around the initial crack-tip; the camera was focused on a 93 mm x 77 mm region (on the target plate) through the vicinity of the initial notch tip. At the start of the experiment, the striker was launched towards the long-bar using the gas-gun. When the striker contacted the long-bar, a compressive stress wave was set-off in the long-bar which propagated along its length before loading the specimen over a small rectangular contact area associated with the tapered long-bar tip. The duration of the loading phase of the pulse generated was ~125 μs. When the striker contacted the long-bar, a trigger signal was also generated. This initiated recording of images at 1 million frames per second after a preset delay of 380 μs. The delay was set such that the camera started recording images well in advance so that a reference image (image where there was no load on the specimen) was available for subsequent correlation of all the recorded speckle images in the deformed state with the one from the undeformed or reference state. A total of 180 images recorded at 1 μs intervals approx. 20 images were recorded well before the sample started to experience stress wave loading. Also, two specimens were studied for establishing repeatability of the observed phenomenon.

Using a reference image, the entire series of recorded images were correlated to obtain instantaneous angular deflections at 1 μs intervals. The recorded image corresponds to approximately 61 x 51 mm^2 region of the specimen plane. (*Note that this region of interest is nearly same as the one used for performing DIC, described at the beginning of*

this chapter.) Each image was segmented into facets/sub-images consisting of 25 x 25 pixels during analysis. An overlap of 20 pixels (i.e., step size of 5 pixels) was used during image correlation. This resulted in a matrix of 146 x 177 data points in the region of interest for each of the two orthogonal angular deflection fields. Subsequently in-plane orthogonal deflections were evaluated using the known distance Δ between the specimen and the target planes.

6.6.2 Crack velocity and Stress Intensity Factor (SIF) histories

The position of the crack-tip in each digitized image was used to measure the instantaneous crack length. Subsequently, the crack velocity (V) was estimated from the crack length history using backward difference method. The perspective effect described in the previous section was taken into consideration during analysis to obtain both velocities and SIFs. The mode-I and mode-II SIFs were evaluated from an over-deterministic least-squares analysis of the crack-tip data in conjunction with the asymptotic equation (See Chapter 4 for details).

The two orthogonal angular deflection fields ϕ_x and ϕ_y (on the specimen plane) at three select time instants are shown in Fig. 6.16. They correspond to a time instant before crack initiation (t = -4 μs), at crack initiation ((t = 0 μs) and during mode-I crack growth (t = +4 μs). As expected, the two orthogonal angular deflection fields representing stress gradients in the direction along and perpendicular to crack growth are symmetric and antisymmetric, respectively, relative to the mode-I crack plane. Also, as noted at the

beginning of this Chapter, locating the tip of a hairline crack in soda-lime glass is quite challenging when random speckles are used/present in the images. However, locating the same after image analysis is relatively simple due to the singular nature of the crack-tip fields being measured. That is, in each of these images the crack-tip location can be identified easily by making use of the singular nature of the two orthogonal stress gradients along with symmetry or antisymmetry requirements for each field. The change in the contour sign along the *x*- and *y*-axes in these fields is very helpful in this regard. Also, shown in Fig. 6.16 are numerically integrated values of stress gradients resulting in contours of $(\sigma_x + \sigma_y)$ using a higher-order finite-difference-based least-squares integration (HFLI) scheme demonstrated in Ref. [118]. Evidently, the smoothing effect of the integration scheme based on the measured data (in columns 1 and 2) is evident in the contours with the essential features of the crack growth phenomenon in a finite plate. The left hand edge of the sample being loaded by the long-bar produces compressive stress waves as evident from the negative contour values adjacent to left vertical edge of the images. The right edge of the plate containing the initial notch shows positive stress contours hugging it, again consistent with the reflected compressive stress waves turning tensile upon reflection at the vertical free-edge. The crack-tip is surrounded by bean shaped (epicycloids) positive contours expected for $(\sigma_x + \sigma_y)$ $\left(\propto f(V) K_I(t) r^{-1/2} \cos(\theta/2)\right)$ based on linear elastic fracture mechanics.

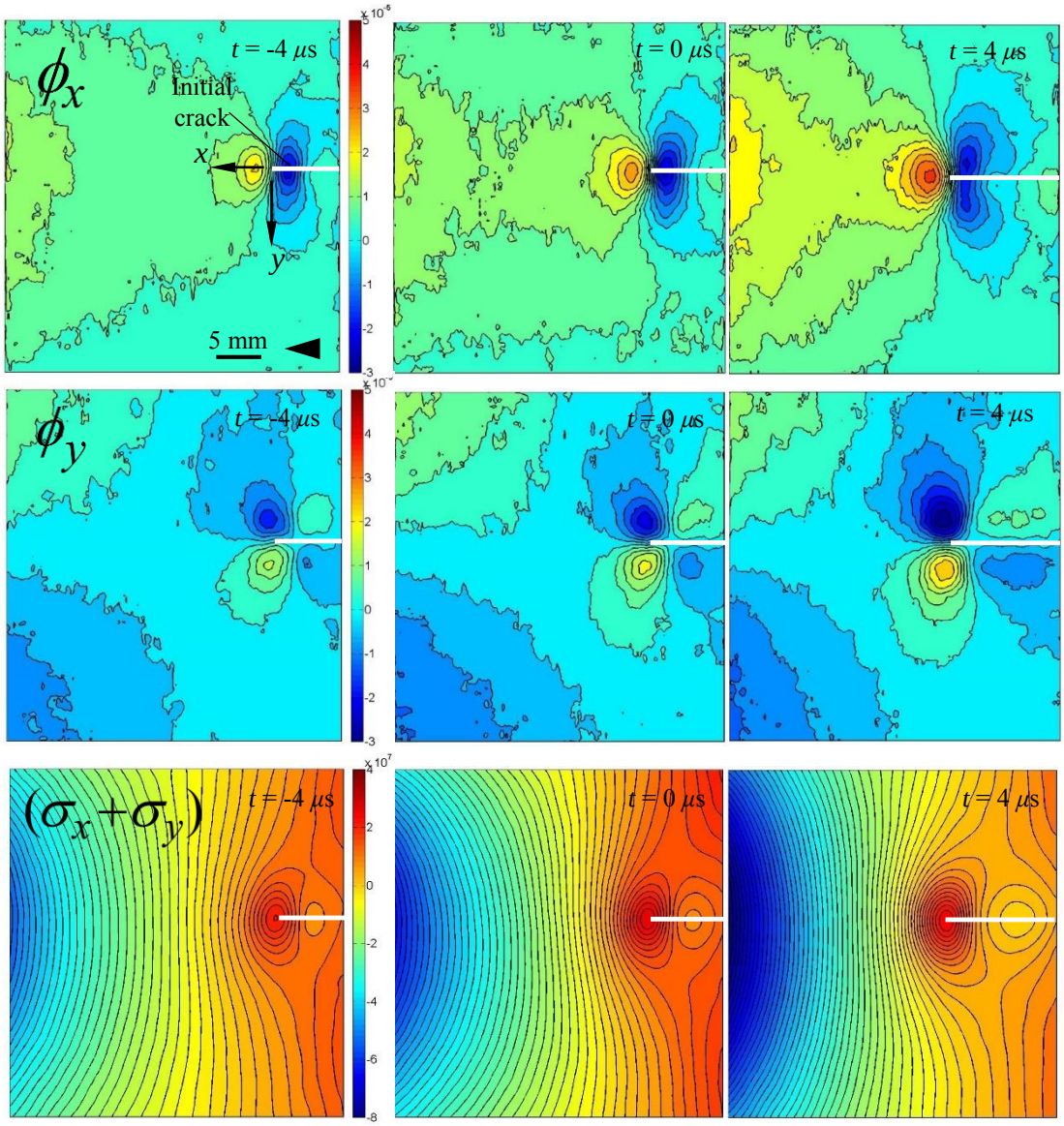

Figure 6.16: Angular deflection contour plots (contour interval = 4×10^{-6} rad) for a soda-lime glass SEN specimen subjected to dynamic edge loading along with the first stress invariant (contour interval = 2 MPa) obtained by integrating the DGS data using HFLI. The arrow shows the crack growth direction. (Note that t = 0 µs in these correspond to the crack initiation at original notch tip.)

Fig. 6.17 shows the crack velocity history during crack growth for two different specimens. The velocity histories for both the specimens essentially overlap on each other. It should be noted that the instantaneous crack-tip was located in each image after performing correlation with the reference image. The crack velocity increases from 0 to 1320 m/s within a few microseconds after initiation. Subsequently the crack reaches a stable velocity of ~1450 m/s which is similar to that reported by Doll [33]. This corresponds to a very high crack acceleration of approx. 3×10^8 N/m^2 (or $30 \times 10^6 g$, where g is the acceleration due to gravity). The photograph of the fracture surface during the steady crack growth region is shown as an inset in Fig. 6.17. It can be seen that during the stable crack growth, the crack surface shows a "mirror" like finish [26].

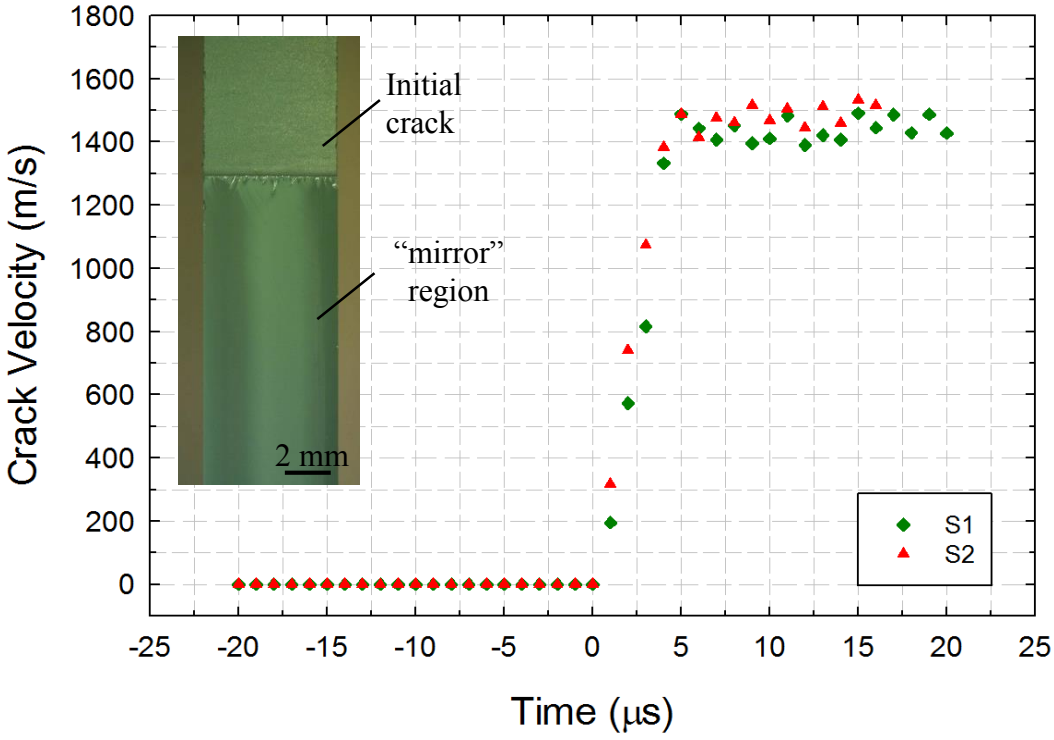

Figure 6.17: Velocity histories of propagating cracks from two different specimens, S1 and S2. Inset: photograph of fractured surface of the specimen. (t = 0 μs corresponds to crack initiation at the original notch tip.)

The optical fields measured using DGS were analyzed using least-squares analysis to extract the fracture parameter $K_I(t)$ before and after crack initiation. The stress intensity factors have been evaluated by fitting Eqs. (6.6) and (6.7) discussed earlier to the measured $\phi_x(t)$ data shown in Fig 6.18 as a time history (the SIFs for two different specimens tested are overlaid). The good agreement between the SIFs for both specimens shows good experiment repeatability and the robustness of the SIF extraction methodology. During the initial loading phase, the notch tip experiences a stress intensity factory evolution consistent with the loading phase of the stress pulse generated using the Hopkinson bar (see, inset). The monotonic and rapid increase in $K_I(t)$ occurs until crack initiation ($t = 0$) whereas $K_{II}(t)$ remains nearly zero as expected in this mode-I dominant configuration. Ideally, $K_{II}(t)$ should be zero for a mode-I crack, hence the non-zero values of $K_{II}(t)$ can be considered as the experimental error in the least-squares analysis. At crack initiation (average $K_I(t)$ ~0.81 MPa√m; dK_I/dt ~1.5x10^5 MPa√m/s) there is a distinct dip in the $K_I(t)$ history that punctuates unloading in the region of analysis. The post-initiation $K_I(t)$ values recover rapidly within a couple of microseconds and increase monotonically until the end of the observation window at progressively decreasing rates. The $K_{II}(t)$ in the post-initiation period also remains nearly zero suggesting that the crack was indeed traveling under dominant mode-I conditions.

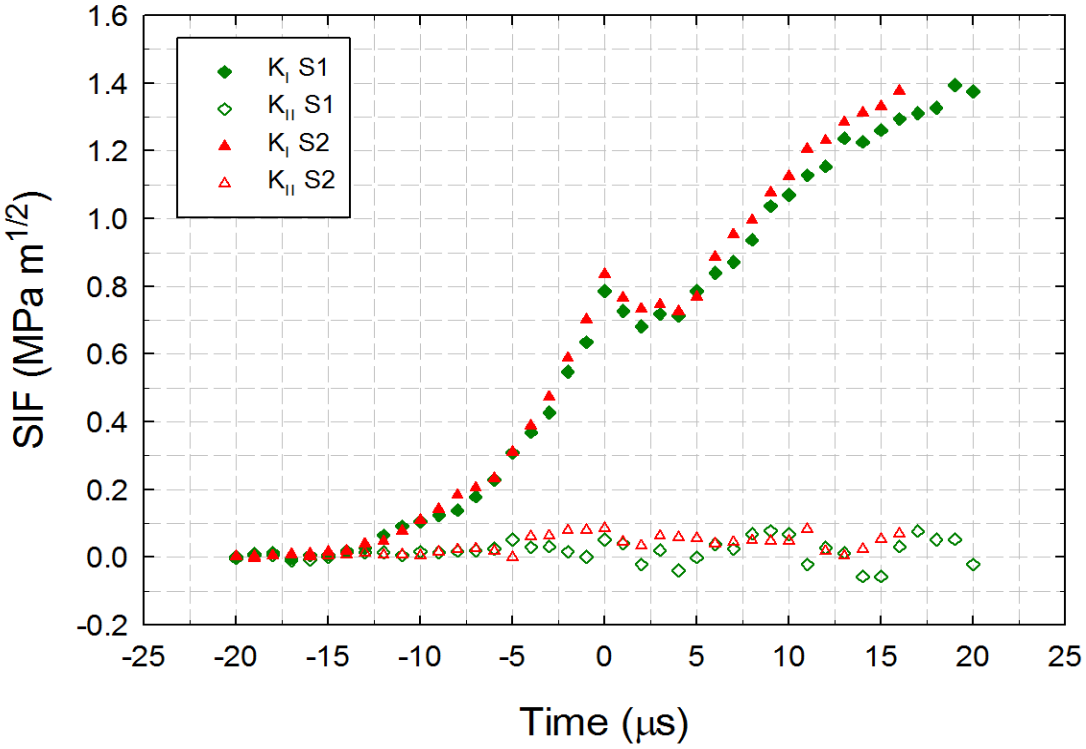

Figure 6.18: Stress intensity factors (SIFs) evaluated from experiments for two soda-lime glass specimens. (t = 0 μs in these correspond to the crack initiation at original notch tip.)

6.6.3 Finite element simulation

Complementary elasto-dynamic finite element simulations of reverse impact induced mode-I deformations in SEN glass specimen was carried out using ABAQUS®/Explicit structural analysis software. The specimen and loading configuration is shown in Fig. 6.15. The long-bar in the loading setup was also modeled for performing this simulation. The impact end of the long-bar was rectangular as in the experiments. The model consisted of 64,226 and 563,509 solid 3D tetrahedral elements, respectively. The discretized model with the crack opening displacements is shown in Fig. 6.19(a). The time steps during the analysis were automatically controlled by the time-integration scheme.

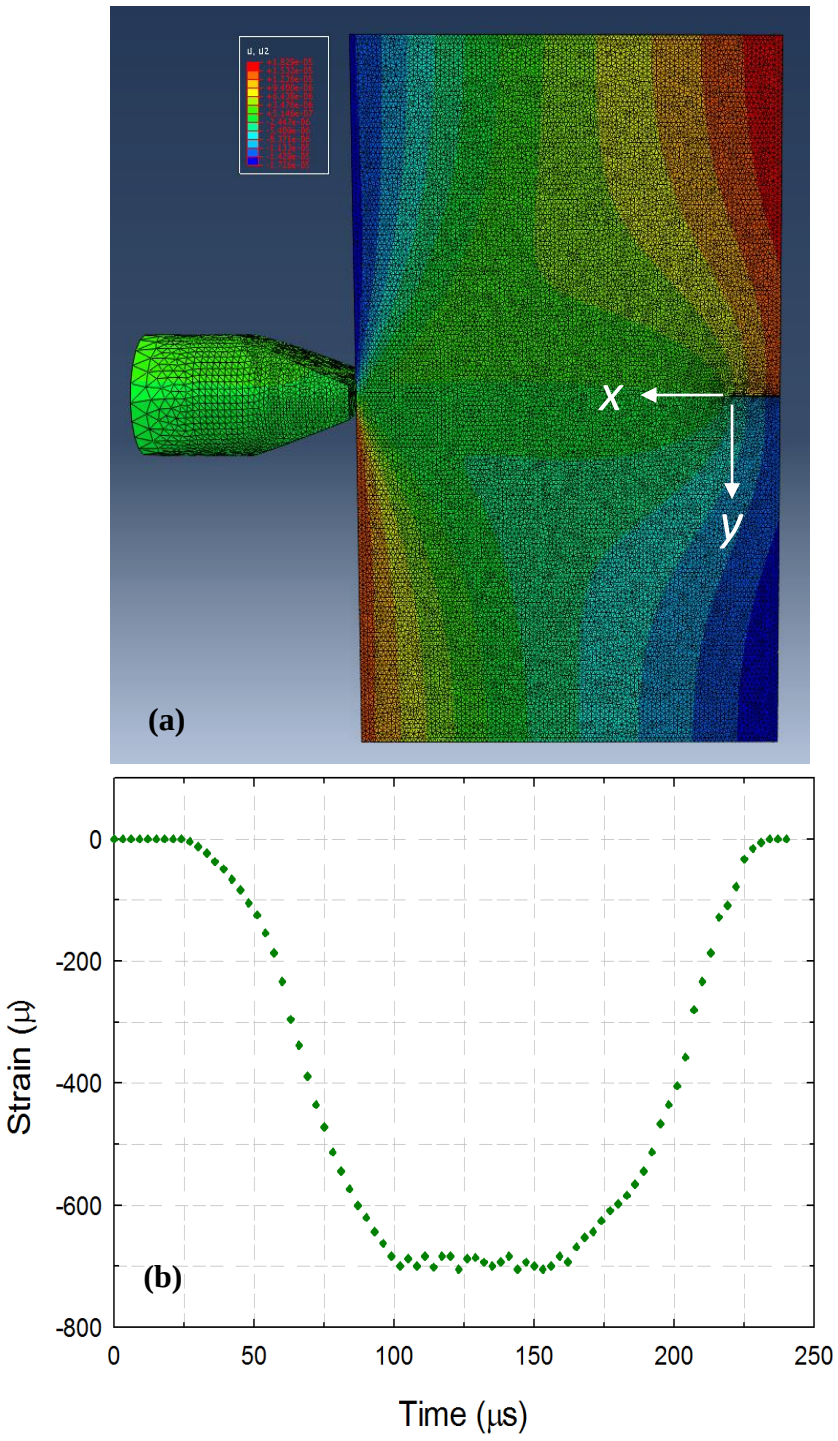

Figure 6.19: (a) Discretized finite element model of SEN soda-lime glass specimen subjected to dynamic edge loading with an overlay of displacements in the *y*-directions. (b) The strain history recorded on the Hopkinson bar used as input into the FE simulation.

Table 6.1 shows the material properties of soda-lime glass and the maraging steel long-bar used. The particle velocity obtained from strain gage readings (see Fig. 6.19 (b)) on the Hopkinson pressure bar experiment was input into the analysis. The instantaneous crack opening (v) and crack sliding (u) displacements were extracted along the two crack faces. This was repeated for each time step. The apparent mode-I and mode-II stress intensity factors, $(K_I)_{app}$ and $(K_{II})_{app}$ at each step were computed using [94],

$$(K_I)_{app} = \frac{E\sqrt{2\pi}}{8\sqrt{r}} v, \text{ and } (K_{II})_{app} = \frac{E\sqrt{2\pi}}{8\sqrt{r}} u; \quad (r, \theta = \pi) \tag{6.9}$$

Parameter	**Maraging Steel**	**Soda-lime Glass**
Density	8000 kg/m^3	2500 kg/m^3
Elastic modulus	200 GPa	72 GPa
Poison's ratio	0.3	0.22

Table 6.1: Dynamic material properties of maraging steel and soda-lime glass used for FE simulation.

The comparison of the computed $K_I(t)$ (for one of the two specimens) until crack initiation with the counterpart from FE simulations are shown in Fig. 6.20. It should be noted that the $K_{II}(t)$ value at crack initiation was forced to match the experimental counterpart in this comparison due to uncertainty in the time instant of impact and uncertainty in the material properties of the bar and the specimen. A good agreement between the measured and computed values of SIFs all the way back to the early time instants of loading can be seen.

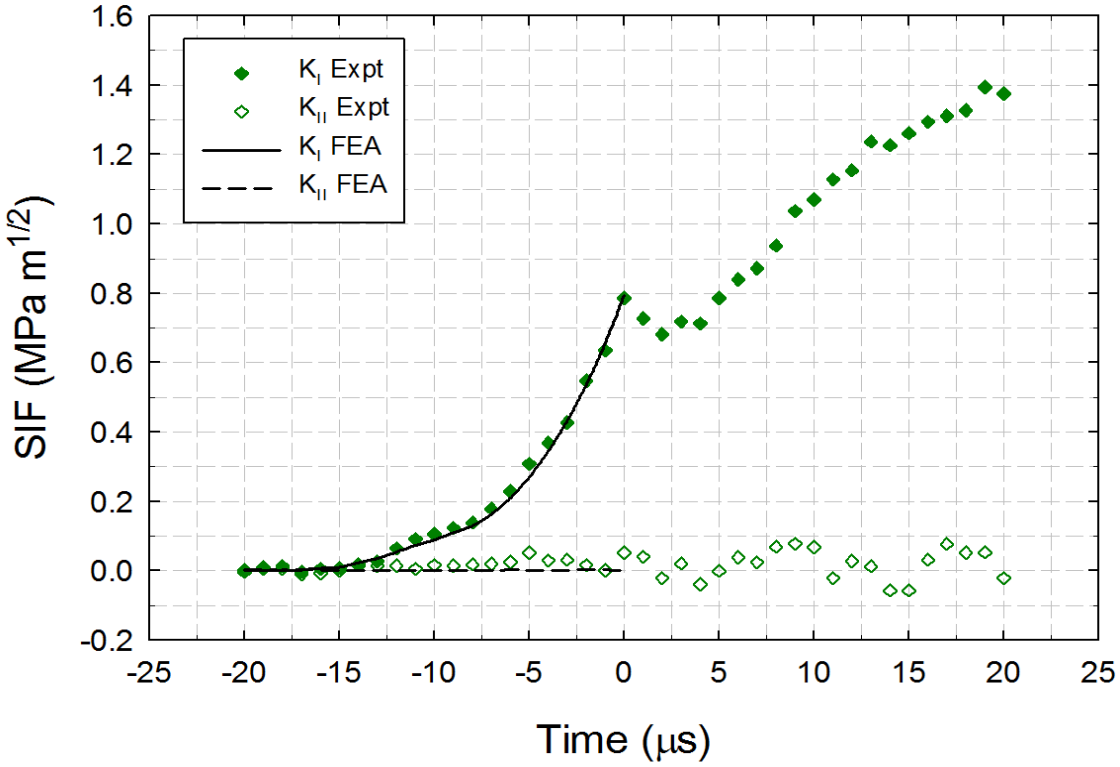

Figure 6.20: Stress intensity factors (SIFs) evaluated from finite element simulation upto crack initiation overlaid with SIFs from experiments for soda-lime glass specimen. (t = 0 μs in these correspond to the crack initiation at original notch tip.)

Chapter 7

DYNAMIC CRACK BRANCHING IN SODA-LIME GLASS SHEET

In this chapter, the phenomenon of dynamic crack branching in monolithic soda-lime glass is examined. First, the feasibility of two different specimen geometries (wedge loading and reverse impact) that produce crack branching during dynamic growth are investigated. The experimental details involving Hopkinson pressure bar used to dynamically load the specimen and the optical measurement technique are elaborated. The crack velocity and SIF histories leading up to, during, and after crack branching are reported and analyzed. Using the measured fracture parameters, a mechanism of crack branching is put forward.

7.1 Specimen geometry

A geometry and loading configuration needs to be selected to study dynamic crack branching in soda-lime glass caused by a propagating mode-I crack. There are different geometries to produce mode-I self-similar crack propagation under dynamic conditions. The two that are amenable for optical measurements are a reverse impact geometry and a wedge loading geometry. Both these geometries are shown schematically in Fig. 7.1(a)-(b). In the former geometry, Fig. 7.1(a), an initial notch was machined into one edge of the specimen and subjected to a compressive loading pulse on the opposite edge, in-line with the notch. The compressive stress waves upon reflection from the free surface (edge)

containing the crack turn tensile upon reflection and load the crack in mode-I conditions. The drawback of this geometry is that as the reflected tensile stress waves that load the crack-tip continuously interact with the incoming compressive stress waves as well as the waves reflected from other free edges. This influences crack propagation behavior.

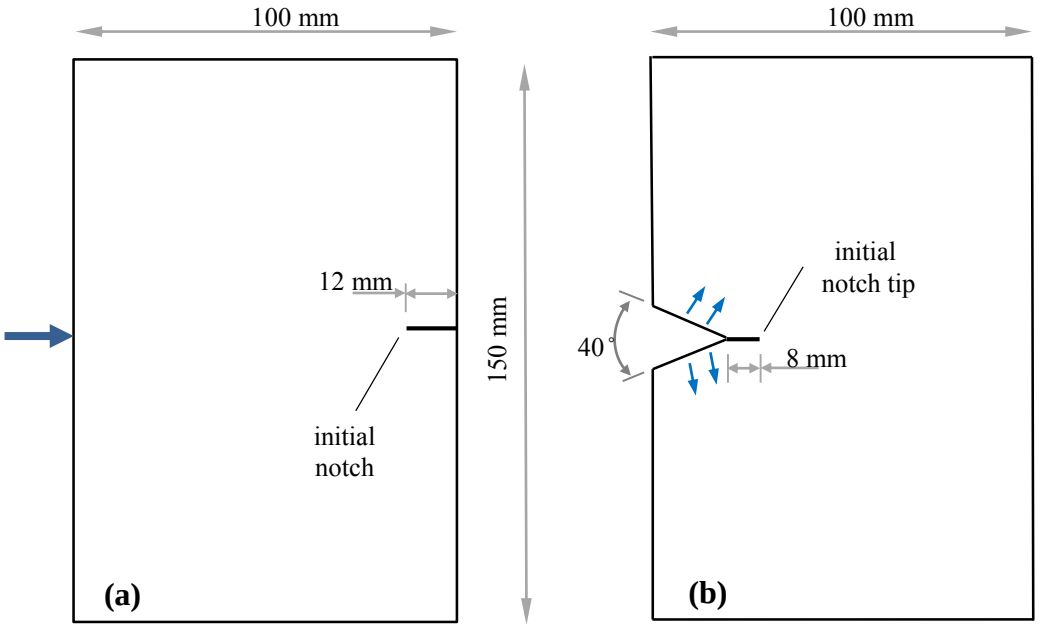

Figure 7.1: Loading and specimen geometries considered: (a) Reverse impact loading and (b) wedge loading.

In case of the latter geometry, Fig. 7.1(b), a V-notch is pre-cut into the specimen and further extended as the initial crack-tip. The specimen is loaded using a conforming wedge/chisel tip to impose a stress pulse. The flanks of the V-notch are loaded symmetrically by a contacting wedge driving a symmetric mode-I dynamic crack into the specimen. The crack-tip initially experiences tensile stress from the loading pulse as it initiates and propagates. The crack-tip starts to experience the reflected stress waves only after propagating certain distance in the material depending on the size of the specimen.

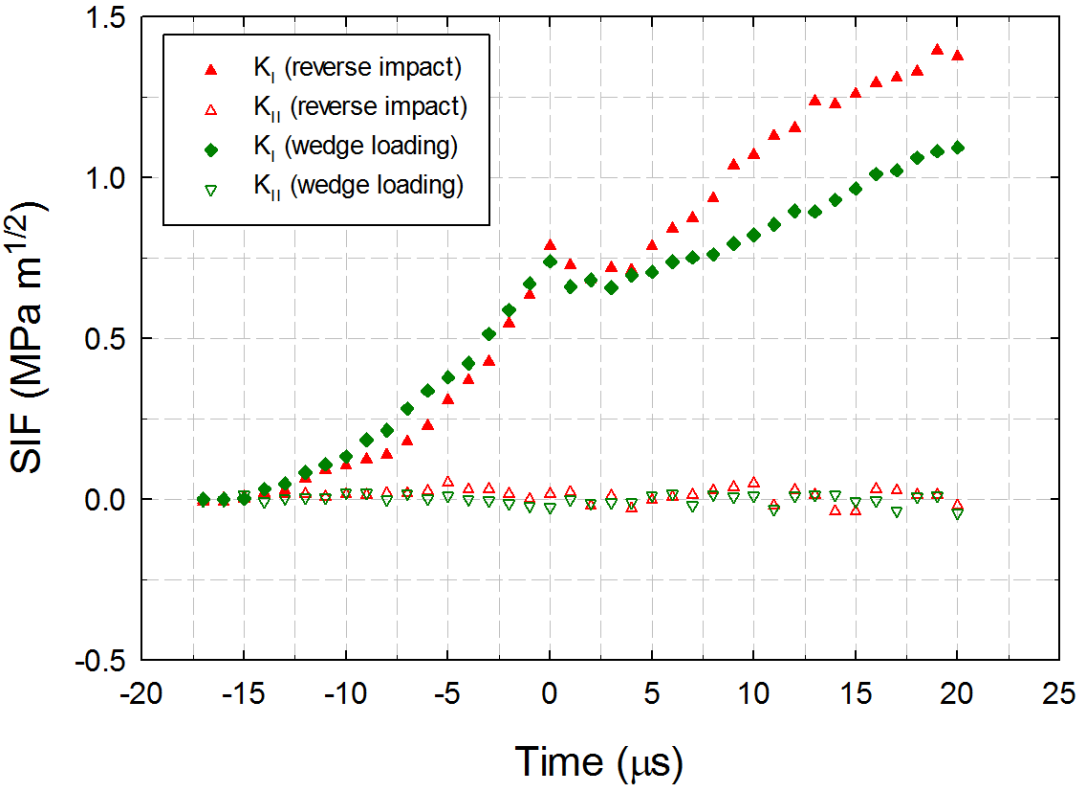

Figure 7.2 The mode-I and -II SIF histories for soda-lime glass specimen loaded using reverse impact and wedge loading configuration.

This effect can be readily seen in the SIF histories as well and are shown in Fig. 7.2 in these two geometries. The details of the experimental setup, optical measurements and analysis are same as described in Chapter 6. It can be seen that mode-II SIFs are nearly zero for both the loading geometries as expected. The reverse impact geometry shows a steeper increase in mode-I SIF during both pre-initiation as well as post-initiation regimes when compared to the wedge loaded counterpart. The crack initiated at nearly the same SIF in both the geometries with a marginally lower value for wedge loaded geometry. This difference in the slope of the SIF histories is attributed to the interaction of reflected stress waves from the boundaries in case of reverse impact geometry whereas in wedge loaded

geometry there is no interactions of reflected stress waves occur until the crack propagates significant distance in the specimen.

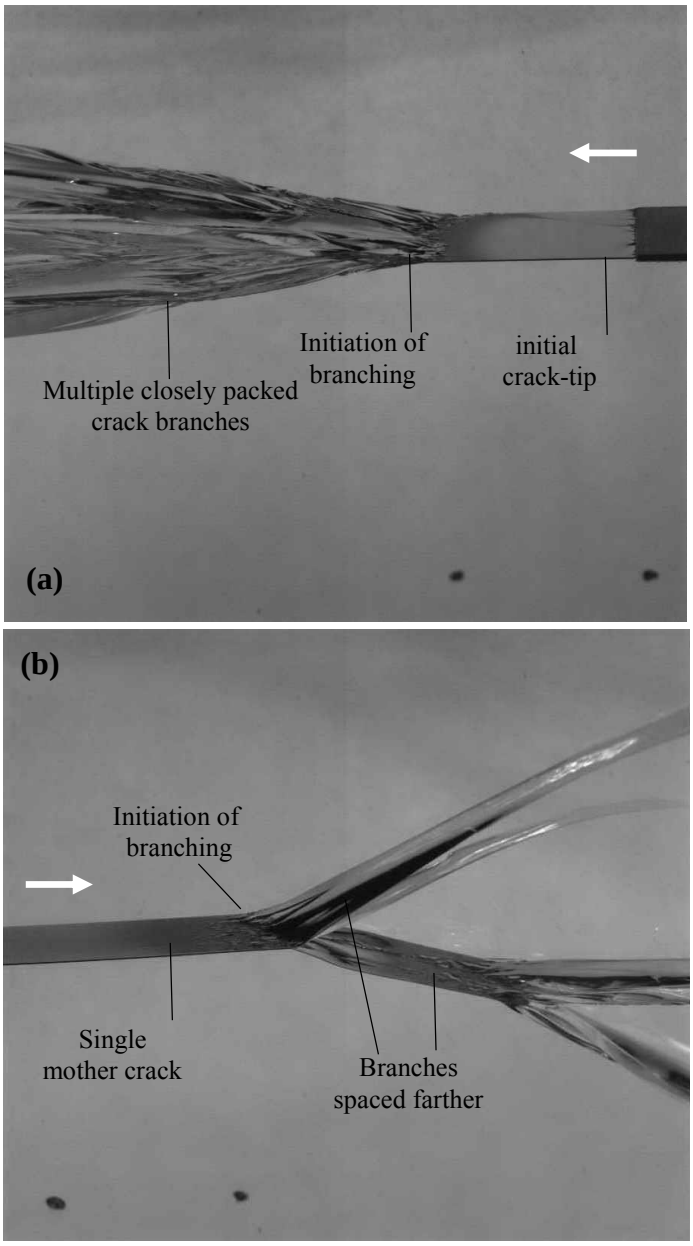

Figure 7.3: Photographs of fractured specimen for (a) reverse impact and (b) wedge loading configurations. The two black dots on the photographs are 10 mm apart on the specimen plane. White arrow shows the crack growth direction

Further, this effect of geometry translates to crack growth morphology as well. The photographs of fracture fronts in these two geometries are shown in Fig. 7.3. It can be seen that in Fig. 7.3(a) the crack branches into a fan of cracks with a relatively small angle between them whereas in Fig. 7.3(b) the crack branches into two at a large angle. It is challenging to make optical measurements and study the crack branching phenomena when multiple crack-tips in close vicinity interact with each other. Hence the wedge loading geometry was chosen over reverse impact geometry for this study.

7.2 Experimental details

The optical method of DGS in conjunction with high-speed photography was used to study dynamic crack branching in soda-lime glass. The experimental setup is same as the one described in Chapter 4 except for the use of maraging steel striker and the long-bar. A 150 mm x 100 mm x 4.65 mm rectangular specimen with a 'V' notch was machined into commercially procured soda-lime/plate glass (see Fig. 7.4). The 'V' notch was extended by 8 mm using a diamond impregnated circular saw of 300 μm thickness. (The notch length was more than in the polymeric counterparts to limit interactions between the V-notch tip and the crack-tip to generate a quiescent crack initiation.) The schematic of the specimen configuration and the loading geometry is shown in Fig. 7.4. The Hopkinson pressure bar (or the long-bar) was used to wedge load the specimen. The experimental details and image analysis are again same as the one described in Chapter 6. An additional measurement namely, the resultant angular deflection, ϕ_r, was obtained from measured in-plane orthogonal angular deflections using the expression, $\phi_r = \sqrt{\phi_x^2 + \phi_y^2}$.

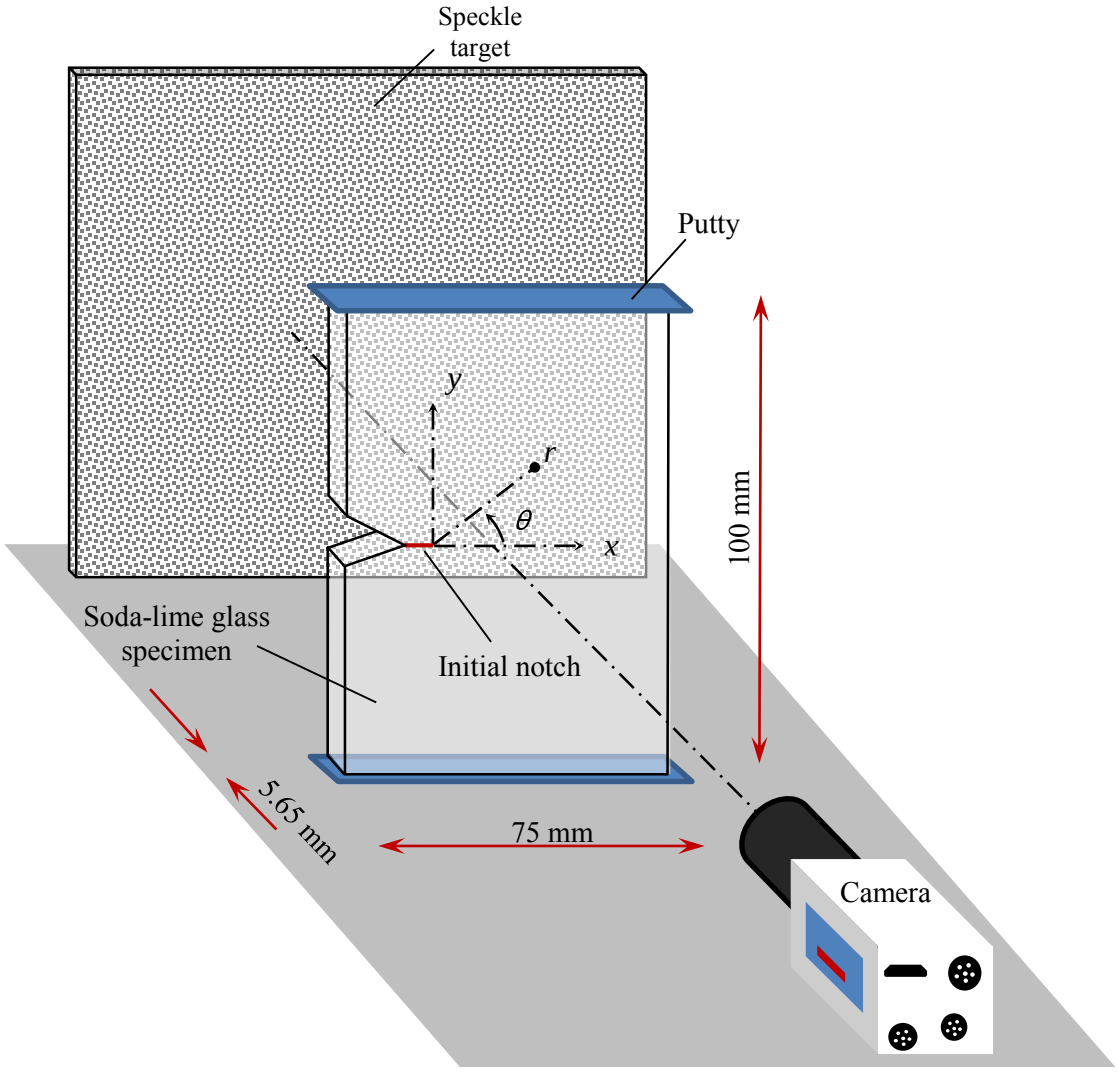

Figure 7.4: Schematic of the specimen loading configuration used to measure deformations due to dynamically imposed line-load on the edge of a soda-lime glass specimen using a Hopkinson bar (not shown).

7.3 Evaluation of crack velocity and Stress Intensity Factor (SIF) histories

The position of the crack-tip was determined from the measured angular deflection fields, specifically ϕ_x and ϕ_r. Using the crack-tip location, the instantaneous crack length and subsequently the crack velocity (V) were estimated using backward difference method. The

SIFs were evaluated the same way as described in Chapter 4. The data in the region $0.5 \le r/B \le 1.5$ and angular extent $-170^0 \le \theta \le -130^0$, $-110^0 \le \theta \le 110^0$ and $130^0 \le \theta \le 170^0$ near the crack-tip was used for analysis. The perspective effect described in Chapter 6 was taken into consideration during analysis to obtain both crack velocities and SIFs.

7.4 Crack path and angular deflection measurements

Fig. 7.5 shows the photograph of the fractured specimen. It can be seen that a single crack that originated from the initial notch branched into two nearly symmetric daughter cracks, each inclined at an angle 24˚relative to the initial crack growth direction.

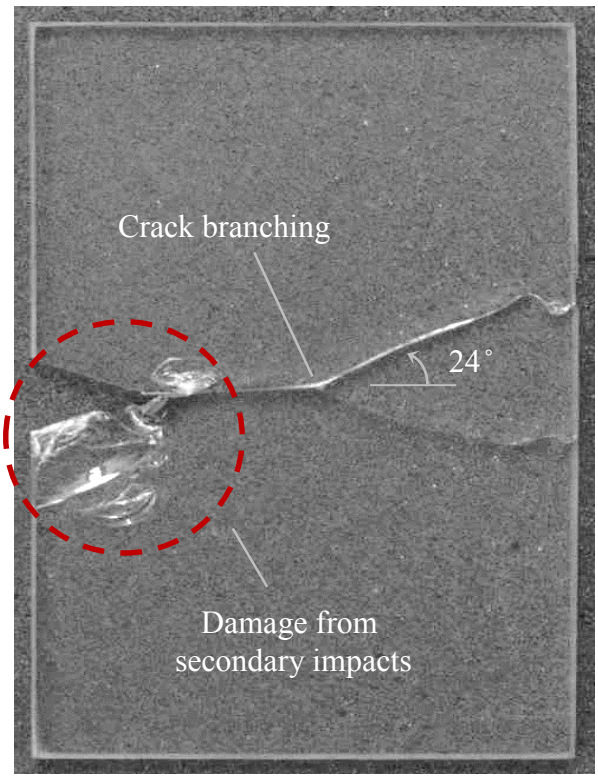

Figure 7.5: Photograph of typical fractured specimen.

Two representative images recorded by the camera, one in the undeformed and another in the deformed states, are shown in Fig. 7.6. The deformations around the propagating crack-tip are not apparent in the deformed image unless observed closely. However, these deformations become very evident when the speckle image pairs are correlated to obtain the angular deflections. The two orthogonal angular deflection fields ϕ_x and ϕ_y along with the resultant angular deflection ϕ_r, all defined on the specimen plane, at three select time instants are shown in Fig. 7.7. They correspond to a time instant before crack branching (t = 14 μs), soon after crack branching (t = 22 μs) and at a later time instant during mixed-mode crack growth of the two resulting daughter cracks (t = 30 μs). As expected, the two orthogonal angular deflection fields representing stress gradients in the direction along and perpendicular to the initial mode-I crack growth are symmetric and antisymmetric, respectively, relative to the crack plane. Also, locating the tip of a hairline crack in soda-lime glass is quite challenging when random speckles are present in the images. However, locating the same after correlating the speckle image pairs is simpler due to the singular nature of the crack-tip field being measured by DGS. In this work ϕ_x and ϕ_r were used to locate the propagating crack-tip as mentioned in the previous section.

The digitized location of crack-tip obtained from ϕ_x and ϕ_r fields are shown in Fig. 7.8. The *x*-*y* domain shown is the ROI with the left bottom corner of the ROI as the origin (0, 0). The crack-tip locations obtained from both these fields match very well.

Further, locating the crack-tip location from the measured ϕ_r field is relatively straight forward as they form closed loops of zero magnitude around the crack-tip.

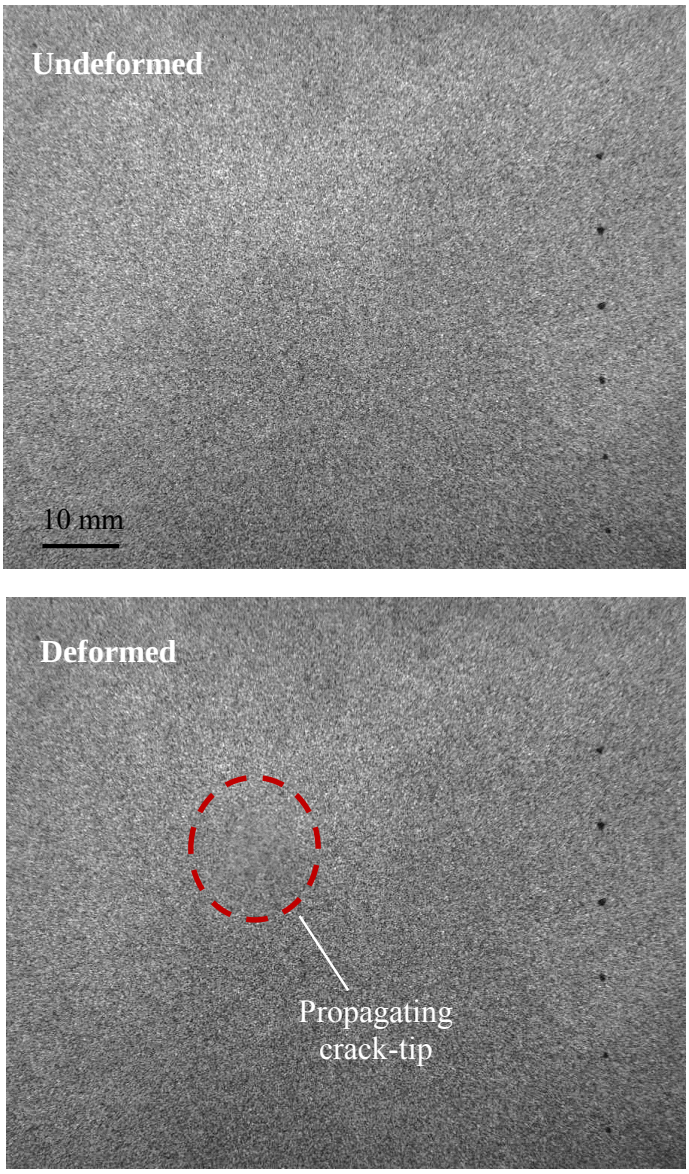

Figure 7.6: Speckle images in the undeformed (top) and deformed (bottom) states for a propagating crack-tip recorded by the camera through the soda-lime glass specimen. (Very little can be gathered directly from these images apart from a slightly smeared speckle region around the vicinity of the growing crack.)

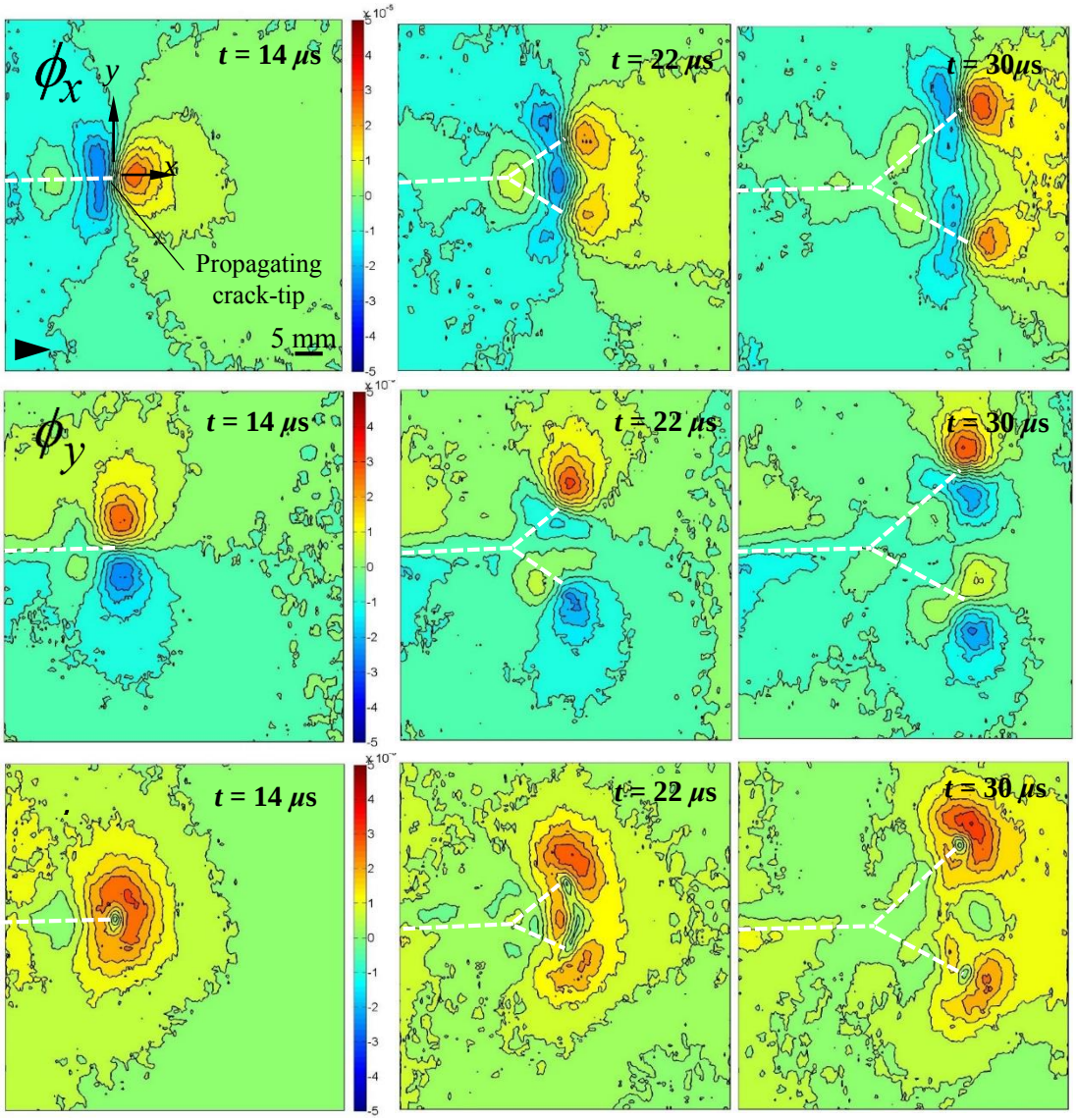

Figure 7.7: Angular deflection contour plots (contour interval = 5×10^{-6} rad) for a soda-lime glass subjected to dynamic wedge loading. The arrowhead shows the crack growth direction. Dotted white lines are overlaid on the plot to show the approximate crack path. (Note that t = 0 μs in these correspond to the crack initiation at original notch tip.)

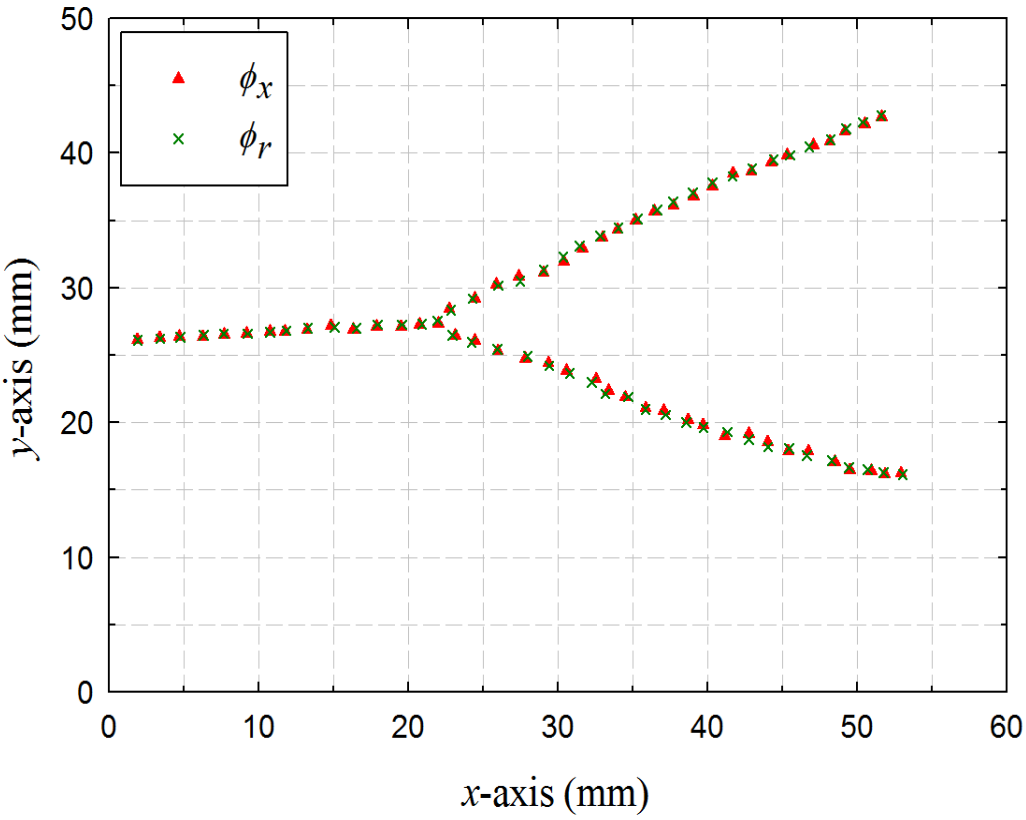

Figure 7.8: Crack-tip locations obtained from measured angular deflections of ϕ_x and ϕ_r

.

Also shown in Fig. 7.9(a)-(c) are numerically integrated values of stress gradients using a higher-order finite-difference-based least-squares integration (HFLI) scheme resulting in contours of $(\sigma_x + \sigma_y)$ as demonstrated by Miao et al. [118]. In Fig. 7.9(a), where the single crack is propagating in the material, it is surrounded by bean shaped (epicycloids) positive (tensile) contours expected for $(\sigma_x + \sigma_y)$ $\left(\propto f(V) K_{II}(t) r^{-1/2} \cos(\theta/2)\right)$ based on linear elastic fracture mechanics.

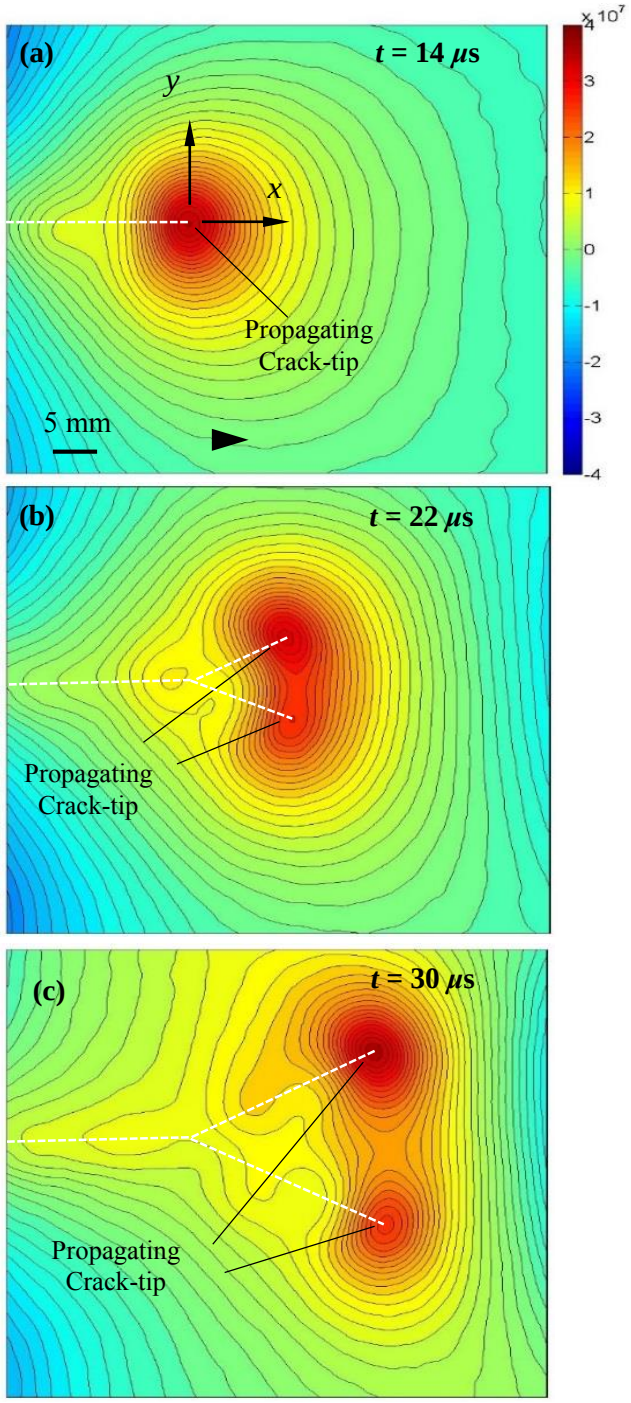

Figure 7.9: Contours of $(\sigma_x + \sigma_y)$ (contour interval = 1.5 MPa) for a soda-lime glass specimen subjected to dynamic wedge loading obtained by integrating the DGS data using HFLI. The arrowhead shows the crack growth direction. Dotted white lines are overlaid on the plot to show the approximate crack path. (Note that t = 0 μs in these correspond to the crack initiation at original notch tip.)

As expected, the maximum tensile stress is observed at the crack-tip location. As we move away from the crack-tip, the stresses reduce to zero and later change to negative values attributed to reflected stress waves from the boundaries. After the occurrence of crack branching, the two dominant daughter cracks with distinct stress singularities are produced as seen in Fig 7.9(b). The two daughter crack-tips are very close to each other and hence interactions between them could be significant. Hence, they could not be satisfactorily analyzed due to the limited spatial resolution. Despite this, the two crack-tips can be located clearly as evident from the plot. The bottom crack-tip shows a slightly lower peak stress relative to the upper one, suggesting that their SIFs may be different at this time instant. Fig. 7.9(c) shows the stress contours when the two propagating daughter cracks are better separated when compared to the one in Fig. 7.9(b). The crack-tips can be located clearly in this case as well. Further, it should be noted that these stress plots can also be used to determine the instantaneous propagating crack-tip location as the 'center' of the peak tensile stress contour value in the event an independent evaluation of crack-tip location is necessary in addition to angular deflection fields is necessary.

7.5 Crack velocity histories and fractography

Fig. 7.10 shows the crack velocity history based on the crack length measured from the digitized crack-tip location shown in Fig. 7.8. In the initial region of steady propagation, the crack velocities range from 1400 m/s to 1600 m/s. This velocity range is similar to that reported by Doll [33] and Field [31]. As the crack approaches the branching phase, the crack evidently slows down to 1000 m/s - 1100 m/s. Next, as the crack branches into two

dominant daughter cracks, the velocity increases rapidly to about 1900-2000 m/s almost instantaneously, within 1-2 μs. Later the crack velocities drop down to the initial steady state value of 1400-1600 m/s. As the daughter cracks propagate, velocities marginally reduce to 1300 m/s to 1500 m/s. Again, this trend is somewhat similar to that observed in an experimental investigation by Field [31] and recently simulated by Ha and Bobaru [43] by using peridynamics. The photographs of the fracture surface during steady crack growth and subsequent branching is shown in Fig. 7.11(a)-(c). It can be seen that during the 'stable' crack growth phase, the crack surface shows a "mirror" like finish as evident in Fig. 7.11(a). After stable crack growth, the onset of instabilities is accompanied by the "mist" region as shown in Fig. 7.11(b). The instabilities continue to magnify until when crack branching becomes imminent. This is characterized by the onset of the "hackle" region identified in Fig. 7.11(c). Once the fracture surface begins to 'hackle,' the crack branching is generally the outcome unless external interference in form of a compressive stress is imposed on the crack by using geometry or a second stress wave generator as in Ravi-Chandar and Knauss [24]. Following crack branching, the crack surfaces turn back to the "mirror" condition suggesting the return of stable crack growth as shown in Fig. 7.11(d).

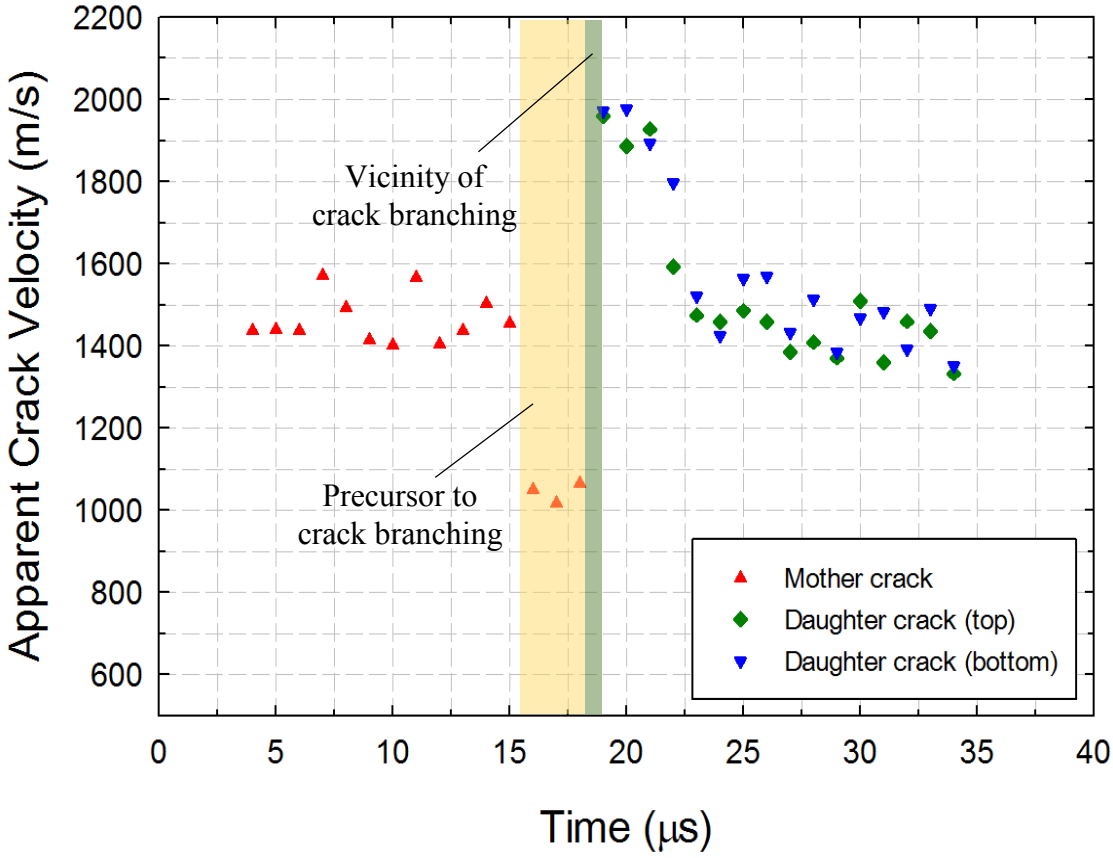

Figure 7.10: Apparent velocity histories of propagating crack along with the velocities of the both the daughter cracks after branching. (t = 0 μs corresponds to crack initiation at the original notch tip.)

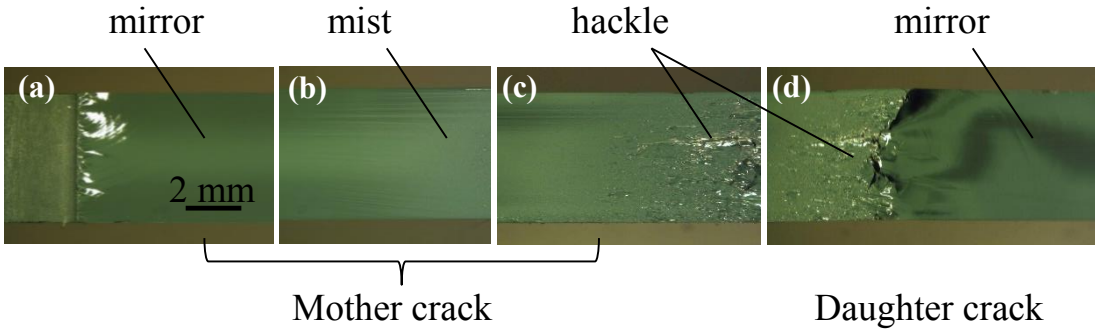

Figure 7.11: Photograph of the fracture surface showing the (a) "mirror" region soon after initiation, (b) "mirror" to "mist" transition region as the instabilities set in, (c) "mist" to "hackle" region as instabilities increase until crack branching is imminent, and (d) "hackle" to "mirror" region soon after the crack has branched.

7.6 Stress intensity factor histories

The SIF histories of growing crack/s corresponding to the pre- and post-crack branching event are shown in Fig. 7.12. With time $t = 0$ μs representing crack initiation at the original crack-tip, the mode-I SIF values for the mother crack increase approx. between 4 to 8 μs ('mirror' zone). The mode-I apparent SIFs between 8-13 μs seem to be nearly constant as the crack transitions from 'mirror' to 'mist' behavior. Subsequent mode-I SIF values show an increasing trend as the crack enter the 'hackle' phase between 13-19 μs. During this entire 'mirror' to 'hackle' transition, mode-II SIF are nearly zero (to within the accuracy of SIF determination using least-squares analysis of optical data) as expected for mode-I crack growth. The mode-I mother crack branches into two mixed-mode daughter cracks (upper and lower branches) at 20 μs and the mode-I values in the next several frames show a noticeable dip in the mode-I SIF whereas the corresponding mode-II values show a jump in magnitude but are of the opposite sign. Following branch formation, both the mixed-mode daughter cracks show a tendency to attain a locally mode-I state as evident from a precipitous drop in the magnitude of K_{II} to near zero value whereas the corresponding K_I values gradually increase but to levels corresponding to the 'mirror' and 'mist' states in the window of observation up to 35 μs. It should be emphasized that though there are significant uncertainties in the SIF values soon after crack branching occurs, say for a couple of data points, the overall trends conform to the description presented.

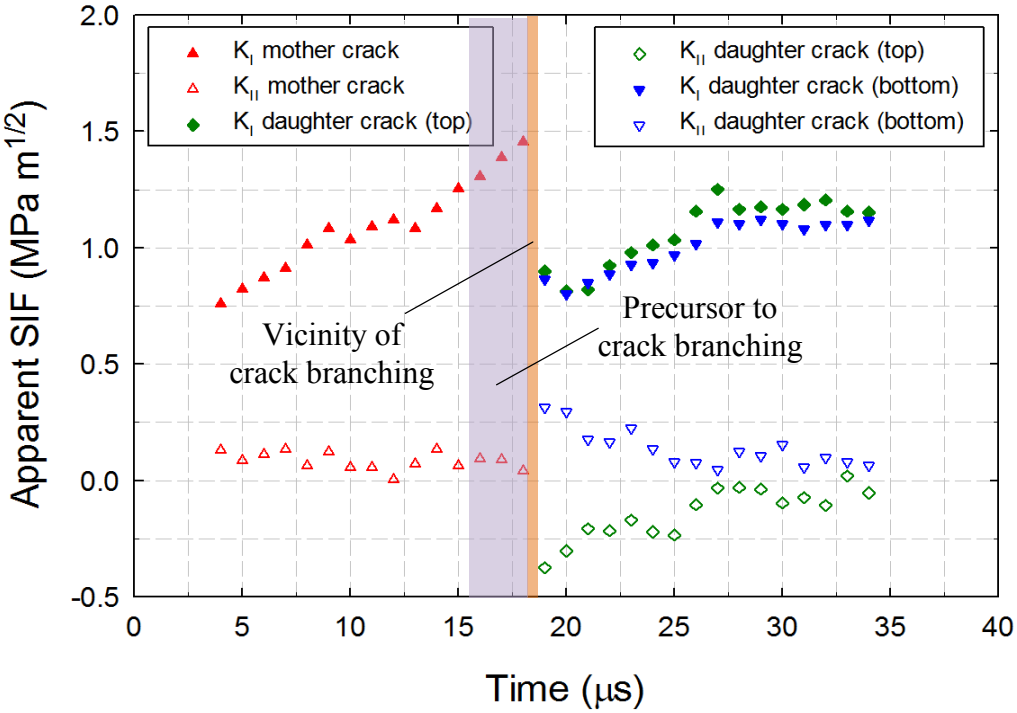

Figure 7.12: Apparent stress intensity factors (SIFs) evaluated for soda-lime glass specimen subjected to wedge loading. (t = 0 μs in these correspond to the crack initiation at original notch tip.)

7.7 Repeatability

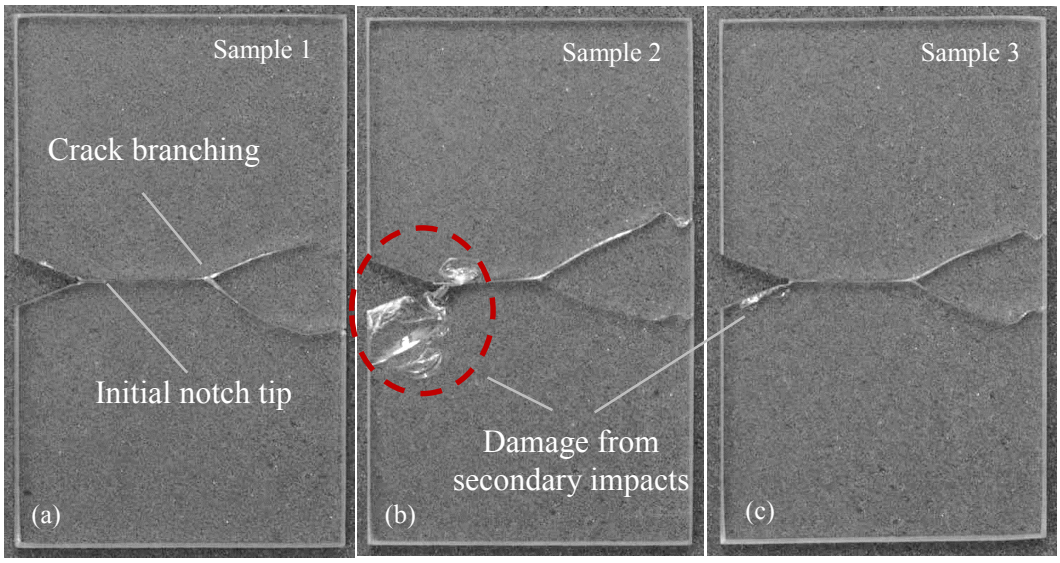

Figure 7.13: Photographs of three fractured specimens showing experiment repeatability of the crack growth morphology.

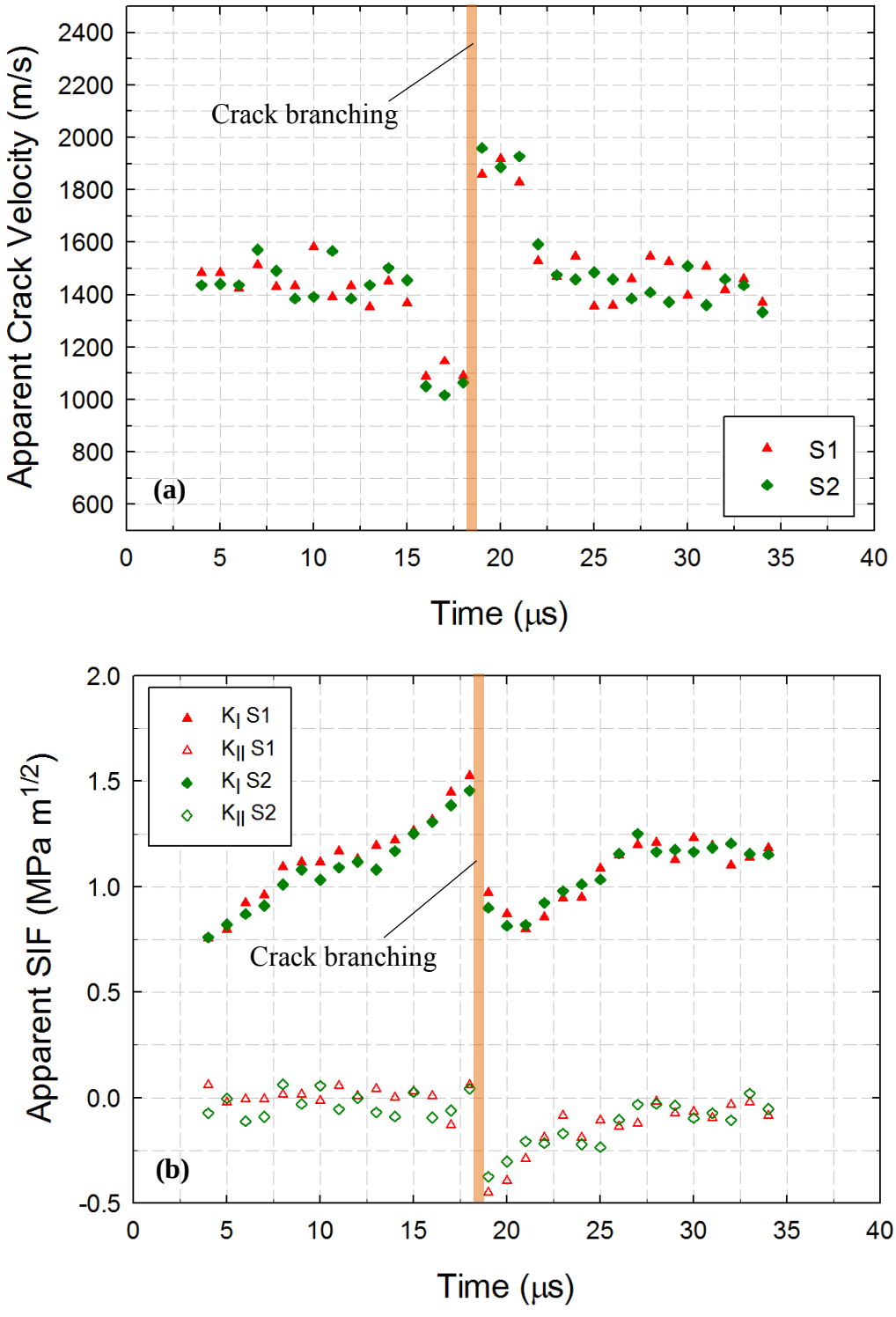

Figure 7.14: Experimental repeatability for two different specimens (S1 and S2): (a) Apparent crack velocity and (b) Apparent stress intensity factor histories for two different specimens of soda-lime glass subjected to dynamic wedge loading.

Multiple experiments were carried out to ensure repeatability in terms of dynamic fracture behavior as well as the measured fracture parameters. Figs. 7.13(a)-(c) shows photographs of three fractured specimens. A relatively high degree of reproducibility in terms of crack paths even during such highly transient fracture events is clearly evident from these photographs. The crack velocity and SIF histories for two of these samples are shown in Fig 7.14(a) and (b), respectively. For brevity, parameters for only one of the two crack branches are shown here. From these plots a high degree of repeatability is evident.

7.8 Crack branching

The instantaneous crack-tip stress fields in the vicinity of a steadily growing can be expressed as [3],

$$\sigma_{ij} = \frac{K_I(t)}{\sqrt{2\pi r}} \sum_{ij}(\theta; V), \quad i, j = x, y \tag{7.1}$$

where,

$$\sum_{xx} = \frac{1}{D}\left\{ \frac{\left(1+\alpha_S^2\right)\left(1+2\alpha_L^2-\alpha_S^2\right)}{\sqrt{\gamma_L}} \cos\left(\frac{\theta_L}{2}\right) - \frac{4\alpha_S\alpha_L}{\sqrt{\gamma_S}} \cos\left(\frac{\theta_S}{2}\right) \right\}$$

$$\sum_{yy} = -\frac{1}{D}\left\{ \frac{(1+\alpha_S^2)^2}{\sqrt{\gamma_L}} \cos\left(\frac{\theta_L}{2}\right) - \frac{4\alpha_S\alpha_L}{\sqrt{\gamma_S}} \cos\left(\frac{\theta_S}{2}\right) \right\},$$

$$\sum_{xy} = \frac{2\alpha_L\left(1+\alpha_S^2\right)}{D}\left\{ \frac{1}{\sqrt{\gamma_L}} \sin\left(\frac{\theta_L}{2}\right) - \frac{1}{\sqrt{\gamma_S}} \sin\left(\frac{\theta_S}{2}\right) \right\},$$

$$D = 4\alpha_S\alpha_L - \left(1+\alpha_S^2\right)^2, \quad \alpha_{S;L} = \sqrt{1-\left(\frac{V}{C_{S;L}}\right)^2},$$

$$\gamma_{S;L} = \sqrt{1-\left(\frac{V\sin\theta}{C_{S;L}}\right)^2}, \quad \tan\theta_{S;L} = \alpha_{S;L}\tan\theta.$$

In the above, $K_I(t)$ is the instantaneous mode-I SIF, V is the crack velocity and C_S and C_L are the shear and longitudinal wave speeds of the material. These stresses can be transformed to obtain the local hoop (or tangential) stress σ_h, the principal stress σ_1, and the maximum in-plane shear stress $\tau_{\max}$, as,

$$\begin{aligned}
\sigma_h &= \frac{K_I(t)}{\sqrt{2\pi r}} \sum_h(\theta;V) \\
\sigma_1 &= \frac{K_I(t)}{\sqrt{2\pi r}} \sum_1(\theta;V) \\
\tau_{\max} &= \frac{K_I(t)}{\sqrt{2\pi r}} \sum_\tau(\theta;V)
\end{aligned} \tag{7.2}$$

The variations of these stresses as a function of θ around the crack-tip for a constant value of $\frac{K_I(t)}{\sqrt{2\pi r}}$ are shown in Figs. 7.15(a)-(c), respectively. For crack speeds less than $0.6C_S$, the hoop stress attains its maximum value along $\theta \sim 60^\circ$ (see Fig. 7.15(a)). However, for crack speeds greater than $0.6C_S$, the maximum value is along $\theta \sim 60^\circ$. This suggests that as the crack speed increases beyond $0.6C_S$, the peak hoop stress occurs at a location inclined relative to the crack growth direction causing the crack to propagate in that direction. However, the crack branching has been observed in this work to occur well before the crack reached the transition velocity of $0.6C_S$ (at $V \sim 0.54C_S$) which is similar to that reported in the literature [27] [31] [32] [33] [119] [120].

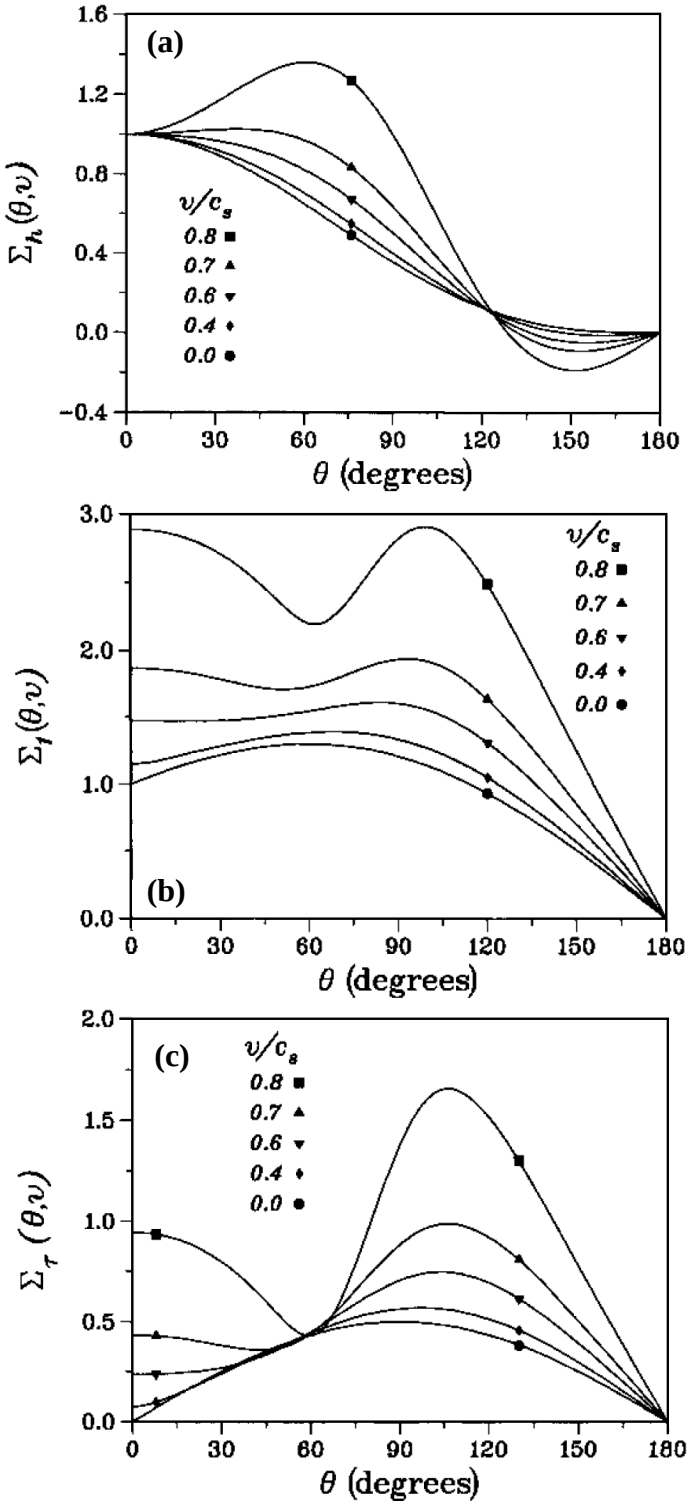

Figure 7.15: Variation of the circumferential (hoop), largest principal, and maximum in-plane shear stresses with angle θ around the crack-tip for various normalized crack speeds (Reproduced from Ref. [3]).

Furthermore, the crack path after branching shows a half angle of ~25˚(see Fig.7.5) which is significantly less than the predicted value of 60˚. Thus, the hoop stress near the crack-tip vicinity in conjunction with the attainment of critical speed appears neither a necessary nor sufficient condition for the observed crack branching in experiments [3]. Other investigators [121] have suggested that branching could be due to the attainment of the maximum principal stress on some plane becoming equal to the tensile strength of the material. The angular variation of this stress, Fig. 7.15(b), shows a shallow maximum between approx. 60º and 90º at low speeds. For higher speeds ($> 0.6C_S$), however, the maximum shifts to values beyond 90º. The maximum shear stress variation shown in Fig. 7.15(c) suggests that maxima occurs at different angles with increasing crack speed at various angles. For brittle solids such as soda-lime glass, however, this variation is not important although it may be relevant for shear driven failures such as dislocation glide, twinning, etc. in inelastic materials.

Another aspect worth pointing out is about the ratio of the two normal stresses σ_{yy}/σ_{xx} ahead of the crack-tip. A plot of the same as a function of crack speed is shown in Fig. 7.16. For a stationary crack-tip, the in-plane principal stresses are equal to the Cartesian stress components along $\theta = 0^\circ$ and are nearly equal for low crack speeds. However, this is not true as the crack speeds increase. This ratio rapidly decreases as the crack travels at higher velocity especially after $0.5C_S$. Thus, at higher crack speeds, the larger of the in-plane principal stresses ahead of crack-tip acts on planes perpendicular to the crack growth direction. This may be the underlying reason for the observed tendency for fast cracks to develop rough surfaces and produce “hackles” prior to branching. Note

that as the crack speed approaches $\sim 0.93C_S$ (or Rayleigh wave speed, C_R), the ratio drops to zero implying that the mode-I crack growth crack cannot exceed that speed.

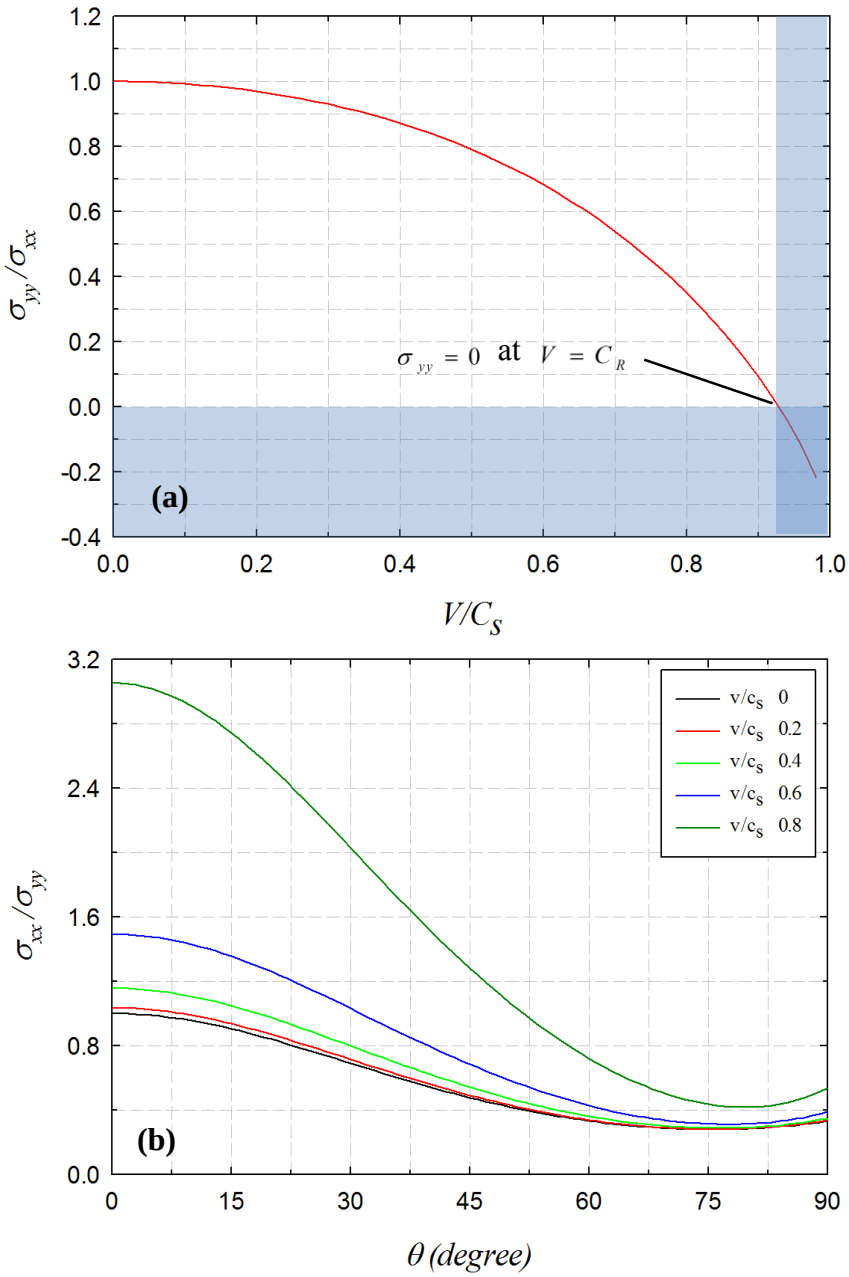

Figure 7.16: Variation of in-plane stress ratio (a) as a function of crack speed, (b) as a function of angle θ.

As can be seen from the variation of inverse stress ratio $(\sigma_{xx}/\sigma_{yy})$ with the angle around the crack-tip as shown in Fig. 7.16(b), though the maximum is always along $\theta = 0^{\circ}$, it increases with crack velocity reaching values as large as ~1.5 at $V = 0.6C_S$. Thus, tensile stresses in the growth direction are significantly higher than the ones perpendicular to it. This leads to a conjecture namely, at higher crack speeds there is a tendency for micro crack nucleation (say, penny shaped cracks) to occur perpendicular to the growing mother crack and ahead of the current tip if a local weakness were to prevail. The distance at which such a nucleation of micro cracks could occur increases with crack speed. The coalescence of the mother crack-tip with the nucleated daughter crack-tip/s of different yet finite size micro cracks could explain "mirror", "mist" and eventually "hackle" formations prior to the eventual branching phenomenon. However, this does not explain the angle of branching but one can conceivably perform an investigation at a higher spatial resolution to reveal fracture mechanics along the lines of those discussed in Chapter 5 for PMMA bilayers. The potential contribution of so-called T-stress or the first higher order term in the asymptotic expansion for σ_{xx} on the eventual propagation angle is also discussed in the literature [122] [123] and is not addressed in this research.

In this context, assuming σ_{xx} could nucleate micro cracks ahead of the mother crack-tip, Eq. (7.1) was used to obtain the instantaneous radial distance $r(t)\big|_{cr}$ at which the material experiences the tensile stress equal to its tensile strength using,

$$r(t)\big|_{cr} = \frac{1}{2\pi}\left(\frac{K_I(t)}{\sigma_{xx}(t)}\sum_{xx}(\theta=0;V(t))\right)^2 \tag{7.3}$$

The tensile strength σ_{cr} of soda-lime glass has been reported to vary widely in the literature between 20 MPa-131 MPa. In this work the one reported by Wereszczak et al. [124] ~ 62 MPa is used. Using optically measured fracture parameters $K_I(t)$ and $V(t)$ in the above equation along with the tensile strength for $\sigma_{xx}(t)=\sigma_{cr}$, the maximum distance ahead of the current mother crack-tip where critical failure stress occurs in the material is plotted at every time instant in Fig. 7.17.

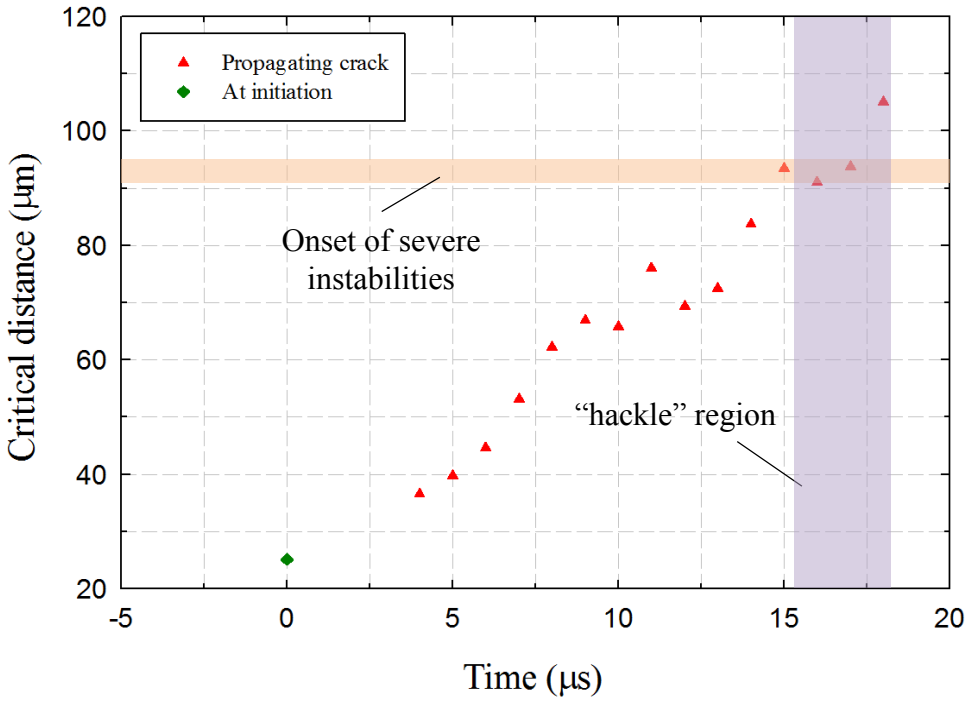

Figure 7.17: History of critical radial distance along $(\theta=0^\circ)$, from the mode-I mother crack-tip experiencing the critical tensile stress during crack growth.

Using the condition $K_I(t) = K_{Icr}$, where K_{Icr} is the value obtained in Chapter 6 (0.81 MPa√m) at crack initiation and Eq. (7.3), this critical distance at crack initiation was evaluated as ~25 μm; it is plotted in Fig. 7.17 as well. Based on the visual evidence of the hackle zone occurring between 15-18 μs in this study, the critical length or critical distance for soda-lime glass is estimated from the plot to be ~90 μm (at $V = 0.54C_S$). This distance is more than three times that when the crack initiates at the original tip.

Chapter 8

FAILURE BEHAVIOUR OF TRANSPARENT graft-IPNs

In this chapter, synthesis and failure characterization of novel transparent graft-Interpenetrating Polymer Networks (graft-IPNs) are discussed. Elastomeric polyurethane (PU) phase and a stiff acrylate-base copolymer (CoP) phase were used to synthesize graft-IPNs. Poly(tetramethylene ether) glycol (PTMG) of two different molecular weights (650g/mol and 1400g/mol) were used to synthesize the PU phase, thus producing two different grades of graft-IPNs. In each grade, the CoP:PU ratio were varied from 90:10 to 60:40 to obtain different graft-IPNs. Quasi-static and dynamic tension and fracture tests were performed on those graft-IPNs. The results suggests an optimum range of CoP:PU in graft-IPNs to produce enhanced fracture toughness and fracture energy absorption capabilities when compared to PMMA.

8.1 Material synthesis

The polyurethane phase (PU) was synthesized by employing three different polyols: 2-ethyl-2-(hydroxymethyl)-1,3propanediol (TRIOL) from Acros Organics, (USA), and poly(tetramethylene ether) glycol (PTMG) average $M_n \sim 650$ and ~1400 g mol^{-}

[1] from Sigma-Aldrich, (USA). A mix of TRIOL and PTMG was made beforehand through melting. The mixture was kept melted in an oven under strong vacuum in order to remove any moisture. The same procedure was repeated for different PTMGs employed in the synthesis. The isocyanate used was hexamethylene diisocyanate 98.0% (DCH) from TCI, (USA). Dibutylin dilaurate, 98% (DD) by Pfaltz & Bauer, (USA) and triphenylbismuth, 99+% (TB) from Alfa Aesar, (USA), were used as catalyzers for the synthesis, while ethyl acetate was employed as an analogue for both catalyzers.

The synthesis of the copolymer (CoP) phase was carried out by employing bisphenol A bis(2-hydroxy-3-methacryloxypropyl) ether (BisGMA) from Esstech, (USA) and two different acrylic monomers: methyl methacrylate (MMA) 99% stabilized from Alfa Aesar, (USA) or triethylene glycol dimethacrylate (TEGDMA) stabilized from TCI, (USA). 2,2'-azobis(2-methylpropionitrile), (AIBN) 98% from Sigma-Aldrich, (USA) was used as a thermal initiator for the reaction.The graft-IPNs were synthetized in a single-step procedure where the polyurethane and copolymer phases were prepared separately at room temperature. In order to prepare the copolymer phase, a mix of acrylic monomer (MMA or TEGDMA) and the BisGMA resin was made by keeping a mass ratio of 90:10 acrylate:BisGMA. A 1 wt% of the total copolymer mass was fixed as the amount added of thermal initiator for the polymerization. To prepare the polyurethane phase, the diisocyanate was added to the PTMG/TRIOL mixture keeping the following ratio: 0.19eq TRIOL: 0.12eq PTMG: 0.31eq DCH. An additional amount of DCH was added to generate crosslink points between networks, according to the equivalence ratio of 1:1 DCH:BisGMA. Following this, both precursor mixtures were mixed together and both

catalyzers were added to the mixture. After this, all samples were placed in an oven at 40°C for 17 h after which the samples were transferred to a water bath where the temperature was raised to 60°C for 24 h and finally the temperature was raised to 80°C for 24 h.

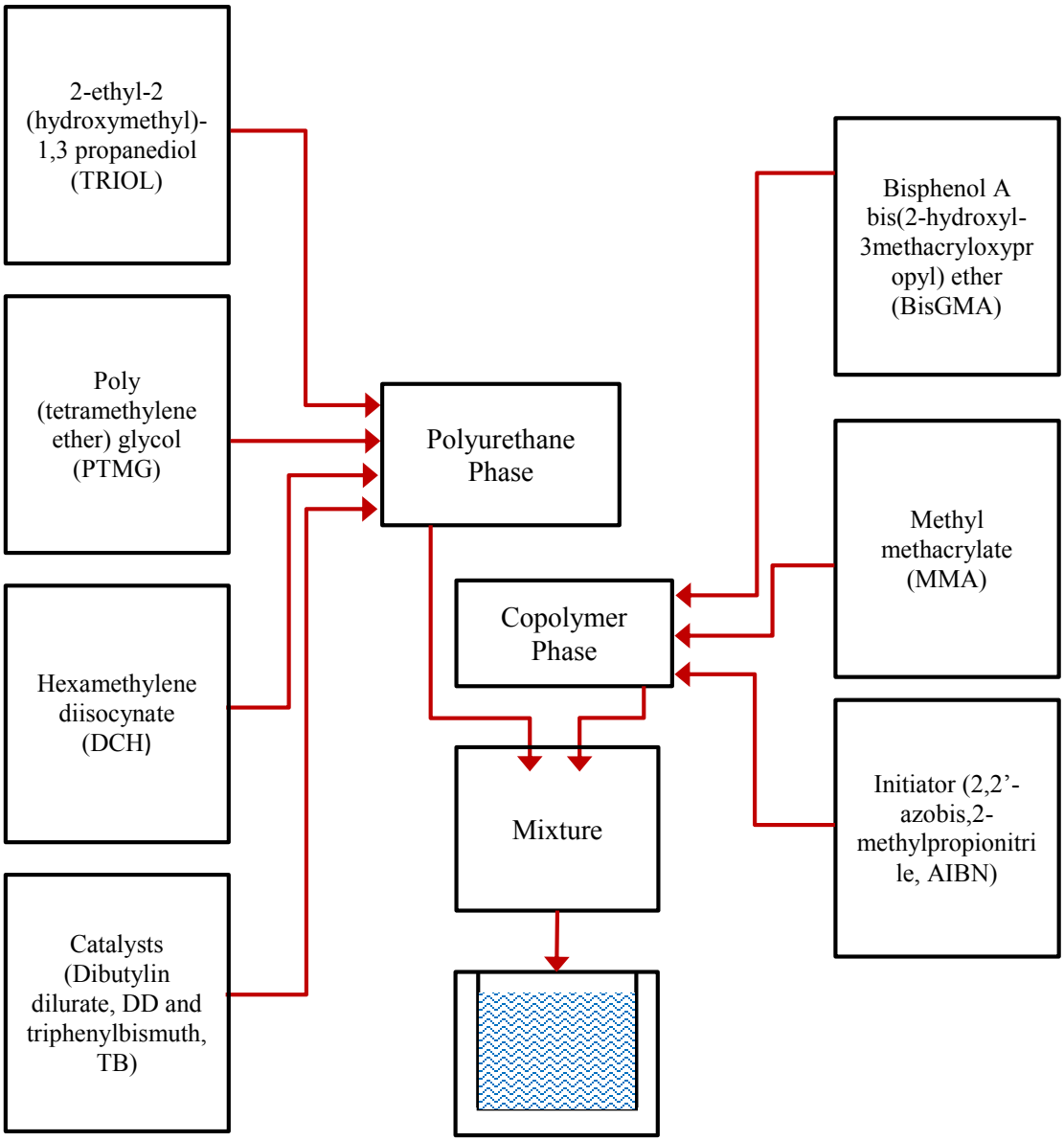

Cured at 40˚C for 17 h, 60˚C for 24 h and 80˚C for 24 h

Figure 8.1: Schematic of graft-IPNs synthesis steps.

The graft-IPNs samples with different compositions were produced following the aforementioned procedure. The CoP to PUe ratio was varied from 90 wt% and 10 wt% respectively to 60 wt% and 40 wt% respectively. This change in the ratio was applied for two grades of graft-IPNs obtained by using 650 $gmol^{-1}$ and 1400 $gmol^{-1}$ of PTMG in synthesis of PU phase. The various compositions synthesized are tabulated in Table 8.1.

MMA:BiSGMA ratio in CoP by wt	Mol wt of PTMG in PU	CoP:PU ratio by wt	Grade
90:10	650 g/mol	60:40,70:30,75:25,80:20 and 90:10	1
	1400 g/mol	60:40,70:30,75:25,80:20 and 90:10	2

Table 8.1: The list of all compositions of graft-IPNs synthesized.

8.2 Optical transparency

The graft-IPNs were examined using UV-visible spectroscopy to measure its optical transmittance [125]. The transmittance of PMMA, CoP and PU were also measured and compared with graft-IPNs. Fig. 8.3(a) and (b) show the plots of wavelength of light and corresponding transmittance of various compositions of grade-1 and -2 graft-IPNs, respectively. The graft-IPNs presented a relatively high degree of transparency with transmittance between 75% and 90%, comparable to that for PMMA and much higher than the PU phase. These results also confirm a high degree of interpenetration achieved on both systems regardless of the molecular weight of the PTMG used.

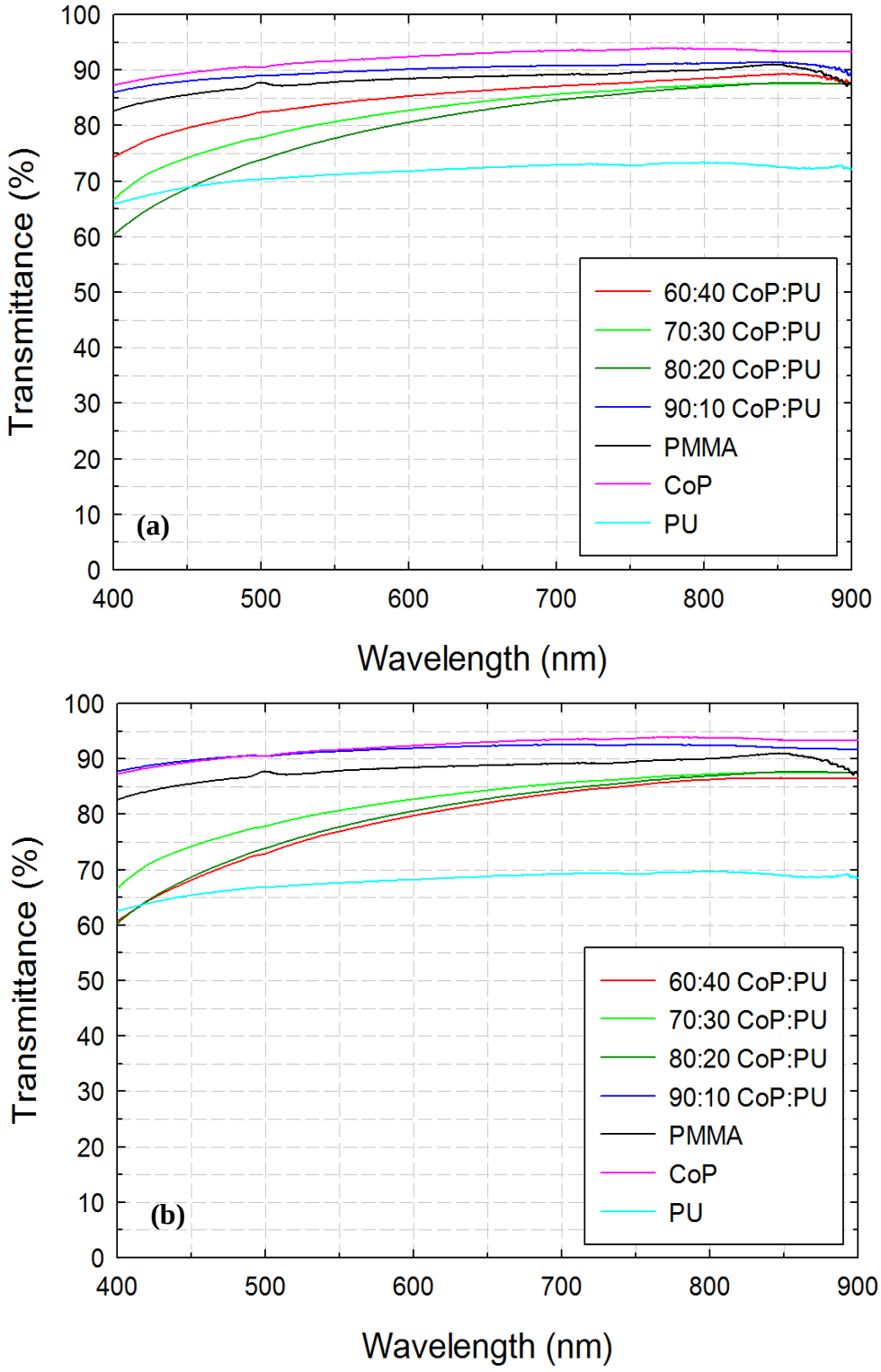

Figure 8.2: Plot of optical transmittance obtained using UV-visual spectroscopy for (a) grade-1 and (b) grade-2 graft-IPNs.

Figure 8.2 shows the photograph of Auburn University logo through a select composition (70:30 CoP:PU) of grade-1 graft-IPN. The logo is uniformly and clearly visible through the specimen. From the photograph it can be seen that there is no visible evidence of macroscopic phase separation.

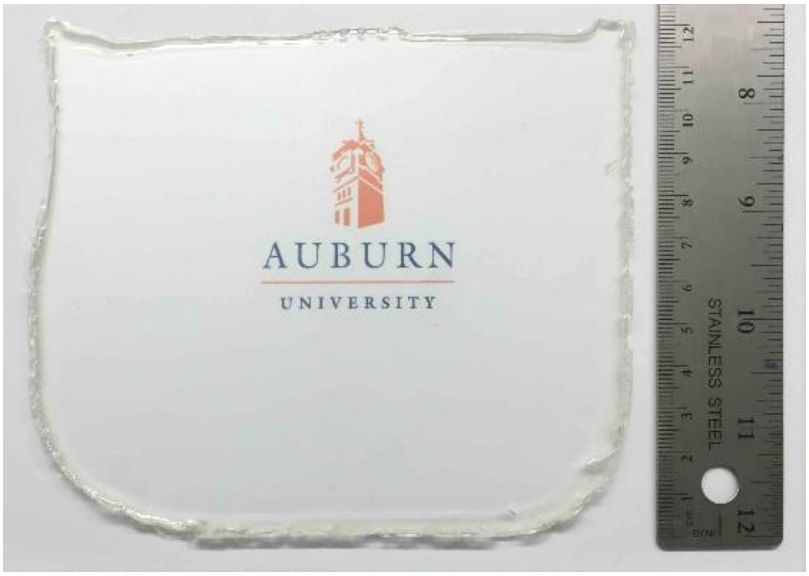

Figure 8.3: A clear and sharp photograph of Auburn University logo through the cast specimen of select (70:30 Cop:PU) grade-1 graft-IPN.

8.3 Specimen fabrication and geometry

The specimen geometries used in this study are shown in Fig. 8.4(a)-(c). The cured graft-IPN sheets of 2.8 mm thickness were machined to dog-bone shaped specimens for performing tension tests (see fig. 8.4(a)). For quasi-static fracture tests, the graft-IPN sheets of 2.8 mm thickness were machined into rectangular SEN samples of dimension 70 mm x 15 mm for grade-1 graft-IPNs and 70 mm x 20 mm for grade-2 graft-IPNs. An edge notch was machined on the longer edge using a diamond impregnated wafer blade, which was further sharpened using a razor blade before testing.

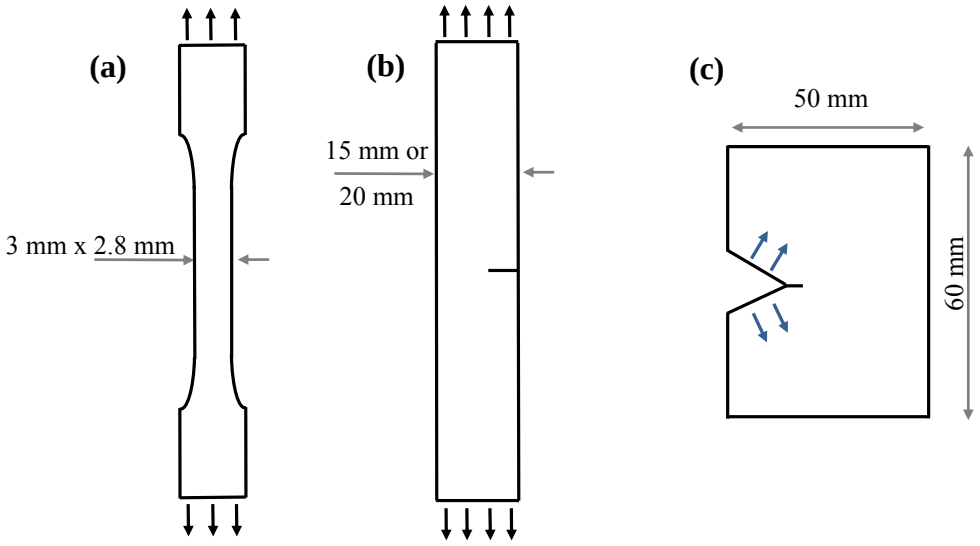

Figure 8.4: The schematic showing the specimen geometry and loading configuration used for (a) quasi-static tension test, (b) quasi-static fracture test, and (c) dynamic fracture test.

For dynamic fracture experiments, the specimens were cast with a slightly higher thickness of 4 mm to avoid buckling and bending of specimens during the initial compressive stress pulse loading. Plate specimens of dimensions 60 mm x 50 mm (see Fig. 8.4(c)) with a 'V' notch of 40˚was machined on the longer edge which matched the impact end of the long-bar. Again, using a diamond impregnated wafer blade, the notch was extended by 2 mm and sharpened using a razor blade as in the static counterparts.

8.4 Quasi-static tests

8.4.1 Uniaxial tension

The uniaxial tension tests were carried out using Instron 4665 UTM under displacement control (crosshead speed 0.005 mm/s). Three specimens were tested for each

composition. An extensometer (gage length 6.35 mm) was used to measure the longitudinal strain. The loading configuration is shown in Fig 8.4(a).

The tensile response (stress-strain plot) of grade-1 graft-IPNs along with commercial PMMA counterpart is shown in Fig. 8.5(a). Initial response indicates a linear elastic region, followed by a nonlinear region leading to sudden failure in case of PMMA, whereas, graft-IPNs show significant nonlinearity. Except for 90:10 compositions which failed at ~3% strain, rest of them did not fail up to 20% of strain, the maximum strain capacity of the extensometer used. The graft-IPNs 90:10 the failure occurs at ~61.5 MPa, whereas 80:20, 70;30, 75:25 and 60:40 have ultimate stress of ~60 MPa, ~52 MPa, ~37 MPa and ~18 MPa, respectively. It can be seen that there is substantial decrease in the ultimate stress as the PU content is increased. The elastic modulus for each composition was determined from the slope of the stress-strain curve at <0.2% strain (see Fig. 8.5(b) inset) and are as shown in Fig. 8.5(b). Each data point represents an average value based on multiple specimens (typically three, due to limited availability of material) and the error bars corresponds to the standard deviation. There is evidence of decrease in the elastic modulus with increase in PU content. Similarly, the tensile response of grade-2 graft-IPNs is shown in Fig. 8.6(a). Similar stress-strain response is observed in this case as well. Except for 90:10 compositions which failed at ~11% strain, rest of them did not fail up to 20% strain. The graft-IPNs 90:10, 80:20, 70:30, 75:25 and 60:40 have an ultimate stress of ~76 MPa, ~53 MPa, ~47 MPa, ~35 MPa and ~18 MPa, respectively. Similar to grade-1 graft-IPNs, there is substantial decrease in the ultimate stress as the PU content is increased.

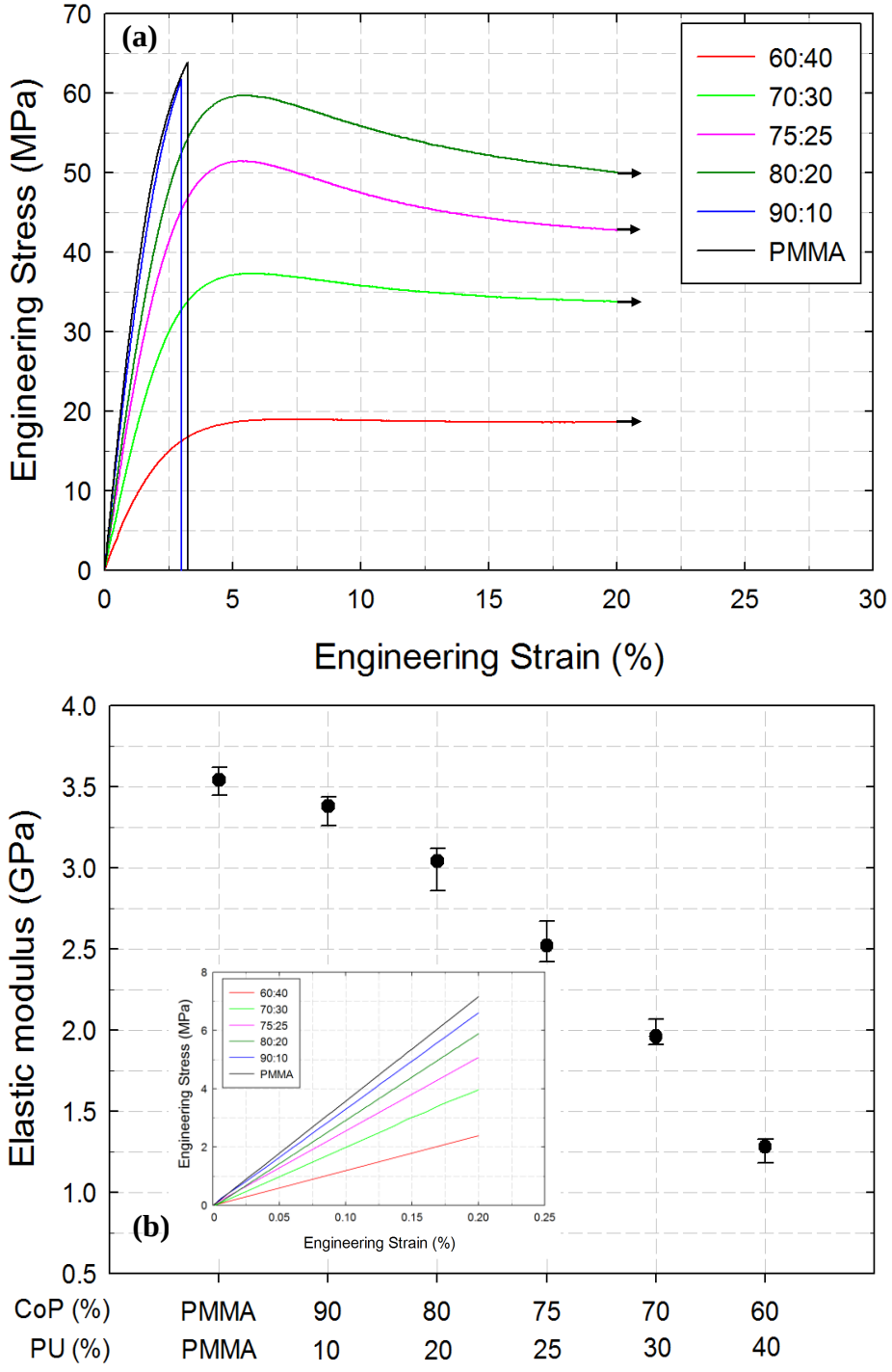

Figure 8.5: (a) Stress strain response from tension tests and (b) compilation of the elastic modulus for grade-1 graft-IPNs compared with commercially procured PMMA. Inset shows the stress strain response up to 0.2% strain used to evaluate the elastic modulus. (Note the arrow at the end of the plot shows that the specimen did not fail at the maximum strain of 20%)

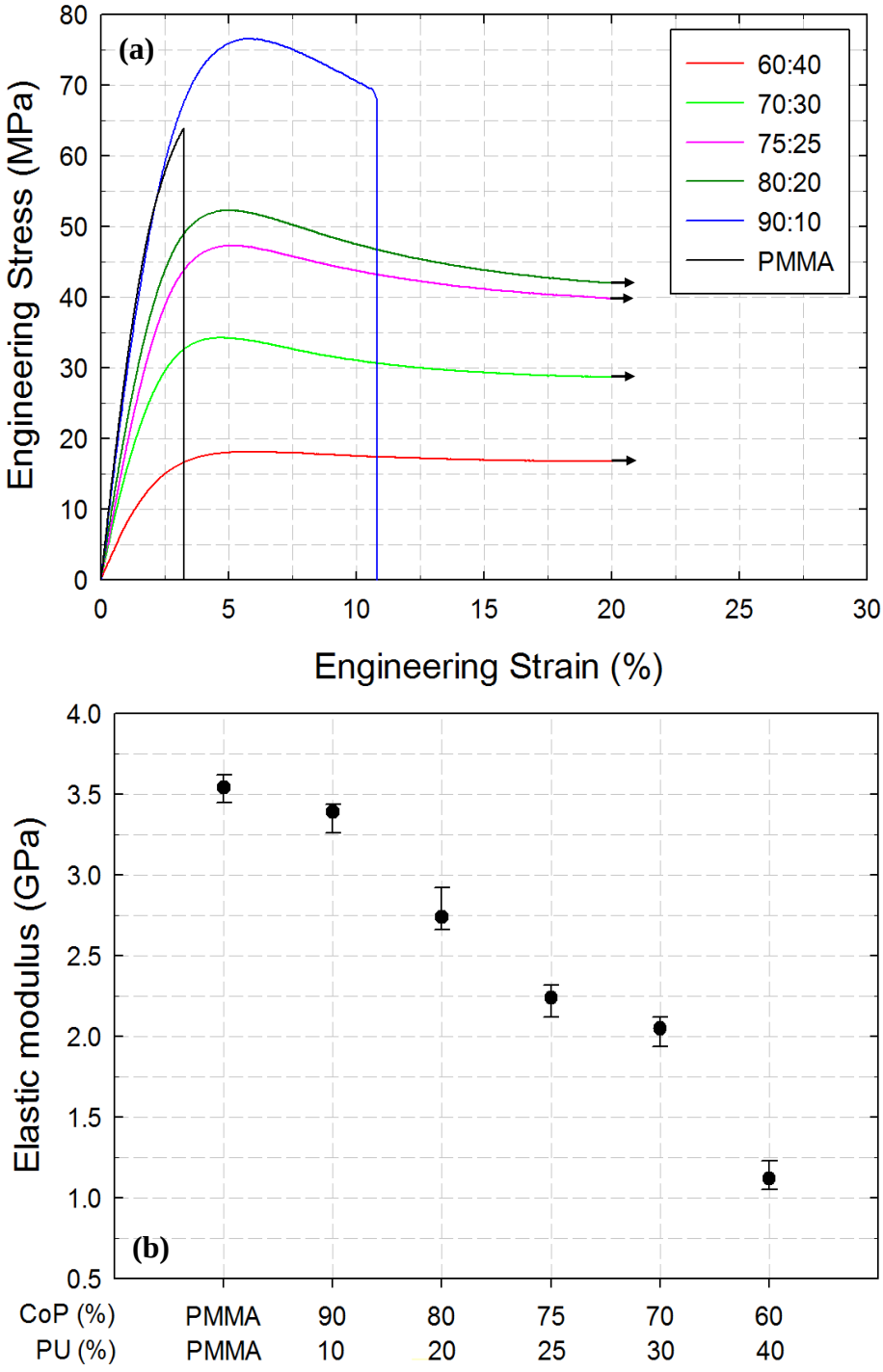

Figure 8.6: (a) Stress-strain response from tension tests and (b) compilation of the elastic modulus of grade-2 graft-IPNs compared to that for commercially procured PMMA. (Note the arrow at the end of the plot shows that the specimen did not fail at the maximum strain of 20%)

The elastic modulus for each composition was determined from the slope of the stress-strain curve at <0.2% strain as shown in Fig. 8.6(b). Again, each data point represents the average value from multiple specimens (three) and the error bars correspond to the standard deviation. Similar to grade-1 graft-IPNs, there is a decrease in the elastic modulus with increase in PU content. These trends are similar to those reported by others [81] [80]. This behavior can be attributed to the contribution of the PU phase. Further, in case of grade-2 graft-IPNs, the elastic modulus for each composition is higher than their counterparts in grade-1. Similar differences between grade-1 and -2 graft-IPNs were observed for the ultimate stress and failure strain as well. Hence the increase in molecular weight of PTMG used to synthesize graft-IPNs was favorable in terms of the elastic modulus.

8.4.2 Fracture tests

Quasi-static fracture tests were performed under tensile loading conditions. The loading configuration is shown in Fig 8.4(b). The SEN sample was loaded in displacement control (crosshead speed 0.005 mm/s) mode using Instron 4665 UTM. The load-extension data was recorded up to crack initiation and during stable crack growth phase that occurred in a few compositions. The critical mode-I stress intensity factors (SIF) at crack initiation, K_{Ic}, were calculated from the measured peak load as [125] at crack initiation,

$$K_{Icr} = \frac{F\sqrt{\pi a}}{Bw} f\left(\frac{a}{w}\right) \tag{8.1}$$

where $f\left(\frac{a}{w}\right)=\left[1.12-0.23\left(\frac{a}{w}\right)+10.6\left(\frac{a}{w}\right)^2-21.7\left(\frac{a}{w}\right)^3+30.4\left(\frac{a}{w}\right)^4\right]$, F is the peak load, B is the specimen thickness, a is the initial crack length and w is the width of the specimen. Four specimens were tested for each composition based on the availability of the material.

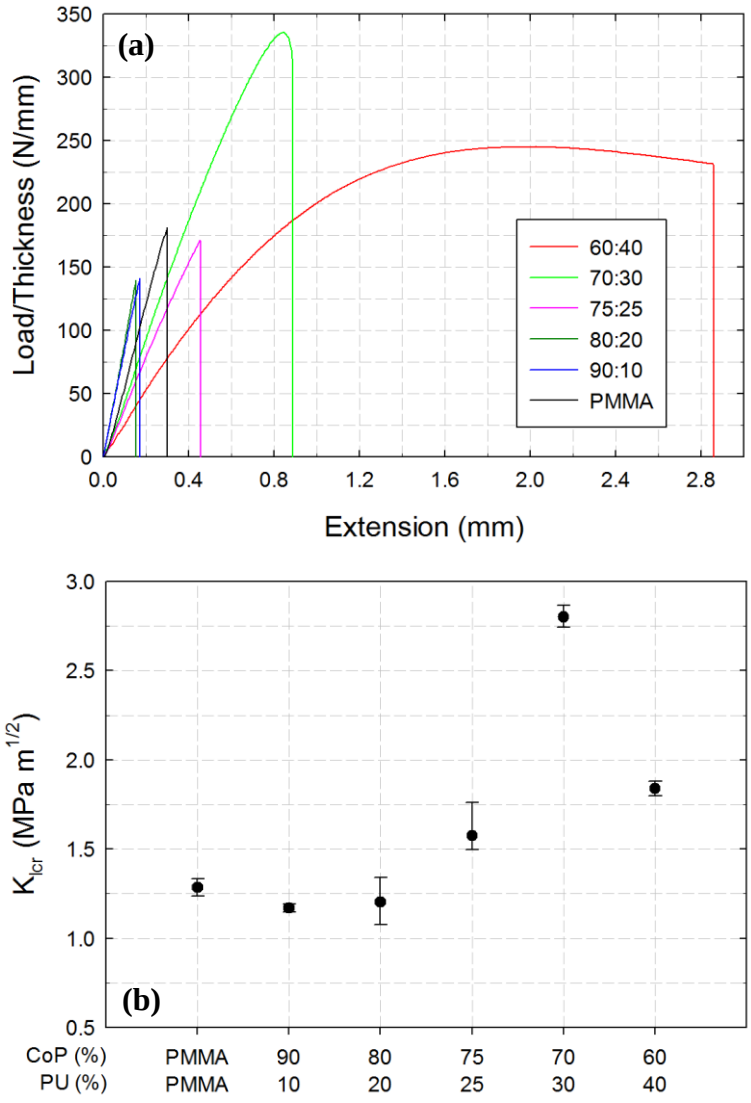

Figure 8.7: Quasi-static fracture results for grade-1 graft-IPN: (a) Plot of load/thickness vs. extension obtained from fracture tests, and (b) compilation of the K_{Icr} compared to commercially procured PMMA.

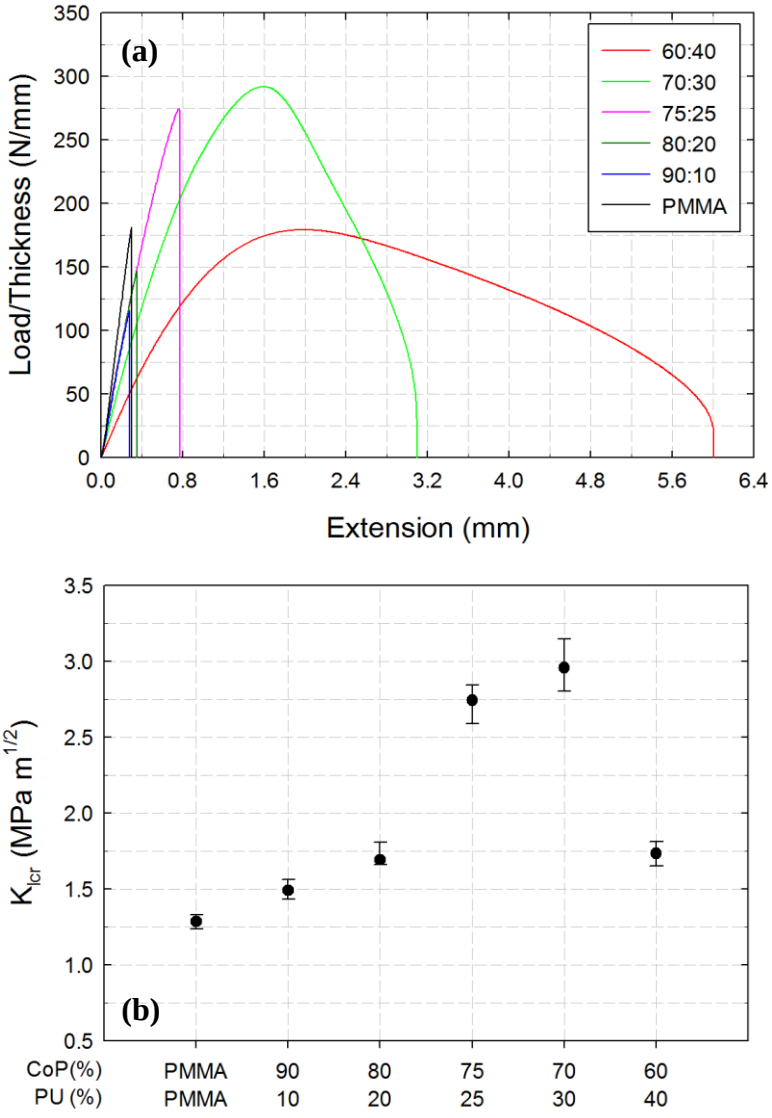

Figure 8.8: Fracture test results for grade-2 graft-IPNs relative to commercially procured PMMA: (a) plot of load per unit thickness and extension (b) compilation of the K_{Icr} compared with commercial PMMA counterpart.

Quasi-static fracture tests on graft-IPNs along with commercial PMMA were performed. The normalized (with specimen thickness) load-deflection curves for grade-1 graft-IPNs and commercial PMMA are shown in Fig 8.7(a). Commercially procured PMMA showed a linear response up to the peak load followed by sudden drop signaling

crack initiation/failure. The graft-IPNs, except for 70:30 and 60:40 compositions, showed a similar response. The 70:30 composition showed as linear response for the major part until the very end where a modest nonlinearity can be seen before reaching the peak load and subsequently failure. As for the 60:40 composition, the initial response was linear but it quickly changed to nonlinear response for a while before reaching a peak load followed by a stable crack growth where a decrease in load until failure can be seen. The extent of nonlinearity increased with the PU content. This nonlinearity in the pre-peak load region can be attributed to crack-tip blunting and crazing prior to crack initiation. Moreover, propagation of the macro-crack required increasing of the applied load. Further, the crack tended to deviate from its original propagation path. The highest peak load was observed for the 70:30 composition and the largest area under the load-deflection curve representing the strain energy absorbed was for 60:40 compositions. The quasi-static crack initiation toughness, K_{Icr}, was calculated using the load at crack initiation in each case. The variation of K_{Icr} with CoP:PU ratio along with that of commercial PMMA is shown in Fig. 8.7(b). Each data point is again an average of multiple (four) measured values of K_{Icr}. The trends in K_{Icr} values with increasing PU suggest that there is an optimum range of CoP:PU ratio for which the quasi-static fracture toughness is the highest. In this work, the 70:30 graft-IPNs showed the highest improvement of 115% in K_{Icr} (2.78 MPa√m) over commercially procured PMMA (1.28 MPa √m).

The normalized load-deflection curve (load normalized by the sample thickness) and compiled K_{Icr} for grade-2 graft-IPNs along with the one for commercial PMMA are shown in Fig 8.8(a) and (b), respectively. Similar trends as in grade-1 graft-IPNs are seen

in this case as well with optimum composition being 70:30 CoP:PU with K_{Icr} of 2.95 MPa √m. When compared to grade-1 graft-IPNs, grade-2 graft-IPNs show an improvement in the fracture toughness (critical stress intensity factor) for each composition. Comparing the optimum composition of 70:30 Cop:PU of grade-1 graft-IPN with that of grade-2 graft-IPN, latter showed 6.2% improvement in K_{Icr} over the former.

8.5 Elasto-optic constant for graft-IPNs

The elasto-optic constant of graft-IPNs were evaluated using the Flamant problem as described previously (see Chapter 3). That is, a line-load was quasi-statically applied on an edge of a large planar sheet and optical measurements were made. A rectangular sheet of 50 mm x 50 mm and thickness 4 mm was placed on a flat rigid platform and subjected to a line-load as shown in Fig. 8.9. An Instron 4465 universal testing machine was used for loading the specimen in a displacement control mode (crosshead speed of 0.005 mm/sec). A target plate coated with random black and white speckles was placed behind the specimen at a distance of 28.1 mm from the mid-plane of the specimen. A Nikon D100 digital SLR camera fitted with a 70-300 mm focal length lens and extension tube was used to record the speckles. The camera was placed in front of the specimen at a distance (L) of ~600 mm with the camera focused on a uniformly illuminated target plane through the specimen. A camera resolution of 1504 x 1000 pixels was used to acquire 8 bit images.

An undeformed image of the target plate through the specimen was recorded at no-load condition (1 pixel ~30 μm on the target plane). As the sample was loaded, the

deformed images of the target plate were recorded at 0 N, 300 N, 400 N, 600 N and 800 N loads. Two representative speckle patterns, one in the reference (no-load) state and another in the deformed state, are shown in Fig. 8.10(a) and (b), respectively. Sufficient care was exercised to obtain a near Gaussian distribution of gray scales for each image in the mid-range of 0-255 (8 bit) scale by adjusting the illumination and the numerical aperture of the lens. The speckles are noticeably distorted in Fig. 8.10(b) at the top edge of the specimen near the contact area due to deformations and the local stress field.

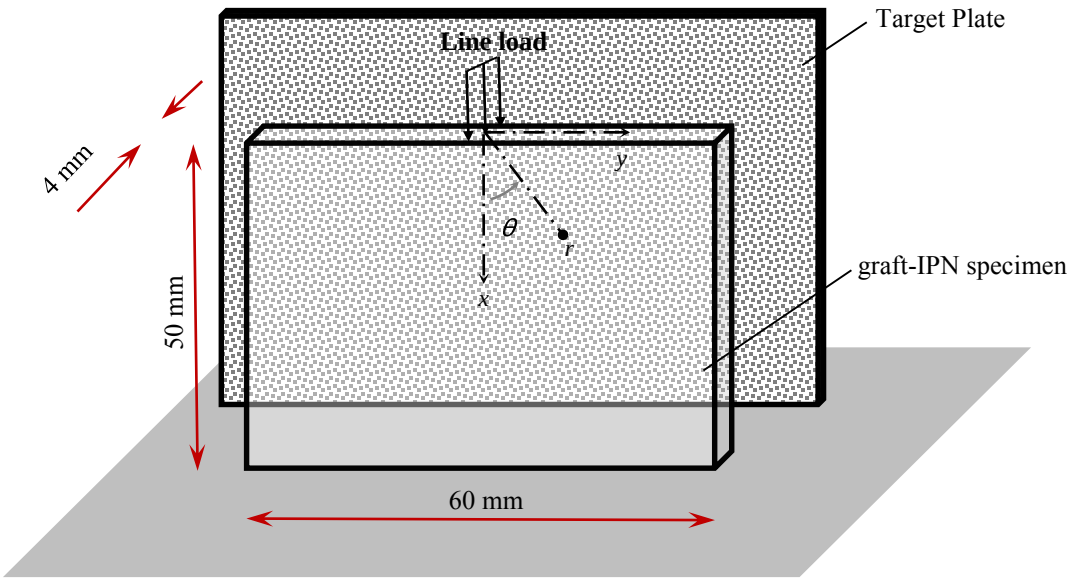

Figure 8.9: Experimental setup for line loading on a graft-IPN sheet to evaluate elasto-optic constant.

The digitized speckle images (1504 x 1000 pixels) in the deformed state were correlated with the image from the undeformed state using ARAMIS®. A sub-image size of 25 x 25 pixels with an overlap of 20 pixels (i.e., step size of 5 pixels) was used during image correlation. The angular deflection contours in the horizontal (y-z) and vertical (x-z)

planes for a compressive load of 800 N for a select composition (80:20 CoP:PU) of grade-1 graft-IPN is shown in Fig. 8.11.

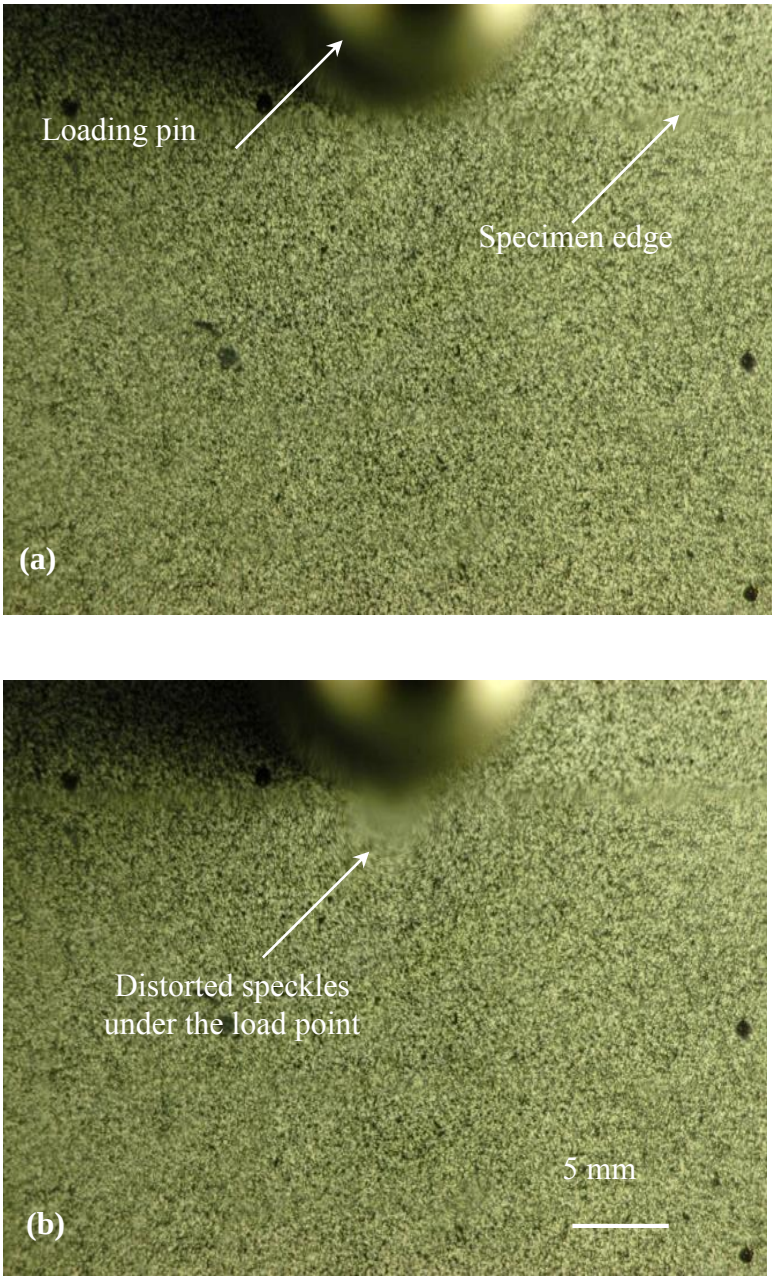

Figure 8.10: Speckle images of a select graft-IPN (Grade-1 80:20 composition) under the line-load: (a) undeformed and (b) deformed.

The angular deflections measured in two in-plane orthogonal direction are related to stresses as [99],

$$\phi_x = C_\sigma \frac{2F}{\pi} \frac{\cos(2\theta)}{r^2}$$
$$\phi_y = C_\sigma \frac{2F}{\pi} \frac{\sin(2\theta)}{r^2} \tag{8.2}$$

where C_σ is the elasto-optic constant, F is the applied load, B is the specimen thickness and (r,θ) denote the polar coordinates relative to the loading point. The far field values of the angular deflections were forced to be zero based on the known boundary conditions. This accounted for any potential rigid body motion while conducting the experiments and/or the electronic noise. Liner regression was performed on measured data using Eq. 8.2 at each load step to obtain C_σ which was averaged. Table 8.2 shows the elasto-optical constant for all the graft-IPNs synthesized.

graft-IPN configuration	CoP :PU	C_σ ($\times 10^{-10}$ m^2/N)
650 g/mol PTMG (Grade-1)	90:10	1.12
	80:20	1.21
	75:25	1.25
	70:30	1.32
	60:40	1.48
1400 g/mol PTMG (Grade-2)	90:10	1.13
	80:20	1.21
	75:25	1.23
	70:30	1.39
	60:40	1.46

Table 8.2. Elasto-optic constants evaluated for various graft-IPNs

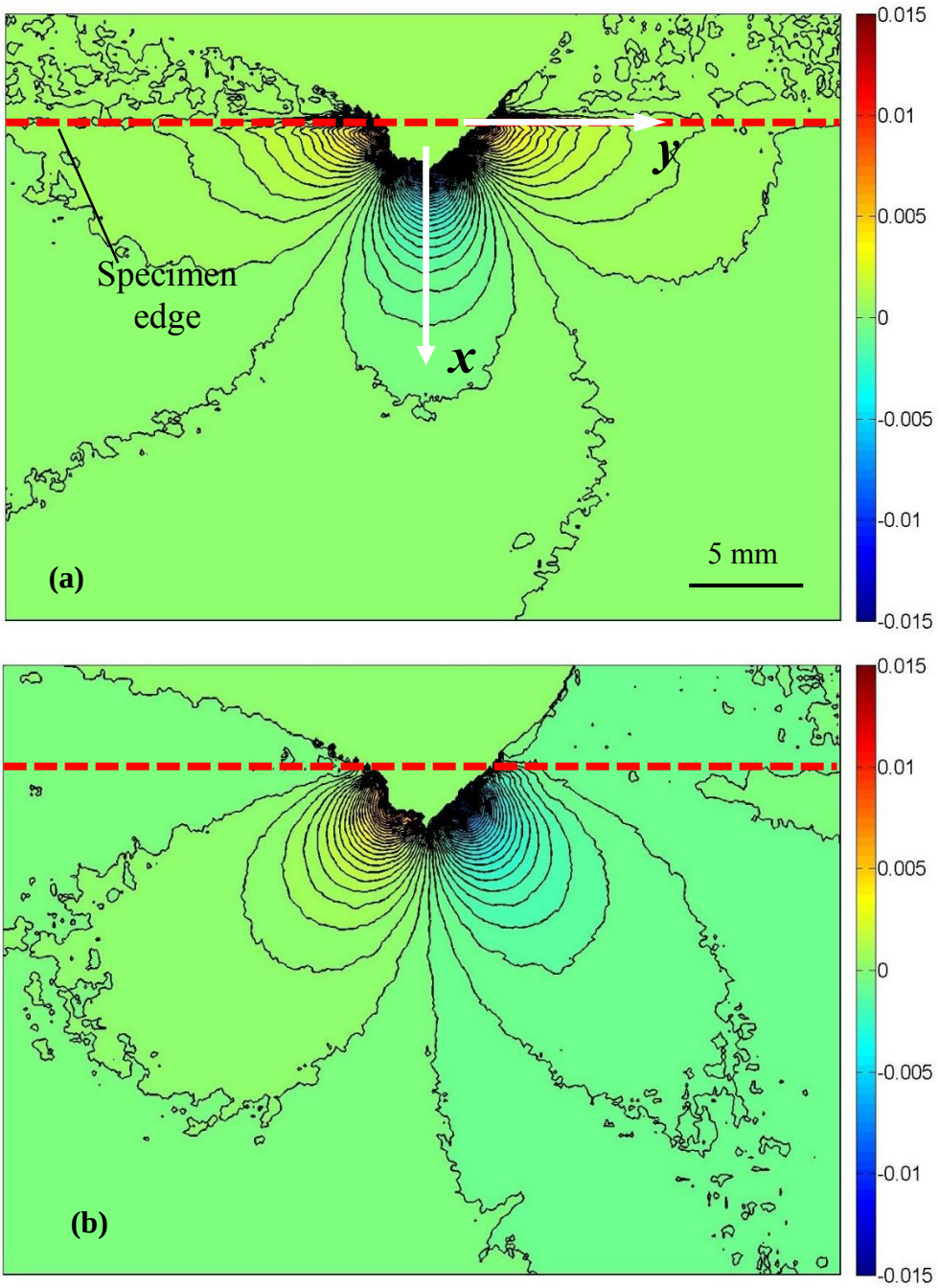

Figure 8.11: Angular deflection contour plots (contour interval = 3×10^{-4} rad) proportional to stress gradients of $(\sigma_{xx}+\sigma_{yy})$ in the (a) *x*- and, (b) *y*-directions for a select composition (80:20 CoP:PU) of grade-1 graft-IPN subjected to a line-load of 800 N.

8.6 Dynamic fracture tests

8.6.1 Experimental details

The dynamic fracture of graft-IPNs was studied using transmission-mode DGS technique in conjunction with ultrahigh-speed digital photography. A Hopkinson pressure bar was used for loading the pre-notched ('V' notch extended by rectangular slot of 300 μm width and 2 mm length) specimen. The experimental setup and other details are same as that in Chapter 4. The scale factor was ~0.042 mm/pixel. The region of interest in this study was in the vicinity of the initial crack-tip which was ~ 42 mm x 42 mm. The velocity and the stress intensity factor of the crack-tip were evaluated as described in Chapter 3.

8.6.2 Speckle images and angular deflections

The recorded images, one in the undeformed and another in the deformed state for a select composition (80:20 CoP:PU) of grade-1 graft-IPN are shown in Fig. 8.12(a) and (b), respectively. In the deformed image the distortion of speckles can be clearly seen in the vicinity of the propagating crack-tip. Fig. 8.13 shows the angular deflection contours measured using DGS at three different time instants. A clear increase in size of the contours can be seen with the passage of time suggesting an increase in SIF.

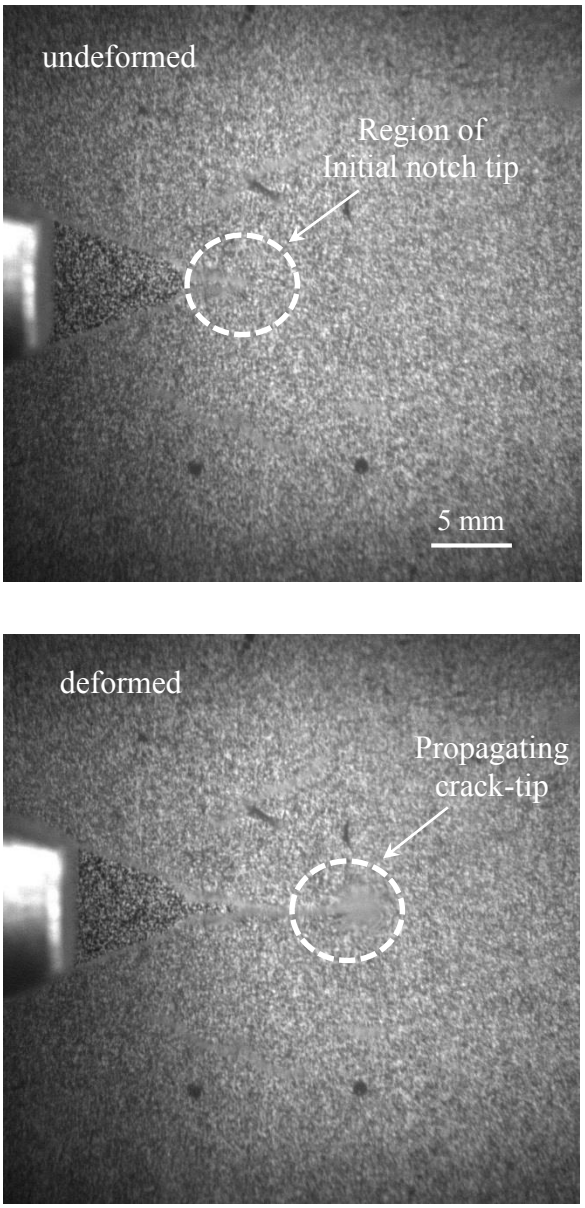

Figure 8.12: Speckle images in the undeformed (top) and deformed (bottom) states recorded by the high-speed camera though a select graft-IPN specimen (80:20 CoP:PU grade-1)

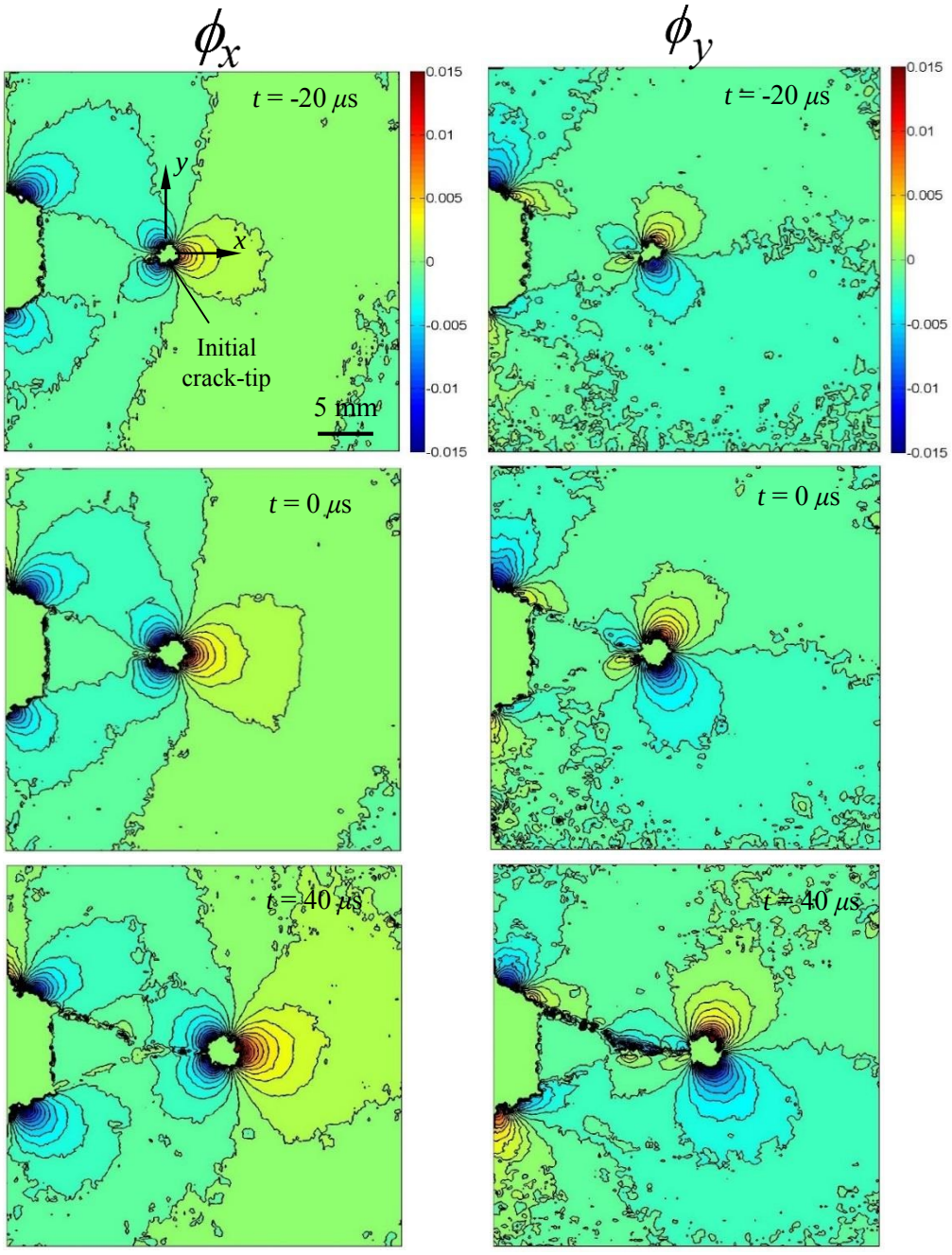

Figure 8.13: Angular deflection contour plots (contour interval = 1×10^{-3} rad) proportional to stress gradients of $\left(\sigma_x+\sigma_y\right)$ in the *x*- and *y*-directions for a select graft-IPN specimen (80:20grade-1). (Note that $t = 0$ in these correspond to the time instant at crack initiation.)

8.6.3 Crack velocity histories

Fig. 8.14(a) shows the crack velocity histories for grade-1 graft-IPNs along with commercial PMMA. Here $t = 0$ denotes crack initiation at the original notch tip. It can be seen that after initiation the crack accelerated to attain a maximum velocity, followed by a steady but oscillatory velocity. As the PU content increased the velocity increased at 10% of PU but subsequently dropped sharply at 20% and later increased until 40% of PU (the maximum PU content studied). The steady state crack velocity for PMMA specimens were ~320 m/s whereas graft-IPNs show a velocity between 120-450 m/s with 80:20 composition having the lowest and 60:40 the highest. This suggests a potential change in micromechanism when the CoP:PU ratio reached 80:20. The variation of this steady state velocity is shown as function of CoP:PU ratio in Fig 8.14(b). Similar trends in velocity histories were seen for grade-2 graft-IPNs as well. The variation of its steady state crack velocity is shown in Fig. 8.15(a).

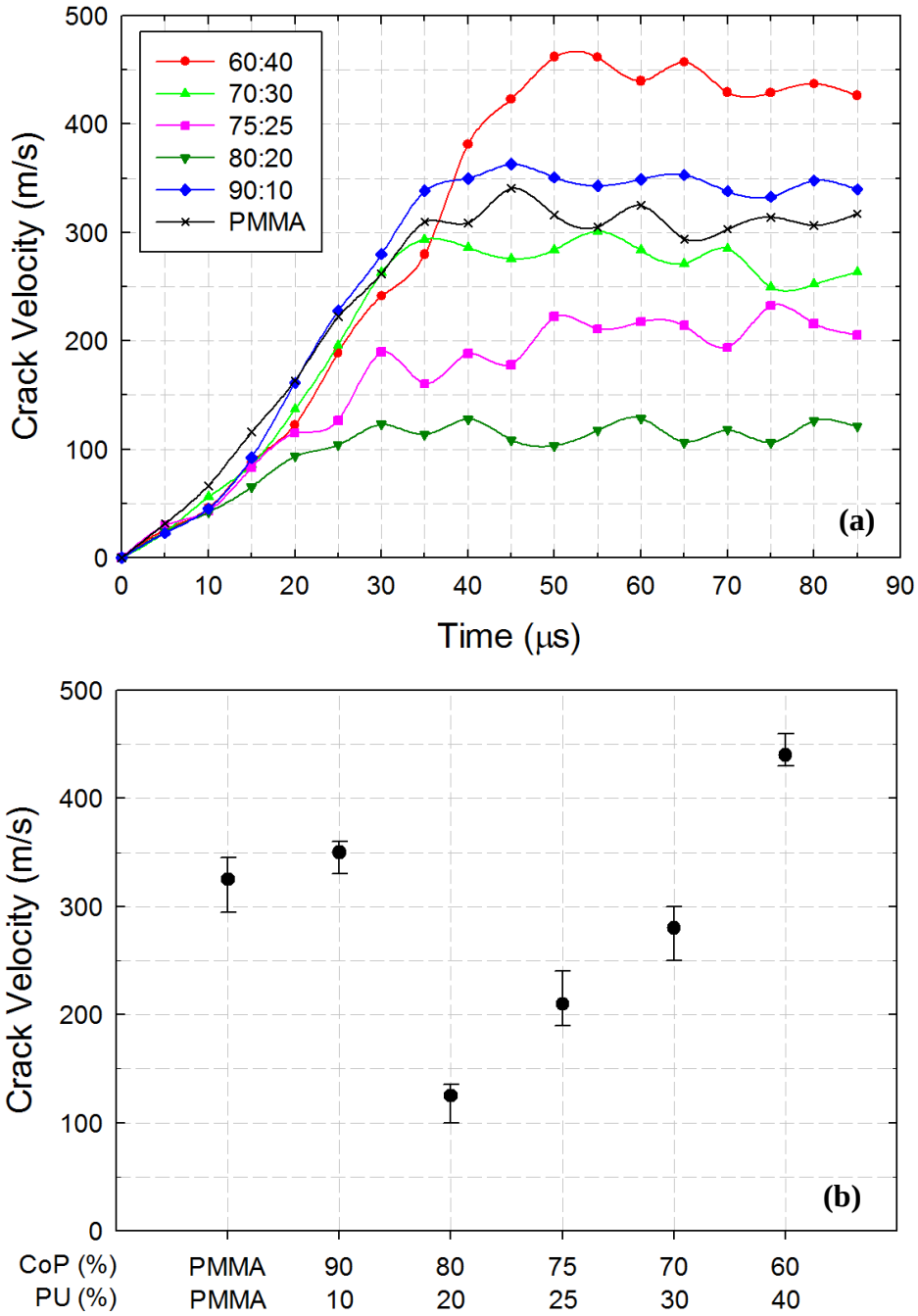

Figure 8.14: Crack growth behavior ofgrade-1 graft-IPNs: (a) Crack velocity histories and (b) steady state crack velocity variation (t = 0 corresponds to crack initiation.)

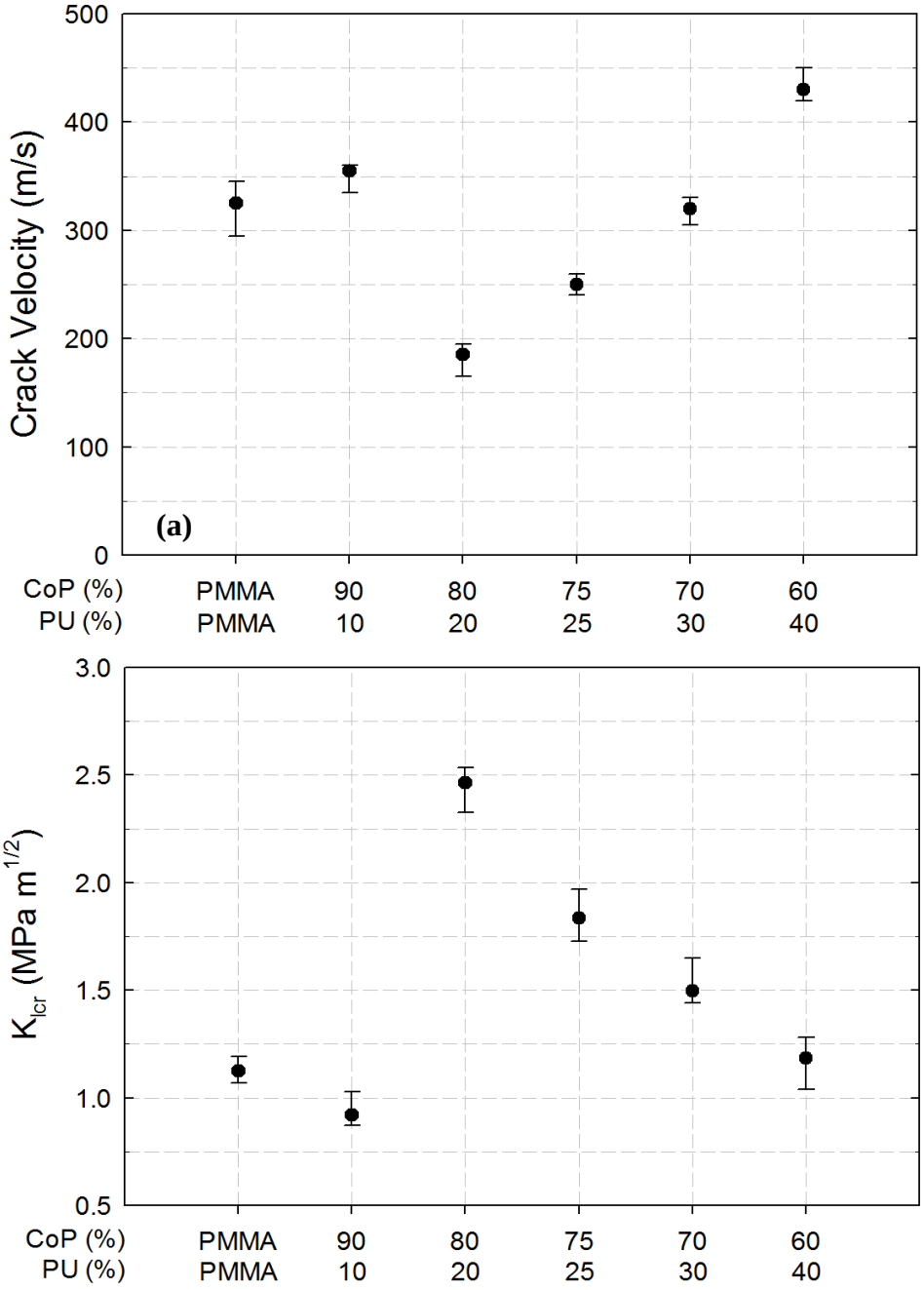

Figure 8.15: Variation of steady state crack velocity (a) and the corresponding dynamic K_{Icr} for grade-2 graft-IPNs (b).

8.6.4 Stress Intensity Factor (SIF) histories

The measured stress intensity factor histories for grade-1 graft-IPNs are shown in Fig 8.16(a). Time $t = 0$ represents the instant of crack initiation at the original sharpened notch tip. During the pre-initiation period, it can be seen that there is a monotonous increase in K_I (largely linear) until it reaches a critical value at which the crack initiates. This behavior is typical for all graft-IPN compositions. Further, there is a reduction in the overall SIF as the PU content is increased until 10% after which there is an increase until 20%, and later it again decreases until 40% (maximum PU content studied). This correlates well with the observed crack velocity histories. That is, as the crack velocity decreased the critical SIF values and hence resistance to crack growth increased showing a higher resistance to crack initiation and possibly growth resulting in slower speeds. Further, note that the 80:20 composition showed a delayed crack initiation compared to other compositions (say, 60:40) described by longer loading curve in the pre-initiation period indicating that the crack initiation can be altered by changing the CoP:PU ratio. The SIF at crack initiation for various compositions are shown in Fig 8.16(b). When compared with PMMA (1.08 MPa√m), the optimum composition of 80:20 (3.12 MPa√m) show ~190% improvement in K_{Icr}. These trends can be observed in both pre-initiation and post-initiation regimes. When compared with the K_{Icr} for polycarbonate (2.27 MPa √m) reported by Sundaram and Tippur [99] under similar loading conditions, the 80:20 composition showed ~38% improvement and 75:25 showed a similar result (2.08 MPa √m). Hence some compositions of graft-IPNs have a fracture response similar to if not better than those for commercially procured polycarbonate. The SIF histories of grade-2 graft-IPNs show

similar trend as that of the former. Fig 8.15(b) show the K_{Icr} for grade-2 graft-IPNs. Unlike the quasi-static results, under dynamic loading conditions, grade-1 graft-IPN performed better than grade-2 graft-IPN.

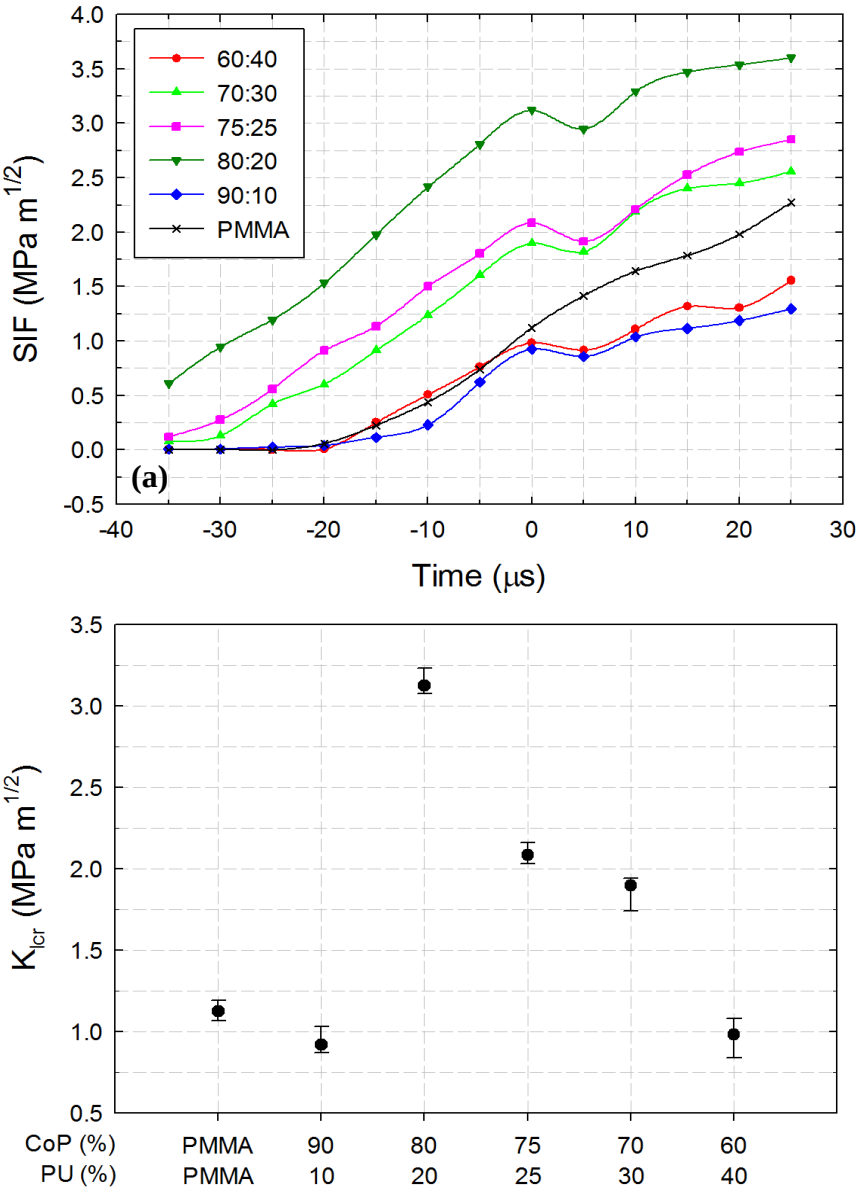

Figure 8.16: Dynamic fracture response of grade-1 graft-IPNs: (a) Dynamic stress intensity factor (SIF) histories and (b) variation of K_{Icr} with composition. ($t = 0$ corresponds to crack initiation).

8.6.5 Fracture surface morphology

Scanning electron microscopy (SEM) was performed on fractured surfaces to understand the mechanism governing fracture in graft-IPNs. The SEM micrographs of the fractured surfaces for grade-2 of graft-IPNs are shown in Fig 8.17(a)-(d). It can be seen that regardless of the PU content, no significant effect on the surface roughness can be seen. This is unlike the work on IPNs by Bird et al. [80] where an increase in the fracture surface area with an increase in PU content correlated with the crack initiation toughness increase. Such a mechanism was not observed in case of graft-IPNs although a decrease in the elastic modulus and higher failure strain was observed with the increased PU content. These observations suggest that there is a need for further exploration into the mechanism governing the variation in fracture toughness observed in graft-IPNs.

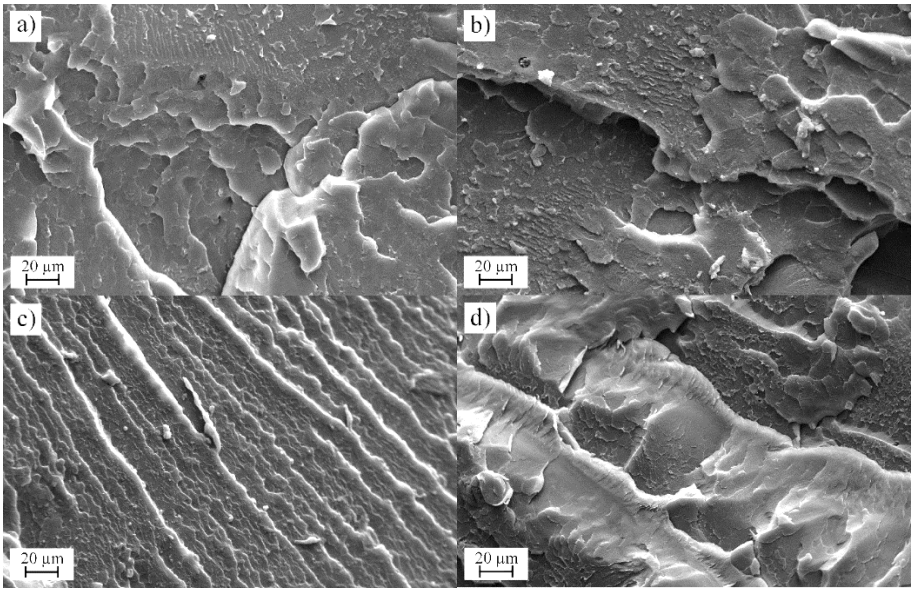

Figure 8.17: SEM photos of grade-2 graft-IPNs with CoP:PU ratios of (a) 60:40, (b) 70:30, (c) 80:20, and (d) 90:10 [125].

Chapter 9

CONCLUSIONS

In this research dynamic fracture of monolithic and layered transparent materials were investigated experimentally. The monoliths considered were PMMA, PC, glass, and graft-IPNs whereas the layered system consisted of PMMA bilayers. A full-field optical method called DGS that can measure angular deflections of light rays propagating through transparent phase solids was used to quantify and visualize deformations. A methodology involving DGS was successfully developed to evaluate stress intensity factors (or SIFs) of a stationary and growing crack-tip subjected to static or dynamic mixed-mode loading conditions. The newly developed methodology was calibrated first using a tensile specimen with an inclined edge crack subjected to far field quasi-static stress. The mixed-mode SIFs were successfully evaluated. Later, dynamic fracture experiments on SEN specimens subjected to eccentric loading were carried out. Both mode-I and mode-II SIFs during the loading phase and during the propagation phase of the crack-tip were evaluated. The SIFs evaluated from both quasi-static and dynamic tests were compared with numerical simulations and a good agreement was demonstrated. The SIF data at crack initiation was used to establish a fracture envelope for both PMMA and PC.

The experimental approach was used subsequently to examine the interaction of dynamically growing crack in PMMA bilayers with discrete plane of weakness made by

joining two PMMA plates along a straight interface using an acrylic adhesive. Further, the thickness of the interface was controlled from 25 μm to 1300 μm to vary the fracture toughness. Two specific interface thicknesses, 25 and 100 mm and identified as 'strong' and 'weak' interface, were subsequently used in this research. The acrylic adhesive was characterized for its elastic modulus relative to PMMA, and the interface was characterized for its mode-I and mixed-mode fracture toughness, tensile strength and shear strength. Both the 'strong' and 'weak' interfaces were weaker than virgin PMMA; the former had ~75% and the latter ~50% crack initiation toughness relative to PMMA monoliths under quasi-static conditions. Unlike monolithic specimens, a mode-I crack branched at the interface and mixed-mode crack propagation ensued in layered counterparts. These experiments were accomplished using a gas-gun assisted long-bar impactor with a wedge shaped tip pressed into a matching V-notch cut along the edge of bilayer specimen to dynamically initiate a mode-I crack in the first layer that propagated towards the interface. The SIF and crack velocity histories for growing cracks entering and exiting an interface as well as when trapped in the interface show significant gyrations. Final crack velocities/crack lengths observed in layered specimens suggest that interfaces can effectively obstruct and perturb crack propagation in these elastically homogeneous architectures. The energy release rate for branched cracks in both 'strong' and 'weak' interface cases was lower than the monolithic counterpart at advanced stages of crack growth; the final value of energy release rate for the 'weak' and 'strong' interfaces were lower than the monolithic case by ~54% and ~52 %, respectively with former attaining the value much earlier. Further, the higher mode-mixity and strain energy release rate throughout the fracture event in the specimen

with a ‘weak’ interface (relative to the ‘strong’ interface) showed it to be a more favorable configuration. More importantly, the higher energy absorption was achieved without altering the weight or the overall geometry of the configuration.

In the second part of this dissertation, the underlying crack penetration vs. branching mechanics of the observed crack growth morphology during dynamic fracture of PMMA bilayers was investigated. Dynamic penetration and bifurcation of a mode-I crack upon its arrival at the interface were produced in a controlled manner by positioning the interface at four different distances from the initial crack-tip. The deformations in the crack-tip vicinity were quantified again using DGS and ultrahigh-speed photography. The optical measurements were used in conjunction with the prevailing crack-tip field descriptions to extract stress intensity factors along with crack length and velocity histories during the dynamic event. The mechanical properties of the adhesive evaluated earlier were used to explain the witnessed phenomena and a rich array of fracture mechanics. The major observations and conclusions of this part are as follows:

- The mode-I crack penetrated the interface and the second layer (layer-II) of the bilayer did not perturb the crack growth morphology when the interface was located near the initial crack-tip. On the other hand, when the interface was located farther away from the initial crack-tip, the mode-I mother crack bifurcated into two interfacial cracks that propagated in opposite directions by nearly equal amounts and then penetrated the second layer as two mixed-mode daughter cracks all the while maintaining global symmetry relative to the loading/specimen geometry.

- In cases when the mode-I mother crack bifurcated at the interface, the amount of interfacial crack growth increased with the initial distance of the interface whereas the kink angle of the daughter cracks and hence the mode-mixity of the penetrated cracks as they entered the second layer decreased. Eventually, both daughter cracks showed a tendency to attain a mode-I condition.

- From the measured crack velocity histories it was observed that the crack simply penetrated the interface and the second layer as a single mode-I crack when the crack velocity upon its arrival at the interface was the lowest among the four cases whereas it bifurcated and grew interfacially before producing two daughter cracks in the second layer at higher incident velocities.

- The stress intensity factor histories examined in conjunction with the dynamic crack-tip fields suggest that at higher incident crack velocities, the interface directly ahead of the crack-tip experienced a large enough tensile stress, exceeding the strength of the interface, resulting in the nucleation of a debond *before* the arrival of the mode-I mother crack, causing two interfacial daughter cracks to grow in opposite directions along the interface. The amount of interfacial crack growth increased with the incident crack velocity and continued until they penetrated the second layer when it became energetically favorable. That is, due to competition between mixed-mode crack growth along the interface and mixed-mode crack growth into the subsequent (second) layer.

- An interesting empirical observation involving the resultant (effective) stress intensity factor and crack velocity at the instant of crack incidence on the

interface in each of the three branched crack configurations showed the product $K_{eff} \times V$ to be nearly a constant. Further, the corresponding values for each branched mixed-mode daughter crack when the second layer was penetrated were approximately one half of the corresponding incident value of $K_{eff} \times V$. The implications of this observation are, however, mechanistically unclear at the moment but are worth further exploration.

- Increase in impact velocity increased the propensity for crack branching. This was observed for multiple configurations consisting of bilayers with varied interface strength and interface position. Yet, the crack branching vs. penetration mechanism proposed earlier governed the observed fracture behavior when the impact velocity was varied.

In the third part of the dissertation, the feasibility of DGS to measure impact induced deformations and deformations around a crack-tip under quasi-static and dynamic loading conditions in soda-lime glass has been investigated. The 2D DIC, which is widely used these days to study dynamic fracture behavior of solids was used first and its limitations for this material system were realized. Accordingly, the feasibility of using DGS to study this challenging problem was explored. Typical challenges of studying failure of high stiffness and low toughness transparent ceramics using full-field speckle-based optical methods have been successfully overcome. The feasibility of DGS to map stress gradient fields due to quasi-statically applied line-load on the edge of a uniformly supported plate and on a symmetrically bent beam with a single edge notch was demonstrated first. The full-field measurements have been analyzed to back calculate the applied load and mode-I stress intensity factor, respectively, in these configurations with

good accuracy. Subsequently, the viability of DGS has been demonstrated for stress wave loading conditions using ultrahigh-speed digital photography at 1 million frames per second. In these experiments, stress gradient fields due to a transiently applied line-load on the edge of a free standing glass plate have been mapped first. The measured fields have been analyzed over-deterministically using least-squares method to evaluate applied force history which was found to match well with the counterparts measured using strain gage instrumentation. Next, the crack-tip fields generated during reverse impact on an edge cracked plate have been mapped using DGS in conjunction with ultrahigh-speed photography. The evolution of instantaneous optical fields around the crack-tip has been visualized up to crack initiation and during fast fracture. The challenges associated with locating the crack-tip when a sharp crack grows in glass at speeds in excess of 1500 m/s have been addressed and mode-I stress intensity factor histories have been successfully extracted. The two orthogonal stress gradient fields have been used in conjunction with a higher order least least-squares integration scheme to obtain $\left(\sigma_x + \sigma_y\right)$ maps around rapidly moving crack-tip.

In the next part, the dynamic crack branching problem in brittle monolithic solids was examined by studying soda-lime glass. The crack velocity and SIF histories during propagation leading to branching and post branching period were evaluated. The instabilities in crack propagation were observed at crack speeds of ~1600 m/s characterized by vthe increased surface roughness. Further, the mother crack was observed to slow down just prior to the occurrence of branching. The transition of surface roughness from “mirror” to “mist” to “hackle” appearance and finally back again to “mirror” after branching was

observed. The SIFs were observed to increase monotonically until crack branching. A sudden drop by ~50% of its pre-initiation values was seen in the recorded SIFs soon after branching. Using the measured crack velocity and SIF histories, a mechanism of defect nucleation and coalescence leading to crack branching is put forward. It consists of potential nucleation of micro cracks ahead of the mother crack propagating at very high speeds due to the normal stress in the growth direction and subsequent coalescence of the mother crack-tip with the micro crack-tip/s. A material based critical length scale (approx. 90 μm) for soda-lime glass has been identified as a characteristic associated with crack branching.

Finally, the fracture behavior of transparent graft Interpenetrating Polymer Networks (graft-IPNs) synthesized from acrylic copolymer (CoP) made of poly (methyl methacrylate) (PMMA) as the stiff phase and polyurethane (PU) as the ductile phase was examined. Various compositions of graft-IPNs used in this study were obtained by varying CoP:PU ratios and the mass density (650 g/mol and 1400g/mol) of poly(tetramethylene ether) glycol (PTMG) used. The graft-IPNs were first synthesized as rectangular sheets and the specimens were machined from them. Quasi-static tests were performed to evaluate the elastic modulus and mode-I crack initiation toughness followed by dynamic fracture tests. These quasi-static tests showed that an optimum ratio of CoP:PU equal to 70:30 enhanced the fracture toughness by ~130% when compared to PMMA especially with higher molecular mass PTMG. Under high strain rate loading, the 80:20 composition of graft-IPNs with 650 g/mol PTMG showed the highest fracture toughness improvement of ~170% over PMMA and ~38% over commercial PC (Lexan 9034).

9.1 Future work

In the initial part of this research, DGS was extended to study mixed-mode fracture under both quasi-static and dynamic loading conditions and was calibrated using PMMA. This methodology is very powerful and can be used for studying dynamic fracture problems in other transparent structural polymers such as homalite-100, PVB, PC, etc. and transparent ceramics namely glass, sapphire, quartz, etc. Further, as transparency is relative to the wave length of light used, this methodology to study fracture can be potentially extended to some materials that are opaque in the visible wave length but transparent in others such as infrared. For example, silicon which is opaque in the visible wave lengths is transparent in the infrared wave lengths.

The mechanism of dynamic crack interaction with a weak interface was studied in PMMA bilayers. Again, this can be extended to other bilayers and with different interface strengths and characteristics. They could also be bi-material systems such as PMMA-PC or PC-glass systems similar to the ones found in many real world systems such as toughened glass. Further, multi-layered structures could be investigated to increase energy absorption due to impact and cause crack arrest.

DGS measures gradients of in-plane normal stresses $\left(\sigma_x + \sigma_y\right)$. This data can be integrated numerically to obtain $\left(\sigma_x + \sigma_y\right)$ equal to $\left(\sigma_1 + \sigma_2\right)$ for plane stress. As the optical technique of photoelasticity can measure the in-plane maximum shear stress, $\left(\sigma_1 - \sigma_2\right)/2$, these two techniques can be combined to obtain the principle stresses. Further details on some of these future works are described in Appendix-A.

REFERENCES

[1] M. R. Edwards, "Land-based military application," in *Comprehensive Composite Materials-Vol 6*, Oxford, Elsevier Science, 2000, pp. 681-699.

[2] P. J. Hazell, M. R. Edwards, H. Longstaff and J. Erskine, "Penetration of a glass-faced transparent elastomeric resin by a lead-antimony-cored bullet," *International Journal of Impact Engineering,* vol. 36, no. 1, pp. 147-153, 2009.

[3] L. B. Freund, Dynamic fracture mechanics, New York: University Press, 1990.

[4] R. W. Hertzberg, Deformations and fracture mechanics of engineering materials, New York: Wiley, 1989.

[5] M. F. Kanninen and C. H. Popelar, Advanced fracture mechanics, New York: Oxford University Press, 1985.

[6] F. Erdogan and G. C. Sih, "On the crack extension in plates under plane loading and transverse shear," *Journal of Basic Engineering,* vol. 85, no. 4, pp. 519-525, 1963.

[7] K. B. Broberg, Cracks and fracture, San Diego: Academic Press, 1999.

[8] L. R. Xu, Y. Y. Huang and A. J. Rosakis, "Dynamic crack deflection and penetration at interfaces in homogeneous materials: Experimental studies and model predictions," *Journal of the Mechanics and Physics of Solids,* vol. 51, no. 3, pp. 461-486, 2003.

[9] P. G. Washabaugh and W. G. Knauss, "A reconciliation of dynamic crack growth velocity and Rayleigh wave speed in isotropic brittle solids," *International Journal of Fracture,* vol. 65, pp. 97-114, 1994.

[10] A. J. Rosakis, O. Samudrala and D. Coker, "Crack faster than shear wave speed," *Science,* vol. 284, pp. 1337-1340, 1999.

[11] S. Winkler, D. A. Shockey and D. R. Curran, "Crack propagation at supersonic velocities I," *International Journal of Fracture Mechanics,* vol. 6, pp. 151-158, 1970.

[12] G. Marder and S. Gross, "Origin of crack tip instabilities," *Journal of the Mechanics and Physics of Solids,* vol. 43, no. 1, pp. 1-48, 1995.

[13] F. F. Abraham, R. A. Brodbeck and W. E. Rudge, "Instability dynamics of fracture: A computer simulation investigation," *Physical Review Letters,* vol. 73, no. 2, pp. 272-275, 1994.

[14] A. Nakano, R. K. Kalia and P. Vashishta, "Dynamics and morphology of brittle cracks: A molecular-dynamics study of silicon nitride," *Physical Review Letters,* vol. 75, no. 17, pp. 3138-3141, 1995.

[15] S. N. Zhurkov, "Kinetic concept of the strength of solids," *International Journal of Fracture,* vol. 26, no. 4, pp. 295-307, 1984.

[16] D. R. Curran, D. A. Shockey and L. Seaman, "Dynamic fracture criteria for a polycarbonate," *Journal of Applied Physics,* vol. 44, no. 9, pp. 4025-4038, 1973.

[17] K. Ravi-Chandar and B. Yang, "On the role of microcracks in the dynamic fracture of brittle materials," *Journal of the Mechanics of Physics and Solids,* vol. 45, no. 4, pp. 535-563, 1997.

[18] J. W. Dally, "Dynamic photoelastic studies of fracture," *Experimental Mechanics,* vol. 19, pp. 349-381, 1979.

[19] A. S. Kobayashi and S. Mall, "Dynamic fracture toughness of Homalite-100," *Experimental Mechanics,* vol. 11, pp. 11-18, 1978.

[20] A. J. Rosakis and A. T. Zehnder, "On dynamic fracture of structural materials," *International Journal of Fracture,* vol. 27, pp. 169-186, 1985.

[21] K. Ravi-Chandar and W. G. Knauss, "An experimental investigation into dynamic fracture: I. Crack inititation and arrest," *International Journal of Fracture,* vol. 25, no. 4, pp. 247-262, 1984.

[22] K. Ravi-Chandar and W. G. Knauss, "An experimental investigation into dynamic fracture: II. Microstructural aspects," *International Journal of Fracture,* vol. 26, no. 1, pp. 65-80, 1984.

[23] K. Ravi-Chandar and W. G. Knauss, "An experimental investigation into dynamic fracture: III. On steady-state crack propagation and crack branching," *International Journal of Fracture,* vol. 26, no. 2, pp. 141-154, 1984.

[24] K. Ravi-Chandar and W. G. Knauss, "An experimental investigation into dynamic fracture: IV. On the interaction of stress waves with propagating cracks," *International Journal of Fracture,* vol. 26, no. 3, pp. 189-200, 1984.

[25] W. G. Knauss and K. Ravi-Chandar, "Some basic problems in stress wave dominated fracture," *International Journal of Fracture,* vol. 27, pp. 127-43, 1985.

[26] E. H. Andrews, "Stress waves and fracture surfaces," *Journal of Applied Physics,* vol. 30, no. 5, pp. 740-743, 1959.

[27] E. Sharon and J. Fineberg, "Microbranching instability and the dynamic fracture of brittle materials," *Physical Review B,* vol. 54, no. 10, pp. 7128-7139, 1996.

[28] E. Sharon, S. P. Gross and J. Fineberg, "Local crack branching as a mechanism for instability in dynamic fracture," *Physical Review Letters,* vol. 74, no. 25, pp. 5096-5099, 1995.

[29] E. B. Shand, "Experimental study of fracture of glass: I, the fracture process," *Journal of the American Ceramic Society,* vol. 37, no. 2, pp. 52-60, 1954.

[30] F. P. Bowden, J. H. Brunton, J. E. Field and A. D. Heyes, "Controlled fracture of brittle solids and interruption of electric current," *Nature,* vol. 216, pp. 38-42, 1967.

[31] J. Field, "Brittle fracture: Its study and application," *Contemporary physics,* vol. 12, no. 1, pp. 1-31, 1971.

[32] T. Cramer, A. Wanner and P. Gumbsch, "Crack velocities during dynamic fracture of glass and single crystalline silicon," *Physica status solidi,* vol. 164, no. 1, pp. R5-R6, 1997.

[33] W. Doll, "Investigation of the crack branching energy," *International Journal of Fracture,* vol. 11, pp. 184-186, 1975.

[34] S. Aratani, Y. Yamauchi, J. Kusumoto and K. Takahashi, "Dynamic fracture process of thermally tempered glass studied by the method of caustics," *Journal of the Ceramic Society of Japan,* vol. 101, no. 1175, pp. 804-808, 1993.

[35] N. Murphy, M. Ali and A. Ivankovic, "Dynamic crack bifurcation in PMMA," *Engineering Fracture Mechanics,* vol. 73, pp. 2569-2587, 2006.

[36] Y. B. Zhang, C. A. Tang, H. Li, Z. Z. Liang, S. B. Tang and Y. F. Yang, "Numerical investigation of dynamic crack branching," *International Journal of Fracture,* vol. 176, pp. 151-161, 2012.

[37] D. Xu, Z. Liu, X. Liu, Q. Zeng and Z. Zhyang, "Modeling of dynamic crack branching by enhanced extended finite element method," *Computational Mechanics,* vol. 54, no. 2, pp. 489-502, 2014.

[38] F. Armero and C. Linder, "Numerical simulation of dynamic fracture using finite elements with embedded discontinuities," *International Journal of Fracture,* vol. 160, pp. 119-141, 2009.

[39] J. Song, H. Wang and T. Belytschko, "A comparative study on finite element methods for dynamic fracture," *Computational Mechanics,* vol. 42, no. 2, pp. 239-250, 2008.

[40] P. D. Zavattieri, "Study of dynamic crack branching using intrinsic cohesive surface with variable initial elastic stifness," *GM Research & Development Centre,* pp. R&D-9650, 2003.

[41] F. Zhou and J. F. Molinari, "Dynamic crack propogation with cohesive elements: A methodology to address mesh dependency," *International Journal of Numerical Methods in Engineering,* vol. 59, pp. 1-24, 2004.

[42] G. Paulino, Z. Zhang and W. Celes, "Dynamic failure, branching and fragmentation using cohesive zone modeling," in *XVIII Convegno Nazionale IGF*, Cetraro, 2006.

[43] Y. D. Ha and F. Bobaru, "Studies of dynamic crack propagation and crack branching with peridynamics," *International Journal of Fracture,* vol. 162, no. 1, pp. 229-224, 2010.

[44] F. Bobaru and G. Zhang, "Why do cracks branch? A peridynamic investigation of dynamic brittle fracture," *International Journal of Fracture,* vol. 196, no. 1, pp. 59-98, 2015.

[45] X. Zhou, Y. Wang and Q. Qian, "Numerical simulation of crack curving and branching in brittle materials under dynamic loads using the extended non-ordinary state-based peridynamics," *European Journal of Mechanics A/Solids,* vol. 60, pp. 277-299, 2016.

[46] J. W. Hutchinson and Z. Suo, "Mixed mode cracking in layered materials," in *Advances in Applied Mechanics*, vol. 29, New York, Academic Press, 1991, pp. 63-191.

[47] S. Suresh, Y. Sugimura and E. K. Tschegg, "The growth of a fatigue crack approaching a perpendicularly-oriented, bimaterial interface," *Scripta Metallurgica et Materialia,* vol. 27, no. 9, pp. 1189-1194, 1992.

[48] V. B. Chalivendra and A. J. Rosakis, "Interaction of dynamic mode-I cracks with inclined interfaces," *Engineering Fracture Mechanics,* vol. 75, pp. 2385-2397, 2008.

[49] H. Park and W. Chen, "Experimental investigation on dynamic crack propagating perpendicular through interface in glass," *Journal of Applied Mechanics,* vol. 78, no. 5, 2011.

[50] J. Cook and J. E. Gordon, "A mechanism for the control of crack propogation in all-brittle systems," *Proceedings of the Royal Society A: Mathematical, Physical and Engineering Sciences,* vol. 282, no. 1391, pp. 508-520, 1964.

[51] M. Y. He and J. W. Hutchinson, "Crack deflection at an interface between dissimilar elastic materials," *International Journal of Solids and Structures,* vol. 25, no. 9, pp. 1053-1067, 1989.

[52] V. Gupta, A. S. Argon and A. Suo, "Crack deflection at interface between two orthotropic materials," *Journal of Applied Mechanics,* vol. 59, no. S2, pp. S79-S87, 1992.

[53] D. Leguillion, C. Lacroix and E. Martin, "Interface debonding ahead of a primary crack," *Journal of the Mechanics and Physics of Solids,* vol. 48, no. 10, pp. 2137-2161, 2000.

[54] J. P. Paramgiani and M. D. Thouless, "The role of toughness and cohesive strength on crack deflection at interfaces," *Journal of the Mechanics and Physics of Solids,* vol. 54, no. 2, pp. 226-287, 2006.

[55] S. Xia, L. Ponson and G. Ravichandran, "Toughening and symmetry in peeling of hetrogeneous adhesives," *Physical Review Letters,* vol. 108, no. 19, p. #196101, 2012.

[56] H. Tippur and A. J. Rosakis, "Quasi-static and dynamic crack growth along bimaterial interfaces: A note on crack-tip field measurements using coherent gradient sensing," *Experimental Mechanics,* vol. 31, no. 3, pp. 243-251, 1991.

[57] R. P. Singh, J. Lambros, A. Shukla and A. J. Rosakis, "Investigation of the mechanics of intersonic crack propagation along a bimaterial interface using coherent gradient sensing and photoelasticity," *Proceedings of the Royal Society of London A,* vol. 453, no. 1967, pp. 2649-2669, 1997.

[58] D. R. Curran, D. A. Shockey and S. Winkler, "Crack propagation at supersonic velocities II. Theoretical model," *International Journal of Fracture Mechanics,* vol. 6, pp. 271-278, 1970.

[59] L. R. Xu and A. J. Rosakis, "An experimental study of impact-induced failure events in homogeneous layered materials using dynamic photoelasticity and high-speed photography," *Optics and Lasers in Engineering,* vol. 40, pp. 263-288, 2003.

[60] J. Lambros and A. J. Rosakis, "Shear dominated transonic crack growth in bimaterial-I: Experimental observation," *Journal of the Mechanics and Physics of Solids,* vol. 43, no. 2, pp. 169-188, 1995.

[61] A. J. Rosakis, O. Samudrala, R. P. Singh and A. Shukla, "Intersonic crack propagation in bimaterial systems," *Journal of the Mechanics and Physics of Solids,* vol. 46, no. 10, pp. 1789-1813, 1998.

[62] D. Coker and A. J. Rosakis, "Experimental observation of intersonic crack growth in symmetrically loaded unidirectional composite plates," *Philosophical Magazine-A,* vol. 81, no. 3, pp. 571-595, 2001.

[63] L. R. Xu and P. Wang, "Dynamic fracture mechanics of failure mode transistions along weakened interfaces in elastic solids," *Engineering Fracture Mechanics,* vol. 73, no. 12, pp. 1597-1614, 2006.

[64] N. D. Parab and W. W. Chen, "Crack propagation through interfaces in a borosilicate glass and a glass ceramic," *International Journal of Applied Glass Science,* vol. 5, no. 4, pp. 353-362, 2014.

[65] M. Timmel, S. Kolling, P. Osterrieder and P. A. DuBois, "A finite element model for impact simulation with laminated glass," *International Journal of Impact Engineering,* vol. 34, no. 8, pp. 1465-1478, 2007.

[66] T. Siegmund, N. A. Fleck and A. Needleman, "Dynamic crack growth across interface," *International Journal of Fracture,* vol. 85, no. 4, pp. 381-402, 1997.

[67] W. Hu, Y. Wang, J. Yu, C. F. Yen and F. Bobaru, "Impact damage on a thin glass plate with a thin polymer backing," *Internationl Journal of Impact Engineering,* vol. 62, pp. 152-165, 2013.

[68] L. G. Liu, Z. C. Ou, Z. P. Duan, A. G. Pi and F. L. Huang, "Strain-rate effects on deflection/penetration of crack terminating perpendicular to bimaterial interface under dynamic loadings," *International Journal of Fracture,* vol. 167, no. 2, pp. 135-145, 2011.

[69] C. Vasile and A. K. Kulshreshtha, Handbook of polymer blends and composites, Shawbury: Rapra Technology Ltd., 2003.

[70] L. H. Sperling and V. Mishra, "The current status of interpenetrating polymer networks," *Polymers for Advanced Technologies 7,* pp. 197-208, 1996.

[71] J. R. Millar, "Interpenetrating polymer networks. Styreneodivinylbenzene copolymers with two and three interpenetrating networks, and their sulphonates," *Journal of the Chemical Society,* pp. 1311-1317, 1960.

[72] L. H. Sperling, Interpenetrating Polymer Networks and Related Materials, New York: Plenum Press, 1981.

[73] L. H. Sperling and D. W. Friedman, "Synthesis and mechanical behaviour of interpenetrating polymer networks: poly(ethyl acrylate) and polystyrene," *Journal of Polymer Science Part A-2: Polymer Physics,* vol. 7, no. 2, pp. 425-427, 1969.

[74] H. L. Frisch, D. Klempner and K. C. Frisch, "A topologically interpenetrating elastomeric network," *Journal of Polymer Science Part B: polymer Letters,* vol. 7, no. 11, pp. 775-779, 1969.

[75] N. Gupta and A. K. Srivastava, "Interpenetrating polymer networks: A review on synthesis and properties," *Polymer International,* vol. 35, no. 2, pp. 109-118, 1994.

[76] L. H. Sperling, Polymeric multicomponent materials: An introduction, New York: Wiley, 1997.

[77] X. Ramis, A. Cadento, J. M. Morancho and J. M. Salla, "Polyurathane-unsaturated polyester interpenetrating polymer networks: Thermal and dynamic mechanical thermal behaviour," *Polymer,* vol. 42, no. 23, pp. 9469-9479, 2001.

[78] C. H. Chen, W. J. Chen, M. H. Chen and Y. M. Li, "Simultaneous full-interpentrating polymer networks of blocked polyurethane and vinyl ester part I. Synthesis, swelling ratio, thermal properties and morphology," *Polymer,* vol. 41, no. 22, pp. 7961-7967, 2000.

[79] L. H. Fan, C. P. Hu and S. K. Ying, "Thermal Analysis during the formation of polyurethane and vinyl ester resin interpenetrating polymer networks," *Polymer,* vol. 37, no. 6, pp. 975-981, 1996.

[80] S. A. Bird, D. Clary, K. C. Jajam, H. V. Tippur and M. L. Auad, "Synthesis and characterization of high performance, transparent interpenetrating polymer networks with polyurethane and poly (methyl methacrylate)," *Polymer Engineering and Science,* vol. 53, no. 4, pp. 716-723, 2012.

[81] K. C. Jajam, S. A. Bird, M. L. Auad and H. V. Tippur, "Tensile, fracture and impact behaviour of transparent Interpenetrating Polymer Networks with polyurethane-poly(methyl methacrylate)," *Polymer Testing,* vol. 32, pp. 899-900, 2013.

[82] K. H. Hsieh and J. L. Han, "Graft interpentrating polymer networks of polyurethane and epoxy. II. Toughening mechanism," *Journal of Polymer Science Part B,* vol. 28, no. 6, pp. 783-794, 1990.

[83] K. H. Hsieh and J. L. Han, "Graft interpentrating polymer networks of polyurethane and epoxy. I. mechanical behaviour," *Journal of Polymer Science Part B,* vol. 28, no. 5, pp. 623-630, 1990.

[84] K. H. Hsieh, J. L. Han, C. T. Yu and S. C. Fu, "Graft interpenetrating polymer networks of urethane-modified bismaleimide and epoxy (I): mechanical behaviour and morphology," *Polymer,* vol. 42, no. 6, pp. 2491-2500, 2001.

[85] C. Periasamy and H. V. Tippur, "Full-field digital gradient sensing method for evaluating stress gradients in transparent solids," *Applied Optics,* vol. 51, no. 12, pp. 2088-2097, 2012.

[86] C. Periasamy and H. V. Tippur, "Measurement of orthogonal stress gradients due to impact load on a transparent sheet using digital gradient sensing method," *Experimental Mechanics,* vol. 53, no. 1, pp. 97-111, 2013.

[87] M. L. Williams, "On the stress distribution at the base of a stationary crack," *Journal of Applied Mechanics,* vol. 24, pp. 109-114, 1959.

[88] C. Periasamy and H. V. Tippur, "Measurement of crack-tip and punch-tip transient deformations and stress intesity factors using digital gradient sensing technique," *Engineering Fracture Mechanics,* vol. 98, pp. 185-199, 2013.

[89] H. V. Tippur, S. Krishnaswamy and A. J. Rosakis, "Optical Mapping of crack-tip deformations using the methods of transmission and reflection coherent gradient sensing," *International Journal of Fracture,* vol. 52, pp. 91-117, 1991.

[90] B. M. Sundaram and H. V. Tippur, "Dynamic crack growth normal to an interface in bi-layered materials: An experimental study using digital gradient sensing technique," *Experimental Mechanics,* vol. 56, pp. 37-57, 2016.

[91] R. J. Butcher , C. E. Rousseau and H. V. Tippur, "A functionally graded particulate composite: Preparation, measurements and failure analysis," *Acta Materialia,* vol. 47, no. 1, pp. 259-268, 1998.

[92] H. Prautzsch, W. Boehm and M. Paluszny, Bezier and B-spline techniques, Berlin Heidelberg New York: Springer-Verlag, 2002.

[93] K. C. Jajam and H. V. Tippur, "Role of inclusion stiffness and interfacial strength on dynamic matrix crack growth: An experimental study," *International Journal of Solids and Structures,* vol. 49, no. 12, pp. 1127-1146, 2012.

[94] B. M. Sundaram and H. V. Tippur, "Dynamics of crack penetration vs. branching at a weak interface: An experimental study," *Journal of the Mechanics and Physics of Solids,* vol. 96, pp. 312-332, 2016.

[95] C. E. Rousseau and H. V. Tippur, "Compositionally graded materials with cracks normal to the elastic gradient," *Acta Materialia,* vol. 48, pp. 4021-4033, 2000.

[96] M. S. Kiruguluge and H. V. Tippur, "Mixed-mode dynamic crack growth in functionally graded glass-filled epoxy," *Experimental Mechanics,* vol. 46, no. 2, pp. 269-281, 2006.

[97] Y. Li, N. Fantuzzi and F. Tarnabene, "On mixed-mode crack initiation and direction in shafts: Strain energy density factor and maximum tangential stress criteria," *Engineering Fracture Mechanics,* vol. 109, pp. 273-289, 2013.

[98] J. Krautkramer and H. Krautkramer, Ultrasonic testing of materials, Berlin: Springer-Verlag, 1990, pp. 13-14,533-534.

[99] B. M. Sundaram and H. V. Tippur, "Dynamic mixed mode fracture behaviours of PMMA and polycarbonate studied using digital gradient sensing," *Engineering Fracture Mechanics,* 2017.

[100] D. Rittel and R. Levin, "Mode-mixity and dynamic failure mode transitions in polycarbonate," *Mechanics of Material,* vol. 30, no. 3, pp. 197-216, 1998.

[101] C. T. Sun, Fracture Mechanics, Waltham: Academic Press, 2012.

[102] A. Faye, V. Parameswaran and S. Basu, "Effect of notch-tip radius on dynamic brittle fracture of polycarbonate," *Experimental Mechanics,* vol. 56, no. 6, pp. 1051-1061, 2016.

[103] L. Xu and H. V. Tippur, "Fracture parameters for interfacial cracks: An experiemental-finite element study of crack tip fields and crack initiation toughness," *Internation Journal of Fracture,* vol. 71, no. 4, pp. 345-363, 1995.

[104] N. P. O'Dowd, C. F. Shih and M. G. Stout, "Test geometries for measuring interfacial fracture toughness," *International Journal of Solids and Structures,* vol. 29, no. 5, pp. 571-589, 1992.

[105] W. C. Oliver and G. M. Pharr, "Measurement of hardness and elastic modulus by instrumented indentation: Advances in understanding and refinements to methodology," *Journal of Materials Research,* vol. 19, no. 1, pp. 3-20, 2004.

[106] W. C. Oliver and G. M. Pharr, "An improved technique for determining hardness and elastic modulus using load and displacement sensing indentation experiments," *Journal of Material Research,* vol. 7, no. 6, pp. 1564-1583, 1992.

[107] J. J. Mason, J. Lambros and A. J. Rosakis, "The use of a coherent gradient sensor in dynamic mixed-mode fracture mechanics experiments," *Journal of the Mechanics and Physics of Solids,* vol. 40, no. 3, pp. 641-661, 1992.

[108] R. Kitey and H. V. Tippur, "Dynamic crack growth past stiff inclusion:Optical investigation of inclusion eccentricity and inclusion matrix adhesion strength," *Experimental Mechanics,* vol. 48, no. 1, pp. 37-54, 2008.

[109] L. B. Freund and A. J. Rosakis, "The structure of the near-tip field during transient elastodynamic crack growth," *Journal of the Mechanics of Physics and Solids,* vol. 40, pp. 699-719, 1992.

[110] V. Chalivendra and A. Shukla, "Transient elastodynamic crack growth in functionally graded materials," *Journal of Applied Mechanics,* vol. 71, pp. 237-248, 2005.

[111] M. J. Maleski, M. S. Kirugulige and H. V. Tippur, "A method for measuring mode-I crack tip constraint under static and dynamic loading conditions," *Experimental Mechanics,* vol. 44, no. 5, pp. 522-532, 2004.

[112] B. Pan, K. Qian, H. Xie and A. Asundi, "Two-dimensional digital image correlation for in-plane displacement and strain measurement: a review," *Measurements Science and Technology,* vol. 20, no. 6, p. 062001 (17pp), 2009.

[113] M. S. Kirugulige, H. V. Tippur and T. S. Denny, "Measurements of transient deformations using digital image correlation method and high-speed photography: application to dynamic fracture," *Applied Optics,* vol. 46, no. 22, pp. 5083-5096, 2007.

[114] K. C. Jajam and H. V. Tippur, "Quasi-static and dynamic fracture behaviour of particulate polymer composites: A study of nano- vs. micro-size filler and loading-rate effects," *Composites: Part B,* vol. 43, pp. 3467-3481, 2012.

[115] D. Lee, H. V. Tippur and B. Phillip, "Quasi-static and dynamic fracture of graphite/epoxy composites: An optical study of loading-rate effects," *Composites: Part B,* vol. 41, pp. 462-474, 2010.

[116] G. C. Sih, Experimental evaluation of stress concentration and stress intensity factor, Boston: Martinus Nijhoff publishers, 1981.

[117] M. Creager and P. C. Paris, "Elastic field equations for blunt cracks with reference to stress corrosion cracking," *International Journal of Fracture Mechanics,* vol. 3, no. 4, pp. 247-252, 1967.

[118] C. Miao, B. M. Sundaram, L. Huang and H. V. Tippur, "Surface profile and stress field evaluation using digital gradient sensing method," *Measurement Science and Technology,* vol. 27, no. 9, p. 095203 (16pp), 2016.

[119] J. Fineberg, S. P. Gross, M. Marder and H. L. Swinney, "Instability in dynamic fracture," *Physical Review Letters,* vol. 67, no. 4, pp. 457-460, 1991.

[120] S. P. Gross, J. Fineberg, M. Marder, W. McCromick and H. L. Swinney, "Acoustic emissions from rapidly moving cracks," *Physical Review Letters,* vol. 71, no. 19, pp. 3162-3165, 1993.

[121] B. R. Baker, "Dynamic stresses created by moving crack," *Journal of Applied Mechanics,* vol. 29, no. 3, pp. 449-458, 1962.

[122] M. Ramulu and A. S. Kobayashi, "Dynamic crack curving-A photoelastic evaluation," *Experimental Mechanics,* vol. 23, no. 1, pp. 1-9, 1983.

[123] M. Ramulu, B. S. Kobayashi, S. J. Kang and D. B. Barker, "Further studies on dynamic crack branching," *Experimental Mechanics,* vol. 23, no. 4, pp. 431-437, 1983.

[124] A. A. Wereszczak, T. P. Kirkland, M. E. Ragan, K. T. Strong Jr., H. Lin and P. Patel, "Size scaling of tensile failure stress in a float soda-lime-silicate glass," *International Journal of Applied Glass Science,* vol. 1, no. 2, pp. 143-150, 2010.

[125] R. Ballestero, B. M. Sundaram, H. V. Tippur and M. L. Auad, "Sequential graft-interpenetrating polymer networks based on polyurethane and acrylic/ester copolymers," *eXPRESS Polymer Letters,* vol. 10, no. 3, pp. 204-215, 2016.

APPENDIX A

A1. Dynamic fracture of multi-layer PMMA

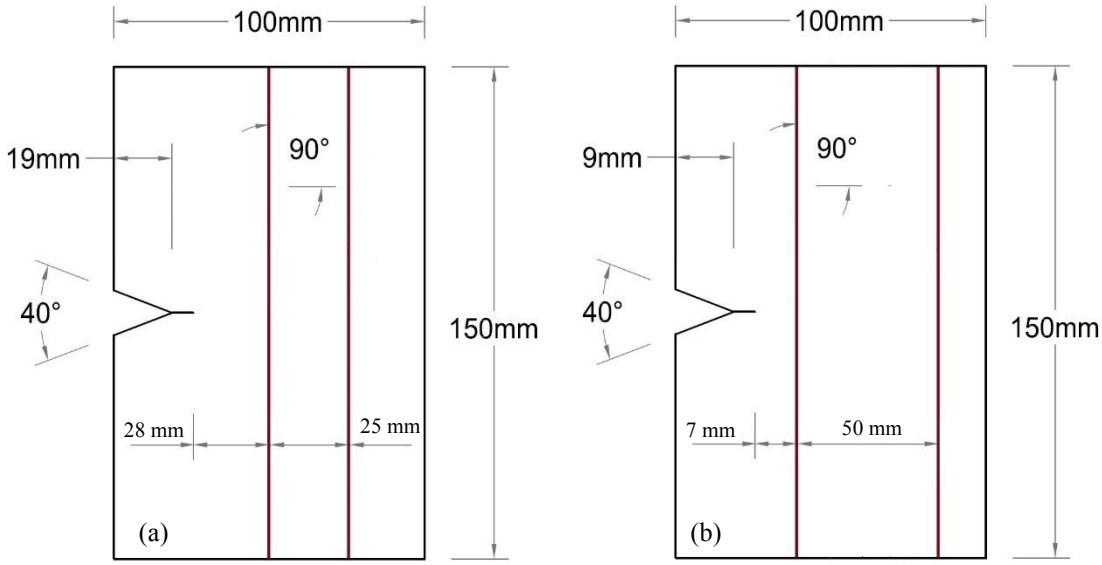

Figure A.1: Tri-layered PMMA Specimen geometry used for dynamic fracture study.

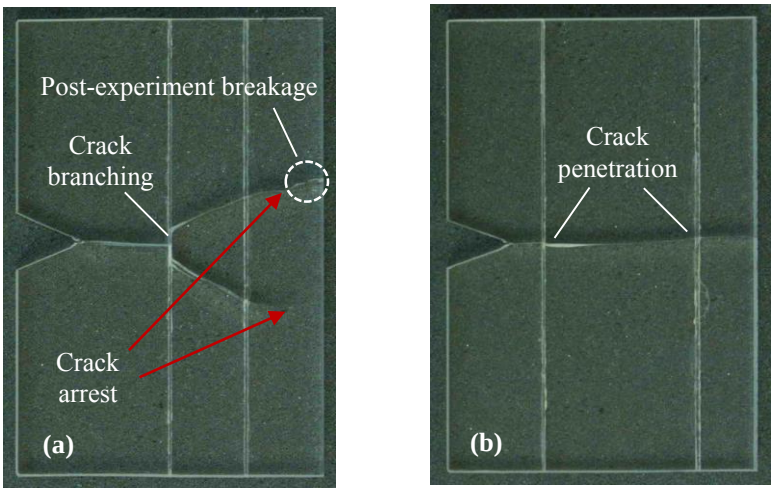

Figure A.2: Photograph of the fractured specimens.

Dynamic fracture behavior of some PMMA tri-layer configurations were initiated during this dissertation research. Tri-layered structures were made by bonding three strips of PMMA machined from cast acrylic sheet using acrylic adhesive Weldon 16 with an interface thickness of 100 μm to produce two nominally similar 'weak' interfaces in otherwise elastically homogeneous plate. The two specimen geometries studied are shown in Fig. A.1; config.1 (Fig. A.1(a)) and config.2 (Fig. A.1(b)). The specimen was dynamically loaded using Hopkinson pressure bar with a V-shaped wedge. The V-notch in the first layer of the specimen matched with that on the long-bar. For this experiment, both the striker and the long-bar were made from AL 7075-T6. The images were recorded at a slower rate of 100,000 frames per second in order to capture interactions over the entire specimen during the fracture event. Refer to Chapter 5 for other experimental details.

Figure A.2 shows the photographs of the fracture specimen of both the configurations. In Fig. A.2(a) it can be seen that the crack branched at the first interface whereas it penetrated the second interface. Subsequently the cracks arrested in layer-III. The region marked by the white open circle shows the fracture of the specimen due to post fracture events such as specimen falling/flying off the loading platform. In Fig. A.2(b), it can be seen that when the first interface is placed closer to the initial crack-tip, the crack penetrated the interface, which is consistent with the results presented in Chapter 5. As in the other configuration, the propagating crack did not branch when it encountered the second interface. As shown in Chapter 5, it is attributed to the lower velocity when the crack impinged on the second layer. Fig. A.3 shows the crack velocity and SIF history for the tri-layered config. 1.

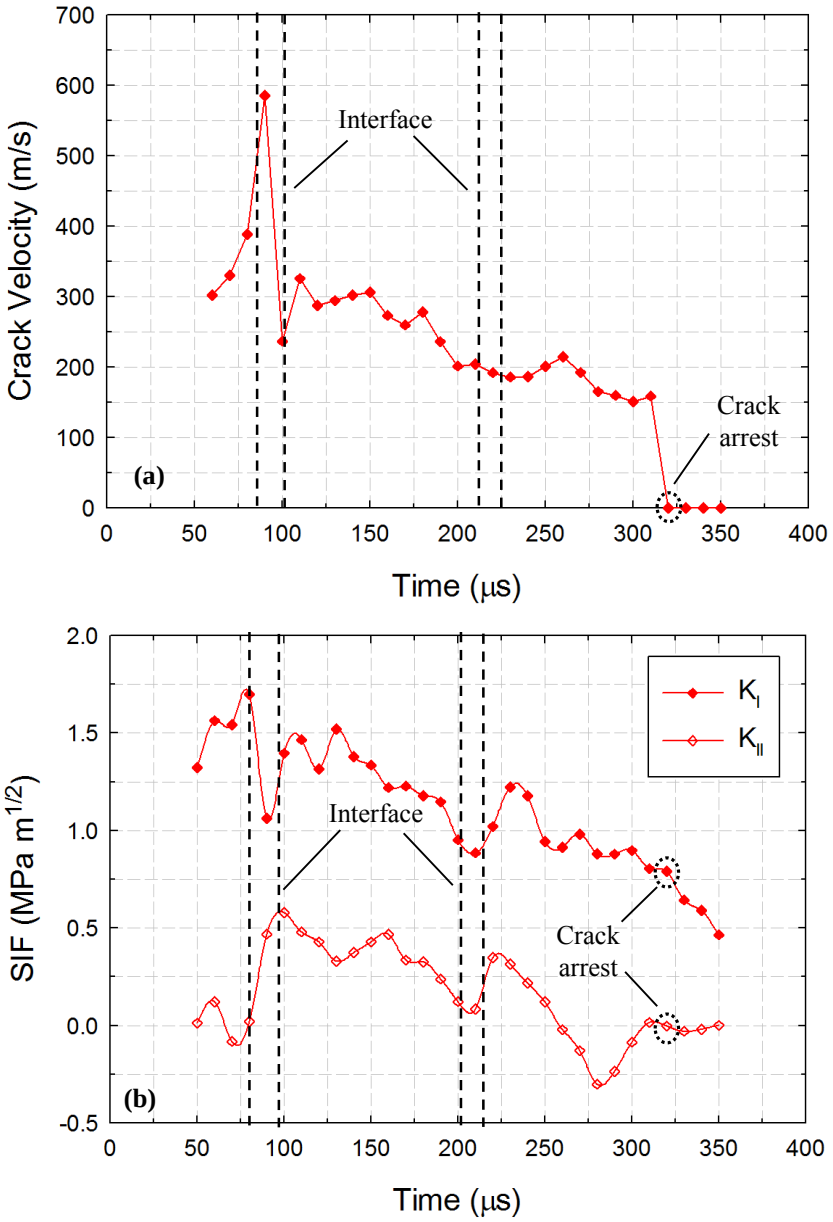

Figure A.3: The velocity and SIF histories for the config. 1 of tri-layered PMMA structure.

From the velocity history shown in Fig. A.3(a) it can be seen that the crack-tip velocity before encountering the first interface was ~380 m/s resulting in crack branching. As it reached the second interface, the velocity reduced to ~200 m/s leading to direct crack

penetration. This is consistent with the mechanism postulated and demonstrated in Chapter 5. Similar observation can be made for SIF histories as well. After the crack penetrated the second interface into layer-III the crack arrest occurred. It should be noted that there was no significant drop in crack velocity before crack arrest whereas SIF dropped down gradually leading to crack arrest. This observation is similar to the ones made by Ravi-Chandar and Knauss in their report [21]. This being a feasibility study where the dynamic fracture study of tri-layered structure is demonstrated with the observation of phenomena of crack arrest observed. This needs to be further investigated.

A2. Evaluation of principal stresses using DGS along with photoelasticity

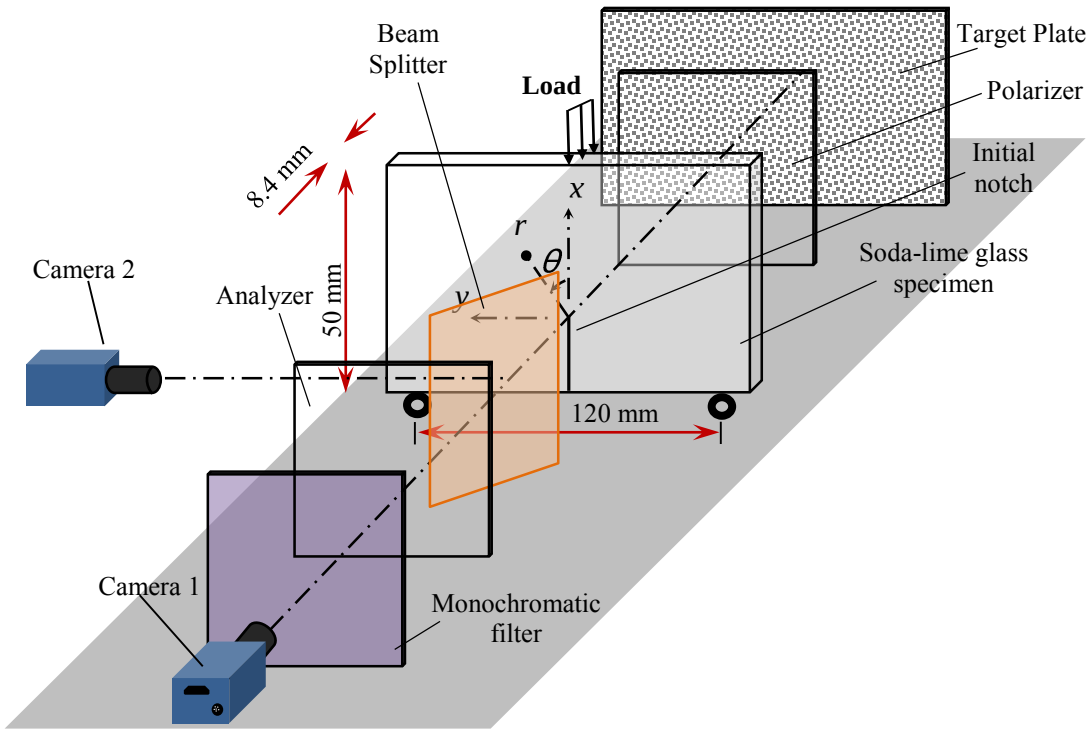

Figure A.4 : The schematic of experimental setup for DGS in conjunction with photoelasticity.

The feasibility of using DGS in conjunction with photoelasticity to evaluate the in-plane principal stresses was considered. The schematic of the experimental setup is shown in Fig. A.4. Camera #1 records the photoelastic fringes whereas camera #2 records angular deflections of light rays. The governing equation of DGS is

$$\phi_{x;y} = \pm C_\sigma B \frac{\partial(\sigma_1 + \sigma_2)}{\partial x; \partial y} \tag{A2.1}$$

where C_σ is the elasto-optic constant of the material, B is its initial thickness, and σ_1 and σ_2 denote thickness wise averages of principal stresses. By integrating the Eqn. A2.1 using HFLI [118] we can obtain,

$$\int \phi_{x;y} dx; dy = C_\sigma B(\sigma_1 + \sigma_2) + f(y); f(x), \text{ or}$$

$$\sigma_1 + \sigma_2 = \frac{\int \phi_{x;y} dx; dy - f(y); f(x)}{C_\sigma B} \tag{A2.2}$$

where, $f(y)$ or $f(x)$ are the constant of integration and that can be evaluated using boundary conditions of the problem. The governing equation for photoelasticity is,

$$\sigma_1 - \sigma_2 = \frac{N f_\sigma}{B} \tag{A2.3}$$

where σ_1 and σ_2 denote thickness wise averages of principal stresses, N is the fringe order, f_σ is the material fringe constant, and B is the specimen thickness. Using Eqns. (A2.2) and (A2.3) the principal stresses σ_1 and σ_2 can be separated.

Figure A.5 (a)-(c) shows the simultaneously measured photoelastic fringes and angular deflections in two orthogonal in-plane direction using DGS, respectively, for a 3-point bending sample with an edge crack in a polycarbonate sheet.

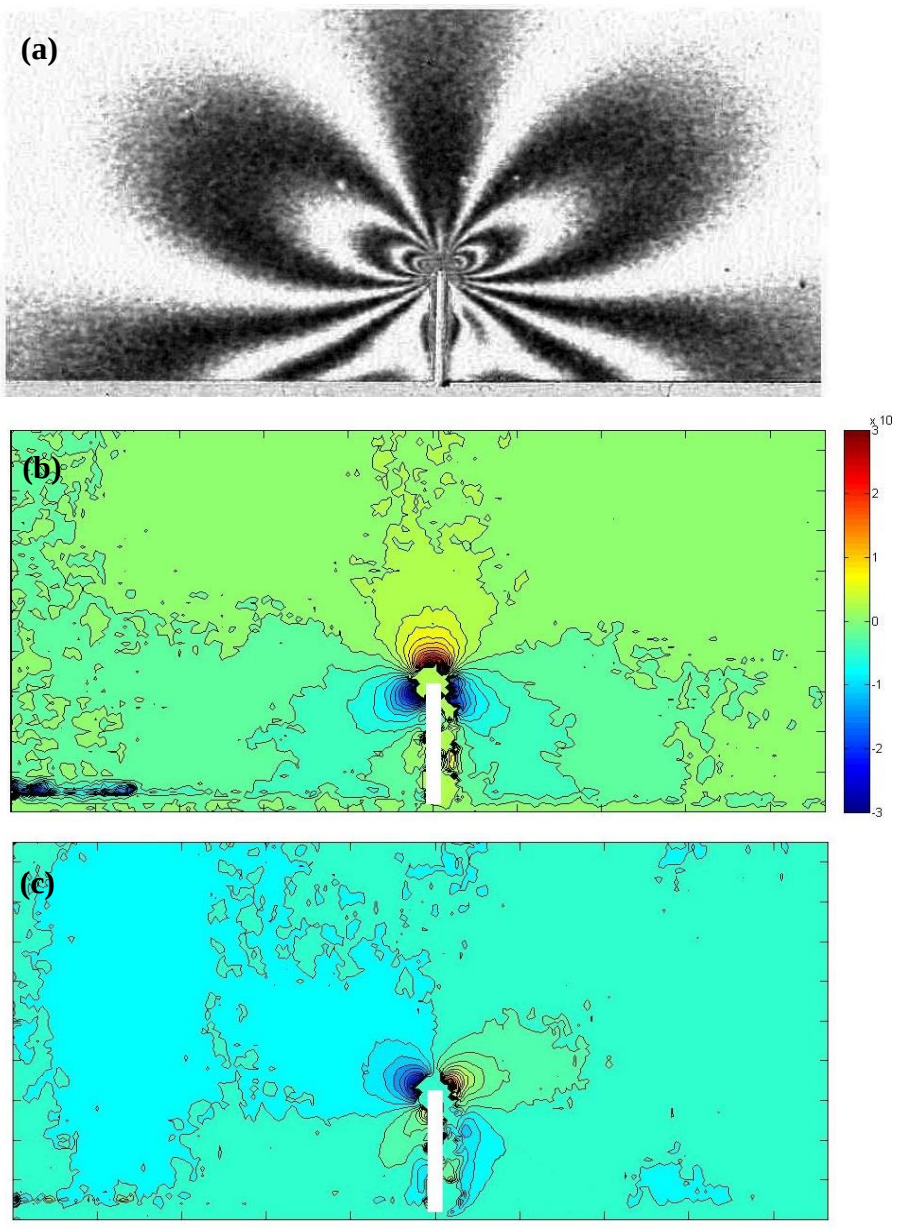

Figure A.5: Measured (a) photoelastic fringes, and (b) angular deflection fields along x-direction and (c) *y*-direction using DGS (contour interval = 5×10^{-4} rad), respectively, in a polycarbonate sheet.